3D in vitro Cancer Models

Combining Biophysical and Biochemical Cues

Rahman, Z.

DOI
10.4233/uuid:81eed34f-9885-494d-9927-b7d21fa0d597

Publication date
2024

Document Version
Final published version

Citation (APA)
Rahman, Z. (2024). *3D in vitro Cancer Models: Combining Biophysical and Biochemical Cues* . [Dissertation (TU Delft), Delft University of Technology]. https://doi.org/10.4233/uuid:81eed34f-9885-494d-9927-b7d21fa0d597

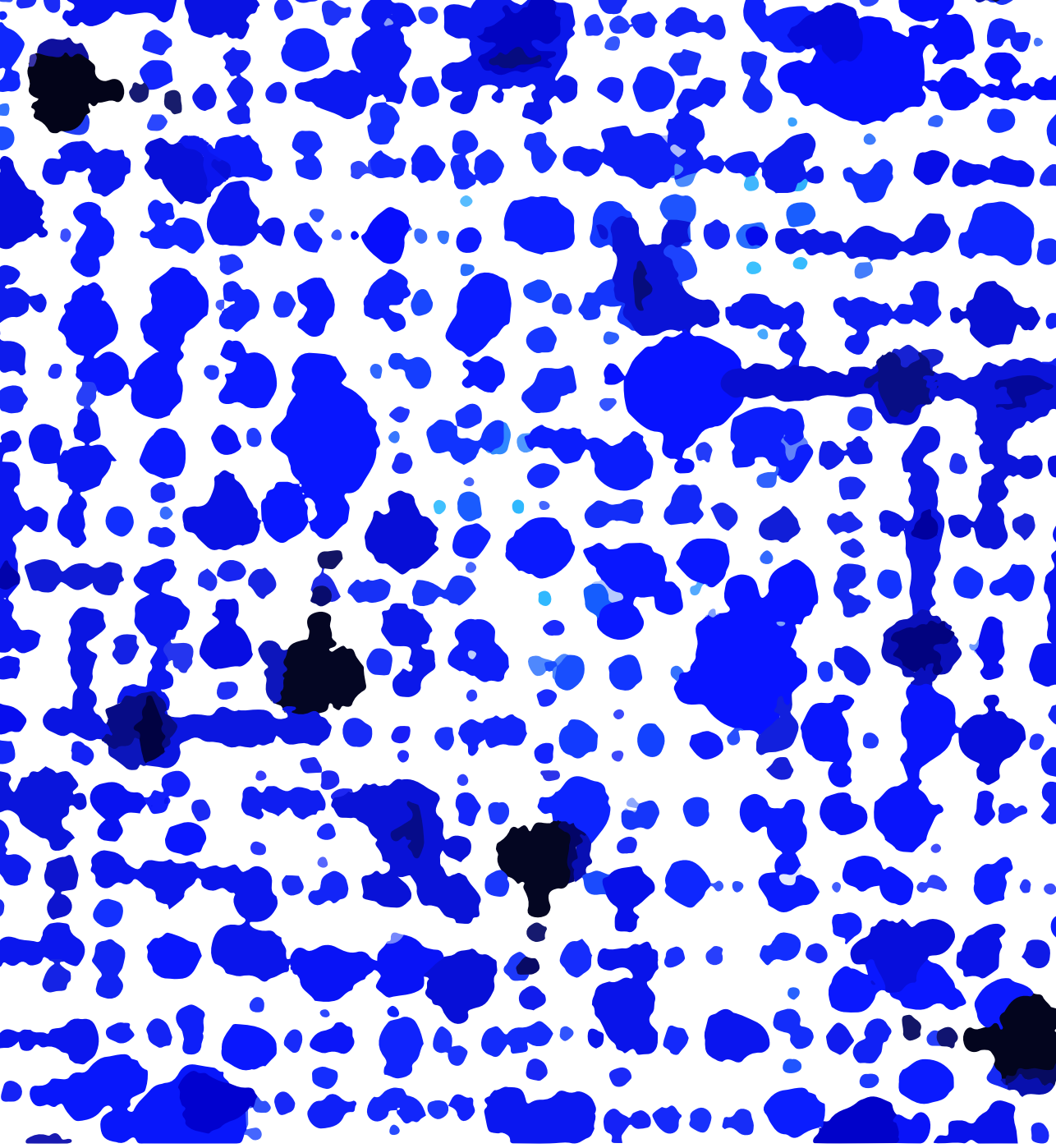

3D in vitro CANCER MODELS

Combining Biophysical and Biochemical Cues

Zaid Rahman

3D IN VITRO CANCER MODELS

COMBINING BIOPHYSICAL AND BIOCHEMICAL CUES

3D IN VITRO CANCER MODELS

COMBINING BIOPHYSICAL AND BIOCHEMICAL CUES

Dissertation

for the purpose of obtaining the degree of doctor
at Delft University of Technology,
by the authority of the Rector Magnificus Prof. dr. ir. T.H.J.J. van der Hagen,
chair of the Board for Doctorates,
to be defended publicly on
Wednesday 2 October 2024 at 12:30 o'clock.

by

Zaid RAHMAN

Master of Science in Nanotechnology,
University of Twente, The Netherlands
born in New Delhi, India.

The dissertation has been approved by

promotor: Dr. P.E. Boukany
promotor: Prof. dr. V. Garbin

Composition of the doctoral committee:

Rector Magnificus,	chairman
Dr. P.E. Boukany	Delft University of Technology (promotor)
Prof. dr. V. Garbin	Delft University of Technology (promotor)

Independent members:

Prof. dr. ir. M. Ottens	Delft University of Technology
Prof. dr. ir. S. Le Gac	University of Twente
Prof. dr. J. Prakash	University of Twente
Prof. dr. L. van der Laan	Erasmus Medical Centre
Prof. dr. F. Hollman	Delft University of Technology, reserve member

This work was financially supported the European Research Council.

Keywords: 3D-microfluidics, tumor microenvironment, interstitial flow, extracellular matrix, hydrogel, cancer invasion, cancer-cell signaling

Printed by: Gilderprint

Front & Back: An artistic impression of the tumor microenvironment and cancer cell invasion by Abhrojit Boral.

ISBN 978-94-6384-634-9

An electronic version of this dissertation is available at
http://repository.tudelft.nl/.

Dedicated to my family and my late grandmother,
Mrs. Ayesha Rehman.

CONTENTS

SUMMARY

Solid tumors represent about 85% of human cancers (for e.g. melanoma, breast, lung, colorectal and prostate cancer) and contribute to a majority of cancer-related mortality. These solid tumors are formed when a healthy cell undergoes several biological alterations and genetic mutations to proliferate uncontrollably. Eventually, cancer cells from the primary tumor spreads through the blood and lymph in the human body reaching distant organ(s), forming a secondary tumor, hence causing metastasis. The invasion of tumor cells is majorly assisted by the tumor microenvironment (TME). The TME consists of several cellular and non-cellular components that contributes towards cancer disease progression. For example, non-cellular component such as the extra-cellular matrix (ECM) or the surrounding tumor tissue that exerts mechanical compression on tumor cells. Another important biophysical factor such as interstitial flow (flow through porous ECM) leads to fluid-induced shear stress on tumor cells. These factors alter many cellular functions and upregulates several cancer-related genes. Additionally, certain biochemicals or cytokines (such as Transforming Growth Factor (TGF)-β or Matrix metalloproteases (MMP)) also play a significant role in modulating cancer-related genes and proteins. These factors collectively result in solid tumors to undergo invasion or an epithelial to mesenchymal transition (EMT), a biological phenomenon occurring in metastatic tumor cells. In a biophysical perspective, solid tumors show a transition from a jammed (non-invasive) to an unjammed (invasive) state where the cells can either migrate collectively (fluid-like) or individually (gas-like) through the surrounding tumor tissue.

In this dissertation, several 3-D in vitro platforms (including microfluidics) were developed to mimic the TME using natural and semi-synthetic hydrogels. These hydrogels recapitulated the ECM micro-architecture varying in stiffness and pore-size. A 3-D microfluidic device was used to generate varying interstitial flow (IF) through the porous hydrogel to recreate the complexity of TME. These models allowed us to investigate the role of biophysical and biochemical cues on cancer cell signaling and invasion activity. Using these platforms, we unraveled: i) a potentiating effect from interstitial flow on the TGF-β induced Smad-signaling activity and increased cell motility in lung cancers embedded in a 3-D microfluidic device (Chapter 3), ii) the pore-size and confinement of the ECM regulates invasion capacity of lung cancer (epithelial-like) and a melanoma (mesenchymal) cancer (Chapter 4) and iii) the unjamming transition of tumors embedded in a 3-D matrix is an interplay between the cell-matrix interactions (Chapter 4).

In chapter 2, we provided a future perspective on the current advancements in 3-D microfluidic platforms for cancer-on-a-chip models. These model systems allow for real-time imaging and quantification of cancer cell invasion activity. Moreover, 3-D microfluidics have additional advantages to recreate a TME with biophysical factors (for eg. compressive and shear stress components). Most importantly we discussed how conventional 2-D and *in vivo* models lack human physiological relevance where microfluidic systems can incorporate key TME components (cellular and non-cellular).

In chapter 3, we fabricated a 3-D microfluidic device and embedded multiple lung cancer spheroids in a semi-synthetic ECM exposed to varying IF. We combined IF with

cytokine (TGF-β) and monitored cell-signaling and invasion activity (over > 70 hours) with real-time imaging. We showed that interstitial flow has a potentiating effect on biochemical (TGF-β)-induced signaling pathway. This led to an enhanced signaling and cellular motion activity in lung spheroids. Moreover, we observed that this enhanced cellular activity is accompanied by an increased mass transport of cytokine to the spheroid core. Hence, a synergistic effect of biophysical and biochemical cues on tumor cells was observed.

Finally, in chapter 4 we investigated the effect of ECM mechanical properties (such as pore-size, density and stiffness) on tumor cell invasion capacity of lung and melanoma cancer spheroids. These spheroids were embedded in a 3-D in vitro model (using hydrogels) that allowed long term culture and imaging to quantify cell invasion. We showed that pore-size has a direct influence on the initiation of invasion in cancer spheroids whereas cell-intrinsic properties (such as enzyme secretion activity) determine the invasion rate. Finally, we extended our investigation to the universal framework of the biophysical phenomenon of jamming-unjamming transition. We developed a comprehensive phase diagram shedding light on the complex interplay of cell-intrinsic and ECM mechanical properties in tumor progression and invasion.

SAMENVATTING

Vaste tumoren vertegenwoordigen ongeveer 85% van menselijke kankersoorten (waaronder bijvoorbeeld huid-, borst-, long-, colorectale en prostaatkanker) en dragen bij aan het grootste deel van sterfte door kanker. Deze vaste tumoren vormen zich wanneer een gezonde cel verschillende biologische veranderingen en genetische mutaties ondergaat om ongecontroleerd te prolifereren. Uiteindelijk verspreiden kankercellen afkomstig van de primaire tumor zich via het bloed en de lymfe in het menselijk lichaam en bereiken verafgelegen organen om een secundaire tumor te vormen, ook wel uitzaaiing geheten. De invasie van tumorcellen wordt voornamelijk ondersteund door de tumormicroomgeving (TMO). De TMO bestaat uit verschillende cellulaire en niet-cellulaire componenten die bijdragen aan de progressie van kanker. Niet-cellulaire componenten zoals de extracellulaire matrix (ECM) of het omringende tumorweefsel oefenen mechanische druk uit op tumorcellen. Een andere belangrijke biofysische factor, interstitiële stroming (stroming door het poreuze ECM) leidt tot vloeistof-geïnduceerde schuifspanning op tumorcellen. Deze factoren veranderen veel cellulaire functies en upreguleren verschillende kankergerelateerde genen. Daarnaast spelen bepaalde biochemicaliën of cytokinen (zoals Transforming Growth Factor-β (TGF-β) of Matrix metalloproteasen (MMP)) ook een belangrijke rol bij het moduleren van kankergerelateerde genen en eiwitten. Deze factoren leiden er gezamenlijk toe dat vaste tumoren gaan uitzaaien, of een epitheliale naar mesenchymale transitie (EMT, een biologisch fenomeen dat optreedt bij metastatische tumorcellen) ondergaan. Vanuit een biofysisch perspectief vertonen vaste tumoren een overgang van een vastgelopen of in het Engels 'jammed' (niet-invasieve) naar een losgelopen 'unjammed' (invasieve) toestand waarbij de cellen ofwel collectief (vloeistofachtig) ofwel individueel (gasachtig) door het omringende tumorweefsel kunnen migreren.

In dit proefschrift werden verschillende 3D in vitro platformen (waaronder microfluïdica) ontwikkeld om de TMO na te bootsen met behulp van natuurlijke en semisynthetische hydrogels. Deze hydrogels bootsten de gevarieerde microarchitectuur van de ECM na, variërend in stijfheid en poriegrootte. Een 3D microfluïdisch apparaat werd gebruikt om een variërende interstitiële stroming door de poreuze hydrogel te genereren om de complexiteit van de TMO na te bootsen. Met deze modellen konden we de rol van biofysische en biochemische factoren op kankercelsignalering en invasieactiviteit onderzoeken. Met behulp van deze platformen ontrafelden we: i) een potentieel effect van interstitiële stroming op de TGF-β geïnduceerde Smad-signaalactiviteit en verhoogde celmotiliteit van longkanker ingebed in een 3D microfluïdisch apparaat (Hoofdstuk 3), ii) hoe de poriegrootte en opsluiting van het ECM de invasiecapaciteit van een longkanker (epitheliaal-achtig) en een melanoom (mesenchymaal) regelen (Hoofdstuk 4) en iii) dat de 'unjammed' overgang van tumoren ingebed in een 3D matrix een samenspel tussen de cel-matrix interacties is (Hoofdstuk 4).

In hoofdstuk 2 gaven we een toekomstperspectief op de huidige vooruitgang in 3D microfluïdische platformen voor kanker-op-een-chip modellen. Deze modelsystemen maken real-time beeldvorming en kwantificering van de invasieactiviteit van kankercellen mogelijk. Bovendien hebben 3D-microfluïdica extra voordelen om een TMO na

te bootsen met biofysische factoren (bijvoorbeeld druk- en schuifspanningscomponenten). Bovenal hebben we besproken hoe conventionele 2D- en in vivo modellen fysiologische relevantie missen voor de mens, terwijl microfluïdische systemen belangrijke TMO-componenten (cellulair en niet-cellulair) kunnen bevatten.

In hoofdstuk 3 hebben we een 3D microfluïdisch apparaat gemaakt waarin we meerdere longkankersferoïden hebben ingebed in een semi-synthetisch ECM en blootgesteld aan verschillende interstitiële stromingen. We combineerden deze stroming met een cytokine (TGF-β) en controleerden de celsignalering en invasieactiviteit (gedurende > 70 uur) met real-time beeldvorming. We toonden aan dat interstitiële stroming een versterkend effect heeft op de biochemische (TGF-β) geïnduceerde signaalroute. Dit leidde tot een verbeterde signalering en cellulaire bewegingsactiviteit in longsferoïden. Bovendien zagen we dat deze verhoogde cellulaire activiteit gepaard ging met een verhoogd massatransport van cytokinen naar de kern van de sferoïden. Er werd dus een synergetisch effect van biofysische en biochemische signalen op tumorcellen waargenomen.

Tot slot onderzochten we in hoofdstuk 4 het effect van mechanische eigenschappen van ECM (zoals poriegrootte, dichtheid en stijfheid) op de invasiecapaciteit van tumorcellen in long- en melanoomkankersferoïden. Deze sferoïden werden ingebed in een 3D in vitro model (met hydrogels) dat langdurige kweek en beeldvorming mogelijk maakte om de celinvasie te kwantificeren. We toonden aan dat de poriegrootte een directe invloed heeft op de initiatie van invasie in kankersferoïden, terwijl celintrinsieke eigenschappen (zoals de afscheiding van enzymen) de invasiesnelheid bepalen. Tot slot hebben we ons onderzoek uitgebreid naar het universele kader van het biofysische fenomeen van de 'jamming-unjamming' overgang. We ontwikkelden een uitgebreid fasediagram dat licht werpt op de complexe wisselwerking tussen cel-intrinsieke en ECM mechanische eigenschappen in tumorprogressie en invasie.

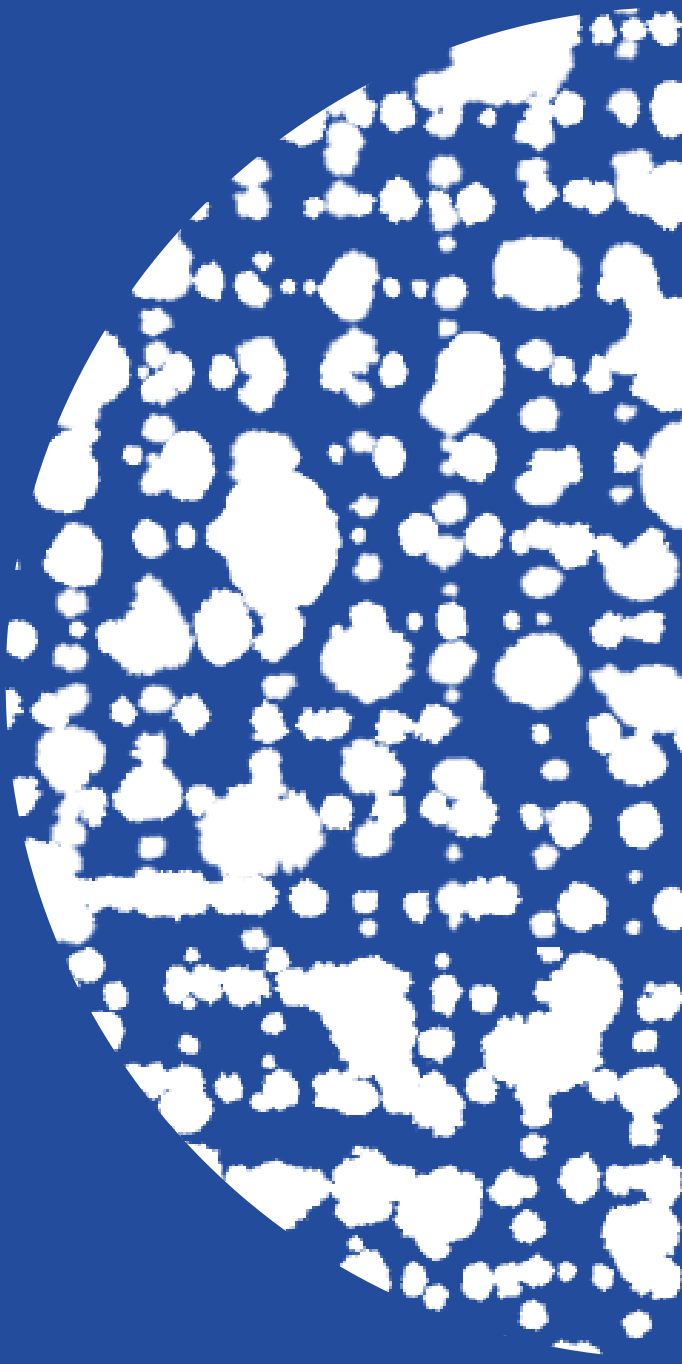

1

INTRODUCTION

1

In solid tumors such as lung or breast cancer, metastasis is the major cause in most cancer-related deaths due to its complexity and poorly understood biophysical and biological mechanisms [1]. Solid tumors eventually become metastatic as it undergoes a series of physiological events that remain undetected with current therapeutic regimens. Metastasis starts when cancer cells disseminate from a primary tumor and starts invading their surrounding tumor tissue, followed by intravasation of tumor cells into the blood vessels and lymphatic capillaries. These circulating tumor cells survive in the blood stream and travel to distant sites in the human body, extravasating at secondary sites and ultimately leading to the formation of a metastatic tumor [2], see Fig. 1.1. The metastatic cascade produces numerous biological alterations in healthy cells that are central in metastatic disease progression and its identification is critical for cancer-associated therapeutics. Moreover, in a recent report of 'Integraal Kankercentrum Nederland' (Netherlands Comprehensive Cancer Organisation) it is predicted that the number of cancer diagnoses in the Netherlands will increase with roughly 33% in the coming 10 years [3] creating an urgent need and importance to investigate the underlying biophysical mechanisms and therapeutic approaches for metastasis.

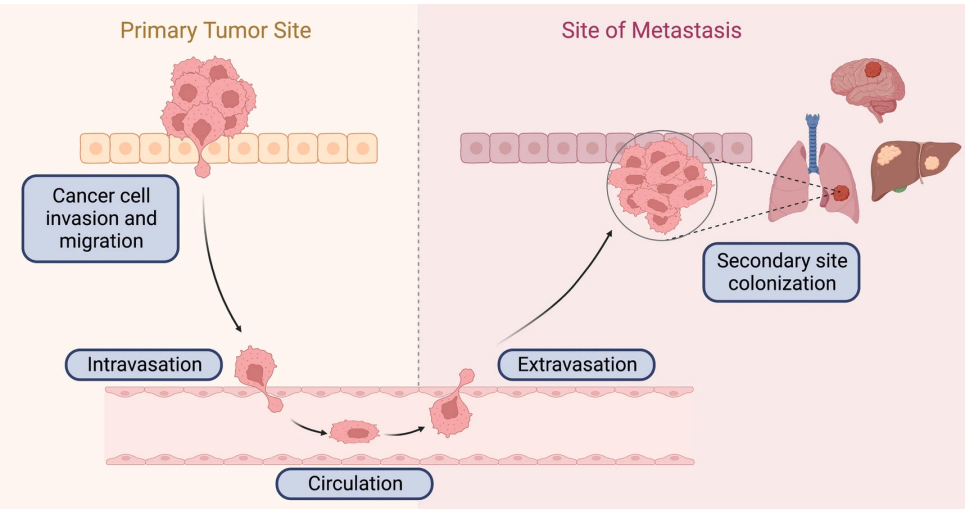

Figure 1.1: **Schematic of a typical cancer metastatic cascade.** Metastasis initiates with cancer cell invasion and terminates with colonizing a distant secondary organ (for e.g. lung, brain, liver). This process involves various biological events such as activation of metastasis-related genes (oncogenes) and cell-signaling pathways. These processes contribute to cancer cell growth, survival and invasion. Adapted from [4].

In the past, classical experimental approaches to study cancer cell invasion were mostly performed using in vitro; 2-D or 3-D cell cultures along with in vivo (animal or xenograft) models [5, 6]. In recent years, researchers and clinical professionals have collaborated to develop advanced 3-D in vitro models to mimic a physiologically relevant tumor microenvironment (TME). These 3-D in vitro models establish superiority over simplified 2D-culture and complex animal models [7]. In pre-clinical research settings, most studies now focus on mimicking the various components of the TME such as extracellular matrix (ECM) using hydrogel (naturally occurring or semi-synthetic); patient-

derived cancer cells to culture a 3-D cellular aggregate (commonly known as spheroids); biochemical compounds (such as cytokines and growth factors) and biophysical forces (for e.g. interstitial flow and compressive stress) [8–10]. These 3-D in vitro platforms promote interactions with cellular and non-cellular components of the TME that induce intra-cellular signaling events in cancer cells. One of the major advantages of 3-D in vitro platforms, such as microfluidics, is the capability to establish dynamic flow conditions mimicking the human tissue physiological conditions. Additionally, it enables real-time imaging to monitor cellular events and allows quantitative analysis such as cell invasion speed, morphology and directionality. Monitoring cellular motion and invasion activity allows a mechanistic understanding of cell migration events arising from cell-cell and cell-ECM interactions [7, 11, 12].

In the past decade, cancer cell invasion studies have been mostly performed using single cancer cells. This does not fully recapitulate the tumor physiological properties. Moreover, most studies reported the effect of biochemical response on the change in genetic/protein expression and failed to establish the interplay between biochemicals and biophysical forces on cancer invasion. Additionally, 3-D cancer invasion studies have poorly recapitulated the wide-ranging ECM mechanical determinants (stiffness, pore-size and density) and micro-architectural features that a cancer cell encounter during multiple stages of metastatic progression. This thesis focuses on developing physiologically relevant TME using 3-D in vitro platforms (including microfluidics) that combines ECM (natural and semi-synthetic hydrogels) and two different cancer cell types. These model systems further involved the use of biochemicals that allowed us to investigate their synergistic effect on cancer cell signaling and invasion activity. To achieve this, the following research questions were raised and addressed as individual chapters:

1. To what extent 3D-microfluidic models mimic the human tumor microenvironment complexities and what improvements are necessary to bridge the gap to preclinical settings ? (Chapter 2)

2. What is the effect of biophysical force (interstitial flow) on the biochemically induced cancer cell signaling and motility in lung tumor spheroids? (Chapter 3)

3. How does matrix mechanical properties (stiffness, pore-size and density) modulate spheroid invasion capacity ? (Chapter 4)

4. What is the key cell-intrinsic determinant (protein expression) and matrix parameter that influence an unjamming transition in spheroid invasion behavior ? (Chapter 4)

In the following sections, several important concepts in cancer cell invasion and its interaction with TME components relevant to the research questions proposed are introduced.

1.1. TUMOR MICROENVIRONMENT

Tumor microenvironment (TME) is an umbrella term used to address the various cellular and non-cellular components present in the formation and survival of a solid tumor. The cellular components are cancer cells, fibroblasts, immune cells (macrophages and

lymphocytes), endothelial cells and stromal cells, see Fig. 1.2. The non-cellular component is the extra-cellular matrix (ECM), made up of distinct compositions of naturally occuring hydrogels such as collagen, fibronectin, hyaluronan and many more [2]. Together they constitute the TME that shows a unique set of biophysical and biochemical characteristics. The TME undergoes dynamic physiological changes (remodelling and degradation) induced by the tumor cells to assist in tumor growth and invasion [13, 14]. These TME components form a suitable microenvironment that enables cell-cell and cell-matrix interactions (involving ECM) to drive inter and intra-cellular signaling events [2, 15]. Moreover, the TME also consists of growth factors, various cytokines and chemokines, and matrix remodeling enzymes that contribute towards interaction between cancer cells and their surrounding ECM [16]. The consequence of these cell-matrix interactions leads to a dynamic cross-talk that results in non-malignant cells to lose their primary function and acquire new phenotypes that contributes in invasion of tumor [17]. Additionally, growth of primary tumor results in formation of abnormal blood vessels (angiogenesis) and creating a hypoxic environment [18, 19]. Since TME plays an important role in cancer disease progression, many studies are developing targeted treatments that disrupts or interferes with tumor cell-ECM cross-talk [20]. To develop effective therapeutic strategies, decoupling TME components to identify complex signaling networks is essential for personalized therapy and drug development [21]. Recapitulating TME remains a major and important challenge to study cancer cell invasion in experimental models [22, 23]. In recent years, 3D platforms such as microfluidic devices have proven to be an efficient and reliable platform to better replicate the TME biology and functionality. These 3D platforms are promising alternatives to bridge the gap between research and pre-clinical settings for effective therapeutic strategies in the near future [20]. To address this in detail, **chapter 2** discusses the most important and recent developments in 3D matrix-based microfluidic approaches that involved the use of multiple TME components to investigate cancer cell invasion.

1.2. EXTRACELLULAR MATRIX

The extra-cellular matrix (ECM) is a complex bio-polymer network in the TME that plays a crucial role in cancer cell invasion [25]. In solid tumors, the ECM is a heterogeneous porous network that forms a 3D scaffold with distinct biomechanical characteristics such as viscoelasticity, stiffness and pore size [15]. These terms refer to the innate architecture of the ECM that comprises of fibrous proteins (collagen, elastin, hyaluronan) that gives mechanical strength (stiffness) or ability to undergo physical deformations [26]. The ECM is subjected to constant physical deformations induced by biomechanical and biochemical stimuli from cancer cells (referred to as remodelling) to assist in tumor invasion [27]. Cancer cells from a primary tumor exerts a biomechanical force (protease-independent) or it can secrete enzymes (such as matrix metalloproteases, MMPs) (protease-dependent) causing the ECM fibers to either remodel or degrade to create invasion tracks [16, 28]. Additionally, cancer associated fibroblasts (CAFs) present in the TME are known to produce high levels of ECM proteins and secrete MMPs that play a major role in ECM dysregulation [16]. On the other hand, cancer cells can sense local ECM membrane proteins through transmembrane integrin receptors that bind to specific adhesion ligands. Cell-matrix interactions may lead to activation of tran-

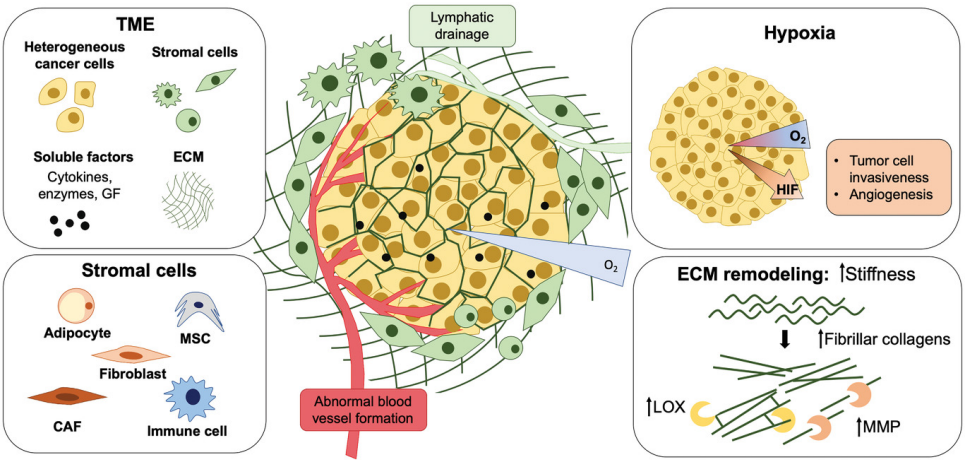

Figure 1.2: **Components of the tumor microenvironment (TME).** The dynamic interplay between different cellular components (cancer cells, stromal cells), cytokines and growth factors (GF) are major contributing factors for cancer cell proliferation and invasion. The result in tumor growth leads to formation of abnormal blood vessels (angiogenesis) and lymphatic drainage resulting in interstitial flow. These events additionally create a hypoxic environment that upregulate hypoxia-inducible factor (HIF). Lastly, cellular components interact with non-cellular components such as the extra-cellular matrix (ECM) through the release of lysl oxidase (LOX) and matrix metalloprotease (MMP) enzymes from cancer cells that degrade and remodel their surrounding microenvironment. This modification enables cancer cells to invade diverse ECM micro-architecture. Adapted from [24].

scription and translation events in cancer cells that may also lead to secretion and deposition of new matrix proteins [26]. As a result, tumor tissues are stiffer than healthy tissue counterparts as frequently observed in breast, liver and pancreatic cancer [29]. The increased stiffness is one of the major factors negatively impacting drug delivery efficacy [28]. Inflammatory cytokines such as transforming growth factor(TGF)-β (secreted by some cancer cells endogenously) acts potently on CAFs to enhance the synthesis of ECM proteins such as collagen [28]. The ECM additionally is subjected to a biophysical force, i.e. interstitial flow (IF) that creeps through the interstitial spaces arising from the leaky lymphatic and blood vessels in the tumor tissue. The change in ECM mechanical due to remodelling and degradation consequently leads to a disturbed fluid flow that leads to fluid deposition that ultimately increases the interstitial fluid pressure (IFP) [30]. This further upregulates the activity of endogenous TGF-β in cancer cells that subsequently activates CAFs to create a positive feedback loop [30].

1.3. INTERSTITIAL FLOW

Fluid-based mechanics (non-cellular component) in TME is one of the important contributing factor to assist in early invasion of cancer cells in primary tumours. In the case of metastasis, three main bodily fluids, blood, lymph and interstitial fluid are exploited by the tumour cells [31]. IF is defined as the movement of fluid between the interstitial spaces guided by the hydrodynamic and osmotic pressure differences through the ECM [32]. The interstitial fluid generated is a result of the cellular and high capillary blood

pressure in a solid malignant tumour, drained by the lymphatic capillaries at sites of lower pressures. The pressure gradient witnessed between the primary tumour site and the neighbouring tissue has an increased risk of metastasis [33]. In malignant tumours, interstitial flow rates are upto $1\,\mu m\,s^{-1}$ in humans and $10\,\mu m\,s^{-1}$ in animal models [30–32]. The interstitial fluid operates under laminar flow with a shear stress of $0.1 - 0.01$ Pa [31]. The increase in pressure is attributed to the continuous deposition of plasma in the extracellular space that is unable to drain due to the tumour growth-induced compression of non-functional lymphatic vessels [31]. An elevated interstitial fluid pressure (IFP) within the tumour causes limited efficiency towards drug delivery [31, 34]. In a TME, cancer cells may sense IF by the glycocalyx layer, integrin receptors or stretch activated ion-channels leading to the activation of adhesion complexes from tensile strain and membrane shear [30, 35]. It also leads to the changes in the distribution of ECM signaling proteins and directional cues by local concentration gradient of chemokines and growth factors that exists around the cancer cells. The increase in IFP upregulates endogenous TGF-β that further leads to the trans-differentiation of fibroblasts into myofibroblasts with high contractility and is crucial for remodelling of ECM [30]. As a whole, the TGF-β activation and expression from matrix stores, influences the fibroblasts to become invasive, thereby establishing the concept of fluid flow promoting cancer cell invasion. Thus, the role of IF expands to multitude of factors influencing cancer cell invasion in the vicinity of blood and lymphatic vessels. Researchers have actively employed microfluidic based devices to study the effect of IF for cancer cell invasion activity in single cells [33, 36]. The combined influence of biophysical forces and biochemical induced intra-cellular signaling behavior in 3-D cancer spheroids is yet to be explored. In **chapter 3**, we investigated the potentiating effect of IF (biophysical force) on the exogenous TGF-β (biochemical) induced signaling activity in lung cancer spheroids in a 3-D matrix-based microfluidic platform [37].

1.4. EPITHELIAL TO MESENCHYMAL TRANSITION

The biological phenomenon of epithelial to mesenchymal transition (EMT) of cells is associated with cancer metastasis depicted by the change in genetic expression of cancer cells [28]. The transition is described as a process in which an epithelial cancer cell undergoes several intra-cellular modifications to produce a mesenchymal phenotype. The onset of EMT can be due to various cytokines such as (TGF)-β, Tumor Necrosis Factor (TNF)-α, Interleukin (IL)-6 and Epidermal Growth Factor (EGF) etc. [38–40] Additionally, biophysical factors such as compressive (arising from ECM dysregulation) or fluid-induced shear stress (from IF) also contribute towards EMT in cancer cells [41–43]. One of the key highlights in EMT, is the downregulation of E-cadherin protein (epithelial marker) responsible for cell-cell adhesion, and upregulation in N-/P-cadherins and Vimentin protein (mesenchymal markers) [44, 45]. Once full EMT is achieved, mesenchymal cells are characterized as cancer cells with increased migratory and invasive capacity, increased production of ECM components and reduced levels of apoptosis (programmed cell death) [45], see Fig. 1.3. Therefore, EMT is often associated with collective to individual cell morphology due to the change in cell contractility and cell adhesion induced by a remodeled actin in the cytoskeleton [46]. The reverse process, known as Mesenchymal to Epithelial transition (MET) occurs when the mesenchymal

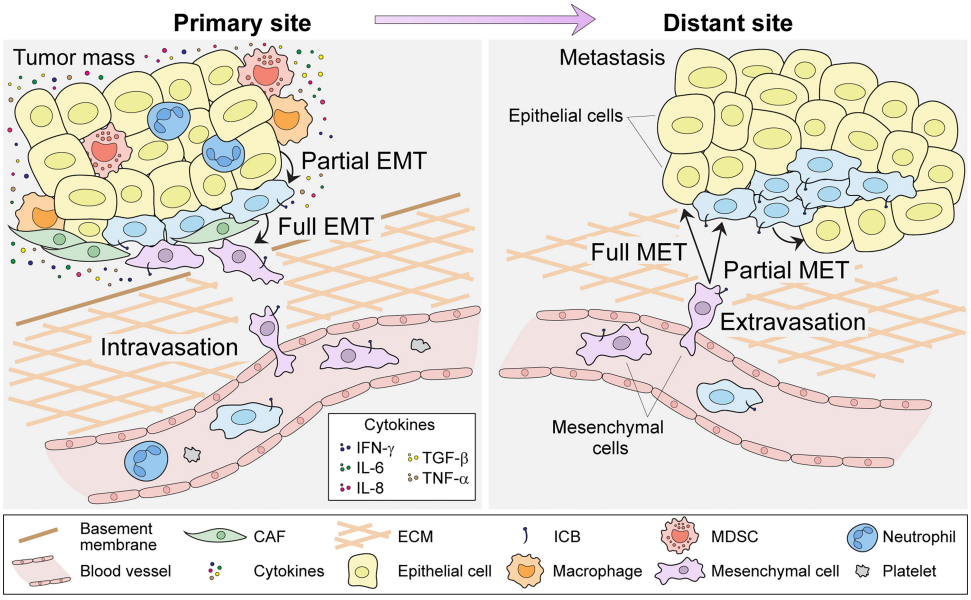

Figure 1.3: **Left: Epithelial to mesenchymal transition (EMT) in tumor cells.** EMT involves multiple stages where cancer cells undergo complex signaling events induced by extracellular signals (cytokines) and the surrounding tumor microenvironment. **Right: Mesenchymal to Epithelial transition (MET).** Eventually, mesenchymal cells are able to intravasate and travel to distant sites to undergo reverse of EMT and colonize a distant organ. These events are marked by changes in EMT proteins such as the loss of E-cadherin (cell-cell contact) and increase in vimentin protein towards a mesenchymal phenotype. Adapted from [49].

cells occupy a distant site to colonize into a secondary tumor [47]. These cancer cells exhibit EMT/MET plasticity to adapt to the changing surrounding microenvironment. However, in some cases, plasticity in cell behavior can be seen through the framework of an unjamming transition where epithelial cells collectively migrate without activating transcription factors usually observed in EMT[8, 48]. In chapter 4, we conducted an in-depth analysis of cell invasion behavior (jammed to unjammed state) in different hydrogel compositions from a soft-matter perspective.

1.4.1. TRANSFORMING GROWTH FACTOR (TGF)-β

In metastatic disease progression, various cytokines are involved that activate several different signaling pathways in cancer cells to become invasive [28]. TGF-β, one of the most important cytokine is primarily responsible for cancer cells to undergo EMT [50]. In the TME, TGF-β exists in the ECM in its inactive form linked to an amino-terminal part called latency associated peptide (LAP) [51]. Latent-TGF-β is activated when proteolytic enzymes (such as MMPs) cleave the LAP or by protease-independent cellular forces upon activation of cell-surface integrins [52]. TGF-β ligands in the ECM present itself to the TGF-β receptors on the cell membrane to undergo active binding for activation of Smad-dependent signaling pathway [51]. This results in transcriptional and translational response towards change in genetic and protein expression to an inva-

sive phenotype similar to those of metastatic cancer cells [53–55]. The TGF-β induced intra-cellular signaling cascade leads to EMT [52]. Several studies have highlighted the role of TGF-β in epithelial cancer type (such as lung, pancreatic etc.) by upregulation of EMT-associated transcriptional factors (such as SNAI1, ZEB, TWIST) and decrease in E-cadherin protein expression [51, 52]. These transcriptional factors are responsible for the rearrangement of cellular proteins that results in a loss of cell-cell adhesion. Targeting TGF-β induced signaling pathways via protein inhibitors and blocking of cell surface receptors are promising aspects in clinical settings for cancer therapeutics [28, 56].

1.5. CELL-MATRIX INTERACTIONS

As previously established, the surrounding ECM of a primary tumor undergoes constant modifications either by cell-secreted enzymes (degradation) and/or through deposition of new proteins (remodelling) from cancer cells. Cancer cells in-turn are subjected to the varying ECM biomechanical determinants (such as stiffness, pore-size, and density) that initiates a series of complex downstream intracellular signaling response [15]. This is due to the ability of cells to sense, integrate and convert biomechanical stimuli into biochemical signals [57]. This phenomenon is referred to as mechanotransduction that leads to activation of signaling pathways, transcriptional response and activated ion-channels [58]. The biomechanical determinants play an important role during cell-matrix interaction as they contribute towards EMT and assist in cancer cell invasion [15]. In recent years, researchers have exploited the use of naturally-derived or semi-synthetic biomaterials to mimic the native ECM architecture [24]. Moreover these biomaterials can be tuned to adjust their mechanical properties to investigate cancer cell behavior in 3D-platforms for better understanding of the role of ECM. For example, ECM mechanical properties play a significant role in anti-cancer therapy, where drug resistance is exhibited by ECM stiffness dependency in breast cancer treatment [59]. To investigate the diverse mechanical nature of ECM in cancer progression, **Chapter 4** investigates the influence of varying ECM mechanical determinants (stiffness, pore-size and density) on invasion capacity. Furthermore, the invasion capacity and rates of an epithelial-like lung cancer and a highly metastatic melanoma cancer establish the role of matrix confinement and cellular proteins (such as MMPs, vimentin protein) on the different phase transitions observed during jamming-unjamming behavior.

1.6. OUTLINE OF THESIS

The aim of this thesis was to develop 3-D in vitro platforms that combined important TME components such as extra-cellular matrix, interstitial flow and introduce biochemicals (such as TGF-β) relevant to cancer spheroid invasion. These platforms allowed us to carefully track and quantify cancer cell signaling and invasion activity in real-time when subjected to varying biomechanical and biochemical stimuli. We investigated two different cancer types, lung and melanoma cancer for their invasive behavior under static and flow conditions (microfluidics) separately. **Chapter 1** briefly introduces the important concepts of the TME and its cellular and non-cellular components responsible in cancer cell invasion relevant to this thesis. A more detailed review is provided in **Chapter 2** that critically examined the most important and recent developments of 3-D microflu-

idic platforms as a promising tool that will influence the future trend in cancer invasion research. In **chapter 3**, a 3D-matrix based microfluidic platform is presented, where lung cancer spheroids are exposed to a combined effect from interstitial flow (IF) and exogenous TGF-β. This chapter focuses on the potentiating effect from IF on TGF-β induced Smad-signaling activity and an increased cellular motion activity. **Chapter 4** reports the influence of ECM mechanical determinants (such as density, pore size and stiffness) using collagen-based hydrogels on cell invasion capacity of an epithelial-like lung cancer and highly metastatic melanoma cancer (mesenchymal). In addition, cell-intrinsic proteins (vimentin, MMPs) were modulated by exposure with TGF-β and broad-spectrum MMP inhibitor to identify the influence on invasion onset and invasion rate. These cancer cells were specifically chosen to investigate framework of jamming-unjamming phase transition in a soft matter perspective. We highlighted that matrix confinement parameters (pore-size) and MMP1 protein secretion levels determine (un)jamming transition. Finally, **chapter 5** discusses key findings that this thesis provides to address the scientific research questions that were posed, and highlights the relevance and importance of 3D in vitro platforms for future advancements in cancer cell invasion studies.

1

REFERENCES

[1] A. W. Lambert, D. R. Pattabiraman, and R. A. Weinberg, *Emerging Biological Principles of Metastasis,* Cell **168**, 670 (2017).

[2] T. R. Cox, *The matrix in cancer,* Nature Reviews Cancer **21**, 217 (2021).

[3] *Aantal kankerpatiënten in Nederland stijgt de komende tien jaar explosief,* .

[4] M. Janin, V. Davalos, and M. Esteller, *Cancer and Metastasis Reviews*, Vol. 42 (Springer US, 2023) pp. 1071–1112.

[5] C. P. Spatarelu, H. Zhang, D. T. Nguyen, X. Han, R. Liu, Q. Guo, J. Notbohm, J. Fan, L. Liu, and Z. Chen, *Biomechanics of Collective Cell Migration in Cancer Progression: Experimental and Computational Methods,* ACS Biomaterials Science and Engineering **5**, 3766 (2019).

[6] H. Xu, X. Liu, and W. Le, *Recent advances in microfluidic models for cancer metastasis research,* TrAC - Trends in Analytical Chemistry **105**, 1 (2018).

[7] P. Mehta, Z. Rahman, P. ten Dijke, and P. E. Boukany, *Microfluidics meets 3D cancer cell migration,* Trends in Cancer **8**, 683 (2022).

[8] J. Mitchel, A. Das, M. O'Sullivan, I. Stancil, S. DeCamp, S. Koehler, J. Butler, J. Fredberg, M. A. Nieto, D. Bi, and J.-A. Park, *The unjamming transition is distinct from the epithelial-to-mesenchymal transition,* bioRxiv , 665018 (2019).

[9] N. Landon-Brace, N. T. Li, and A. P. McGuigan, *Exploring New Dimensions of Tumor Heterogeneity: The Application of Single Cell Analysis to Organoid-Based 3D In Vitro Models,* Advanced Healthcare Materials **2300903**, 1 (2023).

[10] L. Pierantoni, R. L. Reis, J. Silva-Correia, J. M. Oliveira, and S. Heavey, *Spatial -omics technologies: the new enterprise in 3D breast cancer models,* Trends in Biotechnology **xx**, 1 (2023).

[11] Y. Shi, Y. Cai, Y. Cao, Z. Hong, and Y. Chai, *Recent advances in microfluidic technology and applications for anti-cancer drug screening,* TrAC - Trends in Analytical Chemistry **134**, 116118 (2021).

[12] P. C. Searson, *The Cancer Moonshot, the role of in vitro models, model accuracy, and the need for validation,* Nature Nanotechnology , 0 (2023).

[13] L. Hui and Y. Chen, *Tumor microenvironment: Sanctuary of the devil,* Cancer Letters **368**, 7 (2015).

[14] F. Spill, D. S. Reynolds, R. D. Kamm, and M. H. Zaman, *Impact of the physical microenvironment on tumor progression and metastasis,* Current Opinion in Biotechnology **40**, 41 (2016).

[15] A. Saraswathibhatla, D. Indana, and O. Chaudhuri, *Cell–extracellular matrix mechanotransduction in 3D,* Nature Reviews Molecular Cell Biology **24**, 495 (2023).

[16] J. Winkler, A. Abisoye-Ogunniyan, K. J. Metcalf, and Z. Werb, *Concepts of extracellular matrix remodelling in tumour progression and metastasis,* Nature Communications **11**, 1 (2020).

[17] M. Z. Jin and W. L. Jin, *The updated landscape of tumor microenvironment and drug repurposing,* Signal Transduction and Targeted Therapy **5** (2020), 10.1038/s41392-020-00280-x.

[18] J. Song, A. Miermont, C. T. Lim, and R. D. Kamm, *A 3D microvascular network model to study the impact of hypoxia on the extravasation potential of breast cell lines,* Scientific Reports **8**, 1 (2018).

[19] V. Petrova, M. Annicchiarico-Petruzzelli, G. Melino, and I. Amelio, *The hypoxic tumour microenvironment,* Oncogenesis **7** (2018), 10.1038/s41389-017-0011-9.

[20] R. Baghban, L. Roshangar, R. Jahanban-Esfahlan, K. Seidi, A. Ebrahimi-Kalan, M. Jaymand, S. Kolahian, T. Javaheri, and P. Zare, *Tumor microenvironment complexity and therapeutic implications at a glance,* Cell Communication and Signaling **18**, 1 (2020).

[21] C. Roma-Rodrigues, R. Mendes, P. V. Baptista, and A. R. Fernandes, *Targeting tumor microenvironment for cancer therapy,* International Journal of Molecular Sciences **20** (2019), 10.3390/ijms20040840.

[22] A. Johnson, S. Reimer, R. Childres, G. Cupp, T. C. Kohs, O. J. McCarty, and Y. A. Kang, *The Applications and Challenges of the Development of In Vitro Tumor Microenvironment Chips,* Cellular and Molecular Bioengineering **16**, 3 (2023).

[23] A. Privat-Maldonado, C. Bengtson, J. Razzokov, E. Smits, and A. Bogaerts, *Modifying the tumour microenvironment: Challenges and future perspectives for anticancer plasma treatments,* Cancers **11**, 1 (2019).

[24] B. Blanco-Fernandez, V. M. Gaspar, E. Engel, and J. F. Mano, *Proteinaceous Hydrogels for Bioengineering Advanced 3D Tumor Models,* Advanced Science **8**, 1 (2021).

[25] T. R. Cox and J. T. Erler, *Remodeling and homeostasis of the extracellular matrix: Implications for fibrotic diseases and cancer,* DMM Disease Models and Mechanisms **4**, 165 (2011).

[26] N. V. Popova and M. Jücker, *The Functional Role of Extracellular Matrix Proteins in Cancer,* Cancers **14** (2022), 10.3390/cancers14010238.

[27] L. E. Scott, S. H. Weinberg, and C. A. Lemmon, *Mechanochemical Signaling of the Extracellular Matrix in Epithelial-Mesenchymal Transition,* Frontiers in Cell and Developmental Biology **7** (2019), 10.3389/fcell.2019.00135.

[28] J. Huang, L. Zhang, D. Wan, L. Zhou, S. Zheng, S. Lin, and Y. Qiao, *Extracellular matrix and its therapeutic potential for cancer treatment,* Signal Transduction and Targeted Therapy **6** (2021), 10.1038/s41392-021-00544-0.

[29] N. Pasha and N. C. Turner, *Understanding and overcoming tumor heterogeneity in metastatic breast cancer treatment,* Nature Cancer **2**, 680 (2021).

[30] M. A. Swartz and A. W. Lund, *Lymphatic and interstitial flow in the tumour microenvironment: Linking mechanobiology with immunity,* Nature Reviews Cancer **12**, 210 (2012).

[31] G. Follain, D. Herrmann, S. Harlepp, V. Hyenne, N. Osmani, S. C. Warren, P. Timpson, and J. G. Goetz, *Fluids and their mechanics in tumour transit: shaping metastasis,* Nature Reviews Cancer **20**, 107 (2020).

[32] Y. L. Huang, J. E. Segall, and M. Wu, *Microfluidic modeling of the biophysical microenvironment in tumor cell invasion,* Lab on a Chip **17**, 3221 (2017).

[33] E. Um, J. M. Oh, S. Granick, and Y. K. Cho, *Cell migration in microengineered tumor environments,* Lab on a Chip **17**, 4171 (2017).

[34] C. H. Heldin, K. Rubin, K. Pietras, and A. Östman, *High interstitial fluid pressure - An obstacle in cancer therapy,* Nature Reviews Cancer **4**, 806 (2004).

[35] M. A. Swartz and M. E. Fleury, *Interstitial flow and its effects in soft tissues,* Annual Review of Biomedical Engineering **9**, 229 (2007).

[36] W. J. Polacheck, J. L. Charest, and R. D. Kamm, *Interstitial flow influences direction of tumor cell migration through competing mechanisms,* Proceedings of the National Academy of Sciences of the United States of America **108**, 11115 (2011).

[37] Z. Rahman, A. D. Bordoloi, H. Rouhana, M. Tavasso, G. van der Zon, V. Garbin, P. ten Dijke, and P. E. Boukany, *Interstitial flow potentiates TGF-β/Smad-signaling activity in lung cancer spheroids in a 3D-microfluidic chip,* Lab on a Chip **24**, 422 (2024).

[38] F. Xie, L. Ling, H. Van Dam, F. Zhou, and L. Zhang, *TGF-β signaling in cancer metastasis,* Acta Biochimica et Biophysica Sinica **50**, 121 (2018).

[39] P. Peixoto, A. Etcheverry, M. Aubry, A. Missey, C. Lachat, J. Perrard, E. Hendrick, R. Delage-Mourroux, J. Mosser, C. Borg, J. P. Feugeas, M. Herfs, M. Boyer-Guittaut, and E. Hervouet, *EMT is associated with an epigenetic signature of ECM remodeling genes,* Cell Death and Disease **10** (2019), 10.1038/s41419-019-1397-4.

[40] K. Schelch, L. Vogel, A. Schneller, J. Brankovic, T. Mohr, R. L. Mayer, A. Slany, C. Gerner, and M. Grusch, *EGF Induces Migration Independent of EMT or Invasion in A549 Lung Adenocarcinoma Cells,* Frontiers in Cell and Developmental Biology **9**, 1 (2021).

[41] I. Rizvi, U. A. Gurkan, S. Tasoglu, N. Alagic, J. P. Celli, L. B. Mensah, Z. Mai, U. Demirci, and T. Hasan, *Flow induces epithelial-mesenchymal transition, cellular heterogeneity and biomarker modulation in 3D ovarian cancer nodules,* Proceedings of the National Academy of Sciences of the United States of America **110** (2013), 10.1073/pnas.1216989110.

[42] Y. Katsuno and R. Derynck, *Epithelial plasticity, epithelial-mesenchymal transition, and the TGF-β family,* Developmental Cell **56**, 726 (2021).

[43] Q. Liu, Q. Luo, Y. Ju, and G. Song, *Role of the mechanical microenvironment in cancer development and progression,* Cancer Biology and Medicine **17**, 282 (2020).

[44] A. Haeger, M. Krause, K. Wolf, and P. Friedl, *Cell jamming: Collective invasion of mesenchymal tumor cells imposed by tissue confinement,* Biochimica et Biophysica Acta - General Subjects **1840**, 2386 (2014).

[45] J. Yang, P. Antin, G. Berx, C. Blanpain, T. Brabletz, M. Bronner, K. Campbell, A. Cano, J. Casanova, G. Christofori, S. Dedhar, R. Derynck, H. L. Ford, J. Fuxe, A. García de Herreros, G. J. Goodall, A. K. Hadjantonakis, R. J. Huang, C. Kalcheim, R. Kalluri, Y. Kang, Y. Khew-Goodall, H. Levine, J. Liu, G. D. Longmore, S. A. Mani, J. Massagué, R. Mayor, D. McClay, K. E. Mostov, D. F. Newgreen, M. A. Nieto, A. Puisieux, R. Runyan, P. Savagner, B. Stanger, M. P. Stemmler, Y. Takahashi, M. Takeichi, E. Theveneau, J. P. Thiery, E. W. Thompson, R. A. Weinberg, E. D. Williams, J. Xing, B. P. Zhou, and G. Sheng, *Guidelines and definitions for research on epithelial–mesenchymal transition,* Nature Reviews Molecular Cell Biology **21**, 341 (2020).

[46] H. Zou, Z. Yang, Y. S. Chan, S. k. A. Yeung, M. K. Alam, T. Si, T. Xu, and M. Yang, *Single cell analysis of mechanical properties and EMT-related gene expression profiles in cancer fingers,* iScience **25**, 103917 (2022).

[47] W. Lu and Y. Kang, *Epithelial-Mesenchymal Plasticity in Cancer Progression and Metastasis,* Developmental Cell **49**, 361 (2019).

[48] R. M. Lee, M. I. Vitolo, W. Losert, and S. S. Martin, *Distinct roles of tumor associated mutations in collective cell migration,* Scientific Reports **11**, 1 (2021).

[49] A. Sistigu, F. Di Modugno, G. Manic, and P. Nisticò, *Deciphering the loop of epithelial-mesenchymal transition, inflammatory cytokines and cancer immunoediting,* Cytokine Growth Factor Reviews **36**, 67 (2017), sI: NIBIT-Immunotherapy.

[50] R. Derynck, B. P. Muthusamy, and K. Y. Saeteurn, *Signaling pathway cooperation in TGF-β-induced epithelial-mesenchymal transition,* Current Opinion in Cell Biology **31**, 56 (2014).

[51] M. Pickup, S. Novitskiy, and H. L. Moses, *The roles of TGFβ in the tumour microenvironment,* Nature Reviews Cancer **13**, 788 (2013).

[52] Y. Hao, D. Baker, and P. T. Dijke, *TGF-β-mediated epithelial-mesenchymal transition and cancer metastasis,* International Journal of Molecular Sciences **20** (2019), 10.3390/ijms20112767.

[53] S. Hao, L. Ha, G. Cheng, Y. Wan, Y. Xia, D. M. Sosnoski, A. M. Mastro, and S. Y. Zheng, *A Spontaneous 3D Bone-On-a-Chip for Bone Metastasis Study of Breast Cancer Cells,* Small **14**, 1 (2018).

[54] M. Marozzi, A. Parnigoni, A. Negri, M. Viola, D. Vigetti, A. Passi, E. Karousou, and F. Rizzi, *Inflammation, extracellular matrix remodeling, and proteostasis in tumor microenvironment,* International Journal of Molecular Sciences **22** (2021), 10.3390/ijms22158102.

[55] C. L. Chaffer and R. A. Weinberg, *A perspective on cancer cell metastasis,* Science **331**, 1559 (2011).

[56] S. Colak and P. ten Dijke, *Targeting TGF-β Signaling in Cancer,* Trends in Cancer **3**, 56 (2017).

[57] S. Van Helvert, C. Storm, and P. Friedl, *Mechanoreciprocity in cell migration,* Nature Cell Biology **20**, 8 (2018).

[58] R. K. Jain, J. D. Martin, and T. Stylianopoulos, *The role of mechanical forces in tumor growth and therapy,* Annual Review of Biomedical Engineering **16**, 321 (2014).

[59] Y. Jiang, H. Zhang, J. Wang, Y. Liu, T. Luo, and H. Hua, *Targeting extracellular matrix stiffness and mechanotransducers to improve cancer therapy,* Journal of Hematology and Oncology **15**, 1 (2022).

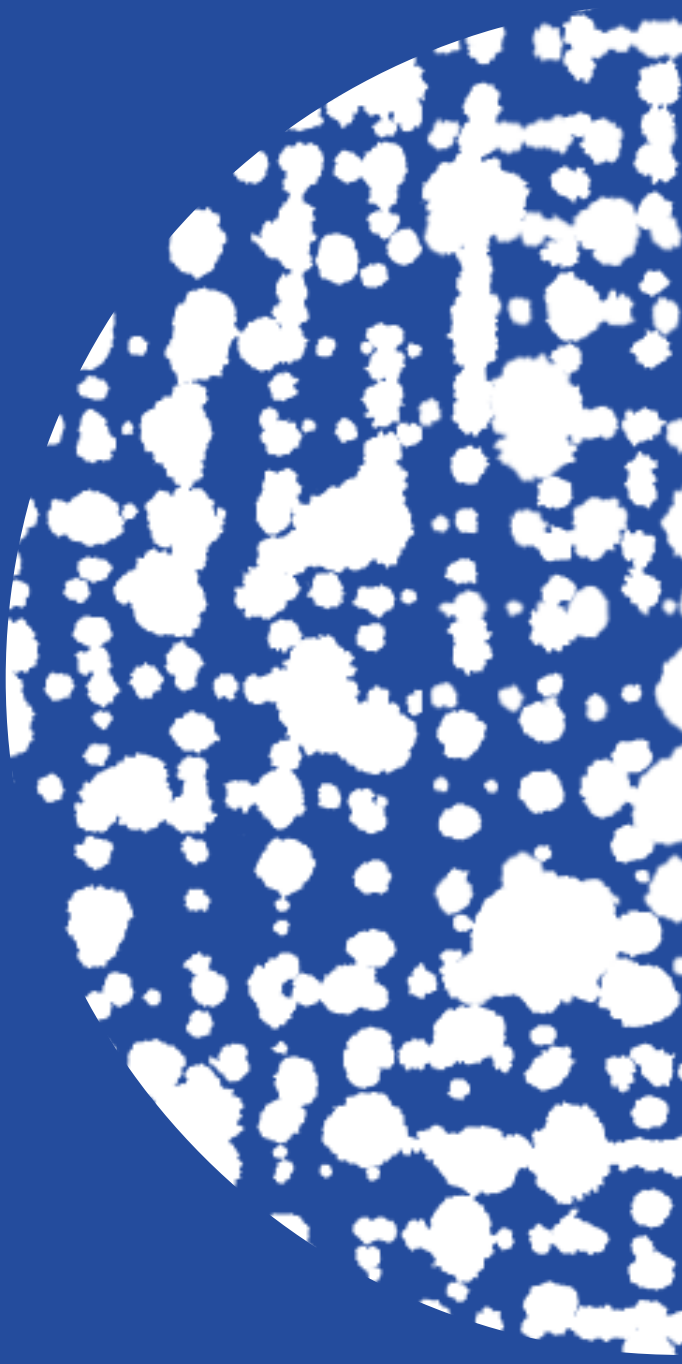

2

MICROFLUIDICS MEETS 3D CANCER CELL MIGRATION

ABSTRACT

The early step of metastasis requires a complex and coordinated migration of invasive tumor cells into the surrounding tumor microenvironment (TME), which contains extracellular matrix (ECM). We discuss how 3D matrix-based microfluidic models have an advantage over conventional in vitro and animal models to study tumor progression events. Recent microfluidic models enabled recapitulation of key mechano-biological features present within the TME to investigate collective cancer cell migration and invasion. Microfluidics also allows for functional interrogation and therapeutic manipulation of specific steps to study the dynamic aspects of tumor progression. In this review, we focus on recent developments in cancer cell migration and how microfluidic strategies have evolved to address the physiological complexities of the TME to visualize migration modes adapted by various tumor cells.

This chapter is published as P. Mehta[+], Z. Rahman[+], P. ten Dijke, P. E. Boukany, *Trends in Cancer (2022)* [1].
([+] equal author contribution)

HIGHLIGHTS

- Microfluidic cancer cell migration models enable an integrated assessment of how cell–cell and cell–matrix interaction, matrix stiffness, interstitial and shear flow, hypoxia and cytokine, and metabolic gradients affect dynamic cancer cell migration.
- While many in vitro static cell migration models fail to mimic the complexities and biomechanical features of the tumor microenvironment (TME), incorporation of microfluidics allows us to investigate cancer cell migration through the TME and invasion under well-controlled pathophysiological conditions associated with tumor progression events.
- Tumor cells can elicit distinct migratory behavior in the form of single or collective cell migration modes in response to extracellular biochemical and biophysical cues

2.1. MICROFLUIDIC MODELING OF CELL INVASION

Metastasis, the spread of cancer cells away from the primary solid tumor and into the body's healthy tissues, eventually leading to the formation of secondary tumors causing organ failure, is responsible for over 90% of cancer-related deaths [2]. Importantly, metastasis requires a complex and coordinated migration of invasive tumor cells into the surrounding tumor microenvironment (TME) containing ECM. The TME plays a critical role in the early stages of metastasis, dictating cancer cell motility, invasion, and spread into neighboring tissues [3]. The key extracellular determinants of cancer cell migration are the biophysical and biochemical cues provided by the ECM, interstitial flows, and cancer cell-TME cell interactions, including the interplay with cancer-associated fibroblasts (CAFs). Conventional tumor models used to study these cell motility mechanisms lie on either extremity of the spectrum: on one end, macroscopic in vitro models are easy and simple, but a poor recapitulation of the local TME characteristics, including biomechanical forces, interstitial flow, fluid shear stress, and ECM remodeling. On the other end, animal experiments have the pathophysiological complexity but are expensive, time-consuming, and still have a degree of error due to the innate differences between animal and human physiology. The use of microfluidics in 2D and 3D models has become an attractive alternative to overcome these challenges. Microfluidics are capable of more closely mimicking the TME by incorporating various physiologically relevant biophysical and biological cues with precise spatiotemporal control (Fig. 2.1) [4, 5]. Furthermore, microfluidics devices also permit real-time imaging of cellular dynamics, enabling it to probe biophysical, biochemical, and (epi)genetic activities present in healthy and diseased multicellular tissues [6]. Today the field of microfluidics continues to launch into new territories of cancer research, extending the development of tumor models ranging from tumor cancer spheroids to cancer-on-a-chip models with relevant TME and (patho)physiological conditions [7, 8]. There are numerous reviews on microfluidic platforms for the study of the metastatic microenvironment, tumor-stroma

interaction, and TME in cancer metastasis and therapy [9–13], cancer extravasation in response to biophysical and chemical cues [13, 14], single-cancer-cell separation, detection, and migration [15], biophysical studies of cancer cells at the single-cell level [16], modeling cancer immune interaction [17] and development of tumor/organ-on-a-chip in personalized cancer therapy [18, 19]. However, a critical perspective review on microfluidics approaches for mechanistic studies of cancer cell migration into surrounding TME, for example, how cancer cells adapt their migratory behavior through different TME, is still missing. The present review aims to fill this gap and complement previous reviews by discussing how cancer cells adapt their migration strategies through different and dynamically changing TMEs, and how novel microfluidics platforms have evolved to unravel the mechanisms of collective cancer cell migration through a tunable TME. Here, we discuss how microfluidics is an effective tool to mimic the metastatic microenvironment for mechanistic investigations (Fig. 2.1). We then discuss the underlying migration mechanisms adopted by cancer cells in a physiologically relevant TME model, with a focus on lung and breast cancer cells; they are well studied but remain two of the most diagnosed cancers worldwide in terms of incidence and mortality due to the complexity of the TME [2, 3]. Next, we highlight the role of tumor heterogeneity, ECM, interstitial and shear flow as biomechanical stimuli, cancer-associated fibroblasts (CAFs), and the cytokine, transforming growth factor-β (TGF-β) as relevant biochemical cues to emphasize tumor invasion properties. Finally, we discuss challenges and new directions in applying 3D matrix-based microfluidic devices in personalized medicine and cancer therapy.

2.2. MICROFLUIDICS IN COLLECTIVE CELL MIGRATION

Both biophysical and cellular cues alter tumor cell responses (from migration modes to the level of invasiveness) inside the dynamic TME, resulting in the dissemination of cancer cells from the primary tumor. 3D in vitro tumor models such as heterogeneous or coculture multicellular spheroid models are widely used to investigate cancer cell migration and invasion [11]. Static (no-flow) 3D cell culture models have been used to examine cell migration through semipermeable membranes or to study the biological response to specific chemoattractants or drugs [14]. Moreover, a programmable and multifunctional 3D cancer cell invasion platform has been recently developed that dynamically releases mature TGF-β to induce invasive migration of cancer cells by assembling functionalized micro-buckets and a tunable ECM that emulates a more complex TME during cancer invasion [20]. A major advantage of using 3D microfluidic platforms is that different cell types can be co-cultured long term in a controlled microenvironment, thus more closely resembling physiology in vivo. Through real-time visualization and the ability to study specific biological cues, 3D microfluidic platforms allow the characterization of individual cellular responses, providing insight into intercellular communication. For example, 3D matrix-based microfluidic models incorporated the use of endothelial cell (EC)-covered microchannels and spatiotemporally controlled ECM compartments consisting of stromal cells, tumor-associated macrophages (TAMs), CAFs, and immune cells to recreate intratumor heterogeneity [14, 21, 22]. Other 3D microfluidic models explored the use of patient-derived cells [10, 23], response of natural killer (NK) or immune cells [24], and drug delivery for drug screening applications [25, 26]. Researchers have also

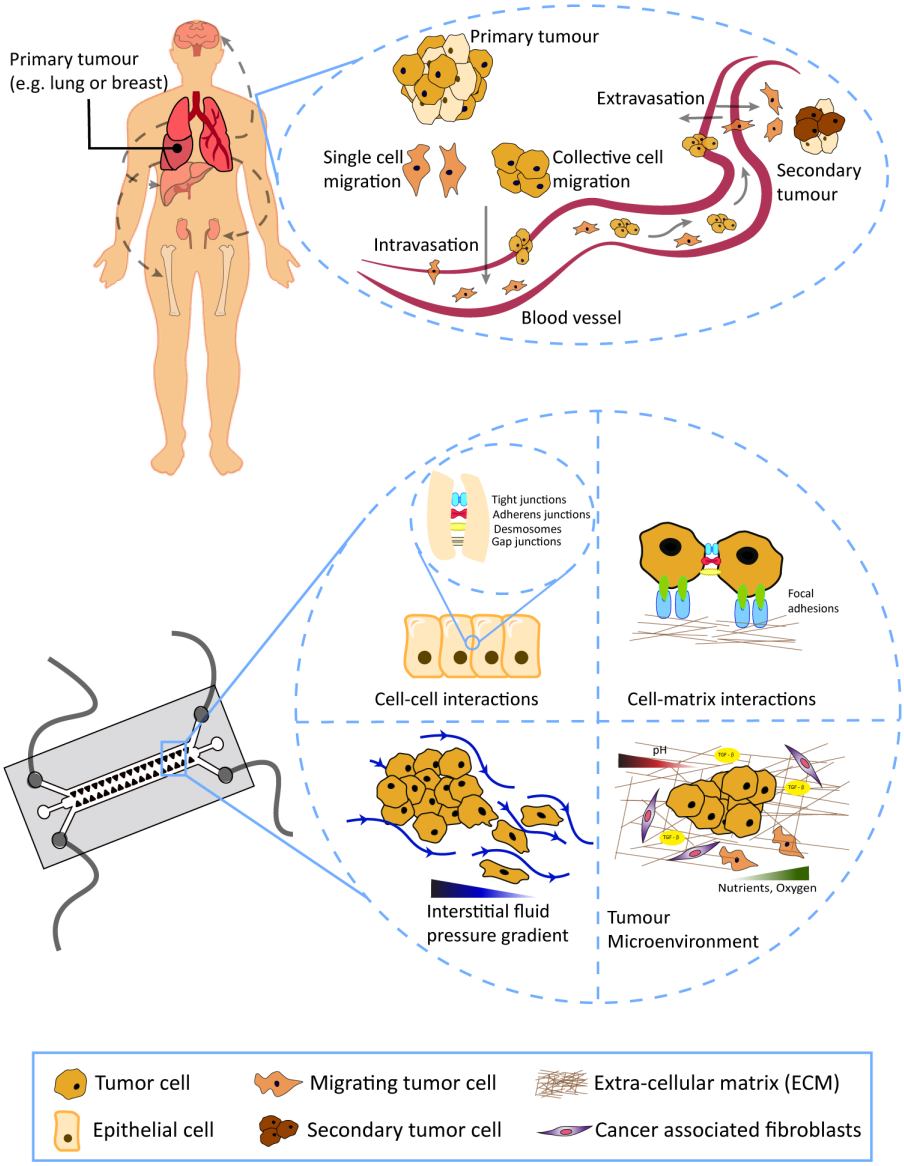

Figure 2.1: Top: invasive cancer cells metastasize from a primary solid tumor (such as the lung or breast) to different parts of the body such as the brain, liver, adrenal glands, and bones. Primary tumors disseminate into a single or cluster of migrating tumor cells with adaptive migration morphology. These disseminated tumor cells can then enter the blood vessel, known as intravasation. Tumor cells travel through the blood vessel and exit at a distant location, known as extravasation. The tumor cells that survive and adapt to the new surrounding microenvironment have the potential to form a secondary tumor (e.g., in the brain). This chain of events is known as the metastatic cascade, where external factors such as biochemical and biomechanical cues influence the migratory behavior of cells from the primary tumor. *Caption continued on next page*

Figure 2.1: Bottom: schematic of a microfluidic device highlighting the important applications used to study various critical biological phenomena ranging from cell/cell and cell/extracellular matrix (ECM) interactions to interstitial flow within tumor microenvironment (TME) associated with the metastatic cascade. Microfluidics gives us the advantage of real-time imaging to study cell–cell and cell–matrix interactions by quantifying biophysical properties such as changes in levels of adhesion proteins. A microfluidic device also provides desirable control to include external forces such as shear stress or interstitial flow, usually referred to as promigratory factors that influence cancer cell migration behavior. Last, recent developments in microfluidic models have focused on building a physiologically relevant TME that can provide a comprehensive understanding of the migratory behavior of specific cancer cell types. This chain of events is known as the metastatic cascade, where external factors such as biochemical and biomechanical cues influence the migratory behavior of cells from the primary tumor. Bottom: schematic of a microfluidic device highlighting the important applications used to study various critical biological phenomena ranging from cell/cell and cell/extracellular matrix (ECM) interactions to interstitial flow within tumor microenvironment (TME) associated with the metastatic cascade. Microfluidics gives us the advantage of real-time imaging to study cell–cell and cell–matrix interactions by quantifying biophysical properties such as changes in levels of adhesion proteins. A microfluidic device also provides desirable control to include external forces such as shear stress or interstitial flow, usually referred to as promigratory factors that influence cancer cell migration behavior. Last, recent developments in microfluidic models have focused on building a physiologically relevant TME that can provide a comprehensive understanding of the migratory behavior of specific cancer cell types.

been able to reconstitute ex vivo a human tumor ecosystem by co-culturing four distinct cell populations (cancer, immune, endothelial, and fibroblasts) in a microfluidic device in 3D. Using this platform to screen for drug interactions and mechanisms, researchers elucidated cancer–immune–CAF cell interactions, illustrating the long time scale (several hours) signaling cascade between cancer and immune cells and CAFs that antagonized the effects of the drug. 3D microfluidic models create a more effective and powerful platform to track intermediate steps to differentiate between single and collective cell migration mechanisms in cancer models with a dynamic interplay of multiple (dynamically phenotypically changing) cell types [27] (Box 1). Various microfluidic models have been developed to investigate metastasis-related phenomena, such as cancer cell migration, epithelial-mesenchymal transition (EMT), cell invasion, intravasation, and extravasation. In the following sections, we take a closer look at the microfluidic models developed for lung and breast cancers highlighting microfluidic modeling parameters and improved biological outcomes. Furthermore, these (3D) microfluidic devices have been adapted to investigate the impact of TME complexity on a wide variety of tumor invasions. An overview of 3D microfluidic models for various cancer types modeled for different tumor progression events and with chemotherapeutic applications is provided in Table 2.1.

BOX 1. MIGRATION DYNAMICS AND EPITHELIAL-MESENCHYMAL PLASTICITY (EMP)

Cell migration can be broadly classified into two modes, individual or single-cell migration and collective cell migration. Morphologically and functionally, single-cell migration can be further classified into amoeboidal and mesenchymal movement. Amoeboid single migrating cells often display structures referred to as plasma membrane blebs, defined by a bulky and rounded morphology, and these blebs are an extension of the plasma membrane caused by local disruption of the membrane actin cortex interactions, high intracellular hydrostatic pressure, and enhanced contractility [28, 29]. Single cells displaying a mesenchymal migration mode, moreover, display actin-rich protrusions and rely on the proteolytic degradation of the surrounding ECM [30, 31].

Collective migration occurs when cells maintain their intercellular junctions and thus migrate jointly as an integrated group. The collective morphology and dynamics of cohesive motility are strongly dependent on the type and stability of their intercellular junctions and extracellular tissue conditions [29]. Collective migration in cancer is characterized by the expression of homophilic cell–cell junctions and epithelial morphologies within the migrating cluster [32]. Protrusive cells at the leading edge, termed leader cells, are connected to the rest of the cluster and have been shown to coordinate multicellular sheet/strand migration [33]. Collectively migrating cancer cells display structural ECM remodeling, further promoting migration and metastasis [34]. Cellular plasticity, the ability to repress or activate specific gene expression and modulate the activity of gene products to allow for optimal migration mechanics or survival, is crucial for collective cell migration. This plasticity allows migrating cancer cells to integrate various mechanical and chemical cues around them and adjust their direction, speed, and mode of migration [29].

Epithelial cancer cells can undergo a switch to a mesenchymal phenotype, a process termed epithelial–to–mesenchymal transition (EMT) [35]. New studies show that EMT is a dynamic plastic process, where cells can acquire different hybrid intermediate states called partial EM states (p-EMT), a process referred to EMP [36, 37]. In such states, cells retain various epithelial features while also expressing EMT markers such as N-cadherin and vimentin intermediate filaments [29]. Cells undergoing complete EMT (c-EMT) transcriptionally suppress the epithelial markers such as the transmembrane protein E-cadherin [36].

Cancer type	Microfluidic model highlights	Biological observations/outcome	Limitations	Refs
Breast cancer				
Type: Tumor Invasion Cells: SUM-159 breast cancer cells and CAFs co-culture	3D-Microfluidic based organotypic model. Focuses on tumor invasion by stroma activation. Co-culture of SUM-159 and patient derived fibroblasts to model patient-specific TME. Allows for tumor-stroma crosstalk.	RNA-seq is applied to profile the transcriptome of breast cancer cells with CAFs to delve deeper into molecular mechanisms in tumor-stroma bidirectional crosstalk. Breast cancer invasion enhanced in the presence of CAFs, is mediated by the expression of glycoprotein nonmetastatic B (GPNMB) in breast cancer cells.	Patient-derived CAFs are heterogeneous expressing varying levels of specific biomarkers. Two out of three patient-derived CAFs showed tumor promoting behavior. No defined single or set of biomarkers was defined owing to CAFs heterogeneity.	[38]

Table 2.1 continued from previous page

Cancer type	Microfluidic model highlights	Biological observations/outcome	Limitations	Refs
Type: Hypoxia driven tumor migration Cells: HUVECs, MCF-10A, MDA-MB-231, MCF-7 and NHLF (Normal Human Lung Fibroblasts)	Microfluidic model consisting of vascular networks to quantify breast cancer extravasation exposed to different oxygen concentrations. Device with three-gel channels, alternated with media channels. An advantage to study different cell lines and conditions of normoxia and varying hypoxia levels in short-term cultures.	Increase in hypoxia inducible factor (HIF-1α) protein levels in hypoxic conditions were linked to elevated levels in metastatic potential. The increase in aggressive phenotype upon hypoxia is independent of the malignancy of different cell lines.	Effect of hypoxia on cell proliferation and viability can be different in cells lines of varying malignancy based on short-term or long-term hypoxic exposure to hypoxic conditions. More studies are need to understand the signaling pathways responsible for hypoxia-induced increased metastatic potential.	[39]

Table 2.1 continued from previous page

Cancer type	Microfluidic model highlights	Biological observations/outcome	Limitations	Refs
Type: tumor extravasation Cells: MDA-MB-231breast cancer cells, monocytes	A 3D vascularized microfluidic model that provides high-resolution visualization of intravascular migration, trans-migration, and differentiation of monocytes through human vasculature. Characterization of tumor cell extra-vasation in the presence of mono-cytes. Physiological differences between inflammatory and patrolling monocyte extravasation patterns were measured by the platform. Potential to study effects of monocytes on tumor progression.	Undifferentiated monocytes present with MDA-MB-231 cancer cells in intraluminal vasculature reduced tumor cell extravasation. Heterogeneity of cancer cell in extravasation mediated by monocyte type was observed. This difference was attributed to the role of myosin IIA in monocyte cell motility.	Future studies should examine media conditioned by cells in 3D compared with 2D system conditioned medium. More studies need to be performed on monocyte homeostasis and extravasation cascade in response to flow. Incorporation of other immune cells.	[17]

Table 2.1 continued from previous page

Cancer type	Microfluidic model highlights	Biological observations/outcome	Limitations	Refs
Lung cancer				
Type: Tumor migration Cells: H1299 lung adenocarcinoma cancer cells	3D-matrix based microfluidic device with mixed hydrogel (collagen, Matrigel) compositions to investigate impact on migration. Quantitative image analysis to measure H1299 lung cancer migration in different hydrogel (ECM) compositions.	Hydrogel composition mimicking the TME. As a disorganized basement membrane at the front of cancer invasion was mimicked using ECM containing hydrogel. An increase in migration speed in Collagen-Matrigel hydrogel compared with collagen only was observed as a result of increased stiffness and pore size. Hydrogel composition was identified as an important determinant for cell migration.	Inconsistency with resultson migration speed and morphology with increasing matrix stiffness and pore sizes. Difficult to identify the exact composition of in vivo ECM based on particular cancer type and their location.	[40]

Table 2.1 continued from previous page

Cancer type	Microfluidic model highlights	Biological observations/outcome	Limitations	Refs
Type: Tumor migration and anti-cancer therapy response Cells: A549 lung cancer cells, miR-497 exosomes.	A 3D microfluidic device in which A549 lung cancer cells and HUVECs are co-cultured that is capable of delivery and controlled regulation of miRNAs via exosomes to explore therapeutic potential. The model permitted the role of VEGF concentration gradient on angiogenic sprouting. miRNA therapeutics combined with microfluidics for a predictive, low-cost development tool for targeted cancer therapy.	Significant inhibition of A549 cell migration and reduced sprouting of HUVECs was observed in the presence of miR-497 exosomes. Exosomes containing miR-497suppressed tumor growth and expression of associated genes.	The model does not consider the inclusion of additional cell types such as CAFs and/or immune cells and hypoxic gradients. Role of ECM composition in the lung TME and the mechanical strain on lung remains uncharacterized.	[41]

Table 2.1 continued from previous page

Cancer type	Microfluidic model highlights	Biological observations/outcome	Limitations	Refs
Pancreatic Ductal Adenocarcinoma (PDAC)				
Type: Heterogeneous tumor invasion Cells: Pancreatic cell line (PCC)	A complex and heterogeneous PDAC model was developed by embedding a duct of genetically engineered PCCs surrounded by collagen matrix. Precisely controlled intratumoral heterogeneity was engineered to enable heterogeneous invasion characteristics as a response to TGF-β1 on EMT and local invasion.	Confirmation of TGF-β type-I promoting EMT and local invasion in different PCC lines. Study revealed complex interaction between different cancer cells making them more aggressive and invasive. Model can be used to study interaction between heterogeneous patient-derived cancer and stromal cells.	The microfluidic model falls short to incorporate CAFs and other ECM components as a part of pancreatic TME.	[42]

Table 2.1 continued from previous page

Cancer type	Microfluidic model highlights	Biological observations/outcome	Limitations	Refs
Type: Tumor progression Cells: PANC-1 pancreatic cells and pancreatic stellate cells	Microfluidic models using pancreaticstellate cells (PSCs) to study their role incancer progression and drug resistance. Co-culture of pancreatic tumor spheroids (made of PANC-1 cells) with PSCs in 3D collagen matrix to mimic in vivo TME to visualize EMT and quantify chemoresistance.	Expression of EMT markers such as Vimentin, TIMP1, IL-8 and TGF-β was higher in cocultured PANC-1 spheroids compared to mono-cultures. PANC-1 cells also showing greater cell-motility. EMT leads to drug resistance, mediated by microenvironment such as stromal cells and their interactions.	Contradicting results whenusing different CAF targeting strategies raises issue on intratumoral CAF heterogeneity.	[43]
Prostate cancer				

Table 2.1 continued from previous page

Cancer type	Microfluidic model highlights	Biological observations/outcome	Limitations	Refs
Type: Chemotherapeuticresponse Cells: DU 145 prostate cancer cells.	Microfluidic platform representing a 3D TME for rapid evaluation of chemotherapeutic drugs on different cancer cells. Multiple chambers equipped with perfusion channels allows screening of multiple drugs to determine right combination in patient-specific manner. Integration of electrical sensing modality with microfluidics to measure electrical (impedance) response of a cancer cell upon exposure through dynamic drug delivery in a 3D matrix environment.	The proposed platform enabled the differentiation between drug susceptible, drug tolerant/resistant cancer cells in less than 12 hours. Impedance measurement of cells seeded in gel provided information on cell growth, morphology and cell density. Potential to study patient-derived samples for personalized medicine in a rapid, low-cost approach for real-time drug screening analysis.	Polydimethylsiloxane (PDMS)-based microfluidic devices have the disadvantage of being porous to molecules less than 500 Da. These molecules can be absorbed creating a difference in concentration of drugs.	[44]

Table 2.1 continued from previous page

Cancer type	Microfluidic model highlights	Biological observations/outcome	Limitations	Refs
Melanoma cancer				
Type: Tumor migration Cells: Fibroblast and keratinocyte	Equipped with air-walls to pattern cells without using conventional hydrogel barriers. Consists of circular chambers with narrow connections. Ability to co-culture melanoma cells with keratinocytes and dermal fibroblasts. Air-walls dissolve progressively and allows for cellular-crosstalk and migration. Optical metabolic imaging provided further insights into different metabolic features of difference cell lines used.	The presence of dermal fibroblasts and keratinocytes led to changes in melanoma cell morphology and growth pattern. The proposed analysis demonstrated upregulation of multiple secreted factors involved in tumor progression.	The chemokine secretion analysis method does not explicitly identify the cell type responsible for secreting the chemokines. Cellular cross-talk can involve multiple mechanisms such as exosomes, RNA or mechanical forces that were not investigated.	[45]

Table 2.1: 3D microfluidic models to study cancer cell migration and anticancer therapeutic approaches in different tumor types

2.2.1. MICROFLUIDIC MODELS INCORPORATING BIO-PHYSICAL AND BIO-CHEMICAL CUES

Biophysical cues, including IF, fluid pressure, and ECM stiffness, play a central role in directing cell movement, migration, and invasion inside the TME. For tumor cells to extravasate into circulation and distinct tissues, they interact by altering their mechanical properties to adjust to the physical changes of the ECM. The ECM architecture goes through constant remodeling, additionally influenced by interstitial fluid flow (IFF) and interstitial fluid pressure (IFP). Tumor cells respond to these biophysical cues by mechanotransduction pathways, which in a dynamically controlled manner, result in cell migration and invasion. For example, increased ECM stiffness activates the EPHA2/ LYN complex, thereby triggering EMT in breast cancer [46]. Increasing collagen density in the ECM diminishes collective cell migration in breast cancer cells [47]. Matrix porosity can also promote single to collective transitions such as cell jamming, the switch between the two being determined by cellular adhesion to the ECM and the extent of actomyosin contractility of the cytoskeleton [47, 48]. Confinement of cells in tissues can also cause structural changes in cells. Cells deform into small unstable blebs so they can squeeze through the confinement [49, 50]. This change can cause damage to the nuclear envelope, leading to DNA damage and aberrant epigenetic regulation [51]. As such, confinement and changes in matrix porosity can lead to mesenchymal-to-amoeboid transition (MAT) [50, 52].

Collagen fiber alignment in conjunction with matrix stiffness regulates cell migration characteristics, such as speed and persistence, and it also affects their ability to migrate collectively [53]. This property is relevant for cell migratory behavior in a 3D matrix environment compared with cells that prefer directional migration on 2D stiffer substrates. Traditional 3D in vitro models, such as Boyden Chambers, and heterogeneous tumor spheroid invasion assays compared with in vivo models are inexpensive, require less expertise to operate, and can better recapitulate cell–cell/ cell–ECM interaction when embedded in hydrogel matrices [54]. Cell migration behavior observed using 3D cell culture and 2D microfluidic models have provided insights into more guided cell trajectory in response to a biochemical signal or to analyze cellular response by mimicking vascular networks using micro-confinement geometries [55, 56]. In conventional 2D/3D culture models, cancer cells are frequently grown on top or within synthetic ECM as monolayers. However, they fail to capture the behavior of cell–cell and cell–matrix interactions present in the 3D cellular architecture of a tumor tissue [57]. These classical in vitro culture models lack the ability to include fluid flow or shear stress that drives tissue deformation and transport across vascular endothelium, all observed in an in vivo TME [5]. Due to these limitations, these models fall short in recreating relevant physical cues, chemokine signals, or hypoxic gradients present in the TME.

Microfluidic models can incorporate biochemical and biomechanical factors by replicating tumor stroma in a controlled microenvironment. Recently, a microfluidic assay was employed to study the role of collagen densities and the biochemical signal, TGF-β, on the migratory behavior of H1299 spheroids [established from a non-small cell lung cancer cell line (NSCLC)] (Fig. 2.2A) [58]. This programmable platform provides controllable conditions to correlate migrating mechanisms from single to collective migration with varying degrees of micro-confinement. Increasing collagen density inhibited sin-

gle cell migration and promoted clustered migration patterns, whilst TGF-β stimulation promoted cell detachment and single cell migration. Furthermore, migrating cells in high-density collagen matrices showed an increase in strand-like collective motility on encountering TGF-β (Fig. 2.2Aii and Aiii) [58]. Jamming transitions under static conditions have also demonstrated that high tissue density or increased confinement can regulate collective migration by driving EMT in epithelial cancer cells via mechanotransduction pathways [47, 58]. When large cell populations encountered enriched matrices, they moved as multicellular sheets or strands, forming weak cell–cell junctions due to EMT. Moreover, the matrix was proteolytically degraded to create migration tracks. It has been proposed that cooperation between homotypic cancer cells increases migration efficiency and directional persistence and minimizes the energy costs needed compared with individual cell migration, and improves cancer cell survival when invading into neighboring tissues [47, 58, 59].

The influence of mechanical confinement and substrate topology are important factors in determining the role of tumor heterogeneity in migratory behavior during cancer cell invasion and progression [56, 60, 61] (Box 2). To investigate such complex tumor–stroma interactions, a novel 3D bio-microfluidic platform was designed to implement microchamber arrays that replicate the hollow mammary glands that are a part of the tumor microstructures [62]. MCF-10A (normal breast epithelium) cell cultures in the microchamber arrays resulted in the formation of cellular aggregates that covered the entire microchamber area. These aggregates with tight cellular adhesions led to the formation of lumen-like structures mimicking epithelial cells that surround the basement membrane. Cocultures of MCF-10A with MDA-MB-231 (a highly invasive triple-negative breast cancer cell line), however, inhibited cluster formation [62]. The inability of MCF-10A cells to form tight cell adhesions was attributed to secretion of matrix-metalloproteases (MMPs) by MDA- MB-231 cells. MMPs mediated the cleavage of E-cadherin on MCF-10A cells, which resulted in poor cell–cell adhesion that prevented cluster formation. The microfluidic channels allow for gradients of biochemical signals, that is, a range of concentrations of MMP inhibitors induced dose-dependent effects on MCF-10A cluster formation. The model, equipped with microchambers surrounded by collagen hydrogel, mimicked the TME and showed the importance of surrounding cell structures (i.e., epithelial layer) and basement membrane. The microfluidic model recapitulated the characteristic property of lumen-like structures around the basement membrane that prevented metastatic cells from intravasating into deeper ECM areas.

BOX 2. CAFS AND ENDOTHELIAL CELLS IN THE TME

Cancer is a highly heterogeneous disease caused by multiple distinct (epi)genetic alterations in epithelial cells [64]. During cell proliferation, intratumoral heterogeneity can arise due to genetic, epigenetic, or proteomic changes in different cells present within a tumor [64]. In addition, cell-extrinsic factors, such as the local varying TME, hypoxia in the tumor core, residing and infiltrating immune cells, endothelial cells (ECs), and CAFs, can contribute to intratumoral heterogeneity [64]. In addition to cancer cells, TME cells display heterogeneity in function, behavior, and origin. For example, the term 'CAFs' describes all activated fibroblasts found within the TME, regardless of their location, phenotype, or function [65]. Recent data show distinct CAF subtypes and subpopulations within the tumor that appear as cancer progresses over time [66, 67]. These CAF subtypes have unique roles within the TME and are plastic, and one subtype can differentiate into another subtype [65, 66]. Forming heterophilic cadherin junctions with cancer cells to lead collective invasion, CAFs can also intricately deposit fibronectin to remodel and produce a fibronectin-rich ECM to promote migration [68]. Intratumoral heterogeneity and signaling cascades between cells (including tumor cells, immune cells, and CAFs) are exacerbated by the presence of growth-induced stresses, IFP, and flow. This further activates mechanotransduction signaling pathways within the TME and promotes intercellular crosstalk between CAFs, immune cells, and tumor cells by creating chemokine gradients [69, 70].

Hypoxia is prevalent in the tumor core and is a key driver of angiogenesis, one of the most vital stages of cancer progression [71]. In adults, ECs are quiescent and have low proliferation rates; however, cancer tumors can induce angiogenesis to sustain themselves, grow and eventually metastasize [38]. In cancer cells, the activation of oncogenes and mutations in tumor suppressor genes cause increased expression of VEGF which in turn activates ECs through paracrine signaling and stimulates their migration, proliferation, and ultimately results in angiogenesis [72]. There exists a high degree of heterogeneity within ECs obtained from the TME [38, 72]. Combining microfluidics with hydrogel scaffolds to incorporate CAFs or ECs with cancer cells provides a unique platform to investigate cell migration characteristics, the role of CAFs/ECs within the TME, and other stages of the metastatic cascade such as tumor dissemination, intravasation, and extravasation.

2.2.2. MICROFLUIDIC MODELS INCORPORATING HYDRODYNAMIC FLOW

Cells can sense IF and fluid shear stress (or pressure) and change cellular behavior [73]. Fluid flow and shear stress dynamically influence activation or inhibition of a series of mechanosensitive molecules, such as insulin growth factor (IGF)-2, vascular endothelial growth factor (VEGF), Rho-associated kinase (ROCK), and caveolin (CAV)-1. IF and shear flow are crucial migratory factors for cancer cell invasion [74, 75]. Flow can trigger increased migration of cells via activation of surface receptors, such as the chemokine

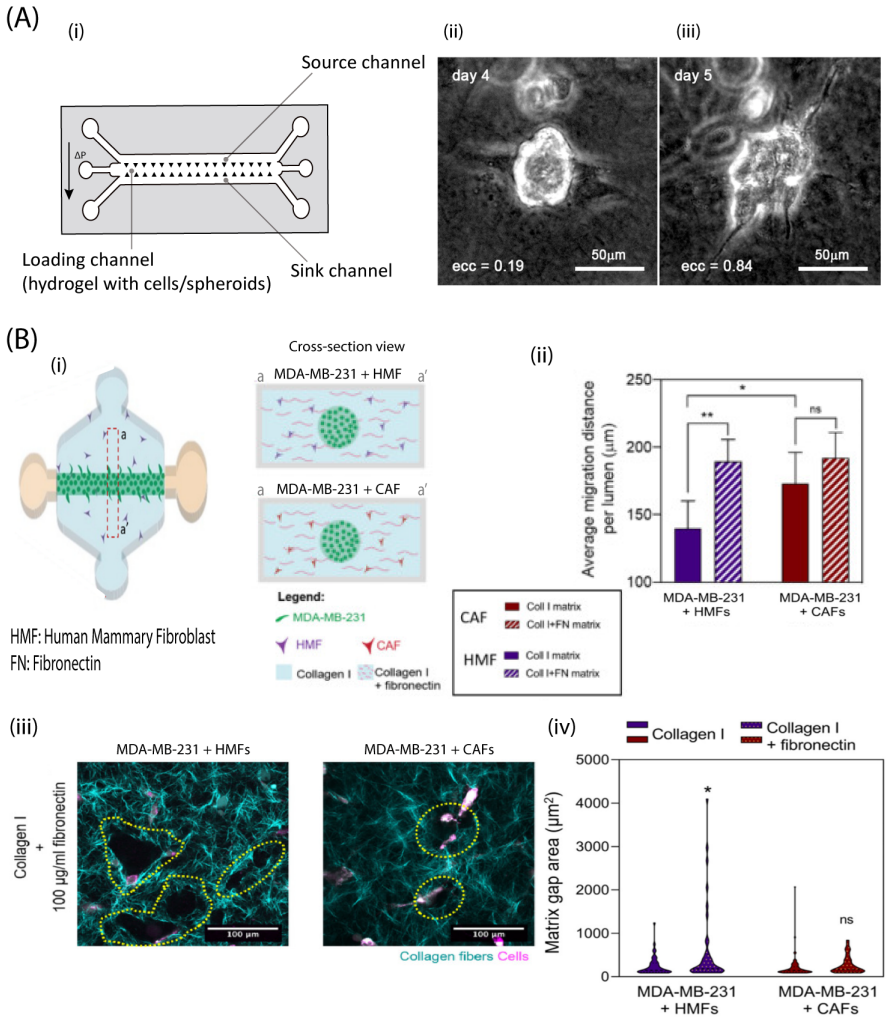

Figure 2.2: 3D matrix-based microfluidic models with physiologically relevant tumor microenvironment (TME) features. (Ai) A microfluidic device with a three-channel geometry. The source and the sink channel ensure proper hydration and study the impact of interstitial flow (IF) on cell migration. This model is very commonly used to study the effect of different cytokines on cell behavior. (Aii) Bright field image of transforming growth factor beta (TGF-β)-treated H1299 cells in a cluster-like morphology after 4 days, (Aiii) same cluster with strand-like morphology after 5 days [58]. (Bi) A 3D matrix-based microfluidic coculture model to recapitulate the TME with incorporation of fibronectin in collagen matrix and human mammary fibroblasts (HMFs) or cancer-associated fibroblasts (CAFs), [63]. (Bii) quantitative analysis of the average migration distance of metastatic cells (MDA-MB-231) from the edge of the lumen after 48 hours when cultured in the presence of HMFs or CAFs and in the presence of collagen without or with fibronectin. *(caption continued on next page)*

Figure 2.2: (Biii) Second harmonic generation (SHG) imaging of collagen fibers depicted in cyan and cells in magenta. Degradation of the collagen matrix (matrix gap area) in the presence of HMFs and CAFs highlighted by yellow broken line(Biv) Quantification of matrix gap areas for the conditions in (Biii) using violin plot representation [63]. (Aii) and (B) are reprinted and adapted from [58, 63] licensed under CC by 4.0. $*$ denotes a significant difference for $P \leq 0.05$ and $**$ for $P \leq 0.01$.

receptor CXCR4 and CCR7 [76]. Autologous chemotaxis, induced by a trans-cellular chemokine gradient, is responsible for driving directional cell migration in the presence of IF [77]. The most significant effect of IF, elevated IFP and solid stresses, leads to constricted and leaky vasculature, which impacts on drug delivery and the collapse of these vessels, which eventually causes hypoxia. These biophysical factors are important in inducing tumor migration events, which are not addressed in conventional in vitro culture models. The first step is to introduce biomimetic and natural matrices to recapture the native architecture of the ECM. To address physical stresses in the TME, a biomimetic ECM must be equipped with perfusion (or relevant IF rates). In recent years, the development of 3D matrix- based microfluidic devices as 3D in vitro cell migration platform addresses the limitations to integrate biophysical cues. Such studies have highlighted the role of 3D microfluidics and the importance of mechanical forces from ECM remodeling and IF in cancer cell migration events [74, 75, 78, 79].

Microfluidic models can generate flow rates and shear stress mimicking those found within tumor tissues. For example, increased interstitial and shear flow can lead to morphological and epige- netic changes that can result in a more aggressive behavior of breast cancer cells [74, 78]. Recent microfluidic models have highlighted the importance of flow-induced hydrodynamic shear stress on EMT in A549 (lung epithelial adenocarcinoma) cells cultured in a 3D microfluidic platform for several days [80]. Striking phenotypic changes were observed in A549 cells within the device when stimulated with shear flow compared with static cultures (no flow). Shear flow and IFP in solid tumors have been implicated in reducing the efficacy of cancer therapeutics [81]. Indeed, when the effect of flow on the efficacy of drugs on A549 cells was investigated, distinct cytotoxic effects were observed compared with static models, highlighting the role of flow in response to drugs [80] [80]. A downregulation of E-cadherin and an increase in vimentin and N-cadherin expression was observed, which is indicative for EMT, a mesenchymal cell phenotype that is frequently associated with therapy resistance [80]. This dynamic microfluidic model serves as a drug screening tool for different cancer types.

IF-induced downregulation of cadherins has also been implicated in increased tumor invasion as shown in a heterogeneous spheroid model consisting of MDA-MB-231 and MCF10A cells embedded in a collagen type I matrix (Fig. 2.3 3B) [78]B. In no-flow experiments, the heterogeneous spheroid does not show any disintegration, and only peripheral MDA-MB-231 cells migrate (Fig. 2.3Bii and iii). When IF was applied, the reduced E-cadherin expression on MCF-10A cells led to the dissociation of MDA-MB-231 cells from the spheroid core (Fig. 2.3Bii and iv). Designed to operate under a flow rate of 2 µm/s, lower than the elevated IF rates observed in animal models (up to 9 µm/s) or human patients (up to 55 µm/s), this platform highlights the importance of biophysical parameters in the TME [78]. This effect is a characteristic of morphological change that occurs if cells switch from a mesenchymal to an amoeboid migration mode. In cells, structural rearrangements are determined by time-dependent adhesion interac-

tions and long-range hydrodynamic interactions along with actin remodeling. In the presence of flow, amoeboid motility is triggered by the lack of molecules such as the fibronectin, which fails to form long-lived adhesions with collagen fibers [82] (Box 1).

Shear flow is a key regulator of cancer cell intravasation. Cancer cells preferentially intravasate in areas of low shear flow as high shear flows can destroy the cells [83, 84]. A microfluidic platform was developed to investigate the mechanism of intravasation and the way in which cells detect shear flow. Cells migrated inside longitudinal microchannels with an orthogonal channel such that cells would encounter an active fluid flow to mimic intravasation [84]. The shear stress sensed by cells due to fluid flow activated the transient receptor potential melastatin 7 (TRPM7), which promoted the influx of extracellular calcium ions and led to the reversal of migration direction via RhoA/Myosin-II and CDC42 pathways [84]. This study shows that cancer cells with high TRPM7 expression are not able to intravasate into blood vessels, thereby reducing the probability of metastasis [84]. Interstitial and shear flow studies using microfluidic models have improved our understanding of the migratory behavior of cells in the presence of flow and cellular plasticity as influenced by mechanical stimuli.

2.2.3. MICROFLUIDIC MODELS INCORPORATING CELL–CELL INTERACTIONS

As cells migrate collectively into healthy tissues, the dynamic reciprocity between the secreted cytokines and their cell surface receptors governs cell migration. Intercellular signaling cascades between tumor cells and other non-cancerous cells (CAFs, stromal cells, and immune cells) further contribute to tumor progression events [3, 86]. CAFs are frequently one of the most prom- inent and active components in the TME. While their origins remain obscure, recent data suggest that distinct subpopulations of CAFs exist within the tumor and their roles evolve and change as the disease progresses [65, 66]. CAFs, in some cancers, have been shown to lead to collective migration from the front by forming heterophilic junctions with cancer cells [68, 87, 88]. Through secreted cytokines, epigenetic reprogramming, and signaling cascades within the TME, CAFs have been implicated in ECM remodeling, the creation of a hypoxic microenvironment, and the alteration of the metabolic state of tumor cells, resulting in an acidic microenvironment [47, 68, 88, 89]. Tumor angiogenesis is key to cancer progression and metastasis. The creation of a hypoxic TME causes the secretion of VEGF, a key angiogenic factor. VEGF activates endothelial cells (ECs) through paracrine signaling and stimulates cell migration and proliferation of ECs, eventually resulting in the induction of angiogenesis.

3D microfluidic models have been developed to recapitulate TME heterogeneity by introducing CAFs as ECM remodeling components that secrete MMPs. Stromal cells play a key role in the dynamic nature of the TME with an active influence on remodeling, which controls physical properties such as stiffness, viscoelasticity, and pore size of ECM [53]. For example, a 3D matrix-based microfluidic platform was developed to colocalize MDA-MB-231 embedded in fibronectin-rich collagen matrix as a lumen-like geometry with fibroblasts to recreate a 3D tumor-stroma model (Fig. 2.2B). The microfluidic model incorporates human mammary fibroblasts (HMFs) and CAFs, thereby assessing the impact of cancer-stromal crosstalk on the migratory behavior of MDA-MB-231 cells [63]. In the first set of studies, fibronectin-rich matrix showed a qualitative increase in the num-

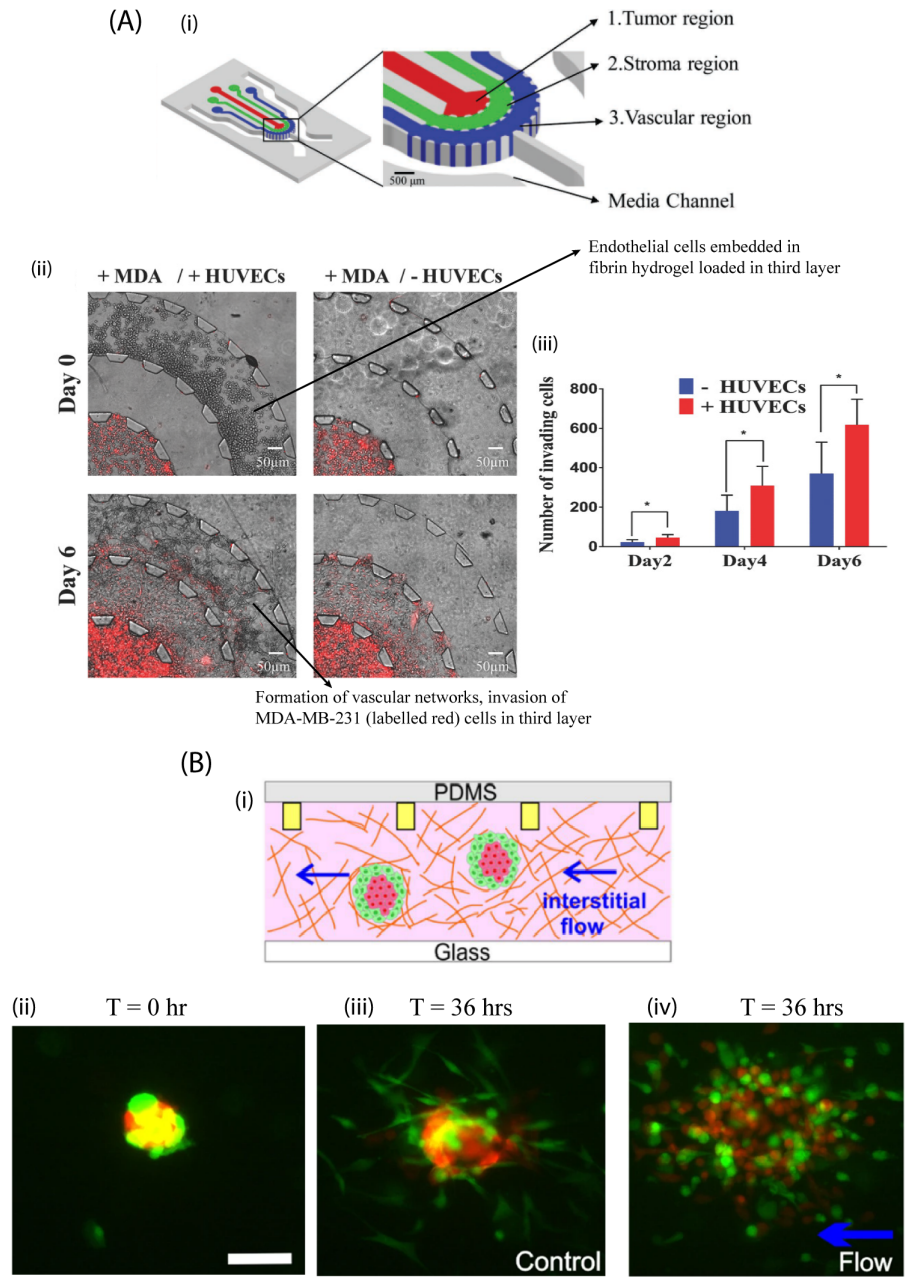

Figure 2.3: 3D microfluidic models to study and investigate invasion and intravasation events. (Ai) Schematic of multilayered tumor–stroma microfluidic model. The microfluidic model consists of three layers: 1.tumor region: consisting of MDA-MB-231 cells embedded in collagen hydrogel, 2.stromal region: to introduce tumor–stroma crosstalk, 3. vascular region: endothelial cells (ECs) embedded in fibrin to produce vascular networks. (Aii) MDA-MB-231 breast cancer cells (red fluorescence) invade the stromal region from the tumor region with simultaneous formation of vascular networks by the end of day 6. *caption continued on next page*

Figure 2.3: (Aiii) Quantitative analysis of MDA-MB-231 breast cancer cells invading into the tumor stromal region in the presence and absence of human umbilical vein endothelial cells (HUVECs) [85]. ∗ indicates a significant difference for $P < 0.05$. (Bi) cross-sectional view: channel filled with collagen hydrogel embedded with spheroids of cocultured MCF-10A normal breast cells and MDA-MB-231 breast cancer cells. (Bii–iv) (enlarged) fluorescence images of MDA-MB-231 cells (in green), MCF-10A (in red), scale bar 100 µm. (Biii) Control experiments (no-flow) do not promote spheroid dissociation, only peripheral MDA-MB-231 cells invaded outwards. (Biv) after application of 36 hours of interstitial flow, tumor dissociation is induced and is demonstrated by the disintegration of the spheroid core [78]. (A) is reproduced from [85] with permission from ©2018 Wiley-VCH Verlag GmbH & Co. KGaA, Weinheim. (B) is reprinted and adapted from [78] licensed under CC by 4.0. Abbreviation: PDMS, polydimethylsiloxane.

ber of cells migrating, regardless of the type of fibroblast present (Fig. 2.2Bii). A second set of studies were performed to observe the effect of HMFs and CAFs on the surrounding matrix degradation due to the secretion of MMPs shown in Fig. 2.2Biii and iv. Matrix degradation was quantified based on the gaps formed that are indicative of struc- tural deformation as assessed by fluorescence imaging. In a TME consisting of fibronectin-rich collagen embedded with HMFs, invasive human breast cancer (MDA-MB-231) cells migrated faster and for longer distances. The fibronectin-rich matrix signals HMFs to produce and secrete MMPs, which are responsible for ECM degradation [63]. These results indicate the influence of biochemical factors inside the TME (i.e., fibroblasts and ECM protein compositions) that directly induces matrix degradation, which results in a biomechanical response. Therefore, microfluidics, with its extensive modeling parameters, allows the incorporation of different cancer cell types and other TME-related biological components to recreate key components of a tumor model. The model provides a platform to study the effect of different chemokines and a combination of matrix materials for a comprehensive understanding of certain metastatic events.

A model developed to simultaneously study cell invasion and intravasation integrates a 3D multilayered microfluidic platform in the tumor stroma with MDA-MB-231 cancer cells em- bedded in a collagen hydrogel. In this model, MDA-MB-231 cells had increased migratory behavior, and they invaded the stromal region in the presence of vascular networks, which mimicked in vivo-like capillaries on day 0 compared with day 6 (Fig. 2.3Aii) [85]. The unique advantage of this model is the spatial control on the 3D tumor, stroma, and the vascular network region that allows for the formation of in vivo-like capillaries by human umbilical vein endothelial cells (HUVECs) embedded in relevant biomimetic ECM matrices. The presence of HUVECs led to the enhanced invasion of MDA-MB-231 cells and the degree of invasiveness was quantified as shown in Fig. 2.3Aiii. The microfluidic design serves asa novel platform to study interactions and biological mechanisms between cells and their TME for invasion and intravasation studies. While the collagen and fibrin matrices used in the study are physiologi- cally relevant, the adaptability of microfluidics enables the incorporation of patient-derived primary tumor cells and decellularized ECM to increase the accuracy of 3D matrix-based microfluidic models [10].

2.3. CONCLUDING REMARKS

3D matrix-based microfluidic models allow for more precise physiological representation and recreation of the TME, enabling us to determine the dominant mechanism of

cancer cell migration events under conditions mimicking more closely the aspects of in vivo situation. By combining relevant physicochemical parameters in a tumor–stroma model, the extent of specific roles of ECM, tissue heterogeneity, chemical signals, biomolecules, and mechanical forces can be explored. In recent years, microfluidic models were able to critically interrogate the influence of biochemical and biomechanical factors in tumor progression events. In addition, the advantage of real-time imaging makes this platform highly suitable to visualize dynamic processes and distinguish between single or collective migratory behavior displayed by tumor cells. The ability to select synthetic biomaterials that can be tuned for properties such as stiffness and pore size and to promote cell–matrix interactions gives an added advantage in decoupling interdependent factors for an in-depth revelation to interpret cell migration mechanisms. This review focuses on recent advances in microfluidic models to study the TME and the migration mechanisms of cancer cells (mostly breast and lung cancer) involved in tumor metastasis events, such as dissemination and invasion. Based on the type of tumor and influencing factors, including CAFs, ECM, TGF-β, and IF, the modes of cancer cell migration differ from each other. These emerging results demonstrate the importance of microfluidic models to determine preclinical therapeutic responses. By consolidating complex features of TME inside microfluidics, we can implement crucial physical and chemical cues (associated with different cancer types) that may enable more relevant drug screening platforms than could be achieved using static models. In addition, it has been confirmed that the increase of vascular density leading to enhanced mechanical forces during tumor growth can drastically diminish the delivery of drugs and oxygen supply at the inner region of the tumor [90]. There exists an opportunity to replace animal models preceding clinical trials for drug screening and anticancer therapeutics in the next decade by establishing specific quality controls for such 3D in vitro models. To fully identify the potential of 3D microfluidic approaches in cancer metastasis modeling and clinical trials, several key challenges and issues must be confronted (see Outstanding questions). To achieve this vision, microfluidics needs to undergo considerable upgrades by integrating it with cutting-edge and complementary research tools such as 3D bioprinting, engineered tissue constructs, artificial intelligence, and computational modeling. This integration will create next generation robust microfluidic models with a vision for personalized therapies by using patient-derived cells and mimicking patients' in vivo TME conditions. In the future, 3D microfluidic models will become more refined and equipped with automation functionalities and artificial intelligence algorithms to automatically identify crucial factors in tumor progression events, improving our understanding of cancer invasion and discovering a new class of drugs for cancer treatment. Therefore, microfluidics will become an ideal analytical tool to systematically investigate these complex and coupled features. Moreover, various types and combination of drugs can be tested to select the most suitable therapeutics for each cancer patient.

OUTSTANDING QUESTIONS

1. How can we adopt microfluidic models further to replicate nearly all of the complexities of the TME?
2. Will the incorporation of microfluidics in multicellular 3D models enable us to recapitulate the multiple steps of the metastatic process, from initial invasion into adjacent tissue, intravasation, survival in circulation, and extravasation to outgrowth in distant tissue?
3. What next steps are needed for microfluidic models to be utilized in routine clinical studies for drug screening and personalized cancer therapy?

ACKNOWLEDGMENTS

Z. R. and P. E. B. gratefully acknowledge funding from the European Research Council (ERC) under the European Union's Horizon 2020 research and innovation program (grant agreement no. 819424). P. M., P. T. D., and P. E. B. gratefully acknowledge funding from the Delft Health Technology grant (between LUMC and TU Delft) and ZonMW grant (09120012010061). P. T. D. is supported by Cancer Genomics Center, The Netherlands (CGC.NL.).

REFERENCES

[1] P. Mehta, Z. Rahman, P. ten Dijke, and P. E. Boukany, *Microfluidics meets 3D cancer cell migration,* Trends in Cancer **8**, 683 (2022).

[2] M. J. Mitchell, R. K. Jain, and R. Langer, *Engineering and physical sciences in oncology: Challenges and opportunities,* Nature Reviews Cancer **17**, 659 (2017).

[3] T. R. Cox, *The matrix in cancer,* Nature Reviews Cancer **21**, 217 (2021).

[4] L. Wan, C. A. Neumann, and P. R. Leduc, *Tumor-on-a-chip for integrating a 3D tumor microenvironment: Chemical and mechanical factors,* Lab on a Chip **20**, 873 (2020).

[5] E. Um, J. M. Oh, S. Granick, and Y. K. Cho, *Cell migration in microengineered tumor environments,* Lab on a Chip **17**, 4171 (2017).

[6] Y. L. Huang, J. E. Segall, and M. Wu, *Microfluidic modeling of the biophysical microenvironment in tumor cell invasion,* Lab on a Chip **17**, 3221 (2017).

[7] G. Vunjak-Novakovic, K. Ronaldson-Bouchard, and M. Radisic, *Organs-on-a-chip models for biological research,* Cell **184**, 4597 (2021).

[8] A. Sontheimer-Phelps, B. A. Hassell, and D. E. Ingber, *Modelling cancer in microfluidic human organs-on-chips,* Nature Reviews Cancer **19**, 65 (2019).

[9] H.-F. Tsai, A. Trubelja, A. Q. Shen, and G. Bao, *Tumour-on-a-chip: microfluidic models of tumour morphology, growth and microenvironment,* Journal of The Royal Society Interface **14**, 20170137 (2017).

[10] J. Rodrigues, M. A. Heinrich, L. M. Teixeira, and J. Prakash, *3D In Vitro Model (R)evolution: Unveiling Tumor–Stroma Interactions,* Trends in Cancer **7**, 249 (2021).

[11] H. Xu, X. Liu, and W. Le, *Recent advances in microfluidic models for cancer metastasis research,* TrAC - Trends in Analytical Chemistry **105**, 1 (2018).

[12] R. Portillo-Lara and N. Annabi, *Microengineered cancer-on-a-chip platforms to study the metastatic microenvironment,* Lab on a Chip **16**, 4063 (2016).

[13] M. F. Coughlin and R. D. Kamm, *The Use of Microfluidic Platforms to Probe the Mechanism of Cancer Cell Extravasation,* Advanced Healthcare Materials **9**, 1901410 (2020).

[14] Y.-H. V. Ma, K. Middleton, L. You, and Y. Sun, *A review of microfluidic approaches for investigating cancer extravasation during metastasis,* Microsystems & Nanoengineering **4**, 1 (2018).

[15] A. F. Sarioglu, N. Aceto, N. Kojic, M. C. Donaldson, M. Zeinali, B. Hamza, A. Engstrom, H. Zhu, T. K. Sundaresan, D. T. Miyamoto, X. Luo, A. Bardia, B. S. Wittner, S. Ramaswamy, T. Shioda, D. T. Ting, S. L. Stott, R. Kapur, S. Maheswaran, D. A. Haber, and M. Toner, *A microfluidic device for label-free, physical capture of circulating tumor cell clusters,* Nature Methods **12**, 685 (2015).

[16] V. C. Shukla, T. r. Kuang, A. Senthilvelan, N. Higuita-Castro, S. Duarte-Sanmiguel, S. N. Ghadiali, and D. Gallego-Perez, *Lab-on-a-Chip Platforms for Biophysical Studies of Cancer with Single-Cell Resolution,* Trends in Biotechnology **36**, 549 (2018).

[17] A. Boussommier-Calleja, R. Li, M. B. Chen, S. C. Wong, and R. D. Kamm, *Microfluidics: A New Tool for Modeling Cancer–Immune Interactions,* Trends in Cancer **2**, 6 (2016).

[18] D. Caballero, S. Kaushik, V. M. Correlo, J. M. Oliveira, R. L. Reis, and S. C. Kundu, *Organ-on-chip models of cancer metastasis for future personalized medicine: From chip to the patient,* Biomaterials **149**, 98 (2017).

[19] H. Aboulkheyr Es, L. Montazeri, A. R. Aref, M. Vosough, and H. Baharvand, *Personalized Cancer Medicine: An Organoid Approach,* Trends in Biotechnology **36**, 358 (2018).

[20] Q. Liu, A. Muralidharan, A. Saateh, Z. Ding, P. ten Dijke, and P. E. Boukany, *A Programmable Multifunctional 3D Cancer Cell Invasion Micro Platform,* Small , 2107757 (2022).

[21] M. Wang, J. Zhao, L. Zhang, F. Wei, Y. Lian, Y. Wu, Z. Gong, S. Zhang, J. Zhou, K. Cao, X. Li, W. Xiong, G. Li, Z. Zeng, and C. Guo, *Role of tumor microenvironment in tumorigenesis,* Journal of Cancer **8**, 761 (2017).

[22] V. Papalazarou, M. Salmeron-Sanchez, and L. M. Machesky, *Tissue engineering the cancer microenvironment—challenges and opportunities,* Biophysical Reviews **10**, 1695 (2018).

[23] Q. R. Guo, L. L. Zhang, J. F. Liu, Z. Li, J. J. Li, W. M. Zhou, H. Wang, J. Q. Li, D. Y. Liu, X. Y. Yu, and J. Y. Zhang, *Multifunctional microfluidic chip for cancer diagnosis and treatment,* Nanotheranostics **5**, 73 (2021).

[24] K. Paterson, S. Zanivan, R. Glasspool, S. B. Coffelt, and M. Zagnoni, *Microfluidic technologies for immunotherapy studies on solid tumours,* Lab on a Chip **21**, 2306 (2021).

[25] K. P. Valente, S. Khetani, A. R. Kolahchi, A. Sanati-Nezhad, A. Suleman, and M. Akbari, *Microfluidic technologies for anticancer drug studies,* Drug Discovery Today **22**, 1654 (2017).

[26] M. Shang, R. H. Soon, C. T. Lim, B. L. Khoo, and J. Han, *Microfluidic modelling of the tumor microenvironment for anti-cancer drug development,* Lab on a Chip **19**, 369 (2019).

[27] C. D. Paul, W. C. Hung, D. Wirtz, and K. Konstantopoulos, *Engineered Models of Confined Cell Migration,* Annual Review of Biomedical Engineering **18**, 159 (2016).

[28] M. Parri and P. Chiarugi, *Rac and Rho GTPases in cancer cell motility control,* Cell Communication and Signaling **8**, 1 (2010).

[29] V. Te Boekhorst, L. Preziosi, and P. Friedl, *Plasticity of Cell Migration in Vivo and in Silico,* Annual Review of Cell and Developmental Biology **32**, 491 (2016).

[30] K. Wolf, I. Mazo, H. Leung, K. Engelke, U. H. Von Andrian, E. I. Deryugina, A. Y. Strongin, E. B. Bröcker, and P. Friedl, *Compensation mechanism in tumor cell migration: Mesenchymal-amoeboid transition after blocking of pericellular proteolysis,* Journal of Cell Biology **160**, 267 (2003).

[31] E. M. Balzer, Z. Tong, C. D. Paul, W. C. Hung, K. M. Stroka, A. E. Boggs, S. S. Martin, and K. Konstantopoulos, *Physical confinement alters tumor cell adhesion and migration phenotypes,* FASEB Journal **26**, 4045 (2012).

[32] P. Friedl and R. Mayor, *Tuning collective cell migration by cell-cell junction regulation,* Cold Spring Harbor Perspectives in Biology **9**, 1 (2017).

[33] L. Qin, D. Yang, W. Yi, H. Cao, and G. Xiao, *Roles of leader and follower cells in collective cell migration,* Molecular Biology of the Cell **32**, 1267 (2021).

[34] M. Anguiano, X. Morales, C. Castilla, A. R. Pena, C. Ederra, M. Martínez, M. Ariz, M. Esparza, H. Amaveda, M. Mora, N. Movilla, J. M. G. Aznar, I. Cortés-Domínguez, and C. Ortiz-de Solorzano, *The use of mixed collagen-Matrigel matrices of increasing complexity recapitulates the biphasic role of cell adhesion in cancer cell migration: ECM sensing, remodeling and forces at the leading edge of cancer invasion,* PLOS ONE **15**, e0220019 (2020).

[35] J. Yang and R. A. Weinberg, *Epithelial-Mesenchymal Transition: At the Crossroads of Development and Tumor Metastasis,* Developmental Cell **14**, 818 (2008).

[36] N. M. Aiello, R. Maddipati, R. J. Norgard, D. Balli, J. Li, S. Yuan, T. Yamazoe, T. Black, A. Sahmoud, E. E. Furth, D. Bar-Sagi, and B. Z. Stanger, *EMT Subtype Influences Epithelial Plasticity and Mode of Cell Migration,* Developmental Cell **45**, 681 (2018).

[37] J. Yang, P. Antin, G. Berx, C. Blanpain, T. Brabletz, M. Bronner, K. Campbell, A. Cano, J. Casanova, G. Christofori, S. Dedhar, R. Derynck, H. L. Ford, J. Fuxe, A. García de Herreros, G. J. Goodall, A. K. Hadjantonakis, R. J. Huang, C. Kalcheim, R. Kalluri, Y. Kang, Y. Khew-Goodall, H. Levine, J. Liu, G. D. Longmore, S. A. Mani, J. Massagué, R. Mayor, D. McClay, K. E. Mostov, D. F. Newgreen, M. A. Nieto, A. Puisieux, R. Runyan, P. Savagner, B. Stanger, M. P. Stemmler, Y. Takahashi, M. Takeichi, E. Theveneau, J. P. Thiery, E. W. Thompson, R. A. Weinberg, E. D. Williams, J. Xing, B. P. Zhou, and G. Sheng, *Guidelines and definitions for research on epithelial–mesenchymal transition,* Nature Reviews Molecular Cell Biology **21**, 341 (2020).

[38] N. Maishi, D. A. Annan, H. Kikuchi, Y. Hida, and K. Hida, *Tumor endothelial heterogeneity in cancer progression,* Cancers **11**, 1511 (2019).

[39] J. Song, A. Miermont, C. T. Lim, and R. D. Kamm, *A 3D microvascular network model to study the impact of hypoxia on the extravasation potential of breast cell lines,* Scientific Reports **8**, 1 (2018).

[40] M. Anguiano, C. Castilla, M. Maška, C. Ederra, R. Peláez, X. Morales, G. Muñoz-Arrieta, M. Mujika, M. Kozubek, A. Muñoz-Barrutia, A. Rouzaut, S. Arana, J. M. Garcia-Aznar, and C. Ortiz-de Solorzano, *Characterization of three-dimensional cancer cell migration in mixed collagen-Matrigel scaffolds using microfluidics and image analysis,* PLoS ONE **12**, e0171417 (2017).

[41] K. Jeong, Y. J. Yu, J. Y. You, W. J. Rhee, and J. A. Kim, *Exosome-mediated microRNA-497 delivery for anti-cancer therapy in a microfluidic 3D lung cancer model,* Lab on a Chip **20**, 548 (2020).

[42] M. J. Bradney, S. M. Venis, Y. Yang, S. F. Konieczny, and B. Han, *A Biomimetic Tumor Model of Heterogeneous Invasion in Pancreatic Ductal Adenocarcinoma,* Small **16**, 1 (2020).

[43] J. H. Lee, S. K. Kim, I. A. Khawar, S. Y. Jeong, S. Chung, and H. J. Kuh, *Microfluidic co-culture of pancreatic tumor spheroids with stellate cells as a novel 3D model for investigation of stroma-mediated cell motility and drug resistance,* Journal of Experimental and Clinical Cancer Research **37**, 1 (2018).

[44] H. J. Pandya, K. Dhingra, D. Prabhakar, V. Chandrasekar, S. K. Natarajan, A. S. Vasan, A. Kulkarni, and H. Shafiee, *A microfluidic platform for drug screening in a 3D cancer microenvironment,* Biosensors and Bioelectronics **94**, 632 (2017).

[45] J. M. Ayuso, S. Sadangi, M. Lares, S. Rehman, M. Humayun, K. M. Denecke, M. C. Skala, D. J. Beebe, and V. Setaluri, *Microfluidic model with air-walls reveals fibroblasts and keratinocytes modulate melanoma cell phenotype, migration, and metabolism,* Lab on a Chip **21**, 1139 (2021).

[46] L. Fattet, H. Y. Jung, M. W. Matsumoto, B. E. Aubol, A. Kumar, J. A. Adams, A. C. Chen, R. L. Sah, A. J. Engler, E. B. Pasquale, and J. Yang, *Matrix Rigidity Controls Epithelial-Mesenchymal Plasticity and Tumor Metastasis via a Mechanoresponsive EPHA2/LYN Complex,* Developmental Cell **54**, 302 (2020).

[47] O. Ilina, P. G. Gritsenko, S. Syga, J. Lippoldt, C. A. La Porta, O. Chepizhko, S. Grosser, M. Vullings, G. J. Bakker, J. Starruß, P. Bult, S. Zapperi, J. A. Käs, A. Deutsch, and P. Friedl, *Cell–cell adhesion and 3D matrix confinement determine jamming transitions in breast cancer invasion,* Nature Cell Biology **22**, 1103 (2020).

[48] A. Haeger, M. Krause, K. Wolf, and P. Friedl, *Cell jamming: Collective invasion of mesenchymal tumor cells imposed by tissue confinement,* Biochimica et Biophysica Acta - General Subjects **1840**, 2386 (2014).

[49] K. M. Stroka, H. Jiang, S. H. Chen, Z. Tong, D. Wirtz, S. X. Sun, and K. Konstantopoulos, *Water permeation drives tumor cell migration in confined microenvironments,* Cell **157**, 611 (2014).

[50] K. Wolf, M. te Lindert, M. Krause, S. Alexander, J. te Riet, A. L. Willis, R. M. Hoffman, C. G. Figdor, S. J. Weiss, and P. Friedl, *Physical limits of cell migration: Control by ECM space and nuclear deformation and tuning by proteolysis and traction force,* Journal of Cell Biology **201**, 1069 (2013).

[51] C. M. Denais, R. M. Gilbert, P. Isermann, A. L. McGregor, M. Te Lindert, B. Weigelin, P. M. Davidson, P. Friedl, K. Wolf, and J. Lammerding, *Nuclear envelope rupture and repair during cancer cell migration,* Science **352**, 353 (2016).

[52] M. Wang, B. Cheng, Y. Yang, H. Liu, G. Huang, L. Han, F. Li, and F. Xu, *Microchannel Stiffness and Confinement Jointly Induce the Mesenchymal-Amoeboid Transition of Cancer Cell Migration,* Nano Letters **19**, 5949 (2019).

[53] F. Spill, D. S. Reynolds, R. D. Kamm, and M. H. Zaman, *Impact of the physical microenvironment on tumor progression and metastasis,* Current Opinion in Biotechnology **40**, 41 (2016).

[54] I. Sigdel, N. Gupta, F. Faizee, V. M. Khare, A. K. Tiwari, and Y. Tang, *Biomimetic Microfluidic Platforms for the Assessment of Breast Cancer Metastasis,* Frontiers in Bioengineering and Biotechnology **9**, 1 (2021).

[55] L. A. Lautscham, C. Kämmerer, J. R. Lange, T. Kolb, C. Mark, A. Schilling, P. L. Strissel, R. Strick, C. Gluth, A. C. Rowat, C. Metzner, and B. Fabry, *Migration in Confined 3D Environments Is Determined by a Combination of Adhesiveness, Nuclear Volume, Contractility, and Cell Stiffness,* Biophysical Journal **109**, 900 (2015).

[56] I. Y. Wong, S. Javaid, E. A. Wong, S. Perk, D. A. Haber, M. Toner, and D. Irimia, *Collective and individual migration following the epithelial-mesenchymal transition,* Nature materials **13**, 1063 (2014).

[57] K. M. Yamada and M. Sixt, *Mechanisms of 3D cell migration,* Nature Reviews Molecular Cell Biology **20**, 738 (2019).

[58] J. Plou, Y. Juste-Lanas, V. Olivares, C. del Amo, C. Borau, and J. M. García-Aznar, *From individual to collective 3D cancer dissemination: roles of collagen concentration and TGF-β,* Scientific Reports **8**, 1 (2018).

[59] J. Zhang, K. F. Goliwas, W. Wang, P. V. Taufalele, F. Bordeleau, and C. A. Reinhart-King, *Energetic regulation of coordinated leader–follower dynamics during collective invasion of breast cancer cells,* Proceedings of the National Academy of Sciences of the United States of America **116**, 7867 (2019).

[60] B. Ladoux and R. M. Mège, *Mechanobiology of collective cell behaviours,* Nature Reviews Molecular Cell Biology **18**, 743 (2017).

[61] J. S. Park, D. H. Kim, H. N. Kim, C. J. Wang, M. K. Kwak, E. Hur, K. Y. Suh, S. S. An, and A. Levchenko, *Directed migration of cancer cells guided by the graded texture of the underlying matrix,* Nature Materials **15**, 792 (2016).

[62] Q. Fan, R. Liu, Y. Jiao, C. Tian, J. D. Farrell, W. Diao, X. Wang, F. Zhang, W. Yuan, H. Han, J. Chen, Y. Yang, X. Zhang, F. Ye, M. Li, Z. Ouyang, and L. Liu, *A novel 3-D bio-microfluidic system mimicking: In vivo heterogeneous tumour microstructures reveals complex tumour-stroma interactions,* Lab on a Chip **17**, 2852 (2017).

[63] K. M. Lugo-Cintrón, M. M. Gong, J. M. Ayuso, L. A. Tomko, D. J. Beebe, M. Virumbrales-Muñoz, and S. M. Ponik, *Breast Fibroblasts and ECM Components Modulate Breast Cancer Cell Migration through the Secretion of MMPs in a 3D Microfluidic Co-Culture Model,* Cancers **12**, 1173 (2020).

[64] F. Lüönd, S. Tiede, and G. Christofori, *Breast cancer as an example of tumour heterogeneity and tumour cell plasticity during malignant progression,* British Journal of Cancer **125**, 164 (2021).

[65] B. A. Pereira, C. Vennin, M. Papanicolaou, C. R. Chambers, D. Herrmann, J. P. Morton, T. R. Cox, and P. Timpson, *CAF Subpopulations: A New Reservoir of Stromal Targets in Pancreatic Cancer,* Trends in Cancer **5**, 724 (2019).

[66] G. Friedman, O. Levi-Galibov, E. David, C. Bornstein, A. Giladi, M. Dadiani, A. Mayo, C. Halperin, M. Pevsner-Fischer, H. Lavon, S. Mayer, R. Nevo, Y. Stein, N. Balint-Lahat, I. Barshack, H. R. Ali, C. Caldas, E. Nili-Gal-Yam, U. Alon, I. Amit, and R. Scherz-Shouval, *Cancer-associated fibroblast compositions change with breast cancer progression linking the ratio of S100A4+ and PDPN+ CAFs to clinical outcome,* Nature Cancer **1**, 692 (2020).

[67] M. Bartoschek, N. Oskolkov, M. Bocci, J. Lövrot, C. Larsson, M. Sommarin, C. D. Madsen, D. Lindgren, G. Pekar, G. Karlsson, M. Ringnér, J. Bergh, Björklund, and K. Pietras, *Spatially and functionally distinct subclasses of breast cancer-associated fibroblasts revealed by single cell RNA sequencing,* Nature Communications **9**, 5150 (2018).

[68] B. Erdogan, M. Ao, L. M. White, A. L. Means, B. M. Brewer, L. Yang, M. K. Washington, C. Shi, O. E. Franco, A. M. Weaver, S. W. Hayward, D. Li, and D. J. Webb, *Cancer-associated fibroblasts promote directional cancer cell migration by aligning fibronectin,* Journal of Cell Biology **216**, 3799 (2017).

[69] G. Follain, D. Herrmann, S. Harlepp, V. Hyenne, N. Osmani, S. C. Warren, P. Timpson, and J. G. Goetz, *Fluids and their mechanics in tumour transit: shaping metastasis,* Nature Reviews Cancer **20**, 107 (2020).

[70] S. Colak and P. ten Dijke, *Targeting TGF-β Signaling in Cancer,* Trends in Cancer **3**, 56 (2017).

[71] R. A. Gatenby, K. Smallbone, P. K. Maini, F. Rose, J. Averill, R. B. Nagle, L. Worrall, and R. J. Gillies, *Cellular adaptations to hypoxia and acidosis during somatic evolution of breast cancer,* British Journal of Cancer **97**, 646 (2007).

[72] K. Hida, N. Maishi, D. A. Annan, and Y. Hida, *Contribution of tumor endothelial cells in cancer progression,* International Journal of Molecular Sciences **19**, 1 (2018).

[73] E. Gordon, L. Schimmel, and M. Frye, *The Importance of Mechanical Forces for in vitro Endothelial Cell Biology,* Frontiers in Physiology **11**, 1 (2020).

[74] A. S. Piotrowski-Daspit, J. Tien, and C. M. Nelson, *Interstitial fluid pressure regulates collective invasion in engineered human breast tumors via Snail, vimentin, and E-cadherin,* Integrative Biology (United Kingdom) **8**, 319 (2016).

[75] W. J. Polacheck, A. E. German, A. Mammoto, D. E. Ingber, and R. D. Kamm, *Mechanotransduction of fluid stresses governs 3D cell migration,* Proceedings of the National Academy of Sciences of the United States of America **111**, 2447 (2014).

[76] W. J. Polacheck, J. L. Charest, and R. D. Kamm, *Interstitial flow influences direction of tumor cell migration through competing mechanisms,* Proceedings of the National Academy of Sciences of the United States of America **108**, 11115 (2011).

[77] J. D. Shields, M. E. Fleury, C. Yong, A. A. Tomei, G. J. Randolph, and M. A. Swartz, *Autologous Chemotaxis as a Mechanism of Tumor Cell Homing to Lymphatics via Interstitial Flow and Autocrine CCR7 Signaling,* Cancer Cell **11**, 526 (2007).

[78] Y. L. Huang, Y. Ma, C. Wu, C. Shiau, J. E. Segall, and M. Wu, *Tumor spheroids under perfusion within a 3D microfluidic platform reveal critical roles of cell-cell adhesion in tumor invasion,* Scientific reports **10**, 9648 (2020).

[79] A. T. Young, O. C. White, and M. A. Daniele, *Rheological Properties of Coordinated Physical Gelation and Chemical Crosslinking in Gelatin Methacryloyl (GelMA) Hydrogels,* Macromolecular Bioscience **20**, 1 (2020).

[80] V. Mani, Z. Lyu, V. Kumar, B. Ercal, H. Chen, S. V. Malhotra, and U. Demirci, *Epithelial-to-Mesenchymal Transition (EMT) and Drug Response in Dynamic Bioengineered Lung Cancer Microenvironment,* Advanced Biosystems **3**, 1 (2019).

[81] C. H. Heldin, K. Rubin, K. Pietras, and A. Östman, *High interstitial fluid pressure - An obstacle in cancer therapy,* Nature Reviews Cancer **4**, 806 (2004).

[82] H. S. Samanta, *Interstitial flows regulate collective cell migration heterogeneity through adhesion,* Physical Review Research **2**, 013048 (2020).

[83] S. P. Chiang, R. M. Cabrera, and J. E. Segall, *Tumor cell intravasation,* American Journal of Physiology - Cell Physiology **311**, C1 (2016).

[84] C. L. Yankaskas, K. N. Thompson, C. D. Paul, M. I. Vitolo, P. Mistriotis, A. Mahendra, V. K. Bajpai, D. J. Shea, K. M. Manto, A. C. Chai, N. Varadarajan, A. Kontrogianni-Konstantopoulos, S. S. Martin, and K. Konstantopoulos, *A microfluidic assay for the quantification of the metastatic propensity of breast cancer specimens,* Nature Biomedical Engineering **3**, 452 (2019).

[85] S. Nagaraju, D. Truong, G. Mouneimne, and M. Nikkhah, *Microfluidic Tumor–Vascular Model to Study Breast Cancer Cell Invasion and Intravasation,* Advanced Healthcare Materials **7**, 1 (2018).

[86] B. Trappmann, B. M. Baker, W. J. Polacheck, C. K. Choi, J. A. Burdick, and C. S. Chen, *Matrix degradability controls multicellularity of 3D cell migration,* Nature Communications **8**, 1 (2017).

[87] A. Labernadie, T. Kato, A. Brugués, X. Serra-Picamal, S. Derzsi, E. Arwert, A. Weston, V. González-Tarragó, A. Elosegui-Artola, L. Albertazzi, J. Alcaraz, P. Roca-Cusachs, E. Sahai, and X. Trepat, *A mechanically active heterotypic E-cadherin/N-cadherin adhesion enables fibroblasts to drive cancer cell invasion,* Nature Cell Biology **19**, 224 (2017).

[88] L. M. Becker, J. T. O'Connell, A. P. Vo, M. P. Cain, D. Tampe, L. Bizarro, H. Sugimoto, A. K. McGow, J. M. Asara, S. Lovisa, K. M. McAndrews, R. Zielinski, P. L. Lorenzi, M. Zeisberg, S. Raza, V. S. LeBleu, and R. Kalluri, *Epigenetic Reprogramming of Cancer-Associated Fibroblasts Deregulates Glucose Metabolism and Facilitates Progression of Breast Cancer,* Cell Reports **31**, 107701 (2020).

[89] L. P. Ferreira, V. M. Gaspar, L. Mendes, I. F. Duarte, and J. F. Mano, *Organotypic 3D decellularized matrix tumor spheroids for high-throughput drug screening,* Biomaterials **275**, 120983 (2021).

[90] F. Mpekris, C. Voutouri, J. W. Baish, D. G. Duda, L. L. Munn, T. Stylianopoulos, and R. K. Jain, *Combining microenvironment normalization strategies to improve cancer immunotherapy,* Proceedings of the National Academy of Sciences of the United States of America **117**, 3728 (2020).

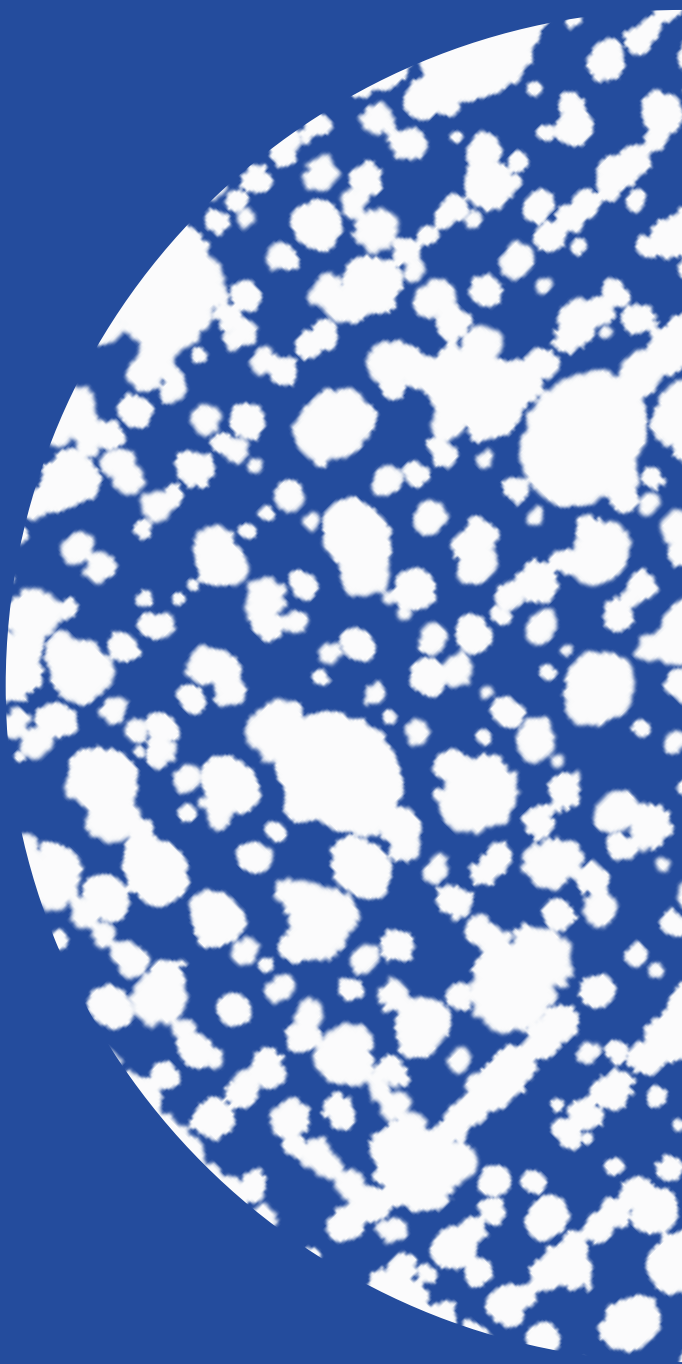

3

INTERSTITIAL FLOW POTENTIATES TGF-β/SMAD-SIGNALING ACTIVITY IN LUNG CANCER SPHEROIDS IN A 3D-MICROFLUIDIC CHIP

ABSTRACT

Within the tumor microenvironment (TME), cancer cells use mechanotransduction pathways to convert biophysical forces to biochemical signals. However, the underlying mechanisms and functional significance of these pathways remain largely unclear. The upregulation of mechanosensitive pathways from biophysical forces such as interstitial flow (IF), leads to the activation of various cytokines, including transforming growth factor-β (TGF-β). TGF-β promotes in part via a Smad-dependent signaling pathway and the epithelial-mesenchymal transition (EMT). The latter process is linked to increased cancer cell motility and invasion. Current research models have limited ability to investigate the combined effects of biophysical forces (such as IF) and cytokines (TGF-β) in a 3D microenvironment. We used a 3D-matrix based microfluidic platform to demonstrate the potentiating effect of IF on exogenous TGF-β induced upregulation of the Smad-signaling activity and the expression of mesenchymal marker vimentin in A549 lung cancer spheroids. To monitor this, we used stably integrated fluorescent based reporters into the A549 cancer cell genome. Our results demonstrate that IF enhances exogenous TGF-β induced Smad-signaling activity in lung cancer spheroids embedded in a matrix microenvironment. In addition, we observed an increased cell motility for A549 spheroids when exposed to IF and TGF-β. Our 3D-microfluidic model integrated with real-time imaging provides a powerful tool for investigating cancer cell signaling and motility associated with invasion characteristics in a physiologically relevant TME.

This chapter is published as Z. Rahman, A. Deep Bordoloi, H. Rouhana, M. Tavasso, G.V.D. Zon, V. Garbin, P. ten Dijke, P.E. Boukany, *Lab on a Chip (2024)* [1]

3.1. INTRODUCTION

The 3D tumor microenvironment (TME) plays a crucial role in the progression and metastasis of primary tumors to secondary tumor sites [2, 3]. It consists of key components such as the extracellular matrix (ECM), biophysical forces (interstitial flow and consequent fluid stresses), tumor cell-TME interactions in the presence of stromal cells, immune cells and cancer-associated fibroblasts (CAFs). The interplay of these components contributes to the metastatic cascade of events from early dissemination to extravasation [4]. However, most tumor cell migration and invasion studies have been performed in 2D/3D in vitro models that poorly recapitulate the characteristics of solid tumors in vivo. To overcome these limitations, microfluidic platforms provide an effective tool to replicate a physiologically relevant TME for studying cancer cell behavior [5].

Recent advances in microfluidic platforms based on a 3-D matrix have allowed for the incorporation of key components of the tumor microenvironment (TME) in cancer cell migration and invasion studies [5, 6]. To mimic the ECM, natural-hydrogel materials with tunable mechanical properties are used [7]. These hydrogels have been further embedded with single cancer cells and/or cancer cell aggregate/spheroids to include cell-matrix interactions. Advancements in modeling and fabrication technologies have improved microfluidic devices to introduce interstitial flow (IF) for long-term perfusion and culture conditions. In the past, IF studies were mostly performed on single cells embedded in a matrix material [8–10]. Recently, researchers have investigated the invasive and migratory cellular response of a breast tumor spheroid model under IF to show morphological and epigenetic changes [11]. However, these studies were limited to highly migratory breast cancer cells and did not include effect of biochemical signals towards EMT signaling pathways.

The role of IF is important due to its direct influence on the remodeling of the ECM, where compressive, tensional and shear forces are sensed by cell-surface receptors that activate mechanotransduction pathways to trigger biochemical signals [8, 12–14]. This further leads to the activation and upregulation of many core EMT cytokines [8], including the TGF-β cytokine, known as a key EMT inducer [15, 16]. In solid tumors, the poorly drained interstitial flow is responsible for interstitial fluid pressure build up in the surrounding healthy tissue [8]. Moreover, the lung tumor tissue is constantly subjected to a mechanical load due to its physiological activities that may aid in cancer cell invasion and migration [17, 18]. Therefore, it is of primary interest to study primary lung tumor models such as A549 lung adenocarcinoma, when subjected to biophysical force induced stresses. It has been proposed that the cancer cells exposed to biomechanical forces (such as IF, fluid-induced shear stress, compressive stress from matrix microenvironment) leads to endogenous TGF-β driven Smad-signaling activity towards EMT response [14, 19, 20]. Moreover, studies have also investigated the role of fluid-induced shear stress to promote mechanotransduction pathways (such as YAP/TAZ) responsible for triggering EMT signaling for cancer cell invasion in non-small cell lung cancer, breast cancer and melanoma tumor [21–23].

TGF-β is capable to promote cancer cell invasion and progression in various tumor types such as lung, breast and pancreatic cancer [24, 25]. TGF-β receptors at the cell-surface upon binding TGF-β activate the intracellular Smad-signaling pathway [24]. Activated Smads can act as transcription factors to mediate EMT associated with cancer.

It is well known that the Smad-signaling pathway contributes to EMT, however Smad-independent pathways may also contribute to EMT via multiple complex intra-cellular signaling events that play an important role in cancer cell invasion [26, 27]. Many researchers have studied the role of TGF-β in static 2D/3D tumor models, highlighting its importance in activating EMT transcriptional factors including SNAI1, TWIST, ZEB1 [24]. Studies conducted on A549 lung adenocarcinoma cells showed EMT behavior upon exposure to TGF-β cytokine [28–31]. Most studies focused on the upregulation of mesenchymal markers (such as vimentin) and an increased expression of transcription factors such as SNAIl and ZEB2 highlighting EMT response [28, 32, 33]. The upregulation of the vimentin mesenchymal marker and downregulation of the E-cadherin (epithelial marker) in A549 lung cancer cells were found to be associated with an aggressive motile response [25]. In recent years, researchers further studied A549 3D cancer models towards EMT behavior [34, 35]. However, these studies were performed in culture conditions devoid of matrix material and IF. Thus, there is an evident lack of research on the effect of IF and exogenous TGF-β on A549 lung tumor EMT response in a relevant matrix microenvironment.

In this research, we employed a 3D-matrix based microfluidic model to investigate the impact of IF and exogenous TGF-β cytokine on epithelial-like A549 spheroids (Fig. 3.1(A) and (B)). Specifically, we investigated the Smad-dependent transcriptional pathway and vimentin biomarker expression in response to varying IF and exogenous TGF-β concentration towards cancer cell invasion(Fig. 3.1(C)). These studies were conducted with genetically modified A549 lung tumor cells with dual artificial reporter constructs for Smad-signaling pathway (CAGA-12-GFP reporter gene) and vimentin biomarker (VIM-RFP reporter gene) (Fig. 3.1C, inset figure). We demonstrate that IF potentiates Smad-dependent transcriptional response when exposed to exogenous TGF-β. The combined effect of IF and TGF-β also showed increased abundance in vimentin protein. Lastly, A549 lung tumor exhibited increased cellular motion on the spheroid periphery showing cancer cell invasion characteristics. These findings suggest that external IF and cellular cues play critical roles in promoting the invasive characteristics of cancer cells within relevant matrix microenvironments, and highlight the importance of incorporating these factors in cancer research models.

3.2. MATERIALS AND METHODS

3.2.1. CELL CULTURE

A549-VIM-RFP cells were acquired from the company, ATCC [36]. These cells are engineered by CRISPR to produce a red fluorescent protein (RFP)-vimentin fusion protein. When cells acquire mesenchymal phenotype they express RFP linked to vimentin protein (VIM-RFP). To construct a dual reporter, A549-VIM-RFP cells were transduced with a lentiviral CAGA-12-GFP construct to produce a green fluorescent protein (GFP) response upon Smad-pathway activation. The dual reporter cell line was a gift from Yifan Zhu (Department of Cell and Chemical Biology, LUMC). The functionality of the CAGA-12-GFP reporter has been validated through several studies. [37, 38]. A549-VIM-RFP cells have been previously reported to exhibit EMT with an upregulation in VIM-RFP fluorescence upon exogenous TGF-β stimulation [39]. The dual-reporter A549 cells were

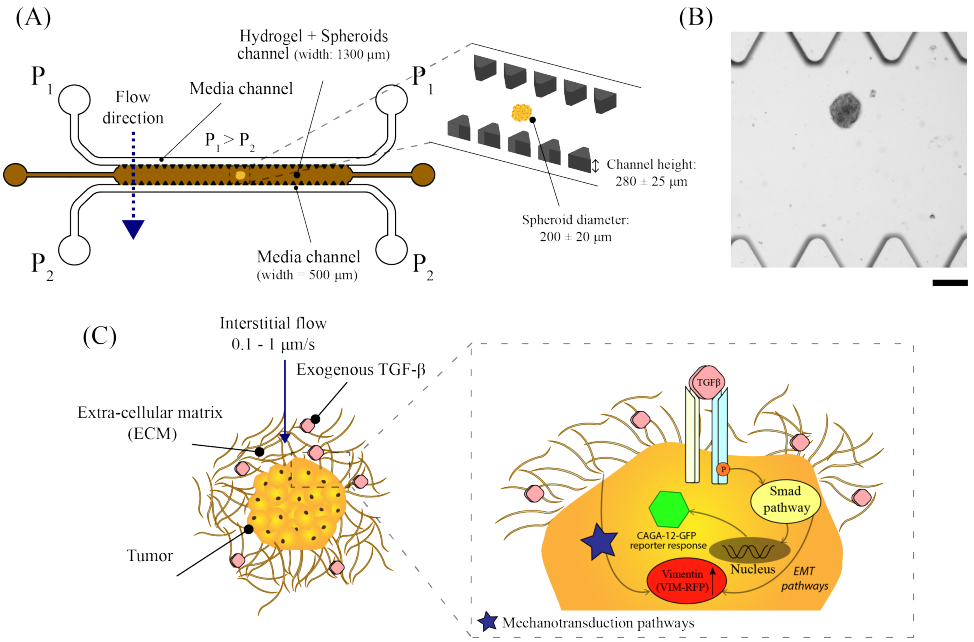

Figure 3.1: 3D-matrix based microfluidic platform to study interstitial flow and TGF-β/Smad-signaling and vimentin expression in A549 lung tumor spheroids. (A) Schematic of the 3D-matrix based microfluidic platform. Inset figure shows the spheroid size and the dimensions of the channel height of the microfluidic chip (not to scale). (B) Bright-field image displaying A549 spheroid embedded in 3D-matrix based scaffold in the hydrogel channel of the microfluidic chip. Scale bar: 200 µm (C) A549 lung tumor spheroid exposed to interstitial flow and exogenous TGF-β embedded in a matrix microenvironment. Inset figure illustrates that exogenous TGF-β molecules specifically binds with TGF-β surface receptors to activate the intracellular Smad-signalling pathway. This results in upregulation of transcriptional reporter gene CAGA-12-GFP activity. TGF-β cytokine also leads to the upregulation in EMT pathways. Upregulation in EMT biomarker (vimentin) can be investigated by determining the VIM-RFP reporter intensity. Moreover, cancer cells sense interstitial flow induced fluid-shear and hydrodynamic stress to initiate mechanotransduction pathways triggering EMT. These biomechanical forces may enforce the TGF-β/Smad activity for increased transcriptional reporter activity (CAGA-12-GFP intensity) and EMT response (VIM-RFP reporter expression).

maintained in Dulbecco's Modified Eagle Medium High Glucose (DMEM,Sigma) containing 4.5 g/L glucose, L-glutamine without sodium pyruvate, and supplemented with 10% Fetal Bovine Serum (FBS, Sigma) and 1% Antibiotic-Antimycotic solution (Gibco). All cells were incubated at 37°C with 5% CO_2 and sub-cultured 2 times per week. Cells were frequently tested for absence of mycoplasma and checked for authenticity by STR profiling.

3.2.2. SPHEROID FABRICATION

Spheroids were grown in a commercially available Corning^{TM} Elplasia^{TM} 96-well plate for high-throughput spheroid production. These well plates are round-bottom with Ultra-Low Attachment (ULA) surface that prevents cell-surface attachment and promotes cell-cell adhesion. We used an initial seeding density of 40 x 10^3 cells (500 cells per microwell) for each well to produce 79 spheroids. Spheroid size is dependent on the initial seeding density, cell proliferation rate and culture duration. Spheroids were ready to use after 4 days of culture in the wells and were 200 ± 20 µm in diameter. We restricted the spheroid diameter to less than 220 µm to avoid a necrotic core and to avoid contact with the glass bottom of the microfluidic chip. Any cancer spheroids that made contact with the microfluidic glass substrate, were excluded from the analysis in this work.

3.2.3. HYDROGEL SYNTHESIS AND CHARACTERIZATION

Gelatin methacryloyl (GelMA), 300g bloom, 60 % degree substitution, was purchased from Sigma Aldrich. Like gelatin, GelMA is still a thermo-reversible gel, however, the methacrylic anhydride groups give the ability to undergo covalent cross-linking under UV light (365 nm) in the presence of a UV photo-initiator. 5wt.% GelMA was used in experiments, with a mass ratio of 1:16 of photo-initiator (Lithium phenyl-2,4,6- trimethylbenzoylphosphinate, LAP; Sigma Aldrich). LAP and GelMA were added together and dissolved in Dulbecco's Phosphae Buffered Saline (DPBS; Gibco). The mixture was dissolved at 37°C in a water bath for about 2 hours. The hydrogel was then crosslinked using Colibri Axio Observer microscope laser 385 nm with a 5x objective lens for 45 seconds. The viscoelastic properties of crosslinked GelMA were investigated with a modular rotational rheometer (DSR 502, Anton Paar) equipped with a parallel plate of a diameter of 25 mm. Full experimental detail can be found in ESI (section 1). The 5wt.% GelMA analyzed at a fixed strain of 1% with frequency sweeps (0.1 to 100 rad/s) at room temperature showed a solid-like behavior, with a storage modulus G'≈ 250 Pa, higher than the loss modulus (G") by at least one order of magnitude (Fig. 3.5). The lung tumor tissue stiffness is reported around 200 Pa in vivo [40]. To replicate the mechanical properties of TME (under in vivo conditions), we employed a matrix material with similar mechanical properties.

3.2.4. MICROFLUIDIC CHIP FABRICATION AND INTERSTITIAL FLOW CHARACTERIZATION

The microfluidic chip was fabricated on a 4-inch silicon wafer by the photo-lithography process in a cleanroom facility using µMLA Laser Writer (Heidelberg Instruments) (full procedure described in ESI, section 2). The microfluidic chip design was inspired by IF

studies performed with single cells and was upgraded to fabricate a channel height of 280 ± 25 µm (Fig.3.1A) [41–43]. From the master mould, polydimethylsiloxane (PDMS) based microfluidic chips were fabricated by soft-lithography technique (refer to ESI, section 2 for a detailed procedure).

The microfluidic chip consisted of three parallel channels separated by triangular pillars (all side lengths: 150 µm and height: 280 ± 25 µm) . The middle channel is loaded with 5 wt.% GelMA hydrogel, which is crosslinked under UV-light (385 nm) for 45 seconds. The top and bottom channels are the fluidic channels. The inlets of the top channel were maintained at a higher pressure (P_1) relative to the bottom channel (P_2) to generate an IF along the pressure gradient (Fig.3.1A). By controlling the pressure of the reservoirs at (P_1) and (P_2), we were able to establish a pressure gradient to generate an IF through GelMA hydrogel across the microfluidic device. The inlet and outlet pressures were controlled by a pressure pump (Fluigent) and operated via InFlow software to pressurize the sample reservoirs. Fig. 3.6 shows the experimental setup for generating a continuous IF using a pressure pump device connected to the 3D-microfluidic chip. According to Darcy's Law, flow velocity through a porous material is directly proportional to the pressure gradient governed by hydraulic permeability (K) of the material. In this case, we first calculated the hydraulic permeability of 5wt.% GelMA and then estimated the average IF velocity (u_m); refer to ESI, section 3 for detailed protocol. We tested two pressure drops ($\Delta P = P_1 - P_2$) of 20 mbar and 30 mbar that corresponded to an interstitial flow velocity of u_m = 0.2 µm/s and 0.45 µm/s obtained via COMSOL Multiphysics using Free and Porous Media Flow interface (Fig. 3.7, A and B). The IF velocity calculated for our 3D-matrix based microfluidic system is physiologically relevant as previously reported. Interstitial flow velocity in tumor tissues, performed in vivo, in vitro or via mathematical modelling are reported in the order of 0.01 - 1 µm/s in various cancer types [8, 44, 45]. Moreover, several studies have highlighted the role of elevated interstitial fluid pressure (IFP) in a tumor tissue as a barrier to tumor treatment [46]. IFP is reported in the order of 10 mbar to 60 mbar in various cancer types such as breast and melanoma skin cancer [46] and other studies (modeling and in vivo experiments) has reported from 1 - 100 mbar [44, 47].

3.2.5. MICROFLUIDIC DEVICE SETUP FOR IF AND EXOGENOUS TGF-β STUDIES

To investigate the effect of IF and exogenous TGF-β on spheroids, we used a step-wise procedure as described below. We first collected A549 spheroids from an Elplasia 96-well plate after 4 days of culture duration. The collected spheroids were then transferred to an empty well of a separate Corning Ultra-Low Attachment (ULA) 96-well plate. Once all the spheroids settled at the bottom of the well after 5 minutes, the cell culture media was aspirated out leaving only the spheroids in the well. A small volume of 5wt.% GelMA was added to this well to make a hydrogel-spheroid suspension. The hydrogel-spheroid suspension was then pipetted into the middle channel of the microfluidic device allowing entry of multiple spheroids. Once the middle channel was full, we gently removed the pipette from the inlet without introducing any air bubbles. The chip was then transferred to a microscope stage for UV-crosslinking at 385 nm laser source for 45 seconds using a 5x objective lens. After UV-irradiation, the hydrogel undergoes irreversible chemical

crosslinking and acts as a 3D scaffold for spheroids (Fig.3.1B). To generate IF, we operated the microfluidic device as described in section 2.4. For experiments to study the effect of interstitial flow on A549 spheroids, the sample reservoir for the top channel was replaced with cell culture medium (DMEM, high glucose, 10% v/v FBS, 1% v/v Antibiotics). For IF with exogenous TGF-β experiments on A549 spheroids, we supplemented the culture medium with exogenous TGF-β (stock concentration; 5µg/mL) to achieve a final concentration of 0.1-10 ng/mL. Brightfield and fluorescent images of the spheroids were captured on an inverted fluorescence microscope (Zeiss Axio-Observer) at an interval of 1 hour for a duration of 70 hours using a 20x/NA 0.16 air objective and ORCA Flash 4.0 V2 (Hamamatsu) digital camera with a resolution of 2048x2048 pixels. We used Software Autofocus strategy with best contrast method to reduce background or out of focus fluorescence signal. For the GFP and RFP fluorescence, we used the 488 LED source (ex: 488 nm; emm: 520 nm) and 543 LED source (ex: 543 nm; emm: 590 nm), respectively. All experiments were conducted at 37^{o}C and 5%CO_2 using a stage top incubator (ibidi). Bright field images were taken at 10% light intensity and 100 millisecond exposure time. Fluorescent signal intensity for GFP and RFP images were analyzed via ImageJ (v1.53t, National Institute of Health, USA). A region of interest was created encircling the entire spheroid area for both GFP and RFP channel images, performed separately. This region of interest was quantified for pixel intensity density at every time point using Measure function in ImageJ. The fluorescent intensity signal values were normalized with respect to the signal intensity at t = 0 hr. CAGA-12-GFP and RFP reporter expression was plotted for multiple spheroids performed in 2 or 3 independent experiments. The device is robustly operational at pressure differences upto 30-35 mbar in the presence of spheroids. Increasing the pressure drop, resulted in the hydrogel structure breaking and interrupted uniform IF after a few hours. Within this pressure drop range, we were able to perform long-term culture experiments (up to 70 hours) to visualize cancer cell spheroid for fluorescence reporter signaling activity, and invasive response.

3.2.6. MICROFLUIDIC DEVICE SETUP FOR 2D CULTURED A549 CELLS UNDER FLOW

Since A549 spheroids embedded in GelMA in a 3D-microfluidic chip cannot be retrieved to perform qPCR for target gene analyses, additional experiments were performed using dual-reporter A549 cells cultured in 2D-microfluidic without hydrogel matrix (see, Fig. 3.8). These 2D-microfluidic experiments (without matrix) enabled us to extract A549 cells after the experiment to run qPCR analyses on TGF-β and EMT target genes to complement CAGA-12-GFP and VIM-RFP reporter expression quantification. Full experimental procedure is described in ESI section 5. These studies additionally provide evidence of CAGA-12-GFP and VIM-RFP reporter expression when A549 single cells were exposed to 2D-flow (without matrix) alone and in combination with exogenous TGF-β conditions, shown in Fig. 3.9(A and B). Reporter expression was quantified in the following conditions: A) No-flow No-TGF-β (control), B) No-flow + TGF-β, C) Flow - No-TGF-β, and D) Flow + TGF-β conditions, shown in Fig. 3.9(C and D) for CAGA-12-GFP and VIM-RFP reporter respectively.

3.2.7. qPCR ANALYSES ON TARGET GENE EXPRESSION

Experiments performed using A549 cells in 2D-microfluidics (without matrix) in ESI section 5, were further used to establish CAGA-12-GFP reporter activity with TGF-β target genes and confirm VIM-RFP expression with EMT target genes (full experimental procedure described in ESI section 6.) We performed qPCR analyses on *CTGF, Serpin* (encoding PAI-1) and *Smad7* for TGF-β target genes and *E-cadherin, N-cadherin* and *Vimentin* for EMT target genes. Fig.S6 and S7 shows the relative change in mRNA expression for each condition with respect to No-flow No TGF-β (control) for TGF-β and EMT target genes respectively. qPCR analyses further helped to establish the effect of 2D-flow and/or exogenous TGF-β induced reporter expression at a molecular level.

3.2.8. STATISTICAL ANALYSIS

All statistical analysis was performed using Microsoft Excel (Microsoft Corporation, USA). The statistical significant differences between the two experimental groups were determined by Student t-test using the function *t-test: two samples with unequal variance* and p values below 0.05 were considered to be significant. We categorize statistical differences as following; $p < 0.001$ $(***)$, $p < 0.01$ $(**)$ and $p < 0.05$ $(*)$.

3.3. RESULTS AND DISCUSSION

3.3.1. EXOGENOUS TGF-β INDUCED CAGA-12-GFP REPORTER RESPONSE UNDER INTERSTITIAL FLOW CONDITIONS

To analyze the effect of exogenous TGF-β under interstitial flow (IF) on Smad3/4-dependent transcriptional reporter response, we first examined the overall CAGA-12-GFP reporter fluorescence intensities at the end of 70 hrs for a fixed C_0 = 10 ng/ml of exogenous TGF-β: (i) with IF ($IF^+TGF\text{-}\beta^+$) and (ii) without IF ($IF^-TGF\text{-}\beta^+$). These two conditions are contrasted with an IF condition without any exogenous TGF-β ($IF^+TGF\text{-}\beta^-$). Fig. 3.2A shows the brightfield images superposed with GFP fluorescence intensity at t = 0 and 70 hrs for these three conditions. The IF conditions were obtained under a fixed pressure gradient of ΔP = 30 mbar, equivalent of an average interstitial fluid velocity, u_m = 0.45 μm/s (measured separately via an independent experiment; see Fig. 3.7(B)). We observed an enhanced CAGA-12-GFP reporter expression with the addition of exogenous TGF-β (3.2A (ii) vs. (iii)), which becomes further amplified across the spheroid under the imposed IF (3.2A (i) vs. (ii)). This observation strongly suggests that IF enhances the exogenous TGF-β induced Smad-signaling activity in A549 spheroids.

The statistics of relative increase in the CAGA-12-GFP reporter expression (I_{70}) at t=70 hrs for these conditions were quantified for multiple spheroids based on the intensity readouts normalized by baseline values (I_0) at t=0 hr. The box plot in Fig.3.2B shows the average reporter signal intensity (I_{70}/I_0) as a function of varying exogenous TGF-β conditions under fixed IF at ΔP = 30 mbar. Among all the reported conditions, we observe the strongest reporter upregulation ($I_{70}/I_0 = 13 \pm 2.73$) for an exogenous TGF-β concentration of C_0 = 10 ng/mL under IF (i.e. IF^+-$TGF\text{-}\beta^+$(10 ng/mL)). We also observed that supplying exogenous TGF-β (10 ng/mL) without IF (IF^--TGF-β(10 ng/mL)) has approximately 73% lower reporter expression when compared to $IF^+TGF\text{-}\beta^+$(10 ng/mL), see Fig. 3.12(A). This result highlights a potentiating effect of IF towards an enhanced

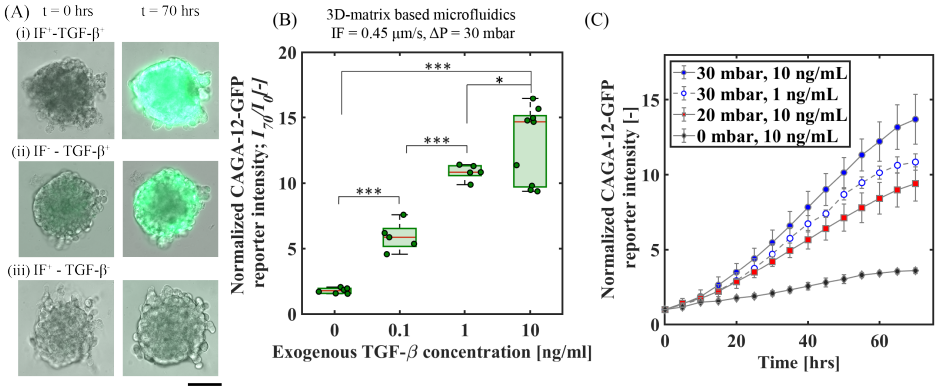

Figure 3.2: Exogenous TGF-β induced CAGA-12-GFP transcriptional reporter response of A549 spheroids under interstitial flow (IF) and no-flow conditions. (A) 20x GFP and bright-field merged microscope images of A549 spheroids at t = 0 and 70 hrs showing transcriptional-reporter intensity upregulation for the following conditions: (i) IF^+-TGF-β^+(10 ng/mL), (ii) IF^--TGF-β^+(10 ng/mL) and (iii) IF^+-TGF-β^-, scale bar: 100 μm. (B): Quantitative measurement of normalized CAGA-12-GFP reporter signal intensity at t = 70 hrs for varying exogenous TGF-β concentrations under fixed IF. (C): Time series quantification of fluorescence signal intensity (with time intervals of 5 hrs) for CAGA-12-GFP upregulation profile under different IF (ΔP = 20 mbar and 30 mbar) and exogenous TGF-β conditions (1 and 10 ng/mL), for n = 3 spheroids in each condition.

exogenous TGF-β induced Smad-signaling activity measured via upregulation in CAGA-12-GFP transcriptional reporter response. In addition, we studied the effect of different IF velocities without exogenous TGF-β supplement for Smad-dependent CAGA-12-GFP reporter activity. We observed minimal reporter gene upregulation at t = 70 hrs which can be linked to the inactivity of the Smad-pathway in the absence of exogenous TGF-β, see Fig. 3.13 (A and C).

To explore this potentiating effect between IF and exogenous TGF-β further, we employed time-lapse imaging to monitor the CAGA-12-GFP reporter expression profile for complete 70 hrs under varying IF (u_m = 0.2 μm/s and 0.45 μm/s at ΔP = 20 and 30 mbar, respectively) and exogenous TGF-β concentrations (C_0 = 1 and 10 ng/mL). Fig.3.2C shows the time-wise variations in $\langle I/I_0 \rangle$ for the following three combinations of IF and exogenous TGF-β concentrations- $IF^+TGF\text{-}\beta^+$: ΔP = 30 mbar; C_0 = 10 ng/ml, ΔP = 20 mbar; C_0 = 10 ng/ml, compared with the ΔP = 0 mbar; C_0 = 10 ng/ml i.e. no-IF condition. We observed a clear influence on the CAGA-12-GFP signal intensity profile with changing IF pressure gradients. For C_0 = 10 ng/ml, the IF condition at ΔP = 30 mbar resulted in the fastest non-linear increase in the fluorescence signal intensity profile that begins to show saturation over the 70-hour time period (Fig.3.2C). For the IF at ΔP = 20 mbar and the no-IF conditions, fluorescence signal intensity showed relatively slower upregulation responses (Fig.3.2C). Interestingly, for the IF condition of ΔP = 30 mbar, decreasing the exogenous TGF-β concentration by an order of magnitude (i.e. C_0 = 1 ng/ml) still resulted in an upregulation response faster than the ΔP = 20 mbar; C_0 = 10 ng/ml condition. This observation indicates that the Smad-dependent transcriptional reporter response is weakly sensitive to the exogenous TGF-β concentration, but shows a strong dependence on the IF. Under the fixed ΔP = 30 mbar, for both C_0 = 1 and 10 ng/ml the up-

regulation rates are nearly equal between 25-55 hrs, after an initial delayed response for the former. Additionally, we performed similar experiments under no-IF conditions with exogenous TGF-β concentration (1 and 10 ng/mL). The CAGA-12-GFP expression for 1 ng/mL and 10 ng/mL under no-IF showed a similar upregulation profile (see Fig.S13), suggesting that the transcriptional response is fairly independent of the exogenous TGF-β concentration greater than C_0 = 1 ng/ml. To follow-up on the potentiating effect of IF in our 3D-microfluidic A549 spheroid experiments, we performed additional experiments in a 2D-microfluidic system (without matrix) using dual-reporter A549 cells (refer to ESI section 5 for detailed experimental procedure). In Fig. 3.9(C),dual-reporter A549 cells showed maximum CAGA-12-GFP reporter expression in the presence of 2D-flow and exogenous TGF-β condition. The reporter response is similar to the observations in 3D-matrix microfluidic experiments with A549 spheroids displaying maximum activity under IF and exogenous TGF-β condition (Fig. 2B). In addition, in 2D-microfluidic experiments without matrix, A549 cells showed only a modest upregulation in CAGA-12-GFP reporter expression under 2D-flow conditions without exogenous TGF-β when compared to control condition with No-flow and No TGF-β, see Fig. 3.9(C). This observation indicates that biophysical forces arising from 2D-flow induced fluid-shear stress feeds into the Smad-pathway that leads to CAGA-12-GFP transcriptional reporter activity. Furthermore, qPCR target gene analysis was performed on A549 cells exposed to 2D-flow and/or exogenous TGF-β conditions (refer to ESI section 6 for full experimental procedure) to confirm for Smad-dependent CAGA-12-GFP transcriptional reporter activity with change in TGF-β target gene expression. Maximum target gene expression for *CTGF*, *Serpin1 encoding PAI-1*, and *Smad7* was observed in A549 cells stimulated with 2D-flow and exogenous TGF-β conditions, see Fig. 3.10. TGF-β target gene expression for cells exposed to only 2D-flow (no exogenous TGF-β) showed an increase in *Serpin1* and *Smad7* target genes. This further highlights that flow alone activates Smad-dependent CAGA-12-GFP reporter response.

It has been proposed that the transcriptional gene response from Smad-signaling pathway is dependent on a chain of reaction kinetics initiated with binding of exogenous TGF-β molecules at the active receptor sites [48]. These reaction kinetics include expression level of TGF-β receptors and Smads and its activation state, ability to translocate into the nucleus, ability to interact with other transcription factors, co-activators, co-repressors, and chromatin modulators etc [48]. The local concentration of available TGF-β should influence the conversion capacity of available receptor sites to activated receptor sites upon successful binding. Additionally, active TGF-β availability is tightly controlled by its interaction with ECM proteins and its ability to present itself to signaling receptors is regulated by co-receptors (without intrinsic enzymatic motif), by integrins and other receptor molecules [24]. The upregulation rate of the transcriptional gene response is controlled by the density of receptor sites (i.e.number of available sites) and the reaction rate constant. To validate the TGF-β receptor binding affinity in the presence of exogenous TGF-β molecules, we used a well-known TGF-β type I receptor inhibitor (SB-431542). This small molecule inhibitor is used to inhibit all TGF-β type I receptor kinase activity. We first performed experiments in 3D-static (without IF) conditions with A549 spheroids embedded in 5wt.% GelMA with and without SB-431542 inhibitor treatment; followed by stimulation with exogenous TGF-β (10 ng/mL), full experimental procedure

is described in ESI section 9(i). Fig. 3.14 shows A549 spheroids stimulated with only exogenous TGF-β showed Smad-dependent CAGA-12-GFP transcriptional activity. On the other hand, A549 spheroids initially treated with SB-431542 (10 μM) inhibitor and subsequently stimulated with exogenous TGF-β (10 ng/mL) showed no CAGA-12-GFP reporter activity. This is a result of receptor kinase activity inhibition. In addition, we saw similar effect of SB-431542 inhibitor treatment on CAGA-12-GFP and VIM-RFP reporter expression in 2D-microfluidic experiments on dual-reporter A549 single cells (without matrix) shown in Fig. 3.15 and 3.16 (full experimental procedure described in ESI section 9(ii) and (iii)). With these experiments we concluded that, CAGA-12-GFP transcriptional reporter activity is Smad-dependent which is a result of TGF-β receptor activation upon binding with TGF-β molecules. In our 3D microfluidic studies, we estimated the evolution of local TGF-β concentration in the vicinity of a spheroid. We performed 2D mass transport simulations using the finite-element method (implemented in COMSOL Multiphysics) by varying the IF conditions and the input concentration of exogenous TGF-β (Fig. 3.17(A)). At 350-400 minute mark, each condition has achieved its respective saturation concentration (C_0) of the exogenous TGF-β (Fig. 3.17(A)). Additionally, we tested the penetration of exogenous TGF-β in the presence of IF and no-IF. To do this, we used FITC-labelled Dextran (20 kDa) tracer particles (similar to TGF-β molecule, 25 kDa). We observed that IF enhanced the penetration of FITC-Dextran particles quantified by the increase in fluorescence intensity at pressure difference of 20 and 30 mbar, compared to 0 mbar, see Fig. 3.17(B). Although IF can increase the penetration of exogenous TGF-β molecules, extrapolating from results obtained with dextran tracer particles, this effect appears moderate (a factor of 2) compared to the fold change due to physical forces (such as shear and compressive stress). Since the upregulation of CAGA-12-GFP was found to be fairly independent of exogenous TGF-β concentration even under no-IF condition (see Fig. 3.18), we expect that all the active binding sites on the spheroid interface are activated for each case by this 250-400 minute mark of the experiment. Comparing this analysis with the results in Fig. 3.2C suggests that besides the exogenous TGF-β, there are additional biophysical forces induced mechanotransduction pathways that influence an enhanced CAGA-12-GFP reporter upregulation from TGF-β induced Smad-signaling activity.

Cancer cells have the ability to respond to mechanical cues (matrix stiffness, fluid shear stress and compressive forces) by activation of cell surface mechanosensors such as integrins, focal adhesion complex, transient receptor potential (TRP) ion channels and YAP/TAZ signaling pathway [22, 49–52]. Activation of mechanotransduction signaling pathways may lead to transcriptional activity of YAP/TAZ, commonly identified to promote cancer cell invasion and trigger EMT signaling pathways [21, 53, 54]. Earlier studies have linked mechanotransduction induced EMT for cancer cells under a flow-induced shear stress of 0.1 - 3 Pa [55–57]. These studies were performed on 2D monolayer culture without an extracellular matrix environment. The shear stress induced by an interstitial fluid flow is typically reported to be in the order of 0.01 Pa [58]. These values are reported for cells cultured on 2D substrate subjected to interstitial flow velocities in microfluidic systems. In our 3D-matrix based microfluidic study, we find that IF generated via a pressure gradient leads to both flow-induced shear stress and compressive stress contributing to the Smad-dependent transcriptional reporter activity. Based on

our simulation, the shear stress on a 2D spheroid model interface embedded in a low permeability matrix (mimicking the properties of GelMA used in the experiments) was found to be relatively low (~ 0.1-0.3 mPa, see Fig. 3.7(C)). The compressive/normal stress caused by hydrodynamic pressure at the spheroid interface is significantly high (~ 1 and 2 kPa, see Fig. 3.7(D)). Previous literature has highlighted the role of matrix stiffness and matrix-induced compressive forces activating key mechanotransduction pathways (Wnt, Hippo, PI3-AKT, TGF-β) for cancer cell proliferation and migration [59–61]. Since our 3D-microfluidic platform does not allow to quickly access A549 spheroids embedded in hydrogel matrix, we are unable to perform qPCR analyses to confirm for specific mechanotransduction pathway underplay. he long time it takes to isolate the spheroids from the device is likely to affect the gene expression profile within the spheroid. A detailed study to identify specific mechanotransduction pathways under IF upregulated in a 3D-TME exposed to IF will shed more light on this hypothesis.

3.3.2. LOCAL FLUORESCENCE PROFILE IN SMAD-DEPENDENT CAGA-12-GFP REPORTER ACTIVITY OF A549 SPHEROID UNDER VARYING IF-EXOGENOUS AND TGF-β CONDITION

To examine the local fluorescence profile of Smad-dependent CAGA-12-GFP transcriptional reporter activity in a spheroid as a consequence of varying IF from different pressure gradient, we compared evolution of fluorescence intensity at different times for a fixed exogenous TGF-β concentration (C_0 = 10 ng/mL) under two different values of IF (ΔP = 20 and 30 mbar) and no-IF conditions. To represent the local heterogeneity in fluorescence intensity of a spheroid exposed to varying IF, we used the Polar Transformer function in ImageJ. An example of methodology for this analysis technique on one set of spheroid images at different time intervals is shown in ESI section 12. This image analysis function converts a 2D-microscope image from a Cartesian coordinate system to a Polar coordinate system (r, θ), see Fig. 3.19(A and B). Using this function, we then measured the radially averaged intensity of a polar coordinate (r, θ) transformed image at different time intervals (t = 0, 24, 48 and 70 hrs) of a particular spheroid, see Fig. 3.19(B). We then plot the radially averaged intensity on the azimuthal scale, i.e. θ = 0 to 360 degrees, see Fig. 3.19(C), which constructs the evolution of fluorescence intensity profile corresponding to the spheroid fluorescence intensity at different time intervals. The intensity profile for each spheroid was normalized to its initial fluorescence value at t = 0 hrs. The difference in intensity of fluorescence signal among these conditions are influenced by the varying IF conditions (as previously discussed in section 3.1, Fig.3.2C). Fig.3.3 compares the intensity profiles of spheroids under varying IF (Fig.3.3A and B) and no-IF condition (Fig.3.3C). The fluorescence intensity ($I(t)/I_0$) is plotted on the scale 0-15 (represented in blue). Averaged fluorescence intensity at each time point (denoted with different colors) is represented with a solid line and standard deviation in intensity with its corresponding shaded region. The azimuthal axis, θ (counterclockwise, in red) is used to represent the local fluorescence profile of the spheroid. When spheroids are exposed to IF, we can observe the asymmetry by the averaged fluorescence intensity profile of spheroids (n = 3) at θ = 90 (top) and 270 (bottom) degrees, shown in Fig.3.3. In Fig.3.3A, spheroids under IF at ΔP = 30 mbar, show an average fluorescence intensity at the top of the spheroid (θ = 90 degree) is 12.3 ± 2.65 and at the bottom (θ = 270 de-

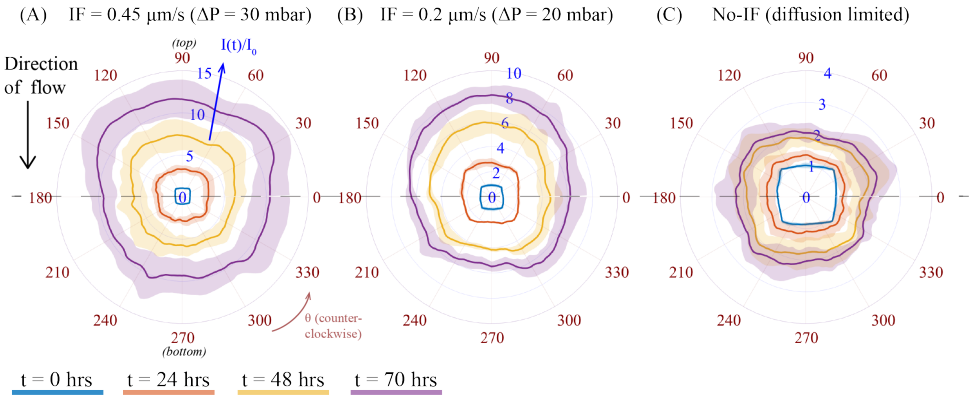

Figure 3.3: CAGA-12-GFP reporter fluorescence profile under a fixed exogenous TGF-β concentration (10 ng/mL) and varying interstitial flow and no-flow conditions. Polar plot of radially averaged fluorescence intensity is denoted in $I(t)/I_0$ (in blue) at different time intervals (represented with solid lines of different color). The solid line and the shaded region of a particular color of a particular time point show averaged and standard deviation of fluorescence intensity respectively for n = 3 spheroids. The evolution of fluorescence intensities at the top and bottom half of the spheroid (from the dashed line) shows the distribution of reporter expression for conditions: (A) IF$^+$(0.45 µm/s)TGF-β$^+$, (B) IF$^+$(0.2 µm/s)TGF-β$^+$, and (C) No flow, IF$^-$TGF-β$^+$.

gree) is 9.8 ± 2.17 at t = 70 hrs (in purple). We observe a similar trend in heterogeneity of fluorescence intensity for spheroids under IF at ΔP = 20 mbar (Fig.3.3B). Fig.3.3C shows that the fluorescence intensity profiles of spheroids under no-IF condition shows axisymmetry, i.e. no noticeable change in fluorescence intensity at the top/bottom of the spheroid. In no-IF condition, fluorescence intensity is not influenced by any hydrodynamic effect or fluid induced shear/compressive stress. We suspect that the absence of biomechanical stress (IF) and inactivation of mechanotransduction pathways justifies axisymmetric fluorescence profiles in only exogenous TGF-β exposed A549 spheroids. The top-bottom asymmetry in CAGA-12-GFP upregulation profiles along the direction of flow (top to bottom) is a result of the applied IF conditions originating from varying hydrodynamic pressure.

3.3.3. EXOGENOUS TGF-β INDUCED VIMENTIN ACTIVITY EXPOSED TO INTERSTITIAL FLOW IN A549 SPHEROIDS

To further explore the potentiating effect of interstitial flow (IF) with exogenous TGF-β, we examined the upregulation of vimentin as measured by determining the VIM-RFP reporter response. Vimentin, a key mesenchymal biomarker, is upregulated in lung cancer cells in the presence of TGF-β towards EMT response [28, 30, 31]. We measured the upregulation in vimentin expression activity by quantifying VIM-RFP reporter expression under IF and no-flow conditions in the presence of exogenous TGF-β. Fig.3.4A shows the superposed microscope images of brightfield and RFP channels at t = 0 and 70 hrs. We observed an enhanced VIM-RFP reporter expression with IF and exogenous TGF-β (IF$^+$TGF-β$^+$) (Fig. 3.4A (i)) compared to IF$^-$TGF-β$^+$ (Fig. 3.4A (ii)) condition). Fig.3.4B shows the quantified VIM-RFP signal upregulation for the same conditions (described in section 3.1). We observed that the strongest reporter upregulation (I_{70}/I_0 =

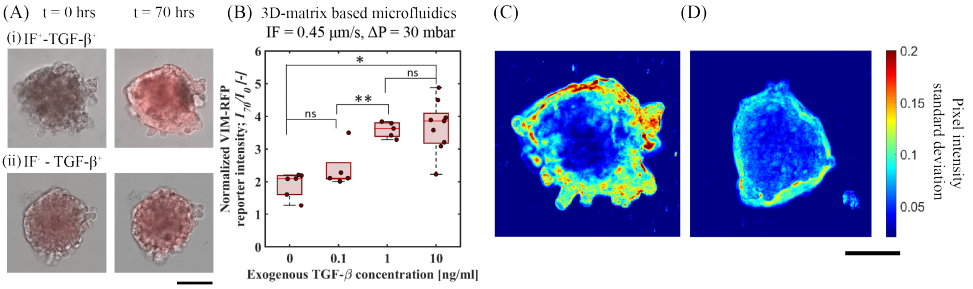

Figure 3.4: Upregulation in vimentin expression as measured via VIM-RFP reporter gene response toward cell motility in A549 spheroids. (A) 20x RFP and bright-field channel merged microscope images of A549 spheroids at t = 0 and 70hrs showing gene-reporter intensity upregulation in the following conditions. (i) IF^+-TGF-β^+ (10 ng/mL) and (ii) IF^--TGF-β^+ (10 ng/mL), scale bar: 100 µm. (B) Quantitative measurement of normalized VIM-RFP reporter signal intensity at t = 70 hrs for varying exogenous TGF-β under fixed IF (0.45 µm/s) at ΔP = 30 mbar. (C) and (D) Standard deviation analysis showing cellular motion activity at spheroid periphery of A549 spheroids under IF and no-flow conditions with exogenous TGF-β (10 ng/mL), scale bar: 100 µm.

3.7± 0.74) with an exogenous TGF-β concentration of 10 ng/mL under IF (ΔP = 30mbar) (i.e. IF^+-TGF-β^+(10 ng/mL)). We also observed that the upregulation of VIM-RFP intensities for TGF-β concentration 10 ng/mL and 1 ng/mL (I_{70}/I_0 = 3.6± 0.2) under IF (Fig.3.4B) showed no significant difference. Moreover, the VIM-RFP expression induced by exogenous TGF-β (10 ng/mL) under no-flow (I_{70}/I_0 = 1.41± 0.08) is 62% lower compared to spheroids under IF with exogenous TGF-β (10 ng/mL), refer Fig. 3.12(B). In addition, we studied the effect of varying IF without exogenous TGF-β for VIM-RFP reporter response. We observed no change in reporter activity at t = 70 hrs in A549 spheroids as a result of varying IF conditions, see Fig. 3.13(B and C). Following up with 2D-microfluidic experiments, we observed maximum VIM-RFP expression for 2D-flow and exogenous TGF-β conditions, similar to observations made in 3D-microfluidics in A549 spheroids. In addition, A549 cells exposed to 2D-flow (without matrix) showed upregulation in VIM-RFP reporte expression when compared to No-flow No TGF-β (control) condition, see Fig. 3.9(B and D). Therefore, we propose that the IF in the presence of exogenous TGF-β has a potentiating effect that is further responsible for producing an increased VIM-RFP reporter expression corresponding to a higher vimentin abundance. These results highlight the potential involvement of mechanotransduction induced signaling pathways that contribute towards upregulation in mesenchymal marker in A549 cells.

We quantified spheroid peripheral activity for increased cellular motion activity. The cellular motion activity here is referred to as cells at the edge of a spheroid that responds to biophysical and biochemical cues characterized with an increased motility. When stimulated with exogenous TGF-β and IF, we observed an increase VIM-RFP reporter expression corresponding to increase in vimentin abundance protein. This is identified as a mesenchymal biomarker, that is often associated with a phenotype observed in motile cancer cells. To quantify cellular motion activity, we performed temporal standard-deviation analysis of bright-field time-lapse images. This analysis technique detected the change in pixel intensity value at each time point for the duration of the entire experiment. After processing all images, the final image represents the qual-

itative measurement of the standard deviation change in pixel value corresponding to the cellular motion activity at the spheroid periphery. Fig.3.4C and D demonstrates a comparison of an A549 spheroid under IF (0.45 µm/s, ΔP = 30 mbar) and no-IF both stimulated with exogenous TGF-β (10 ng/mL). Refer to supplementary movie S1 and S2 (corresponding to spheroid in Fig.3.2C and D respectively) for time lapse video of cellular motion at spheroid edges embedded in GelMA matrix. In Fig.3.4C, the A549 lung tumor spheroid shows increased cellular motion activity under IF^{+}-TGF-β^{+} (10 ng/mL) condition with a larger standard deviation measured correlating with increased cellular motion activity. The increase in cell cellular motion activity was mostly observed at the top/side section of the spheroid periphery. From Fig.3.4D, only exogenous TGF-β is insufficient to produce cellular motion activity depicted with low standard deviation of pixel value change. In these conditions, the A549 spheroid periphery does not show active cellular motion (refer to Supplementary movie, S2). The increased activity in the presence of IF and exogenous TGF-β condition can be linked to the hypothesis of mechanotransduction pathway induced activity. Additional experiments performed in 2D-microfluidics for qPCR analyses (refer to ESI section 6, Fig. 3.11) showed that dual-reporter A549 cells exposed to 2D-flow (without matrix) led to downregulation in *E-cadherin* expression and upregulation in *N-cadherin* and *Vimentin* characteristic of EMT target genes. This brings us closer to our hypothesis of normal/shear stress activating mechanosensors for triggering additional mechanotransduction signaling pathways. These findings highlight the importance of IF and exogenous TGF-β that directly influence A549 tumor cells to undergo active cellular motion in a tumor microenvironment.

3.4. CONCLUSIONS AND OUTLOOK

We used a 3D-matrix based microfluidic platform to investigate the potentiating effect of IF on exogenous TGF-β induced Smad-signaling activity in A549 lung cancer spheroids. Our platform allowed us to embed cancer spheroids in 3D using GelMA hydrogel as a relevant ECM material. This integrated platform of porous hydrogel material and cancer spheroid allowed us to mimic interstitial flow (IF) conditions experienced by a tumor in a TME. One advantage of this microfluidic platform was the ability to investigate cancer cell-matrix interactions over time, allowing us to observe the effects of varying biophysical conditions and biochemical signals. By studying the interplay between biophysical components (hydrogel matrix and IF), and the externally introduced cytokine (exogenous TGF-β), we aimed to better understand how these factors contribute to cancer spheroid response and invasive behavior. To this end, we monitored the upregulation in transcriptional reporter response (CAGA-12-GFP) and vimentin abundance protein (VIM-RFP reporter) in A549 lung spheroids using real-time imaging of artificial gene reporter constructs. Our findings suggest that the addition of IF within the 3D-matrix significantly enhances the CAGA-12-GFP reporter response from Smad-signaling activities upregulated by exogenous TGF-β. This also leads to an increase in the abundance of vimentin protein measured via upregulation in VIM-RFP reporter expression and increased cellular motion activity observed at the spheroid periphery in a matrix microenvironment. Additional experiments performed in 2D-microfluidic system (without matrix) further confirmed the mRNA expression of TGF-β and EMT target genes to establish CAGA-12-GFP and VIM-RFP reporter functionality of the dual-reporter A549 cells. In 2D-

microfluidic experiments (without matrix), flow (without exogenous TGF-β) alone has a clear evidence of upregulation in Smad-dependent CAGA-12-GFP reporter activity and *vimentin* gene with qPCR analyses. Moreover, 2D-flow also resulted in downregulation of *E-cadherin*. The fluorescent reporter activity confirmed by target gene analyses indicates that 2D-flow alone activates parallel pathways that feed into the Smad pathway leading to Smad-induced transcriptional reporter activity. In 2D-microfluidic (without matrix) and 3D-microfluidic (with matrix), CAGA-12-GFP and VIM-RFP showed maximum reporter intensity when exposed to flow and exogenous TGF-β. However, in 3D-microfluidic experiments, A549 spheroids embedded in GelMA showed no clear upregulation in reporter expression when exposed to only IF (without exogenous TGF-β), in contrast to 2D-microfluidic experiments. The reporter expression was potentiated by IF only in the presence of exogenous TGF-β. The reporter expression showed clear dependency on the magnitude of IF applied (increasing pressure gradient) and showed less sensitivity to exogenous TGF-β concentration. Using complimentary numerical simulation on a 2D spheroid model, we further characterized the mass transport of TGF-β, flow induced shear and normal stresses on the spheroid interface under different IF conditions. Based on these results and qPCR analyses, we hypothesize that exogenous TGF-β induced Smad-signaling and vimentin expression is further upregulated from potentiating effect of interstitial flow mediated mechanotransduction pathways.

The 3D microfluidic platform introduced in this study has the potential to expand beyond tumor spheroid models, and can be applied to heterogeneous tumor spheroid, stromal cells, cancer-associated fibroblasts (CAFs) and immune cells. This versatility brings us closer to mimicking in vivo tumor microenvironment (TME) conditions.

AUTHOR CONTRIBUTIONS

Z. R., V. B., P. T. D and P. E. B conceived the ideas and designed the experiments. Z. R. carried out the experiments and collected the data. H. R. and M. T. carried out additional experiments on interstitial flow rate measurement and rheology of the hydrogel. G. V. D. Z. performed qPCR analyses for all experiments. Z. R. and A. B. performed data and image analysis. A. B. performed numerical simulations and developed MATLAB codes for image analysis. Z. R. wrote the paper and A. B., V. G., P. T. D and P. E. B. edited it.

ACKNOWLEDGEMENTS

Z. R., A. B. and P. E. B. gratefully acknowledge funding from the European Research Council (ERC) under the European Union's Horizon 2020 research and innovation program (grant agreement no. 819424). P. T. D. and P. E. B. gratefully acknowledge funding from the Delft Health Technology grant (between LUMC and TU Delft) and ZonMW grant (09120012010061). A. B. gratefully acknowledges funding from MSCA Postdoctoral Fellowships 2022 Project ID: 101111247. The authors thank Yifan Zhu for the dualreporter A549 cells.

SUPPLEMENTARY INFORMATION

3.A. STORAGE MODULUS CHARACTERIZATION

The viscoelastic properties of GelMA were investigated with a modular rotational rheometer (DSR 502, Anton Paar) equipped with a parallel plate of diameter of 25 mm. A volume of 500 µL of gel was crosslinked on a glass slide in the same conditions as in the microfluidic device. Amplitude and frequency sweeps allowed to estimate the strain and time-dependent behavior of the sample. Frequency sweeps were performed from low to high frequencies and vice-versa (0.1 to 100 rad/s at a fixed strain of 1%) at room temperature (220^{o}C) as shown in Fig. 3.5. The results are similar as the measurements occur within the linear viscoelastic (LVE) regime of the gel.

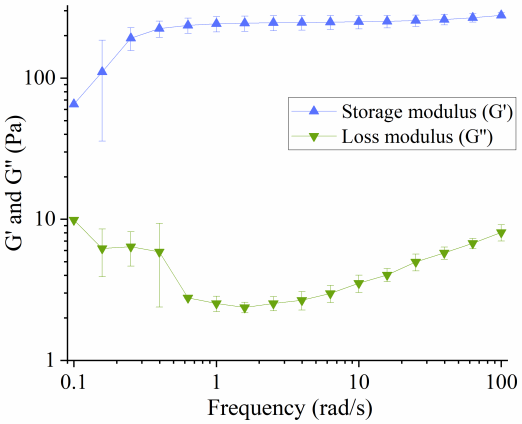

Figure 3.5: Frequency dependence of storage modulus (G') and loss modulus (G") of 5 wt.% GelMA: Characterized in small-amplitude oscillatory shear analysis (at a fixed strain amplitude of 1.0% at room temperature).

3.B. DESIGN AND FABRICATION OF 3-D MICROFLUIDIC CHIP

The master wafer was fabricated by a standard photo-lithography technique using a µMLA laserwriter (Heidelberg Instruments) on a 4-inch silicon wafer at the Kavli Nanolab Delft. The top and the bottom channel are fluidic channels and the middle channel is separated via triangular shaped pillars where spheroids are suspended in a hydrogel. The hydrogel is confined in the middle channel primarily due to the presence of evenly spaced triangular posts [41, 62]. We optimized the photolithography procedure to achieve a final channel height of 280 ± 25 µm to embed cancer spheroids in 3D. To obtain this, we first spin-coated SU-8 2150 (acquired from Kayaku Advanced Materials) negative photoresist in two steps. First step was at 500 rpm for 10 seconds with an acceleration of 100 rpm per second followed by 2300 rpm for 30 seconds with an acceleration of 300 rpm per second. The silicon-wafer with SU-8 was then transferred to a hot plate to soft-bake at 65^{o}C for 15 minutes, followed by 95^{o}C for 90 minutes. After soft-bake, the wafer was loaded onto the laserwriter sample holder stage. The AutoCAD design was uploaded to the laserwriter software to print the design using a 365 nm laser source. The

wafer was post baked at 650C for 15 minutes, followed by 95^{o}C for 5 minutes and developed in SU-8 photo-resist developer (mr-Dev 600, Micro resist technology). The microfeatures are constantly checked under an optical microscope to adjust the photo-resist developing time period in order to avoid over or under-development. The height of the channels was determined by a Dektak profilometer. The profilometer measures channel height 280 µm ± 25 µm. The master wafer was coated with trichloro(1H,1H,2H,2H-perfluorooctyl)silane to create a hydrophobic surface for easy demolding. Polydimethylsiloxane (PDMS) based microfluidic chips were prepared using the mixture of Sylgard 184 and curing agent (at a ratio of 10:1). Individual chips were then cut out and inlets/outlets were punched in the PDMS slab consisting of the design to insert tubings (PTFE, inner diameter: 0.8 mm, outer diameter: 1.6 mm) for fluidic-channel operation. Final bonding is performed by plasma cleaning (Harrick Plasma) of the PDMS slab and a glass coverslip (# 1.5) for two 2 minutes 20 seconds to facilitate final bonding. Finally, the assembled device was kept in the oven at 650C to bond overnight and restore the hydrophobicity of the channels. Afterwards, the microfluidic devices can be stored indefinitely and sterilized by UV-irradiation for 20 minutes before the start of each experiment.

3.C. MEASUREMENT OF HYDRAULIC PERMEABILITY (K) TO CALCULATE IF VELOCITY

To quantify interstitial flow velocity through 5wt.% GelMA hydrogel, we first identified the hydraulic permeability (K) of the hydrogel. We used Rhodamine B (fluorescent dye) as tracer molecule and measured the distance covered by the fluorescent dye through GelMA in a specific time frame. These studies are performed only with the hydrogel material and no spheroids. The microfluidic chip was prepared by first filling the hydrogel channel with 5wt.% GelMA, followed by crosslinking using 5x-obective lens with a LED UV-light source (385 nm) from Colibri Inverted microscope for 45 seconds. We prepared the dye solution by mixing a 1% (v/v) solution of Rhodamine B in 1X Dulbecco's Phosphate Buffer Solution (DPBS, Sigma Aldrich). This dye solution is used as a fluid reservoir connected to the Fluigent MFCS-EZ pressure pump to allow flow into the microfluidic channels. The tubings (inner diameter: 0.8 mm and outer diameter: 1.6 mm) from the reservoir are connected to the inlets (P1) of the top channel. The bottom channel inlets (P2) were connected to an empty reservoir. By applying a pressure gradient, we generated a flow through the porous hydrogel material, see Fig. 3.6 (for experimental setup). To validate IF, we tracked fluorescent dye travel with time-lapse imaging at an interval of 30 seconds. Images were taken on Zeiss Axio Observer Colibri 7 equipped with ORCA Flash 4.0 V2 (Hamamatsu) digital camera with a resolution of 2048 × 2048 pixels using 543 nm LED laser source (excitation/emission: 543 nm/568 nm), at 30% intensity laser and 1.58 seconds exposure time, with objective lens set to 5×. Flow velocity was then calculated using ImageJ for pressure gradients of ΔP: 20 mbar and 30 mbar. These pressure gradients were optimal since a high pressure gradient (> Δ40 mbar) disturbs the mechanical stability of the hydrogel and disrupts uniform interstitial flow. Images are exported from Zeiss software as .tif files and imported as a stack into ImageJ for analysis. The images were then straightened and converted into 8-bit color images. A vertical

line was drawn as area of interest to plot profile of gray value vs. distance. Mean gray value of zero corresponds to the last position of the dye at a specific time, this position was recorded for consecutive images for an average of 10 time points. The velocity was then calculated by dividing the distance traveled by the duration (between two consecutive images) and the average velocity on the line of interest is obtained. The average velocity for ΔP = 20 mbar and 30 mbar is calculated at 0.46 ± 0.21 µm/s and 0.72 ± 0.16 µm/s respectively (see Table 1 for average velocity measurements). All known parameters were plugged into Darcy's law (equation 1) to obtain the hydraulic permeability (K) of the hydrogel.

$$v = (\Delta P \times K)/(L \times \mu) \tag{3.1}$$

Where μ is the fluid velocity across the porous network (m/s), ΔP is the pressure gradient across the porous network (Pa), L is the length of the porous network in the direction of the flow (m), K is the hydraulic permeability (m^2), and is the fluid dynamic viscosity (Pa s). The average permeability constants were measured at approximately 1.35x 10^{-16} m^2 for 5wt.% GelMA. The permeability of 5wt.% GelMA was compared to the values found in literature to be of approximately 0.1 μm^2/Pa.s for a high degree substitution 5wt.% GelMA [63], equivalent to 10^{-16} m^2.

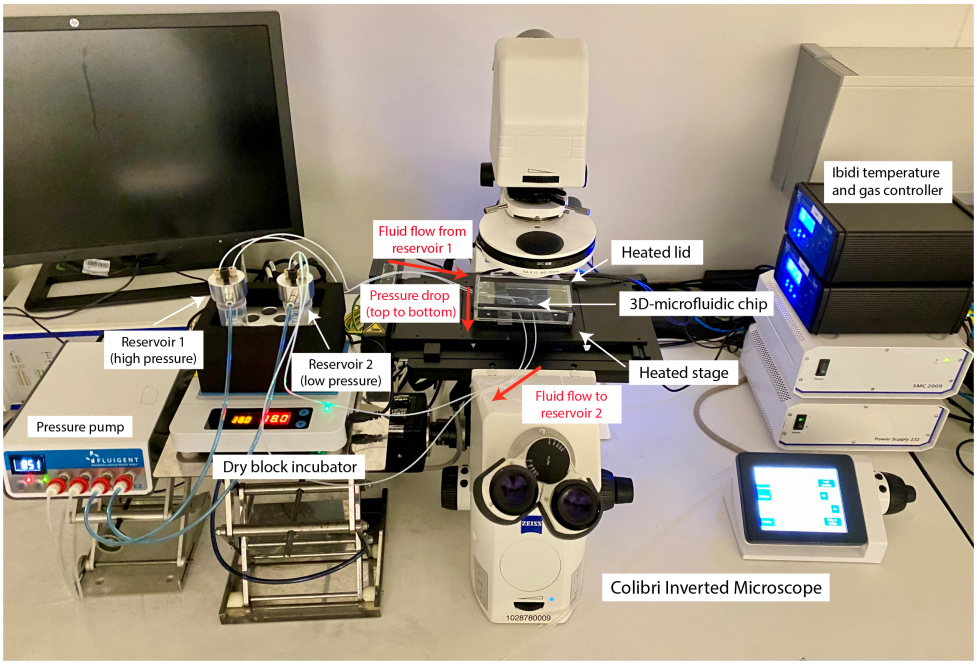

Figure 3.6: Experimental setup to generate interstitial flow in a 3D-microfluidic chip using a pressure pump. The reservoirs are kept in a dry block incubator maintained at 370C. The pressure pump channels are connected to the media reservoirs set at high and low pressure values to create a pressure gradient. The microfluidic chip is placed in a Ibidi stage top incubator equipped with a heated lid and a heated stage. The Ibidi temperature and gas controller box is used to maintain cell culture conditions at 37^oC, 95% humidity and 5%CO_2. Colibri inverted microscope used for time series fluorescence imaging.

Time (sec)	ΔP = 30 mbar		ΔP = 20 mbar	
	Distance travelled (μm)	Calculated average velocity (μm/s)	Distance travelled (μm)	Calculated average velocity (μm/s)
0	0	0	0	0
30	23.97	0.79	8.20	0.27
60	32.18	0.07	21.54	0.71
90	24.61	0.82	18.29	0.61
120	18.23	0.60	10.09	0.33
150	15.14	0.50	22.71	0.75
180	22.72	0.75	5.04	0.16
210	22.08	0.73	12.62	0.42
240	22.08	0.73	20.82	0.69
270	14.51	0.48	1451	0.48
300	23.35	0.77	4.41	0.14
	Average velocity	0.72	Average velocity	0.45
	Standard deviation	0.16	Standard deviation	0.26

Table 3.1: Average velocity measurement for ΔP = 20 and 30 mbar.

3.D. FLUID VELOCITY AND STRESS PROFILES

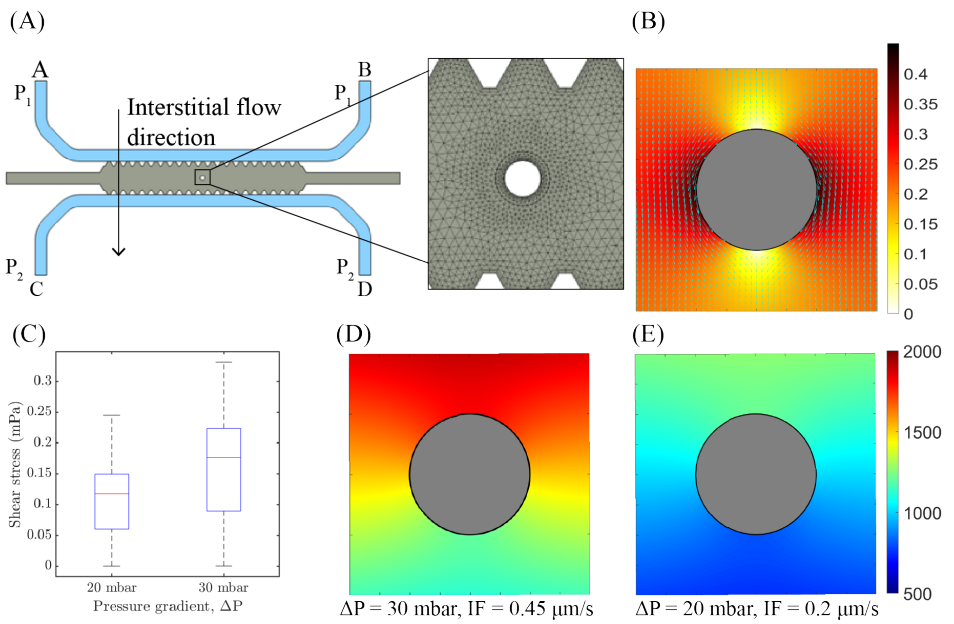

Figure 3.7: COMSOL simulation to compute interstitial fluid velocity and flow induced shear and normal stresses (A) 2D microfluidic model used for performing numerical simulation and the typical unstructured distribution near the spheroid model. (B) An example demonstrating the velocity field (absolute velocity) around the spheroid model at ΔP = 30 mbar (direction of flow: top to bottom, scale: μm/s). (C) IF-induced shear stress distribution at the spheroid interface under two pressure gradient conditions. (D,E) Normal stress experienced by the spheroid model at ΔP = 30 mbar and 20 mbar respectively (scale: Pa).

To compute the interstitial flow velocity in the microfluidic model, we solved 2D incompressible Stoke's flow equations using inbuilt Free and Porous Media Flow interface in COMSOL Multiphysics. For simplicity, the spheroid was modeled as a solid circular region with a rigid boundary. A pressure gradient across the porous matrix was generated by imposing pressure P1 at the inlets (A and B) and P2 (<P1) at the outlets (C and D). The velocity and pressure fields were computed over the domain discretized using a physics based unstructured mesh with approximately 3×105 elements with a minimum size of 1 µm, represented in Fig. 3.7(A). We modeled the hydrogel material using the permeability value (K) of 5wt.% GelMA calculated in section 2. Fig. 3.7(B) shows a representative velocity field around a spheroid model for ΔP = 30 mbar. The computed average flow velocities for ΔP = 20 and 30 mbar are 0.2 µm/s and 0.45 µm/s, respectively. Fig. 3.7(C) shows the statistics of local shear stress at the spheroid interface for the two imposed pressure gradients. The maximum fluid-induced shear stress was measured at 0.3 mPa at the spheroid interface for ΔP = 30 mbar condition. Fig. 3.7(D) and 3.7(E) show the normal stress measured at 1750 Pa at the top spheroid interface for ΔP = 30 mbar condition and 1250 Pa for ΔP = 20 mbar condition, respectively.

3.E. 2D MICROFLUIDIC FLOW EXPERIMENTS FOR QPCR ANALYSES

To further investigate the effect of flow conditions on the upregulation of Smad-signalling pathway and mesenchymal marker vimentin, we performed experiments with dual-reporter A549 cells in a 2D-microfluidic device (without matrix) subjected to flow with and without the presence of exogenous TGF-β. The 2D-flow experiments are performed in a microfluidic chip with a microchannel of dimensions 2 cm x 1 mm x 0.1 mm (length x width x height) as shown in Fig. 3.8, fabricated using standard soft-lithography technique, described in ESI section 2. The microchannels were coated with 20 µg/mL fibronectin (Sigma Aldrich, St. Louis, MO, USA) and kept in a humidified incubator for 6 hrs before seeding dual-reporter A59 cells at a density of 105 cells/mL. The microfluidic chip

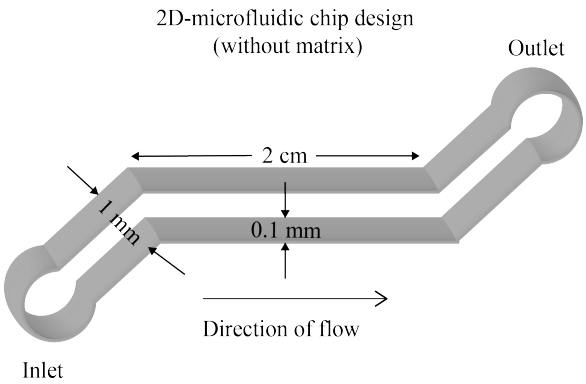

Figure 3.8: 2D-microfluidic chip design (with dimensions, not to scale) for experiments performed with dual reporter A549 single cells under 2D-flow and exogenous TGF-β conditions without hydrogel matrix.

with seeded cells were then kept in a humidified incubator for overnight attachment to achieve a confluent 2D-monolayer. After successful cell attachment, we imaged the cells for their reporter expression (CAGA-GFP and VIM-RFP) at t = 0 hrs with a Zeiss LSM 980 Confocal Microscope at 20x/NA 0.8 M27 air objective at 1024 x 1024 pixel^2 density. For GFP and RFP fluorescence, lasers with excitation wavelength of 488 nm and 543 nm were used, respectively. For the experiment, we prepared two reservoirs, one containing cell culture media supplemented with exogenous TGF-β and the other without exogenous TGF-β. To clearly identify the effect of 2D-flow, two different microfluidic devices were used, one connected to reservoir with TGF-β and the other without TGF-β. The reservoirs and microfluidic chips were placed in a humidified incubator. Next, we connected two syringes on a syringe pump (Harvard Apparatus, Elite 2000) placed outside the incubator. The tubings from the syringes were connected to the outlets of the microfluidic devices inside the incubator. The flow rate was set at 0.1 µL/min using the withdrawal function. We calculated the fluid-induced wall shear stress from the formula;

$$\tau = (6 \times \eta \times Q)/(W \times h^2) \tag{3.2}$$

Where η is the viscosity (in Pa.s), Q is the flow rate (m^3/s), W is the width (m) of the channel and h is the height (m) of the microfluidic channel. This flow rate creates a fluid-induced wall shear stress at 1 x 10−3 Pa. The experiment was performed for 72 hrs and imaged using the same image settings described above. Simultaneously, we prepared samples under 2D-static (no-flow) conditions where A549 cells were stimulated with and without exogenous TGF-β, imaged at t = 0 and t = 72 hrs. Fig. 3.9 (A and B) shows the merged GFP + BF and RFP + BF microscope image of reporter expression CAGA-GFP and VIM-RFP respectively of 2D cultured A549 cells at t = 72 hrs for the following conditions: i) No-flow No TGF-β, ii) No-flow + TGF-β, iii) Flow – No TGF-β, iv) Flow + TGF-β. We analyzed the upregulation in fluorescence intensity for all cases and plotted the intensity measured at t = 72 hrs normalized with respect to control sample at t = 72hrs, see Fig. 3.9(C and D). The reporter expression in 2D-flow (without matrix) condition revealed the activity of Smad-induced CAGA-12-GFP reporter response as well as VIM-RFP indicating abundance of vimentin protein in A549 cells. The experiment was performed in duplicates and each experiment was imaged at 3 different locations of the microfluidic channel (total n = 6 locations for each condition in 2 independent experiments). Statistical analysis on each set was performed using Student's t-test (paired two sample).

3.F. REAL TIME QUANTITATIVE-PCR

After the experiment, the cells from the microchannel are first extracted using trypsin for 3 min and diluted in fresh culture medium followed by centrifugation at 200g for 5 mins. The supernatant is pipetted out leaving behind the cell pellet. Total RNA extraction is performed using NucleoSpin RNA II kit (Macherey-Nagel, Deuren, Germany) according to the manufacturer's instructions. cDNA was generated using the Revert Aid First-Strand cDNA synthesis mix (Thermo Fisher, Bleiswijk, The Netherlands). Quantitative PCR was performed using SYBBR GoTaq qPCR master mix (Promega, Leiden, Netherlands) using 0.5 µM of primers. RT-qPCR was performed on the CFZ connect Real-Time PCR detection system (Bio-Rad, Hercules, CA, USA). Fig. 3.10 shows the relative mRNA

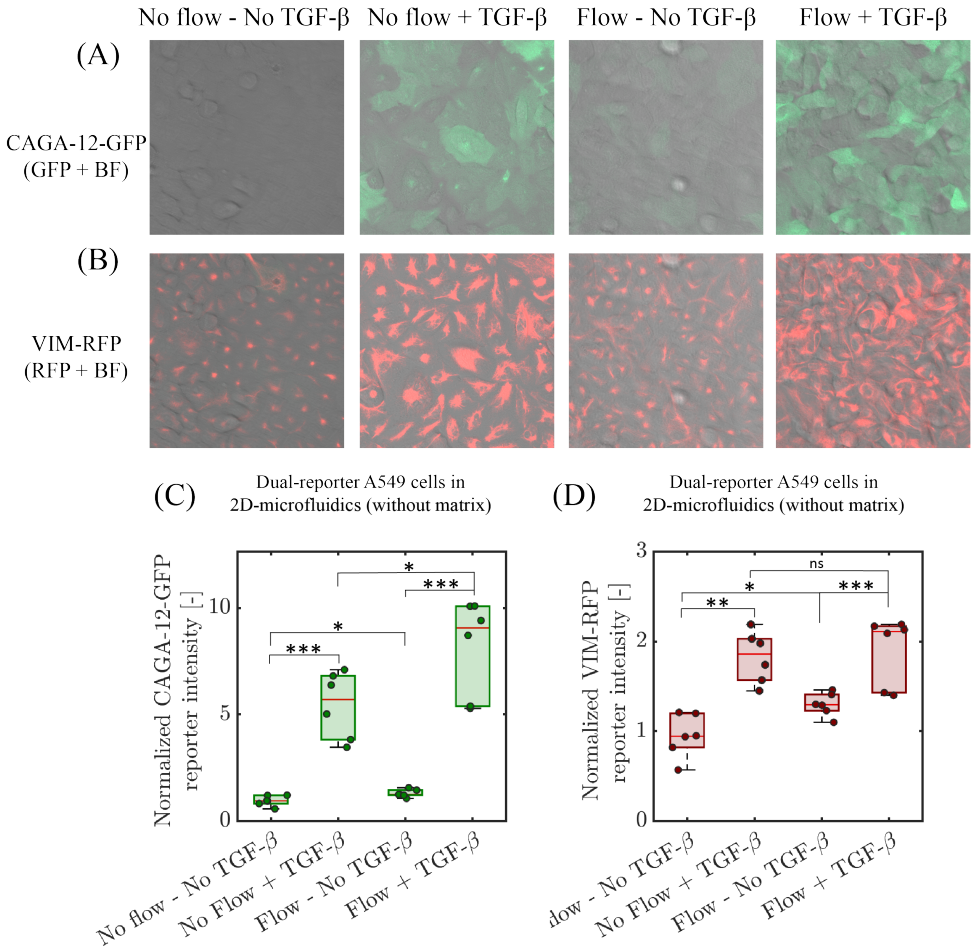

Figure 3.9: 2D-microfluidic (without matrix) experiments performed with dual-reporter (CAGA-12-GFP and VIM-RFP) A549 single cells. (A) Bright-field and GFP channel (merged) image at t = 72 hrs for all experimental conditions for CAGA-12-GFP reporter expression of A549 cells. (B) Bright-field and RFP channels (merged) imaged at t = 72 hrs for VIM-RFP reporter expression of A549 cells. (C) Quantification of CAGA-12-GFP fluorescence signal intensity at t = 72 hrs, normalized to fluorescence intensity of No flow – No TGF-β (control) condition at t = 72 hrs in 2D-microfluidics. (D) Quantification of VIM-RFP fluorescence signal intensity at t = 72 hrs, normalized to No flow – No TGF-β (control) condition at t = 72 hrs in 2D.

expression of TGF-β target genes. Fig. 3.11 shows the relative mRNA expression of EMT target genes. The primers used are listed in Table 3.2. All experiments were performed in triplicates, target gene expression was normalized to the geometric mean (geomean) of ARP and HPRT gene expression. All quantified gene expression is normalized with No flow – No TGF-β (control) condition.

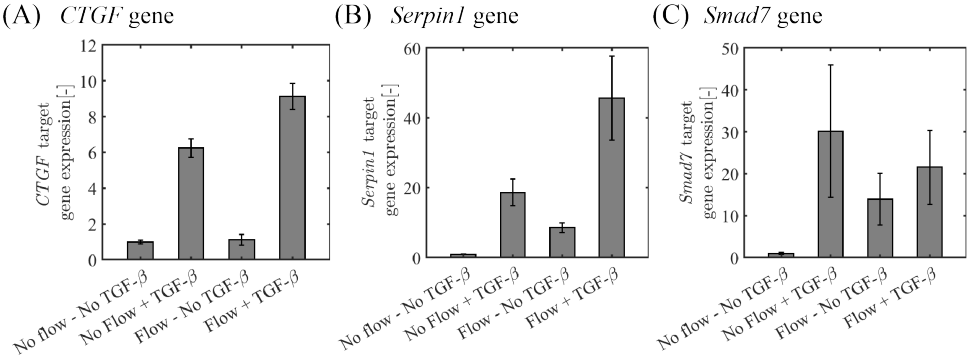

Figure 3.10: TGF-β target gene analysis on 2D cultured dual-reporter A549 cells in a microfluidic chip subjected to flow (fluid-induced shear stress), exogenous TGF-β and combination of flow and exogenous TGF-β conditions, in contrast with no flow and TGF-β condition (as control condition). qPCR results are representative of an average of three technical replicates from two independent experiments for No-Flow conditions and four independent experiments for Flow conditions performed in 2D-microfluidics (without matrix).

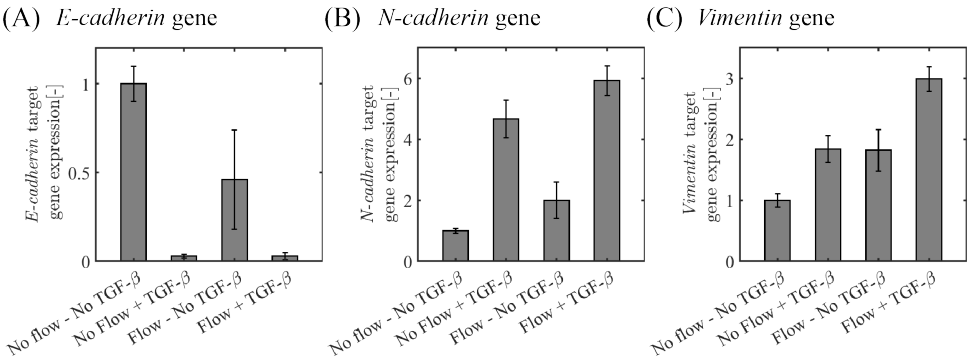

Figure 3.11: EMT marker gene analysis on 2D cultured dual-reporter A549 cells in a microfluidic chip subjected to flow (fluid-induced shear stress), exogenous TGF-β and combination of flow and exogenous TGF-β conditions, in contrast with no flow and TGF-β condition (as control condition). qPCR results are representative of an average of three technical replicates from two independent experiments for No-Flow conditions and four independent experiments for Flow conditions performed in 2D-microfluidics (without matrix).

Gene	Forward (5' - 3')	Reverse (3' - 5')
TGF-β target genes		
CTGF	TTGCGAAGCTGACCTGGAAGAGAA	AGCTCGGTATGTCTTCATGCTGGT
Serpin1	CACAAATCAGACGGCAGCACT	CATCGGGCGTGGTGAACTC
Smad7	TCCAGATGCTGTGCCTTCC	GTCCGAATTGAGCTGTCCG
EMT target genes		
E-cadherin	CCCGGTATCTTCCCCGC	CAGCCGCTTTCAGATTTTCAT
N-cadherin	CAGACCGACCCAAACAGCAAC	GCAGCAACAGTAAGGACAAACATC
Vimentin	CCAAACTTTTCCTCCCTGAACC	CGTGATGCTGAGAAGTTTCGTTGA
Household genes		
ARP	CACCATTGAAATCCTGAGTGATGT	TGACCAGCCGAAAGGAGAAG
HRPT	CTGGCGTCGTGATTAGTGAT	CTCGAGCAAGACGTTCAGTC

Table 3.2: Primer sequence for qPCR gene analysis

3.G. REPORTER EXPRESSION OF A549 SPHEROIDS WITH AND W/O IF

Fig. 3.12 shows the CAGA-12-GFP and VIM-RFP fluorescent reporter activity of A549 spheroids under No flow and IF (um = 0.45 µm/s, ΔP = 30 mbar) conditions at fixed exogenous TGF-β of 10 ng/mL in 3D-matrix based microfluidic chip. Fluorescence intensity is reported at I_{70}/I_0 with statistical difference observed in both CAGA-12-GFP and VIM-RFP for flow and no-flow conditions.

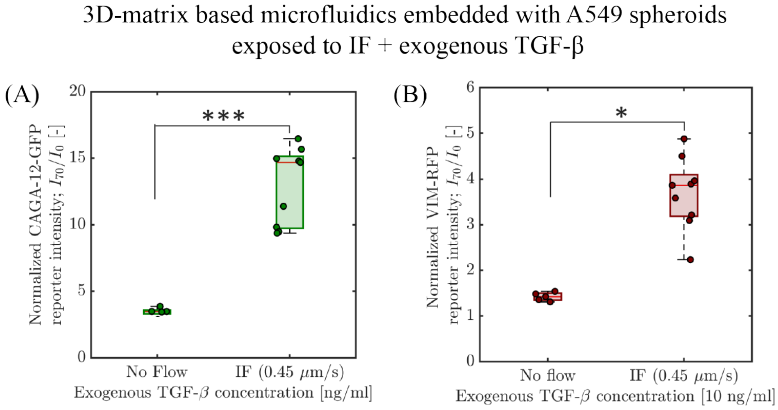

Figure 3.12: A) CAGA-12-GFP reporter and B) VIM-RFP reporter activity when A549 spheroids were exposed to a fixed exogenous TGF-β concentration of 10 ng/mL under no-flow and IF (um = 0.45 µm/s, ΔP = 30 mbar) condition in a 3D-matrix based microfluidic chip.

3.H. REPORTER EXPRESSION OF A549 SPHEROIDS UNDER VARYING IF

Fig. 3.13 shows the fluorescent reporter activity of A549 spheroids subjected to varying interstitial flow rates without exogenoys TGF-β. These experiments were performed to investigate the role of interstitial flow independently whether it has an influence on Smad-signaling activity and increase in vimentin activity. A549 spheroids subjected to varying IF did not result in any visible change in both CAGA-12-GFP activity and VIM-RFP reporter as shown in Fig. 3.13(A and B) at the end of 70 hours. Fig. 3.13(C) shows normalized fluorescent reporter intensity quantification at t = 70 hours.

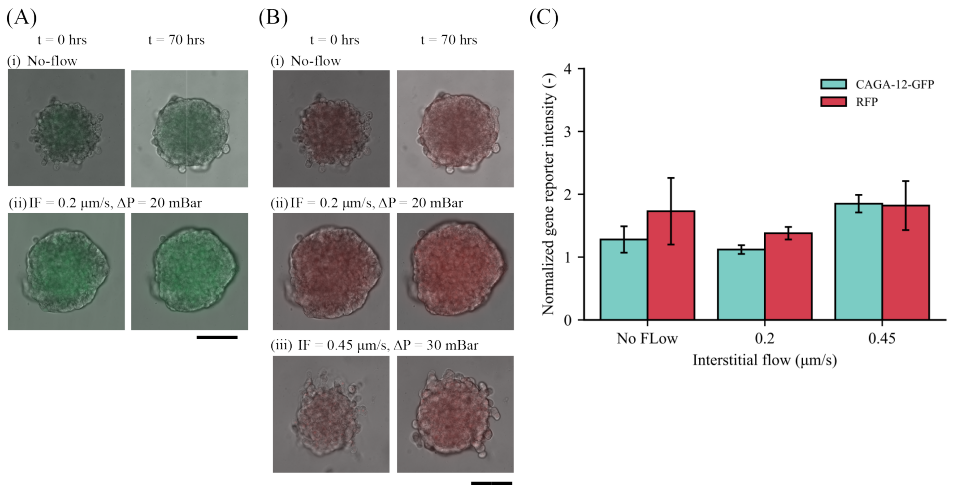

Figure 3.13: Endogenous CAGA-12-GFP and VIM-RFP reporter response under varying interstitial flow conditions. (A) Bright field and GFP channel superposed images of A549 spheroids showing CAGA-12-GFP reporter upregulation at t = 0 and t = 70 hrs for (i) no-flow and (ii) IF (um = 0.2 μm/s) conditions. (B) Bright and RFP channel superposed images for vimentin upregulation in no-flow and IF conditions (scale: 100 μm). (C) Normalized CAGA-12G-GFP and VIM-RFP [I70 / I0] reporter upregulation at t = 70 hrs.

3.I. CAGA-12-GFP REPORTER ASSAY USING SB-431542 INHIBITOR

CAGA-12-GFP REPORTER ASSAY IN 3D STATIC CONDITIONS USING A549 SPHEROIDS

To test for Smad-dependent CAGA-12-GFP transcriptional reporter activity in the presence of exogenous TGF-β, we performed additional validation studies for the reporter activity using TGF-β type I receptor inhibitor (SB-4315422). Experiments were performed in no-flow (static) conditions using 3D-A549 spheroids embedded in 5wt.% GelMA. A549 spheroids were first treated with SB-431542 inhibitor (10 μM) for 6 hrs before adding exogenous TGF-β. The reporter activity was measured in three different conditions: i) Vehicle control (4 mm HCl in DMSO), ii) SB-431542 (10 μM) treated + exogenous TGF-β (10 ng/mL), and iii) only exogenous TGF-β (10 ng/mL), as shown in Fig. 3.14. Imaging was performed using Zeiss LSM 980 Confocal Microscope at 10x/NA 0.3 M27 air objective

with Z-stack for GFP reporter activity at t = 0 hrs (before TGF-β treatment) and t = 72 hrs (after TGF-β treatment). For GFP fluorescence, laser with the excitation wavelength of 488 nm was used at 1024 x 1024 pixel2 density. For image analysis, Z-stack images were converted to 2D-image using the Z-project function at maximum intensity in ImageJ. The fluorescence intensity at t = 72 hrs of spheroids were normalized with respect to fluorescence intensity at t = 0 hrs. Fig. 3.14 shows the relative change in expression for fluorescence intensity at t = 72 hrs for all cases (n = 4 spheroids). CAGA-12-GFP transcriptional reporter activity was only observed when A549 spheroids were stimulated only with exogenous TGF-β. On the other hand, A549 spheroids under control does not show any fluorescence upregulation due to inactivity of Smad signaling activity in the absence of exogenous TGF-β molecules. When A549 spheroids were treated with SB-431542 inhibitor, the addition of exogenous TGF-β resulted in no reporter activity. This is due to the inhibition of type I receptor kinase activity preventing Smad-dependent transcriptional reporter response.

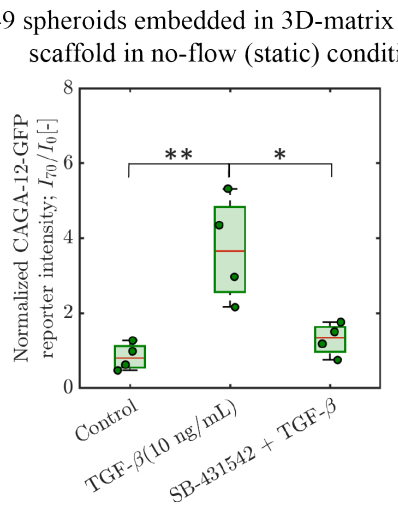

Figure 3.14: CAGA-12-GFP transcriptional reporter activity of A549 spheroids embedded in 5wt.% GelMA (in 3D) at t = 72 hours (n = 4 spheroids for each condition). Reporter expression is highest when stimulated with exogenous TGF-β (10 ng/mL) compared to spheroids first treated SB-431542 (TGF-β receptor kinase inhibitor) followed by exogenous TGF-β (10 ng/mL) stimulation.

CAGA-12-GFP AND VIM-RFP REPORTER ASSAY IN 2D-MICROFLUIDICS UNDER FLOW (WITHOUT EXOGENOUS TGF- β) AND SB-431542 INHIBITOR

To further extend these studies to explore the binding affinity of exogenous TGF- β molecules with TGF- β receptor sites, we performed additional validation studies in 2D-microfluidic device using A549 dual-reporter cells with and without TGF- β inhibitor (SB-431542). 2D-microfluidic devices were prepared by culturing dual-reporter A549 cells 2D in a microfluidic channel according to the method described in section 5 (ESI). In the first experiment, we observed CAGA-12-GFP and VIM-RFP reporter activity of A549 cells cultured in 2D-microfluidics subjected to Flow with and without SB-431542 inhibitor. For

inhibitor treatment experiments, after cell-surface attachment, A549 cells were incubated in the presence of TGF-β receptor kinase inhibitor (SB-431542, 10 µM) for 6 hours. Imaging was then performed at t = 0 hr and t = 72 hrs at 4 different locations of the microfluidic channel with imaging conditions described in section 5 (ESI). We plotted the CAGA-12-GFP and VIM-RFP at t = 72 hrs normalized with respect to t = 0 hr. Fig. 3.15(A) shows that A549 cells treated with SB-431542 (TGF-β receptor kinase inhibitor) blocks all CAGA-12-GFP reporter activity. Whereas, A549 cells under flow produces significant reporter expression. We observe similar effect in VIM-RFP reporter, where cells treated with SB-431542 inhibitor showed reduced RFP reporter expression compared to cells subjected to flow, shown in Fig. 3.15(B). This experiment thus highlights the additional effect of flow in 2D towards Smad-dependent transcriptional reporter response.

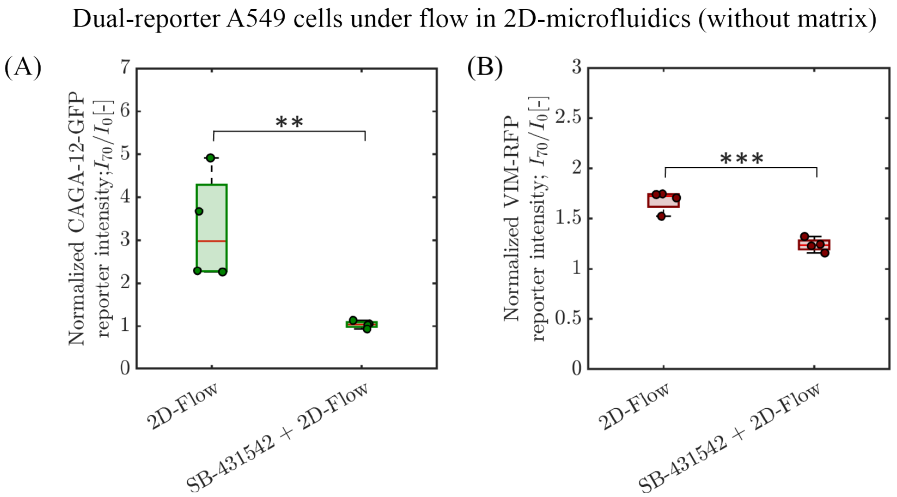

Figure 3.15: CAGA-12-GFP and VIM-RFP reporter expression in 2D-microfluidics (without matrix) under flow treated with and without SB-431542 (TGF-β inhibitor). A) CAGA-12-GFP reporter and B) VIM-RFP expression at t = 72 hrs shows significant reporter upregulation when compared to reporter expression for A549 cells treated with SB-431542 inhibitor.

CAGA-12-GFP AND VIM-RFP REPORTER ASSAY CULTURED IN 2D-MICROFLUIDICS UNDER FLOW CONDITIONS WITH EXOGENOUS TGF-β AND SB-431542 INHIBITOR

In the second experiment, A549 cells in 2D-microfluidics, CAGA-12-GFP and VIM-RFP reporter activity was quantified under flow and exogenous TGF-β with and without SB-431542 inhibitor treatment. These experiments further confirm the CAGA-12-GFP reporter activity is a consequence of the exogenous TGF-β molecules binding with TGF-β receptor sites to undergo Smad signaling. In Fig. 3.16(A), A549 cells treated with SB-431542 inhibitor blocked all TGF-β receptor kinase activity in the presence of exogenous TGF-β molecules to prevent Smad-signaling response. This led to inactivity of CAGA-12-GFP transcriptional reporter upregulation. On the other hand, significant upregulation of CAGA-12-GFP activity was observed when no inhibitor treatment was performed. Similar response was obtained for VIM-RFP reporter activity, where flow and exogenous TGF-β exposure leads to higher vimentin activity, shown in Fig. 3.16(B).

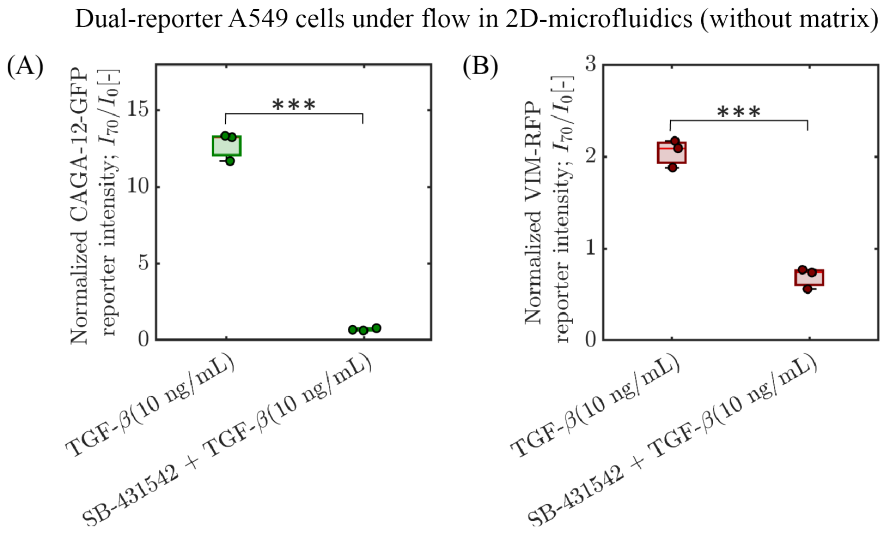

Figure 3.16: CAGA-12-GFP and VIM-RFP reporter expression in 2D-microfluidics with flow and exogenous TGF-β conditions treated with and without SB-431542 (TGF-β inhibitor). A) CAGA-12-GFP reporter and B) VIM-RFP expression at t = 72 hrs shows significant upregulation in reporter expression when compared to reporter expression for A549 cells treated with SB-inhibitor performed in 2D-microfluidics (without matrix).

3.J. EVOLUTION OF TGF-β CONCENTRATION AND SURFACE ADSORPTION

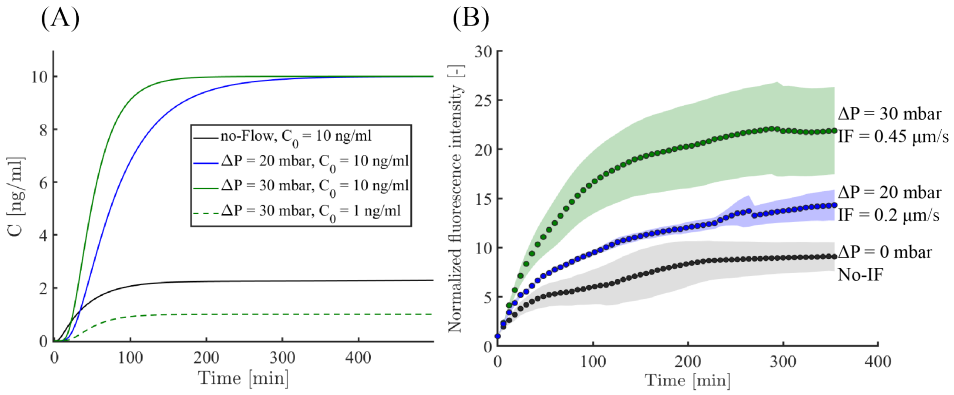

Figure 3.17: Evolution of average concentration of exogenous TGF-β (C_0 = 1 and 10 ng/mL) near a spheroid (within a radial distance of 0.05 mm) at interstitial flow conditions (ΔP = 0 (no-flow), 20 and 30 mbar)

Based on the numerically computed velocity and pressure fields (see Section 4), we measured the temporal evolution of TGF-β concentration within the porous hydrogel matrix by solving the mass transport equations (using the Transport of Diluted Species module in COMSOL Multiphysics). To mimic the experimental conditions, the channel

AB was initially filled with TGF-β (with molecular diffusivity 21.3 $\mu m^2/s$) at concentration C_0, while the remaining domains were kept at zero initial concentration. For the conditions with interstitial flow, the two inlets A and B were supplied with a continuous injection of TGF-β at concentration C_0. For the no-IF condition, the continuous injection condition was removed, and transport was fully dominated by the diffusion of TGF-β from the channel AB to the hydrogel (middle channel) with a spheroid model. The evolution of TGF- β concentration near the spheroid (at a radial distance of 0.05 mm from the interface) for various IF and no-IF conditions are shown in Fig. 3.17(A). Additionally, to test the penetration of exogenous TGF-β under varying IF conditions, we used FITC-labelled Dextran (20 kDa) tracer particles similar to the size of exogenous TGF-β molecules (25 kDa). In this experiment, we used wild-type A549 spheroids (unlabeled) to avoid fluorescence signal crosstalk since the excitation wavelength of CAGA-12-GFP and FITC is the same at 488 nm. A549 spheroids were embedded in 5wt.% GelMA in the microfluidic chip and operated at varying IF and no-IF conditions. Spheroids were imaged at an interval of 6 minutes for 360 minutes at 20x/NA 0.16 objective using Colibri Inverted microscope. The fluorescence intensity of the spheroids was analyzed using ImageJ. Fig. 3.17(B) shows the fluorescence profile of A549 spheroids at varying IF and no-IF conditions. Fluorescence intensity was increased by IF as more FITC-Dextran tracer particles adsorbed or penetrated through the A549 spheroid. This experiment highlights that IF can improve the penetration of exogenous TGF-β molecules in the spheroid.

3.K. CAGA-12-GFP FLUORESCENCE PROFILE UNDER NO-FLOW CONDITIONS IN 3D-MATRIX BASED MICROFLUIDICS

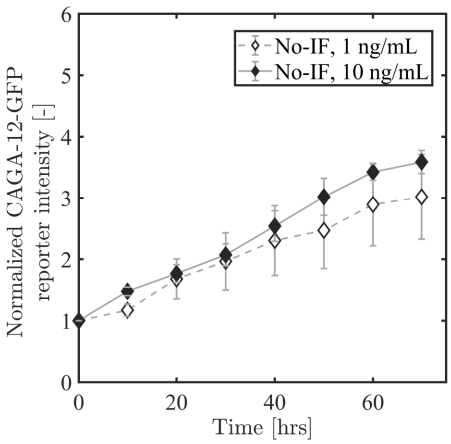

Figure 3.18: CAGA-12-GFP fluorescence upregulation profile of A549 spheroids embedded in GelMA under no-IF (static) condition supplemented with varying exogenous TGF-β concentration of 1 and 10 ng/mL in 3D-matrix based microfluidic chip.

Fig. 3.18 shows the CAGA-12-GFP fluorescence upregulation profile of A549 spheroids

exposed to varying exogenous TGF-β concentrations at 1 and 10 ng/mL under no-flow conditions performed in 3D-matrix based microfluidic chip. The fluorescene upregulation profile for both 1 and 10 ng/mL follows a similar trend in the 70 hour time frame.

3.L. VISUALIZING LOCAL HETEROGENEITY IN FLUORESCENCE EXPRESSION OF A549 SPHEROID

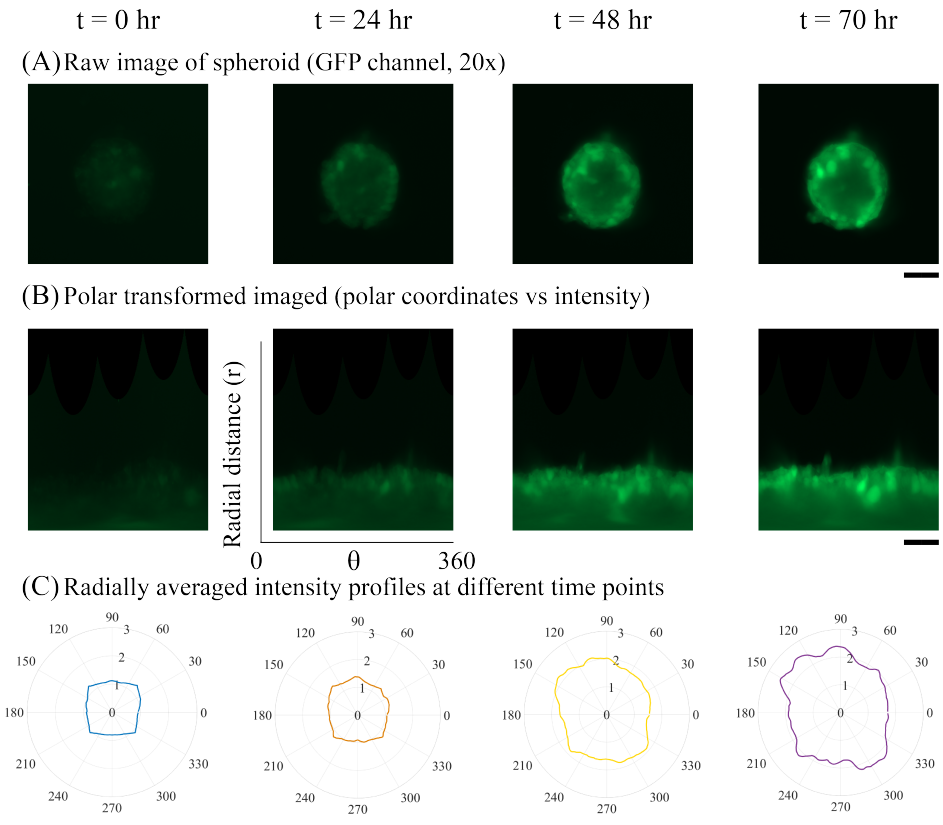

Figure 3.19: Methodology for polar plot analysis: (A) Raw GFP fluorescence channel image (20x) of a spheroid at different time intervals exposed to exogenous TGF-β (10 ng/mL) under no-flow conditions, scale: 100 µm. (B) Cartesian-polar transformed image obtained via Polar transformer plug-in in ImageJ, scale: 100 µm. The spheroid (circular object) is converted into an image represented in polar coordinates (θ=0 to 360 degrees). (C) Polar plot of radially averaged fluorescence intensity at t = 0, 24, 48 and 70 hrs. Each profile is normalized by the intensity at t = 0 hr to show the evolution of signal intensity in radial coordinates.

To visualize the evolution of fluorescence profile of a spheroid over the 70 hrs time frame, we performed image analysis using the Polar Transformer function (ImageJ plug-in), see Fig. 3.19(A). Since a spheroid in general closely represents a circular object (in 2D plane, with xy coordinate), the spheroid can be "unwrapped" by converting this 2D-spheroid image into radius/angle coordinates (polar transformation). We do this for all

spheroid images obtained at time points t = 0, 24, 48 and 70 hour, see Fig. 3.19(B). Using ImageJ, we measured the averaged fluorescence intensity at every angle (θ = 0 to 360 degrees) of the converted polar transformed image (see Fig. 3.19(B). Using a custom-made MATLAB script, we plot the average fluorescence intensity (for every θ), see Fig. 3.19(C).

3.M. SUPPLEMENTARY MOVIES

SUPPLEMENTARY MOVIE S1

Time lapse video of bright-field images of A549 spheroid embedded in GelMA in 3D-microfluidic chip exposed to IF (u_m = 0.45 µm/s, ΔP = 30mbar) and exogenous TGF-β (10 ng/mL). Spheroids show cellular motion activity at spheroid edges over the time-frame of experiment. Most activity is visible in top/side part of the spheroid periphery (in the direction of IF). Scan QR-code in Fig. 3.20A to access the supplementary movie in Youtube.com.

SUPPLEMENTARY MOVIE S2

Time lapse video of bright-field images of A549 spheroid embedded in GelMA in 3D-microfluidic chip exposed to no-IF (ΔP = 0mbar) and exogenous TGF-β (10 ng/mL). Spheroids show minimal cellular motion at spheroid edge over the timeframe of experiment. Scan QR-code in Fig. 3.20A to access the supplementary movie in Youtube.com.

(A) Interstitial flow + TGF-β (B) No-Flow + TGF-β

Figure 3.20: QR-codes for supplementary movies for A549 spheroids A) exposed to interstitial flow and exogenous TGF-β and B) only exogenous TGF-β conditions under no flow conditions.

REFERENCES

[1] Z. Rahman, A. D. Bordoloi, H. Rouhana, M. Tavasso, G. van der Zon, V. Garbin, P. ten Dijke, and P. E. Boukany, *Interstitial flow potentiates TGF-β/Smad-signaling activity*

in lung cancer spheroids in a 3D-microfluidic chip, Lab on a Chip **24**, 422 (2024).

[2] M. J. Mitchell, R. K. Jain, and R. Langer, *Engineering and physical sciences in oncology: Challenges and opportunities,* Nature Reviews Cancer **17**, 659 (2017).

[3] L. Hui and Y. Chen, *Tumor microenvironment: Sanctuary of the devil,* Cancer Letters **368**, 7 (2015).

[4] T. R. Cox, *The matrix in cancer,* Nature Reviews Cancer **21**, 217 (2021).

[5] P. Mehta, Z. Rahman, P. ten Dijke, and P. E. Boukany, *Microfluidics meets 3D cancer cell migration,* Trends in Cancer **8**, 683 (2022).

[6] J. Ahn, Y. J. Sei, N. L. Jeon, and Y. Kim, *Tumor microenvironment on a chip: The progress and future perspective,* Bioengineering **4**, 1 (2017).

[7] D. Vera, M. García-Díaz, N. Torras, M. Álvarez, R. Villa, and E. Martinez, *Engineering Tissue Barrier Models on Hydrogel Microfluidic Platforms,* ACS Applied Materials and Interfaces **13**, 13920 (2021).

[8] M. A. Swartz and M. E. Fleury, *Interstitial flow and its effects in soft tissues,* Annual Review of Biomedical Engineering **9**, 229 (2007).

[9] W. J. Polacheck, R. Li, S. G. M. Uzel, and R. D. Kamm, *Microfluidic platforms for mechanobiology,* Lab on a Chip **13**, 2252 (2013).

[10] Y. L. Huang, C. K. Tung, A. Zheng, B. J. Kim, and M. Wu, *Interstitial flows promote amoeboid over mesenchymal motility of breast cancer cells revealed by a three dimensional microfluidic model,* Integrative Biology (United Kingdom) **7**, 1402 (2015).

[11] Y. L. Huang, Y. Ma, C. Wu, C. Shiau, J. E. Segall, and M. Wu, *Tumor spheroids under perfusion within a 3D microfluidic platform reveal critical roles of cell-cell adhesion in tumor invasion,* Scientific reports **10**, 9648 (2020).

[12] W. J. Polacheck, A. E. German, A. Mammoto, D. E. Ingber, and R. D. Kamm, *Mechanotransduction of fluid stresses governs 3D cell migration,* Proceedings of the National Academy of Sciences of the United States of America **111**, 2447 (2014).

[13] J. A. Pedersen, S. Lichter, and M. A. Swartz, *Cells in 3D matrices under interstitial flow: Effects of extracellular matrix alignment on cell shear stress and drag forces,* Journal of Biomechanics **43**, 900 (2010).

[14] M. A. Swartz and A. W. Lund, *Lymphatic and interstitial flow in the tumour microenvironment: Linking mechanobiology with immunity,* Nature Reviews Cancer **12**, 210 (2012).

[15] F. Xie, L. Ling, H. Van Dam, F. Zhou, and L. Zhang, *TGF-β signaling in cancer metastasis,* Acta Biochimica et Biophysica Sinica **50**, 121 (2018).

[16] Y. Katsuno and R. Derynck, *Epithelial plasticity, epithelial-mesenchymal transition, and the TGF-β family,* Developmental Cell **56**, 726 (2021).

[17] F. Gong, Y. Yang, L. Wen, C. Wang, J. Li, and J. Dai, *An Overview of the Role of Mechanical Stretching in the Progression of Lung Cancer,* Frontiers in Cell and Developmental Biology **9**, 1 (2021).

[18] L. K. Chen, C. C. Hsieh, Y. C. Huang, Y. J. Huang, C. F. Lung, W. E. Hsu, C. L. Yao, T. Y. Tseng, C. C. Wang, and Y. C. Hsu, *Mechanical Stretch Promotes Invasion of Lung Cancer Cells via Activation of Tumor Necrosis Factor-alpha,* Biotechnology and Bioprocess Engineering **6**, 1 (2023).

[19] C. H. Heldin, K. Miyazono, and P. Ten Dijke, *TGF-β signalling from cell membrane to nucleus through SMAD proteins,* Nature **390**, 465 (1997).

[20] S. Vermeulen, N. Roumans, F. Honig, A. Carlier, D. G. Hebels, A. D. Eren, P. t. Dijke, A. Vasilevich, and J. de Boer, *Mechanotransduction is a context-dependent activator of TGF-β signaling in mesenchymal stem cells,* Biomaterials **259** (2020), 10.1016/j.biomaterials.2020.120331.

[21] F. Zanconato, M. Cordenonsi, and S. Piccolo, *YAP/TAZ at the Roots of Cancer,* Cancer Cell **29**, 783 (2016).

[22] H. J. Lee, M. F. Diaz, K. M. Price, J. A. Ozuna, S. Zhang, E. M. Sevick-Muraca, J. P. Hagan, and P. L. Wenzel, *Fluid shear stress activates YAP1 to promote cancer cell motility,* Nature Communications **8** (2017), 10.1038/ncomms14122.

[23] J. M. Rutkowski and M. A. Swartz, *A driving force for change: interstitial flow as a morphoregulator,* Trends in Cell Biology **17**, 44 (2007).

[24] Y. Hao, D. Baker, and P. T. Dijke, *TGF-β-mediated epithelial-mesenchymal transition and cancer metastasis,* International Journal of Molecular Sciences **20** (2019), 10.3390/ijms20112767.

[25] Q. Liu, A. Muralidharan, A. Saateh, Z. Ding, P. ten Dijke, and P. E. Boukany, *A Programmable Multifunctional 3D Cancer Cell Invasion Micro Platform,* Small , 2107757 (2022).

[26] S. Aashaq, A. Batool, S. A. Mir, M. A. Beigh, K. I. Andrabi, and Z. A. Shah, *TGF-β signaling: A recap of SMAD-independent and SMAD-dependent pathways,* Journal of Cellular Physiology **237**, 59 (2022).

[27] R. Derynck, B. P. Muthusamy, and K. Y. Saeteurn, *Signaling pathway cooperation in TGF-β-induced epithelial-mesenchymal transition,* Current Opinion in Cell Biology **31**, 56 (2014).

[28] B. N. Kim, D. H. Ahn, N. Kang, C. D. Yeo, Y. K. Kim, K. Y. Lee, T. J. Kim, S. H. Lee, M. S. Park, H. W. Yim, J. Y. Park, C. K. Park, and S. J. Kim, *TGF-β induced EMT and stemness characteristics are associated with epigenetic regulation in lung cancer,* Scientific Reports **10**, 1 (2020).

[29] M. Kawata, D. Koinuma, T. Ogami, K. Umezawa, C. Iwata, T. Watabe, and K. Miyazono, *TGF-β-induced epithelial-mesenchymal transition of A549 lung adenocarcinoma cells is enhanced by pro-inflammatory cytokines derived from RAW 264.7 macrophage cells,* Journal of Biochemistry **151**, 205 (2012).

[30] V. Tirino, R. Camerlingo, K. Bifulco, E. Irollo, R. Montella, F. Paino, G. Sessa, M. V. Carriero, N. Normanno, G. Rocco, and G. Pirozzi, *TGF-β1 exposure induces epithelial to mesenchymal transition both in CSCs and non-CSCs of the A549 cell line, leading to an increase of migration ability in the CD133+ A549 cell fraction,* Cell Death and Disease **4**, 1 (2013).

[31] P. Peixoto, A. Etcheverry, M. Aubry, A. Missey, C. Lachat, J. Perrard, E. Hendrick, R. Delage-Mourroux, J. Mosser, C. Borg, J. P. Feugeas, M. Herfs, M. Boyer-Guittaut, and E. Hervouet, *EMT is associated with an epigenetic signature of ECM remodeling genes,* Cell Death and Disease **10** (2019), 10.1038/s41419-019-1397-4.

[32] H. Zou, Z. Yang, Y. S. Chan, S. k. A. Yeung, M. K. Alam, T. Si, T. Xu, and M. Yang, *Single cell analysis of mechanical properties and EMT-related gene expression profiles in cancer fingers,* iScience **25**, 103917 (2022).

[33] K. Schelch, L. Vogel, A. Schneller, J. Brankovic, T. Mohr, R. L. Mayer, A. Slany, C. Gerner, and M. Grusch, *EGF Induces Migration Independent of EMT or Invasion in A549 Lung Adenocarcinoma Cells,* Frontiers in Cell and Developmental Biology **9**, 1 (2021).

[34] X. Qi, A. V. Prokhorova, A. V. Mezentsev, N. Shen, A. V. Trofimenko, G. I. Filkov, R. A. Sulimanov, V. A. Makarov, and M. O. Durymanov, *Comparison of EMT-Related and Multi-Drug Resistant Gene Expression, Extracellular Matrix Production, and Drug Sensitivity in NSCLC Spheroids Generated by Scaffold-Free and Scaffold-Based Methods,* International Journal of Molecular Sciences **23** (2022), 10.3390/ijms232113306.

[35] K. Arai, T. Eguchi, M. M. Rahman, R. Sakamoto, N. Masuda, T. Nakatsura, S. K. Calderwood, K. I. Kozaki, and M. Itoh, *A novel high-Throughput3D screening system for EMT inhibitors: A pilot screening discovered the EMT inhibitory activity of CDK2 inhibitor SU9516,* PLoS ONE **11**, 1 (2016).

[36] W. Wang, D. Douglas, J. Zhang, S. Kumari, M. S. Enuameh, Y. Dai, C. T. Wallace, S. C. Watkins, W. Shu, and J. Xing, *Live-cell imaging and analysis reveal cell phenotypic transition dynamics inherently missing in snapshot data,* Science Advances **6** (2020), 10.1126/sciadv.aba9319.

[37] D. L. Marvin, L. You, L. Bornes, M. van Dinther, N. Peters, H. Dang, S. K. Hakuno, M. Hornsveld, O. Kranenburg, J. van Rheenen, J. H. Rohling, M. P. Chien, P. Ten Dijke, and L. Ritsma, *Dynamic Visualization of TGF-β/SMAD3 Transcriptional Responses in Single Living Cells,* Cancers **14**, 1 (2022).

[38] J. Zhang, M. Thorikay, G. van der Zon, M. van Dinther, and P. T. Dijke, *Studying tgf-β signaling and tgf-β-induced epithelial-to-mesenchymal transition in breast cancer and normal cells,* Journal of Visualized Experiments **2020**, 1 (2020).

[39] A. Sinha, P. Mehta, C. Fan, J. Zhang, D. L. Marvin, M. V. Dinther, L. Ritsma, P. E. Boukany, and P. Dijke, *Chapter 5,* **2488**, 47.

[40] T. R. Cox and J. T. Erler, *Remodeling and homeostasis of the extracellular matrix: Implications for fibrotic diseases and cancer,* DMM Disease Models and Mechanisms **4**, 165 (2011).

[41] Y. Shin, S. Han, J. S. Jeon, K. Yamamoto, I. K. Zervantonakis, R. Sudo, R. D. Kamm, and S. Chung, *Microfluidic assay for simultaneous culture of multiple cell types on surfaces or within hydrogels,* Nature Protocols **7**, 1247 (2012).

[42] W. A. Farahat, L. B. Wood, I. K. Zervantonakis, A. Schor, S. Ong, D. Neal, R. D. Kamm, and H. H. Asada, *Ensemble analysis of angiogenic growth in three-dimensional microfluidic cell cultures,* PLoS ONE **7** (2012), 10.1371/journal.pone.0037333.

[43] S. Han, K. Yang, Y. Shin, J. S. Lee, R. D. Kamm, S. Chung, and S. W. Cho, *Three-dimensional extracellular matrix-mediated neural stem cell differentiation in a microfluidic device,* Lab on a Chip **12**, 2305 (2012).

[44] S. Evje and J. O. Waldeland, *How Tumor Cells Can Make Use of Interstitial Fluid Flow in a Strategy for Metastasis,* Cellular and Molecular Bioengineering **12**, 227 (2019).

[45] J. M. Munson and A. C. Shieh, *Interstitial fluid flow in cancer: Implications for disease progression and treatment,* Cancer Management and Research **6**, 317 (2014).

[46] C. H. Heldin, K. Rubin, K. Pietras, and A. Östman, *High interstitial fluid pressure - An obstacle in cancer therapy,* Nature Reviews Cancer **4**, 806 (2004).

[47] T. Stylianopoulos, J. D. Martin, M. Snuderl, F. Mpekris, S. R. Jain, and R. K. Jain, *Co-evolution of solid stress and interstitial fluid pressure in tumors during progression: Implications for vascular collapse,* Cancer Research **73**, 3833 (2013).

[48] B. Schmierer, A. L. Tournier, P. A. Bates, and C. S. Hill, *Mathematical modeling identifies Smad nucleocytoplasmic shuttling as a dynamic signal-interpreting system,* Proceedings of the National Academy of Sciences of the United States of America **105**, 6608 (2008).

[49] I. Jang and K. A. Beningo, *Integrins, CAFs and mechanical forces in the progression of cancer,* Cancers **11** (2019), 10.3390/cancers11050721.

[50] J. C. Dawson, A. Serrels, D. G. Stupack, D. D. Schlaepfer, and M. C. Frame, *Targeting FAK in anticancer combination therapies,* Nature Reviews Cancer **21**, 313 (2021).

[51] J. M. Hope, J. D. Greenlee, and M. R. King, *Mechanosensitive Ion Channels: TRPV4 and P2X7 in Disseminating Cancer Cells,* Cancer Journal (United States) **24**, 84 (2018).

[52] C. L. Yankaskas, K. Bera, K. Stoletov, S. A. Serra, J. Carrillo-Garcia, S. Tuntithavornwat, P. Mistriotis, J. D. Lewis, M. A. Valverde, and K. Konstantopoulos, *The fluid shear stress sensor TRPM7 regulates tumor cell intravasation.* Science advances **7** (2021), 10.1126/sciadv.abh3457.

[53] F. L. Sardo, S. Strano, and G. Blandino, *YAP and TAZ in lung cancer: Oncogenic role and clinical targeting,* Cancers **10**, 1 (2018).

[54] L. K. Chin, Y. Xia, D. E. Discher, and P. A. Janmey, *Mechanotransduction in cancer,* Current Opinion in Chemical Engineering **11**, 77 (2016).

[55] W. J. Polacheck, J. L. Charest, and R. D. Kamm, *Interstitial flow influences direction of tumor cell migration through competing mechanisms,* Proceedings of the National Academy of Sciences of the United States of America **108**, 11115 (2011).

[56] I. Rizvi, U. A. Gurkan, S. Tasoglu, N. Alagic, J. P. Celli, L. B. Mensah, Z. Mai, U. Demirci, and T. Hasan, *Flow induces epithelial-mesenchymal transition, cellular heterogeneity and biomarker modulation in 3D ovarian cancer nodules,* Proceedings of the National Academy of Sciences of the United States of America **110** (2013), 10.1073/pnas.1216989110.

[57] V. Mani, Z. Lyu, V. Kumar, B. Ercal, H. Chen, S. V. Malhotra, and U. Demirci, *Epithelial-to-Mesenchymal Transition (EMT) and Drug Response in Dynamic Bioengineered Lung Cancer Microenvironment,* Advanced Biosystems **3**, 1 (2019).

[58] Q. Huang, X. Hu, W. He, Y. Zhao, S. Hao, Q. Wu, S. Li, S. Zhang, and M. Shi, *Fluid shear stress and tumor metastasis.* American journal of cancer research **8**, 763 (2018).

[59] W. Huang, H. Hu, Q. Zhang, X. Wu, F. Wei, F. Yang, L. Gan, N. Wang, X. Yang, and A. Y. Guo, *Regulatory networks in mechanotransduction reveal key genes in promoting cancer cell stemness and proliferation,* Oncogene **38**, 6818 (2019).

[60] F. Broders-Bondon, T. H. N. Ho-Bouldoires, M. E. Fernandez-Sanchez, and E. Farge, *Mechanotransduction in tumor progression: The dark side of the force,* Journal of Cell Biology **217**, 1571 (2018).

[61] A. Saraswathibhatla, D. Indana, and O. Chaudhuri, *Cell–extracellular matrix mechanotransduction in 3D,* Nature Reviews Molecular Cell Biology **24**, 495 (2023).

[62] C. P. Huang, J. Lu, H. Seon, A. P. Lee, L. A. Flanagan, H. Y. Kim, A. J. Putnam, and N. L. Jeon, *Engineering microscale cellular niches for three-dimensional multicellular cocultures,* Lab on a Chip **9**, 1740 (2009).

[63] A. K. Miri, H. G. Hosseinabadi, B. Cecen, S. Hassan, and Y. S. Zhang, *Permeability mapping of gelatin methacryloyl hydrogels,* Acta Biomaterialia **77**, 38 (2018).

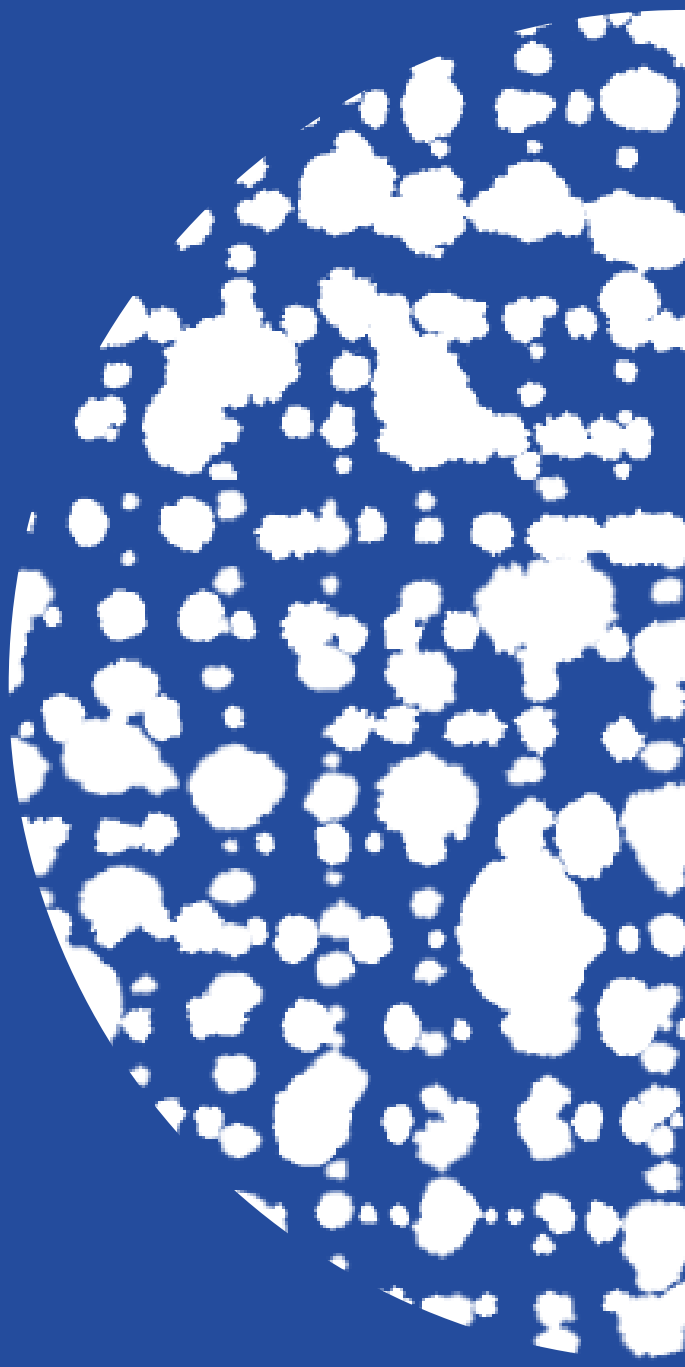

4

UNJAMMING TRANSITIONS IN SPHEROIDS ARE LINKED TO EMT-DEPENDENT CELL-MATRIX INTERACTIONS

ABSTRACT

The plasticity of cancer cells allows them to switch between different migration modes, promoting their invasion into the extracellular matrix (ECM) and hence increasing the risks of metastasis. Epithelial-to-mesenchymal transitions (EMT) and unjamming transitions provide two distinct pathways for cancer cells to become invasive, but it is still unclear to what extent these pathways are connected. Here we addressed this question by performing 3D spheroid invasion assays of epithelial-like (A549) and mesenchymal-like (MV3) cancer cell lines in collagen-based hydrogels, where we varied both the invasive character of the cells (using Transforming Growth Factor (TGF)-β and matrix metalloprotease (MMP) inhibition to modulate cell-mediated matrix degradation) and matrix confinement (varying pore size). By using a robust quantitative image analysis to track spheroid invasion, we discovered that the onset time of invasion mostly depended on the matrix pore-size and corresponded with vimentin levels, while the subsequent invasion rates mostly depended on metalloprotease MMP1 levels and thus cell-matrix interaction. Morphological analysis revealed that spheroids displayed solid-like (non-invasive) behavior in small-pore hydrogels and switched to fluid-like (strand-based) or gas-like (disseminating cells) phases in large-pore hydrogels and when cells were more mesenchymal-like. Our findings are consistent with unjamming transitions as a function of cell motility and matrix confinement predicted in recent models for cancer invasion but show that cell motility and matrix confinement are coupled via EMT-dependent matrix degradation.

A. van der Net^{+}, Z. Rahman^{+}, A. Deep Bordoloi, I. Muntz, P. ten Dijke, P.E. Boukany, G.H. Koenderink *(under revision, $^{+}$ equal author contribution)*

4.1. INTRODUCTION

The dissociation of cancer cells from the primary tumor followed by invasion through the local tumor microenvironment (TME) is a crucial first step during metastasis of solid tumors. These first stages of invasion are often achieved through epithelial to mesenchymal transitions (EMT) that promote cell motility [1] and they are influenced by the composition of the TME. The TME has distinctive cellular components, including cancer-associated fibroblasts (CAFs) and immune cells, as well as non-cellular components, including cytokines, growth factors, and a unique organization of extracellular matrix (ECM) [2]. Tumor cells and CAFs remodel the ECM in the TME, generally turning the fibrous networks from healthy tissues into denser and stiffer matrices with smaller pores [3]. The resulting dysregulated ECM poses physical challenges for the invading tumor cells, as the cells have to tightly squeeze their nuclei while preventing excessive DNA damage [4, 5].

To deal with a wide variety of dysregulated tissue organizations in the TME, cancer cells are known to adapt their phenotype and associated migration strategy in response to their local environments. Tumor cells that migrate individually can adopt three main modes of migration, which can be categorized by their dependency on cell-matrix adhesions and actomyosin contractility. Cancer cells performing mesenchymal migration pull themselves forward on matrix fibers relying on matrix adhesions and cell contractility. In low-adhesion or high-density tissues, cancer cells can migrate through either amoeboid or lobopodial migration and increase their deformability [5]. Next to these individual cell motility modes, cancer cells can also switch to multicellular migration modes. This collective migration strategy is linked to increased survival in the bloodstream and higher metastatic potential[6]. The phenotypic plasticity of cancer cells enables switches between these different migration strategies in response to changes in ECM confinement and stiffness[7, 8], oxygen and energy deprivation [9] and cytokines[10].

While the role of intracellular signaling pathways (such as responses to TGF-β, epidermal growth factor, or cytokines released from CAFs) and the expression of EMT markers [11, 12] in cancer cell invasion are relatively well studied, the molecular mechanisms behind migration mode switches in response to different TMEs remain poorly understood [13]. The increasing attention for the biophysical aspects of tumor invasion in recent years has revealed that matrix confinement, determined by ECM protein density and porosity, is an important regulator of cell migration mode switches[7, 14, 15]. Mechanistically, the link between ECM confinement and cancer cell invasion was has been explained by describing tumors as active liquid crystalline materials that undergo solid-to-liquid like transitions during jamming conversions[5, 16] that are determined by cell-cell adhesions and ECM confinement[17]. Lattice-gas cellular automaton simulations suggested a theoretical jamming phase diagram that describes how variations in both cell-cell adhesions and ECM density (and hence confinement) determine unjamming transitions from a state where no invasion occurs (solid-like phase) towards collective cell invasion (liquid-like phase) or individual cell invasion (gas-like phase) [17]. Later agent-based simulations predicted a non-equilibrium phase diagram that describes these unjamming transitions in terms of 'cell motility' and 'matrix density' [18].

While this conceptual framework is appealing, it is complicated by the fact that these two variables, cell motility and ECM confinement, are not independent. They are cou-

pled since cancer cells can actively modify the ECM composition and architecture, while conversely the ECM can induce changes in cell motility [19]. Cancer cells adhere to the ECM via integrin receptors, activating intracellular signalling pathways that trigger cellular responses such as ECM deposition and the release of matrix metalloproteases (MMPs) [17, 20]. MMPs are proteolytic enzymes secreted by cancer cells to break down ECM proteins such as collagen, forming proteolytic tracks that facilitate cancer cell invasion [21]. In addition, upregulation of collagen deposition by tumor cells (and CAFs) can also promote cell invasion with the formation of specialized anisotropic migration tracks [22, 23]. These complex events together contribute to an abnormal ECM composition, structure and stiffness, which in turn influences cell invasion [2, 24]. In addition, these changes in the ECM alter other cellular characteristics such as cell proliferation, differentiation and cell mechanics, all of which also impact cancer initiation and progression [25–28]. Changes in ECM stiffness and porosity can affect the mode of migration of cancer cells [21, 29] and their invasion capacity [27, 30–33]. Moreover, the ECM can also affect cell migration through the storage and release of growth factors [34], such as the latent form of transforming growth factor-β (TGF-β) [35–37]. TGF-β is a well known cytokine found in the TME that triggers the upregulation of mesenchymal-associated protein markers such as vimentin, and the down-regulation of epithelial protein markers such as E-cadherin, promoting cell motility and invasion through EMT [38, 39]. Furthermore, TGF-β also stimulates the release of MMPs from cancer cells, stimulating the formation of proteolytic tracks that promote invasion [21]. The role of TGF-β in tumor invasion is a clear example of the dynamic reciprocity of cell-ECM interactions during invasion.

Although much work has been done on elucidating the different matrix properties that influence cancer cell invasion, the reported correlations can be inconsistent. For example, increased matrix stiffness correlates with enhanced invasion in 3D *in vitro* models of epithelial cancers in 64% of the studies, but it is also negatively correlated in 36% of the studies [40]. This variability is probably due to the diversity in experimental setups. Especially the time scale over which invasion is monitored is likely important, since invasion is a highly dynamic process. Because of these inconsistencies, there are still many open questions about the roles of matrix properties in invasion, especially in combination with reciprocal cell-ECM interactions where cell motility and matrix properties change in concert. To gain a better understanding of how cell-matrix interactions control cell invasion, we need cellular in vitro model systems that decouple interconnected matrix properties such as stiffness and porosity [41], differentiate between different stages of invasion, and analyse how matrix remodelling and cell signalling impact unjamming phase transitions during invasion.

In this study, we aimed to understand the effect of mechanochemical coupling between matrix confinement and cell motility on tumor invasion. For this, we analysed the invasion efficiencies and migration modes of cancer cells in 3D spheroid-hydrogel assays. We related these phenotypic characteristic to protein levels of EMT markers (vimentin and E-cadherin) and of MMPs, and to the unjamming transitions that describe invasion behaviour [18]. To tune matrix confinement over a wide range, we used two types of hydrogels, natural collagen (bovine type I) and semi-synthetic gelatin methacrylate (GelMA), at different concentrations. GelMA matrices contained pore sizes that were

substantially smaller (≃ 10 nanometer range) than average cell bodies (≃ 10 micrometer range) so cell motility requires matrix degradation, while the pore sizes of collagen type I matrices (≃ micrometric) allowed for cell motility through a combination of cell squeezing and matrix degradation. We systematically compared the invasive capacity of epithelial-like cancer cells (A549, lung adenocarcinoma) and mesenchymal-like, highly metastatic cells (MV3 melanoma). Furthermore, we explored how cell-mediated matrix degradation influences invasion trends, by studying cancer cell invasion upon TGF-β or MMP inhibitor treatments. We used a broad spectrum MMP-inhibitor (Batimastat, BB-94) that consists of collagenases (MMP-1), gelatinases (MMP-2, MMP-9) and more to inhibit cleavage of collagen type I and GelMA hydrogels used in this study. Using a new image analysis method to analyze the spatiotemporal characteristic of tumoroid invasion, we demonstrate that the onset of tumor invasion is regulated by initial matrix confinement and vimentin, while the rate of invasion and unjamming transitions correspond with MMP1 levels. Our findings reveal that EMT-regulated cell-ECM mechanochemical interactions play an important role in 3D spheroid unjamming transitions.

4.2. RESULTS

4.2.1. DESIGN AND CHARACTERIZATION OF THE 3D SPHEROID INVASION MODEL

To identify the impact of ECM confinement on the invasion of cancer cells with different metastatic potentials, we performed 3D spheroid invasion assays using two different human cancer cell lines and two different types of hydrogels. MV3 (melanoma) cells were chosen as they are highly metastatic and mesenchymal-like, in contrast to the epithelial-like character of A549 (lung carcinoma) cells (see schematic in Fig. 4.1A). We confirmed the mesenchymal and epithelial features of the two cell lines by bright-field imaging of the cell morphology (see Fig. 4.8A) and Western blot analysis of the protein levels of E-cadherin and vimentin (see Fig. 4.8B). For hydrogel systems, we chose collagen type I and GelMA hydrogels, because of their contrasting fibrous open-mesh network structure versus dense confining microenvironment, respectively (Fig. 1Bi). Two different concentrations for each type of hydrogel were characterized for stiffness and for the pore size and corresponding fiber density. Measurements of the storage modulus (G') from small amplitude oscillatory shear rheology showed that the hydrogels covered a wide range of stiffnesses, covering a range from 10^1 Pa to 10^3 Pa (see Fig. 4.1C). Pore size measurements were conducted through analysis of confocal microscopy reflection images for collagen networks (Fig. 4.1Bii,iii and Fig. 4.9) and through permeability measurements for GelMA hydrogels (Fig. 4.1Biv,v and Table S4.2). The GelMA hydrogels had pore sizes in the ≃ 10 nanometer range, two orders of magnitude smaller than the micrometric pores of collagen hydrogels (Fig. 4.1D). Furthermore, for both hydrogel types, the pore size decreased with increasing biopolymer concentration (30 versus 50 mg/mL for GelMA; 2.4 versus 8 mg/ml for collagen). As an independent test of matrix porosity, we also compared the fiber densities of the four hydrogels by measuring the void fraction in confocal reflection microscopy images. These estimations showed that the hydrogels with the smaller pores indeed had the highest matrix fiber densities (see Fig. 4.10). These results demonstrate that the ECM-mimicking hydrogels in this study offer a wide range of levels of cell con-

finement, from full confinement of cells in GelMA hydrogels to partial confinement of cells in the collagen hydrogels.

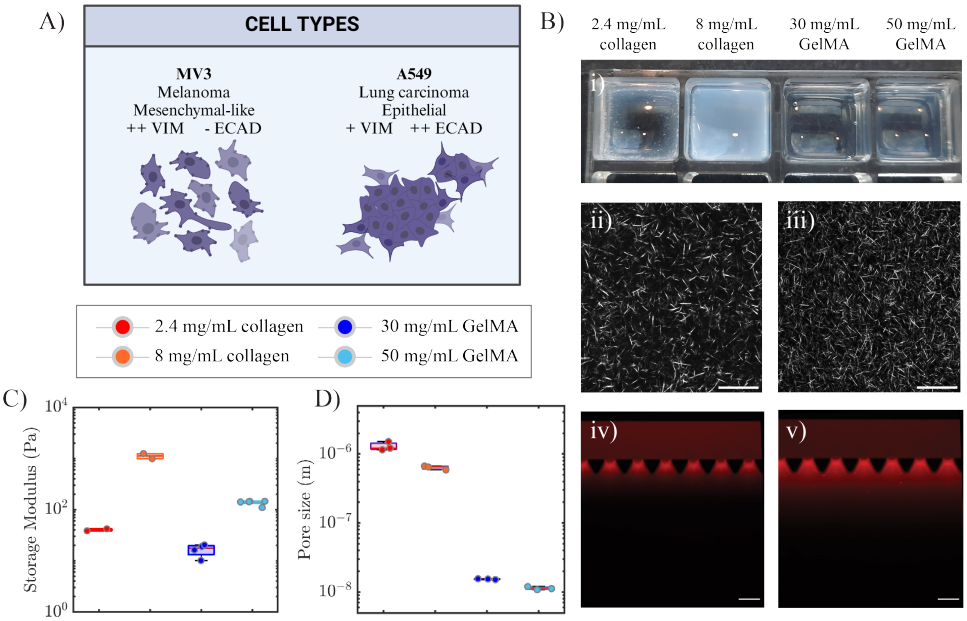

Figure 4.1: **Characterization of the 3D spheroid invasion model.** (A) Schematic showing the distinctive features of MV3 melanoma cells and A549 lung adenocarcinoma cells. MV3 cells are mesenchymal-like, with high vimentin expression (++VIM) and low E-cadherin expression (-ECAD), whereas A549 cells are epithelial-like, with lower vimentin (+VIM) and high E-cadherin (++ECAD) expression and more cell-cell interactions. (B) Structural characterization of the ECM-mimicking hydrogels. (i) Photograph of the four hydrogels in an ibidi 8-well slide (without spheroids), scale bar = 10 mm. The collagen hydrogels are more turbid than the GelMA hydrogels because of the larger width of collagen fibers as compared to GelMA strands. Confocal reflection images of collagen at concentrations of (ii) 2.4 mg/mL and (iii) 8 mg/mL. Scale bars are 25 µm. Permeability analysis of GelMA (30 mg/mL) based on fluorescence images of Rhodamine B dye (red) at (iv) t=0 and (v) t=10 min, performed in a microfluidic chip, scale bar = 200 µm. We inferred the hydraulic permeability from the distance travelled by the dye under a pressure gradient of 20 mbar (top to bottom) using Darcy's law. (C) Storage shear moduli (G') of collagen and GelMA hydrogels obtained by rheology measurements. (D) Pore sizes of collagen and GelMA hydrogels, obtained by image analysis and permeability analysis, respectively.

4.2.2. SPHEROID INVASION DEPENDS ON MATRIX CONFINEMENT AND ON CELL TYPE

To understand the impact of matrix confinement (i.e., pore size) on the ability of the cells to invade, we performed invasion assays by bright-field imaging of 200 µm diameter cancer spheroids embedded in hydrogels at the spheroid equator. For MV3 spheroids in dilute (2.4 mg/ml) collagen, we observed substantial cell invasion already by t=8 hours (hrs), and even more invasion after 24 hrs (Fig. 4.2A). After 24 hrs, the spheroid was par-

tially disintegrated, leaving an intact spheroid core surrounded by many disseminated individual cells. Therefore, the MV3 invasion assay was limited to 24 hrs. In a denser (8 mg/ml) collagen hydrogel, the MV3 spheroids showed a similar invasion pattern (Fig. 4.11A). In 30 mg/mL GelMA hydrogels, the MV3 spheroids also showed an isotropic invasion pattern, but invasion was delayed and the cells reached less far into the gel (Fig. 4.2B). In 50 mg/mL GelMA gels, we could not observe any signs of invasion on a 24 hrs time scale (Fig. 4.11B).

The A549 spheroids showed a very different invasion behavior as compared to MV3 spheroids. Even in the least confining hydrogel (2.4 mg/mL collagen), the A549 spheroids remained compact and developed only a small number of multicellular protrusions from sites that were non-uniformly distributed around the spheroid periphery. Also, there were much fewer disseminated cells (Fig.4.2C). The A549 spheroids furthermore showed a much longer onset time for invasion (t ≈ 24 hrs) compared to the MV3 spheroids (t ≈ 8 hrs) in the same matrix. To allow sufficient time for cell invasion, we therefore performed 72 hrs of time-series imaging for A549 spheroids. In denser 8 mg/mL collagen hydrogels and GelMA hydrogels (30 mg/mL and 50 mg/mL), A549 spheroids showed hardly any protrusions nor disseminated cells even after 72 hrs (Fig.4.2D for 30 mg/mL GelMA and Fig. 4.12 for 8 mg/mL collagen and 50 mg/mL GelMA). These findings demonstrate that the mesenchymal-like MV3 cells are more invasive than the epithelial-like A549 cells and that invasion in both cases is impacted by the matrix density.

To quantify the effects of cell type and matrix density on spheroid invasion, we tracked the spheroid periphery for each time point through automated image analysis of the bright-field time-lapse images. To account for varying spheroid shapes and initial sizes, we computed the effective circular radius normalized by its initial value at t=0 hr. For the MV3 spheroids, we found a clear trend of decreasing cell invasion with decreasing matrix pore size, going from 2.4 mg/mL collagen to 8 mg/mL collagen and to 30 mg/mL GelMA and finally to 50 mg/mL (Fig. 4.2E). In the densest hyrogel (50 mg/mL GelMA), no appreciable invasion took place. The A549 spheroids showed the same trend as MV3 spheroids as a function of matrix pore size and likewise showed complete inhibition of invasion in 50 mg/mL GelMA (Fig. 4.2F). These invasion trends strongly suggest that the matrix pore size is an important determinant of the spheroid invasion capacity. By contrast, the matrix stiffness appeared to have little predictive value, since collagen (2.4 mg/mL) gels and GelMA (30 mg/mL) gels had very different effects on spheroid invasion despite their comparable elastic modulus (40 Pa for collagen (2.4 mg/mL) and 15 Pa for GelMA (30 mg/mL). It is also interesting to note that the GelMA (50 mg/mL) gel had a rather low stiffness of just G' = 200 Pa, yet showed complete inhibition of invasion for both cancer cell types.

4.2.3. INCREASED MATRIX CONFINEMENT DELAYS THE ONSET OF CELL INVASION

The invasion time curves clearly showed a delay time before measurable spheroid invasion occurred, followed by a steady increase of normalized spheroid radius Fig. 4.13. To quantify this delay, we defined the onset time for invasion (t_{ons}) as the time point at which spheroids achieved a 10% increase in normalized radius, shown by the horizontal dashed lines in Fig. 4.2E,F. For MV3 spheroids in collagen, the delay time was shortest

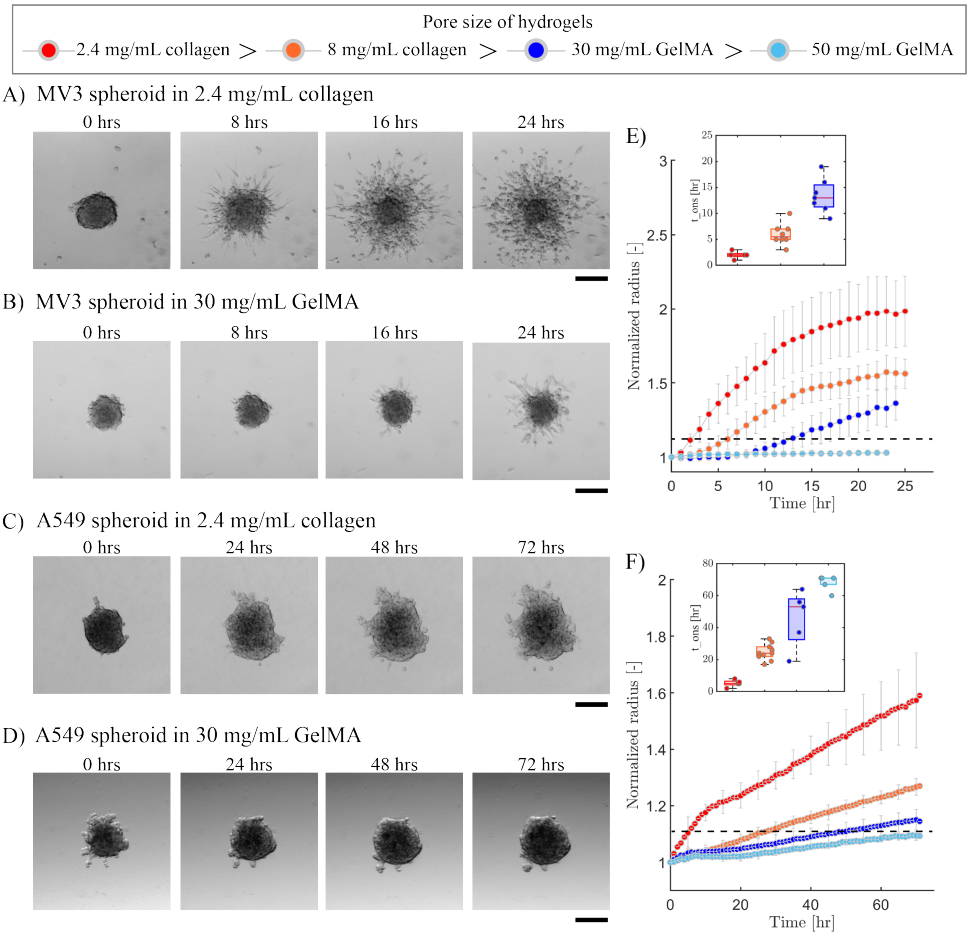

Figure 4.2: **MV3 and A549 spheroid invasion in collagen and GelMA matrices.** Bright-field microscopy images of spheroids at different time intervals for 24 hrs invasion of a MV3 spheroid in A) collagen (2.4 mg/mL) and (B) GelMA (30 mg/mL), and for 72 hrs invasion of an A549 spheroid in (C) collagen (2.4 mg/mL) and (D) GelMA (30 mg/mL). Scale bars: 200µm. Time evolution of the normalized effective circular radius of (E) MV3 and (F) A549 spheroids, for different matrix compositions (see legend on top). Horizontal black dashed lines indicate the onset time for invasion, defined as the time where the normalized radius reaches a value of 1.1. Data are averages with standard deviations of N = 4-10 spheroids (from n = 2 independent experiments). Insets in (E) and (F) show the onset time of invasion in the different matrices (same color code as main plots).

(t_{ons} = 3 hrs) in 2.4 mg/mL collagen, somewhat longer (t_{ons} = 5 hrs) in 8 mg/mL collagen, and even longer (t_{ons} = 11.5 hrs) in 30 mg/mL GelMA (inset of Fig.4.2E). For A549 spheroids, the onset times were always longer than for MV3 spheroids, but there was a similar trend of increasing onset time with decreasing pore size, from t_{ons}) = 15 hrs for 2.4 mg/mL collagen, to t_{ons} = 24 hrs for 8 mg/mL collagen, and t_{ons} = 57 hrs for 30 mg/mL GelMA (inset of Fig.4.2F). In 50 mg/mL GelMA, neither the MV3 nor the A549 spheroids ever reached the threshold of a 10% increase in normalized spheroid radius. Based on

these results, we conclude that the matrix porosity affects the invasion capacity of the spheroids by controlling the onset time of invasion.

4.2.4. MMP-MEDIATED MATRIX DEGRADATION PROMOTES SPHEROID INVASION

Since matrix porosity strongly impacted the invasion capacity of the gels, we hypothesized that MMP secretion might be an important determinant of the invasion capacity. To test this hypothesis, we decided to tune the ability of the cells to degrade the matrix by using treatments with TGF-β to promote MMP secretion [42, 43]. Bright field imaging showed that TGF-β strongly promoted invasion of MV3 spheroids in 8 mg/mL collagen (Fig. 4.3A, left). After 24 hrs, the spheroid was disintegrated, with a partially diminished spheroid core. An even more drastic effect was seen for MV3 spheroids in 2.4 mg/mL collagen, where TGF-β treatment resulted in spheroid disintegration already after 10 hrs and caused the spheroid core to sink to the bottom of the well (Fig. 4.14A). For MV3 spheroids in GelMA (30 mg/mL), we observed a less drastic effect of TGF-β addition (Fig. 4.3A, right). After 24 hrs, the spheroid core did not disintegrate, but we did observe invasion and the presence of individual disseminated cells. For A549 spheroids, we observed qualitatively similar effects of TGF-β treatment. In 2.4 mg/mL collagen, spheroid invasion now was already substantial after 24 hrs, with a completely disintegrated spheroid core that sunk to the bottom of the well (Fig. 4.14B). In denser (8 mg/mL) collagen and in GelMA (30 mg/mL), the A549 spheroids displayed protrusions into the matrix but without any individual cell dissemination (Fig.4.3B). For both cell types, TGF-β treatment was ineffective to produce invasion in 50 mg/mL GelMA hydrogels (Fig. 4.15)). These findings are consistent with our hypothesis that MMP-mediated degradation can promote spheroid invasion in dense matrices, but only up to a point.

Conversely, to test the effect of reduced MMP-mediated matrix remodelling, we repeated the spheroid invasion assays in the presence of the broad-spectrum MMP-inhibitor Batimastat to inhibit MMP activity [44, 45]. Bright field imaging showed a subtle effect on MV3 spheroids in 8 mg/mL collagen, where MMP-inhibitor treatment resulted in shorter cellular protrusions and fewer disseminated individual cells as compared to control conditions (Fig. 4.3C left). A similar behavior was seen for MV3 spheroids in 2.4 mg/mL collagen (see Fig. 4.147A). The effect of the MMP-inhibitor was more pronounced for MV3 spheroids in GelMA (30 mg/ml), where invasion was completely inhibited over the 24 hr time window of observation (Fig. 4.3C right). For the A549 spheroids, MMP-inhibitor treatment completely suppressed spheroid protrusions and cell dissemination, both in collagen hydrogels (Fig. 4.3D left and (Fig. 4.14B) and in GelMA hydrogels (Fig. 4.3D right).

To quantify the observed effects of TGF-β and MMP-inhibitor treatments on invasion, we again measured the normalized spheroid radii as a function of time. Compared to control conditions, TGF-β treatment increased invasion of MV3 spheroids, as quantified by the final spheroid size, by 38% in collagen (8 mg/mL) and by 29% in GelMA (30 mg/mL) (Fig. 4.3E). In 2.4 mg/mL collagen, we observed a 20% increase in final spheroid size compared to control conditions, but we note that in this case we only quantified invasion up to 14 hours since the TGF-β treatment caused spheroid disintegration and sedimentation (Fig. 4.14C). By contrast, MMP-inhibition reduced invasion

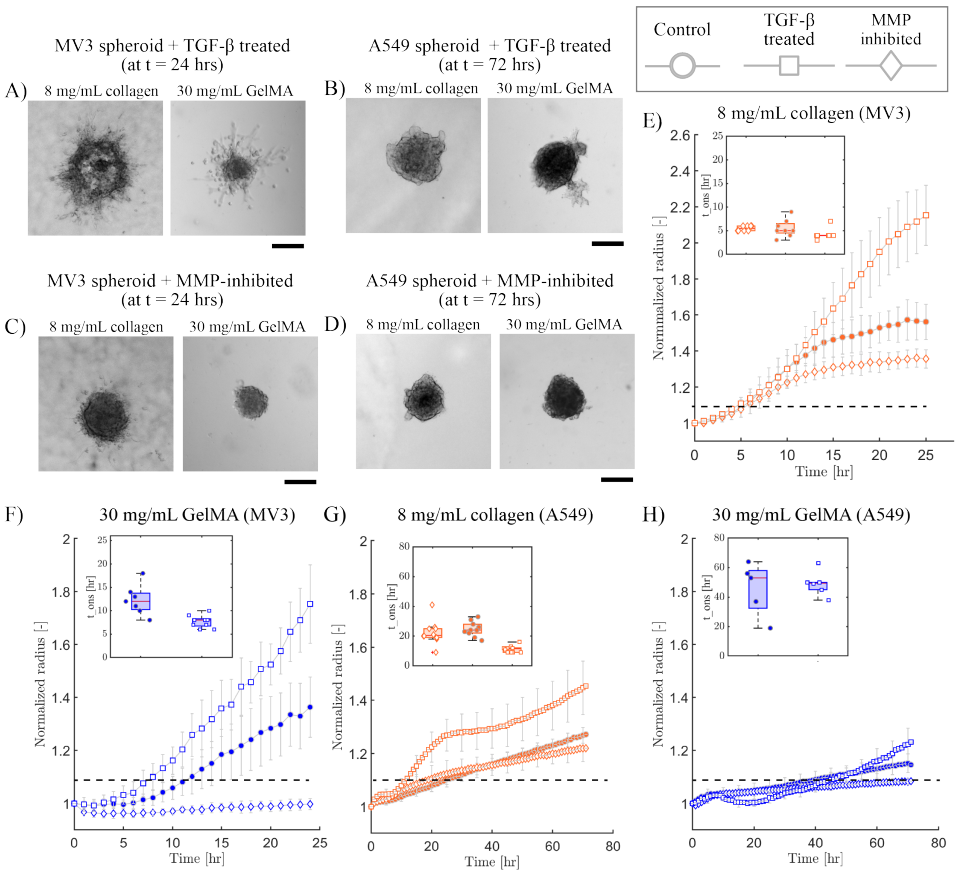

Figure 4.3: **Spheroid invasion in different matrices in the presence of either TGF-β or the broad-spectrum MMP-inhibitor Batimastat.** Bright field images of spheroids after invasion (24 hr for MV3 spheroids, 72 hrs for A549 spheroids) for TGF-β-treated (A) MV3 spheroids and (B) A549 spheroids, and Batimastat-treated (C) MV3 spheroids and (D) A549 spheroids. In all cases, data are shown for spheroids in 8 mg/mL collagen (left) and in 30 mg/mL GelMA (right). Scale bars are 200 µm. Time evolution of normalized effective circular radius of the spheroids for (E) MV3 spheroids in collagen (8 mg/mL), (F) MV3 spheroids in GelMA (30 mg/mL), (G) A549 spheroids in collagen (8 mg/mL) and (H) A549 spheroids in GelMA (30 mg/mL). Horizontal black dashed lines indicate the onset time for invasion, defined as the time where the normalized radius reaches a value of 1.1. Data are averages with standard deviations of N = 5-10 spheroids. Insets: invasion onset times.

of MV3 spheroids as quantified by the final spheroid size, by 15% in 8 mg/mL collagen, 36% in 30 mg/mL GelMA, and 34% in 2.4 mg/mL collagen Fig.S4.14C). The effects of the drugs were similar for A549 spheroids. TGF-β treatment increased invasion (after 72 hrs) by 14% in 8 mg/mL collagen (Fig. 4.3G) and by 10% in 30 mg/mL GelMA (Fig. 4.3H) compared to control conditions. By contrast, MMP-inhibition reduced invasion by 4% in 8 mg/mL collagen, 7% in 30 mg/mL GelMA (Fig. 4.3G, H), and 38% in 2.4 mg/mL collagen (Fig. 4.14D). These findings show that MMP-mediated degradation promotes spheroid invasion in dense matrices (for both cell types) and that it is absolutely required for invasion in dense GelMA gels that present pores smaller than the cell size.

MMP-MEDIATED REMODELLING AFFECTS THE INVASION ONSET TIME MORE STRONGLY IN GELMA THAN IN COLLAGEN

Since we found that confinement influences invasion by delaying the onset time, we tested whether the TGF-β and MMP-inhibitor treatments change t_{ons}. For MV3 spheroids in 8 mg/mL collagen, we observed a trend of reduced onset time with TGF-β treatment (t_{ons} = 4 hrs) and increased onset time with MMP inhibition (t_{ons} = 5.5 hrs) compared to the control condition (t_{ons} = 5 hrs), but the differences were not statistically significant (inset of Fig. 4.3E). For MV3 spheroids in 2.4 mg/mL collagen, we similarly observed a slight increase in onset time (t_{ons} = 3 hrs) with MMP inhibition compared to control and TGF-β treated spheroids (both t_{ons} = 2 hrs) (insets of Fig. 4.14C, D). For MV3 spheroids in 30 mg/mL GelMA, TGF-β treatment significantly reduced the onset time (t_{ons} = 8 hrs) compared to control conditions (t_{ons} = 11.5 hrs), while MMP-inhibition resulted in complete inhibition of invasion (inset of Fig. 4.3F). Thus, MV3 spheroid invasion into this dense matrix was dependent upon MMP-mediated degradation. In 50 mg/mL GelMA the MV3 spheroids never invaded, even when TGF-β was added to upregulate MMP expression (Fig. 4.15C).

For A549 spheroids in 8 mg/mL collagen, we observed a stronger effect of TGF-β treatment on the invasion onset time (t_{ons} = 11.5 hrs) compared to control conditions (t_{ons} = 24 hrs) than for MV3 spheroids (inset of Fig. 4.3G). However, MMP-inhibition did not significantly change the onset time (t_{ons} = 21 hrs). In 2.4 mg/mL collagen, MMP-inhibition did have a major influence on the onset time, increasing it from t_{ons} = 5 hrs to t_{ons} = 30 hrs (Fig. 4.14D). For A549 spheroids in 30 mg/mL GelMA, we did not see a significant difference between the onset time with TGF-β (t_{ons} = 53 hrs) versus control conditions (t_{ons} = 47 hrs), but MMP-inhibition completely suppressed invasion (inset of Fig. 4.3H). This finding again shows that invasion into the dense GelMA networks requires MMP-mediated remodelling. In 50 mg/mL GelMA, TGF-β-treatment caused a slight (2%) increase in final normalized spheroid radius compared to control and MMP-inhibited spheroids (Fig. 4.15D) and a small reduction of the onset time (t_{ons} = 57 hrs) compared to control and MMP-inhibited conditions (t_{ons} = 67.5 hrs and 68 hrs respectively, inset of Fig. 4.15D).

4.2.5. MMP-MEDIATED REMODELLING IMPACTS SPHEROID EXPANSION RATES

The TGF-β and MMP-inhibitor treatments strongly affected the final spheroid radii yet only minimally affected the invasion onset time, particularly in collagen. To understand this discrepancy, we analyzed the rate of expansion of the spheroids after the onset of

invasion. We determined the expansion rates as the power-law slopes of the normalized radius versus time curves. Note that we did not perform any expansion rate analysis for MV3 and A549 spheroids in 50 mg/mL GelMA, since invasion was negligible under these conditions. For MV3 spheroids in collagen, the spheroid radius reached a plateau value around t=20 hrs (Fig. 4.4), likely due to dissociation of cells from the spheroid that are not included in the normalized spheroid radius (Fig. 4.16). We therefore determined the expansion rate over an intermediate time range between the onset time and the time where the normalized radius saturated (Fig. 4.13). For A549 spheroids, the equivalent circular radius showed a steady increase until 72 hrs since there was little to no dissociation of cells, so we calculated the expansion rate from the onset of invasion till the end time-point (Fig. 4.17). The spheroid expansion rates measured under all the different conditions are summarized in Table4.1.

The expansion rate of the MV3 spheroids was enhanced by TGF-β treatment (Fig. 4.4B) and reduced by MMP-inhibition (Fig. 4.4C) as compared to control conditions (Fig. 4.4A). The expansion rate of the A549 spheroids was similarly impacted by TGF-β and MMP-inhibitor treatments. Strikingly, for both cell types, the spheroid expansion rate in control conditions was independent of matrix composition, showing comparable values in collagen (2.4 mg/mL and 8 mg/mL) and in GelMA (30 mg/mL). The expansion rate for MV3 spheroids was about two-fold higher than for A549 spheroids, as expected based on their more mesenchymal-like character. Upon TGF-β treatment, the spheroid expansion rates significantly increased for both cell types, by about 1.5-fold for MV3 spheroids and 2-fold for A549 spheroids. The relative increase for MV3 spheroids was highest in 8 mg/mL collagen, while for A549 spheroids it was highest in 2.4 mg/mL collagen, showing a cell type-dependent factor. By contrast, MMP-inhibition caused a 1.7-fold reduction of the spheroid expansion rates for both A549 and MV3 spheroids in both collagen matrices (2.4 mg/mL and 8 mg/mL). In GelMA (30 mg/mL), there was no detectable invasion at all in MMP-inhibited conditions. Altogether, this analysis demonstrates that the expansion rate of the spheroids is strongly dependent on MMP-mediated matrix remodelling for both cell types.

4.2.6. TGF-β AND MMP INHIBITOR TREATMENTS AFFECT EXPRESSION OF EMT MARKERS

The MV3 and A549 spheroids showed a similar sensitivity to MMP inhibitors, but a slightly different sensitivity to TGF-β treatment. The response to TGF-β likely is a combined effect from multiple upregulated cellular processes besides enhanced MMP expression. To test the effects of the TGF-β as well as MMP inhibitor treatments on these phenotypic changes, we used Western blot analysis to measure the levels of MMPs and EMT marker proteins, specifically vimentin as a mesenchymal marker and E-cadherin as an epithelial marker. For both cell lines, TGF-β treatment resulted in significantly upregulated levels of MMP1 (Fig. 4.5A) and MMP2 (Fig. 4.5B) compared to the control samples. At the same time, TGF-β treatment increased vimentin expression (Fig. 4.5C) and reduced E-cadherin expression (Fig. 4.5D) in A549 cells, confirming that TGF-β treatment induces an EMT switch in these epithelial-like cells. For MV3 cells, TGF-β treatment did not affect vimentin expression (Fig. 4.5C) nor E-cadherin expression (Fig. 4.5D), confirming that these cells are intrinsically already mesenchymal-like and there-

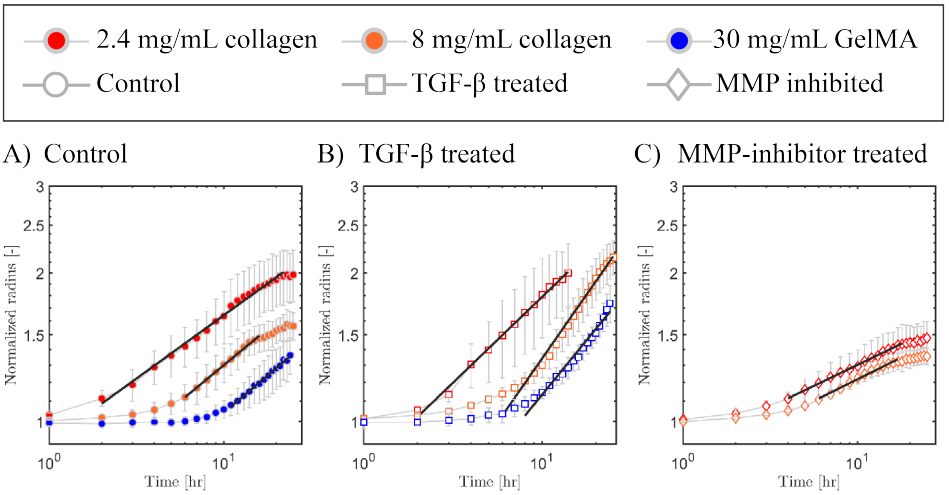

Figure 4.4: **Expansion rates of MV3 spheroids.**. We determined the expansion rates by fitting the increase in normalized spheroid radius with time (symbols) to a power law (black lines) over the indicated temporal range. We compare MV3 spheroid invasion behavior under (A) control conditions with (B) TGF-β treatment and (C) MMP-inhibitor treatment. In each case, data are shown for different matrix compositions (see legend on top). Note that in panel C, we did not include MV3 spheroids in 30 mg/mL GelMA since there was no measurable invasion. Data are averages with standard deviation of N = 4-10 spheroids for each condition.

MV3 spheroid expansion rates			
	2.4 mg/mL collagen	**8 mg/mL collagen**	**30 mg/mL GelMA**
Control	0.26 [0.24 – 0.27]	0.29 [0.28 – 0.31]	0.29 [0.28 – 0.31]
TGF-β treated	0.34 [0.33 – 0.36]	0.51 [0.49 – 0.55]	0.44 [0.40 – 0.48]
MMP-inhibited	0.17 [0.16 – 0.18]	0.17 [0.16 – 0.19]	NA
A549 spheroid expansion rates			
Control	0.15 [0.14 – 0.16]	0.14 [0.13 – 0.14]	0.1 [0.1 – 0.2]
TGF-β treated	0.37 [0.35 – 0.39]	0.19 [0.19 – 0.2]	0.23 [0.21 – 0.25]
MMP-inhibited	0.07 [0.07 – 0.08]	0.08 [0.07 – 0.08]	NA

Table 4.1: **Expansion rates quantified as power law slope values (unit: h^{-1}) obtained from normalized spheroid radius [-] versus time (hrs) curves for control, TGF-β-treated and MMP-inhibited MV3 and A549 spheroids in different hydrogel compositions.** The table represents the average slope value for spheroids in collagen (2.4 and 8 mg/mL) and GelMA (30 mg/mL) with upper and lower limit of error (in square brackets). NA (not applicable) means no slope analysis was performed since no invasion was observed (MMP-inhibited MV3 and A549 spheroids in 30 mg/mL GelMA).

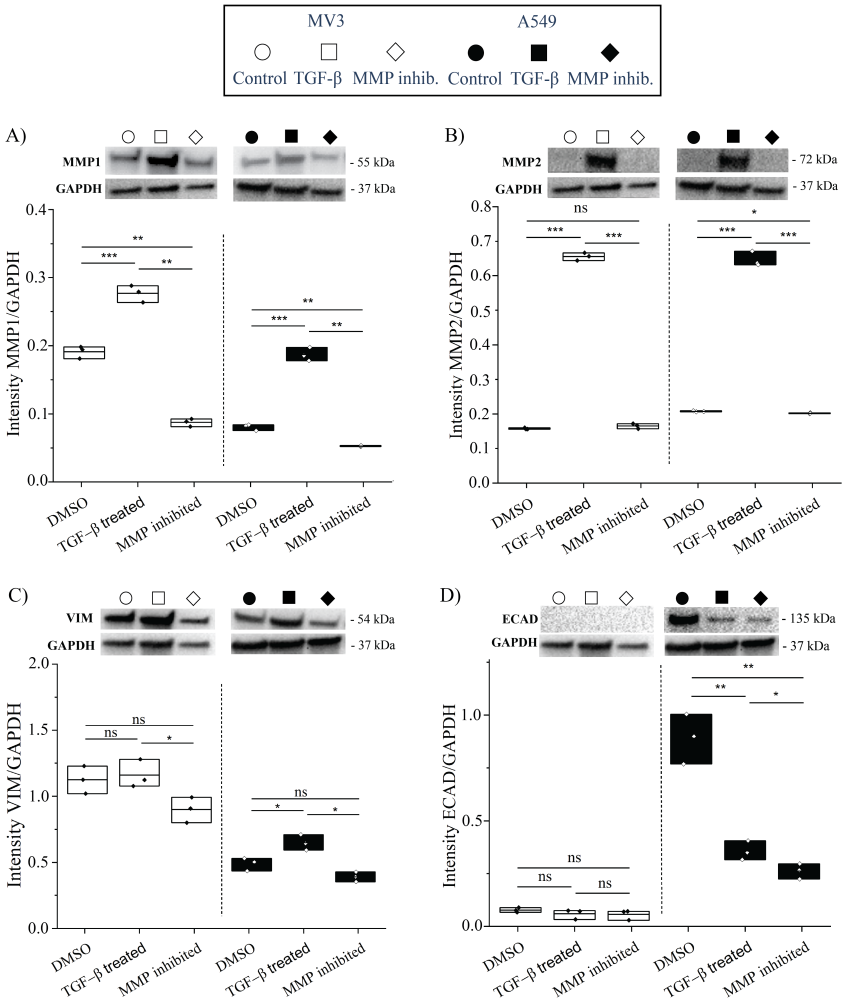

Figure 4.5: **Western blot analysis of A549 and MV3 cells, showing the impact of TGF-β stimulation and MMP inhibition.** Protein levels normalized by the GAPDH levels for MV3 (white, left side) and A549 (black, right side) cells treated with DMSO (control conditions), TGF-β, or the broad spectrum MMP inhibitor Batimastat, for (A) MMP1, (B) MMP2, (C), vimentin (VIM), and (D) E-cadherin (ECAD). P-value results from t-tests are indicated by: (ns) = p≥0.05, (*) = p<0.05, (**) = p<0.01, (***) = p<0.001. Each condition depicts one biological sample (n=1) with three data points based on different background subtractions. The other three biological replicates showed similar trends (Fig. 4.18A,B and Fig. 4.19A,B). Compared band intensities are from the same blots, the complete gels are shown in Fig. 4.18C,D and Fig. 4.19C,D

fore less affected by TGF-β treatment than the A549 cells. The mechanism of action of TGF-β is through activation of the SMAD pathway [37]. To test activation of this pathway and its intrinsic activity in the two cell lines, we analyzed the protein levels of SMAD2

and phosphorylated SMAD2 (pSMAD2) in response to 1 hr TGF-β treatment by Western blot analysis. We observed a clear upregulation of pSMAD2 in response to TGF-β treatment in both cell lines, while the SMAD2 level remained constant (see Fig. 4.20)). This confirms that TGF-β treatment activated the SMAD pathway and that the intrinsic activity of the SMAD pathway in both cell lines was at a similar level that could be upregulated by TGF-β.

Interestingly, the MMP-inhibitor also caused changes in protein expression in both cell lines. MMP inhibition reduced the expression levels of MMP1 and MMP2 (Fig. 4.5A,B) and decreased vimentin expression levels (Fig. 4.5C) in A549 cells compared to control conditions. However, MMP-inhibited MV3 cells showed no significant change in MMP2 and vimentin protein expression and only showed significant difference in MMP1 protein expression. MMP inhibition also reduced E-cadherin expression for A549 cells (Fig. 4.5D). Consistent with the reduction in E-cadherin levels in A549 cells by MMP inhibitor and TGF-β treatment, bright-field imaging showed that the drug-treated cells were more individual with less contact with neighboring cells compared to control conditions (see Fig. 4.21). In summary, the Western blot data confirm that TGF-β and MMP-inhibitor treatments alter MMP-levels in opposite directions and show that both treatments also impact EMT processes, especially in A549 cells.

4.2.7. INVASION ONSET AND SPHEROID EXPANSION RATE ARE CORRELATED WITH MATRIX POROSITY AND LEVELS OF EMT MARKERS

The quantitative analysis of spheroid invasion showed that matrix porosity is a major determinant of the onset of cancer cell invasion. At the same time, the Western blot analysis suggest that the EMT status and MMP expression levels of the cells are also major determinants of invasion. MV3 cells were consistently more invasive than A549 cells, consistent with their higher basal levels of proteolytic MMP enzymes and the mesenchymal marker protein vimentin. TGF-β treatment made both MV3 and A549 cells more invasive, by upregulating MMP and vimentin expression while downregulating E-cadherin expression. Conversely, MMP inhibition made the cells less invasive by blocking MMP activity while also changing MMP and EMT marker expression. To study the interplay between matrix porosity and cell invasiveness, we prepared heat map representations to correlate the invasion onset times and the spheroid expansion rates with the cellular levels of EMT markers (x-axis) and with the hydrogel pore size (y-axis). The color code in the heat maps encodes the invasion onset time (Fig. 4.6A,B) and the spheroid expansion rate (Fig. 4.6C,D). Note that we combined the data for A549 and MV3 cells (distinguishable by symbol color) and for DMSO (control), TGF-β and MMP inhibitor treatments (distinguishable by symbol shape).

The heat maps reveal that the invasion onset time is mainly determined by matrix confinement, with a progressively longer delay as the pore size becomes smaller (Fig. 4.6A,B). In the densest 50 mg/mL GelMA hydrogels, spheroid invasion is even fully blocked under most conditions (black squares). Higher vimentin levels were correlated with shorter invasion onset times (Fig. 4.6B). By contrast, we did not observe any clear correlation with invasion onset time for the other tested EMT markers, MMP1 (Fig. 4.6A), MMP2 (Fig. 4.22A) and E-cadherin (Fig. 4.22B).

The heat maps further reveal that the spheroid expansion rate was rather insensi-

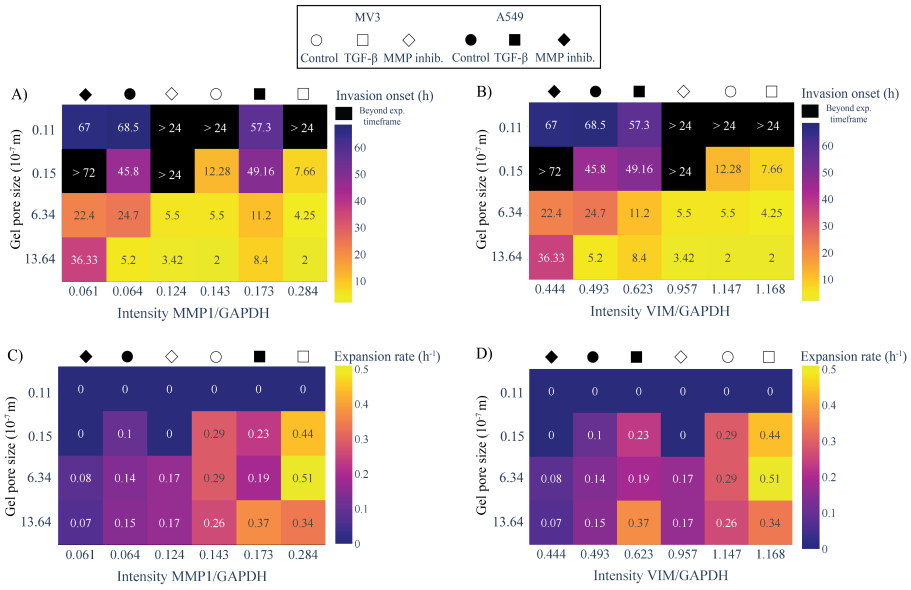

Figure 4.6: **Heat map representations showing the correlation of invasion onset times and spheroid expansion rates with MMP1 and vimentin protein expression levels for MV3 and A549 spheroids.** A) Dependence of the invasion onset time (indicated by the number (in units of hrs) in each square and the color code, see color bar on the right) on hydrogel pore size (y-axis) and expression level of MMP1 (x-axis). B) Corresponding heat map with the expression level of vimentin (x-axis). Note that spheroids that did not invade during the time frame of the assay are shown in black. C) Dependence of the spheroid expansion rate (indicated by the number (in units of hr^{-1}) in each square and the color code, see color bar on the right) on hydrogel pore size (y-axis) and expression level of MMP1 (x-axis). D) Corresponding heat map with the expression level of vimentin on the x-axis. Data for MV3 spheroids (white symbols above the heat maps) and A549 spheroids (black symbols) and for different treatment conditions (see symbol shapes) were pooled. Protein expression levels were normalized by the GAPDH levels.

tive to matrix confinement, except at the smallest pore sizes (50 mg/mL GelMA), where spheroid expansion was blocked (Fig. 4.6C,D). By contrast, the spheroid expansion rate strongly increased with increasing expression levels of MMP1 enzymes (Fig. 4.6C). The expansion rates did not show any clear correlation with the levels of vimentin (Fig. 4.6D), MMP2 (Fig. 4.22C) or E-cadherin (Fig. 4.22). Altogether, the heat maps therefore reveal an intriguing interplay of cellular properties and matrix porosity in determining the onset of invasion onset and the spheroid expansion rate.

4.3. DISCUSSION

Here we studied how matrix porosity and cell motility parameters together determine tumor invasion by quantitative analysis of 3D spheroid invasion in collagen based hydrogels. We found that matrix confinement and cell motility have distinct effects on the initiation of invasion and the subsequent rate of spheroid expansion rate. Matrix confinement and the vimentin expression level of the cells were the main determinants

of the onset time of invasion. Larger pores and higher vimentin expression levels promoted the onset of spheroid invasion. By contrast, the spheroid expansion rates were rather insensitive to changes in matrix confinement except in dense GelMA gels, which completely blocked invasion. The insensitivity of the expansion rate to pore size could potentially be due to cell-mediated matrix remodeling, which may facilitate cell invasion by providing empty space or guiding collagen bundles. The spheroid expansion rate did depend on the MMP1 expression level, suggesting that MMP-mediated matrix degradation aids cell migration and/or cell survival into the matrix. Recent studies have explored the role of other tumor microenvironment components such as the presence of fibroblasts that showed increased proteolytic activity in 3D bio-printed breast cancer model [46]. Additionally, signaling pathways originating from mechanotransduction events revealed a distinct 3D EMT gene signature characterized by extracellular matrix remodelling in 3D culture using collagen and GelMA based hydrogels [47]. It will be interesting in future studies to analyse the roles of different matrix remodelling mechanisms, including matrix degradation, matrix deposition, matrix crosslinking, and active remodeling by actomyosin-based traction forces. Although matrix stiffness is often described as a factor that influences cell invasion [40, 48], the invasion measurements in our assays did not demonstrate any clear dependence on hydrogel stiffness. It may be that the initial stiffness of the hydrogels, which we measured by rheology, does not impact the onset of invasion, and that matrix stiffness is altered through matrix remodelling in later stages. Spheroids and invading single cells are known to generate traction forces onto matrices that induce stiffening, while degradation can soften the ECM [49]. Viscoelasticity of matrices is also known to affect collective strand formation and EMT processes [50]. In our hydrogel characterization, measurements of the viscoelasticity of the matrices showed G' > G", indicating that the hydrogels were solid-like.

Previous studies of spheroid invasion for MCF-10A and MDA-MB-231 breast cancer cells showed that spheroids can undergo unjamming transitions that depend on cell motility and matrix density [7, 18]. Jammed spheroids do not invade and are considered to be in a solid-like state. Spheroids can unjam to a fluid-like state characterized by collectively invading cell strands or to a gas-like state characterized by dissociation of cells that then migrate individually [17]. In addition to these clearly distinct phases, spheroids can also exist in transitional or in-between phases [18, 51]. To test whether this unjamming framework also applies to MV3 and A549 spheroids, we classified the spheroids as solid-like, fluid-like or gas-like based on the morphological appearance of the spheroids at the end point of the experiments (t = 24 hrs for MV3 spheroids, t = 72 hrs for A549 spheroids). Since fluid-like spheroid states are characterized by multicellular strands protruding into the matrix, we developed an image analysis method to detect multicellular protrusions and measure their length (Fig. 4.23). We classified spheroids as fluid-like when the average protrusion length was above 25 µm. We chose this cut-off value since spheroids in their initial state at t = 0 occasionally showed apparent protrusions up to this length. Since gas-like spheroid states are characterized by dissociated individually migrating cells, we furthermore measured the number of dissociated cells for all the spheroids. We classified spheroids as gas-like when the individual cell count was above 10. Spheroids with protrusion lengths below 25 µm and no disseminated cells were classified as solid-like. We found that MV3 spheroids sometimes

showed co-existence between a liquid-like phase (with long multicellular protrusions) and a gas-like phase (with many dissociated cells), especially in collagen (8 mg/mL) and GelMA (30 mg/mL) (Fig. 4.24) in control condition. However, when MV3 spheroids were treated with MMP-inhibitor in collagen (8 mg/mL) and GelMA (30 mg/mL), spheroids only existed in a liquid-like phase (cell count below 10) (Fig. 4.25). Similar analysis was performed for A549 spheroids in control and treated (TGF-β and MMP-inhibitor) conditions to determine the different phase transitions in collagen and GelMA hydrogels (Fig. 4.26).

We then constructed a phase diagram of the 3D spheroid invasion states in terms of the degree of matrix confinement (pore size) and the MMP1 expression level of the cells (Fig. 4.7). Spheroids in matrices with high confinement (small pores) and low cellular MMP1 levels showed solid-like behaviour (blue squares). With increasing MMP1 expression levels, spheroids in collagen (2.4 mg/mL and 8 mg/mL) and GelMA (30 mg/mL) unjammed, initially to a liquid-like state (red squares), and eventually to a gas-like state (yellow squares). Spheroids in GelMA (50 mg/mL) remained solid-like irrespective of the MMP1 expression level. The unjamming phase diagram is qualitatively very similar to earlier unjamming phase diagrams reported for breast cancer cells [7, 18]. However, instead of the 'cell motility' parameter used in earlier studies, we find that the MMP1 expression level is an important determinant of spheroid invasion. The MMP1 expression level depends on cell type (being higher in the mesenchymal-like MV3 cells than in the epithelial-like A549 cells) and it can be tuned in both cell types through TGF-β and MMP-inhibitor treatments, which change the levels of MMP1 and other EMT-markers (vimentin and E-cadherin). Because unjamming transitions and EMT both describe the behaviour of immotile multicellular structures that gain motility, the question has been raised in what way these two processes are related [52]. In epithelial monolayers, it was shown that unjamming transitions can operate without EMT [53]. Our findings suggest that in 3D tumoroid invasion, MMP1 plays an important role among many EMT factors and is coupled to unjamming because the transition to a more mesenchymal state enables cells to proteolytically degrade the matrix and thus reduce confinement. To establish a complete link between EMT and unjamming behavior of tumors, we propose future experiments that includes modulation of other EMT dependent factors such as SNAI1, ZEB1 etc. Moreover, these experiments could be further strengthened by the use of cancer cell lines that shows a complete EMT. Compared to previous experimental studies of spheroid unjamming, which used only collagen gels, we achieved stronger confinement by additionally using GelMA gels with nanometric pores. This allowed us to identify a new regime in the phase diagram where cells that are in principle highly motile (with high MMP1 and vimentin levels) undergo a jamming transition and turn solid-like again. Moreover, MV3 cells under control and TGF-β-treated conditions in 30 mg/mL GelMA often showed amoeboid-like behaviour, characterized by cells migrating with a round morphology and blebbing (see Fig. 4.7, orange square). This behavior suggests the presence of a fourth (or transitional) spheroid phase, in which high matrix confinement pushes highly motile cells towards an amoeboid migration mode before jamming. This behaviour is consistent with described mesenchymal-to-amoeboid transitions of (cancer) cells in response to highly confining microchannels [54, 55] and micropatterns [14]. Moreover, a recent study reported that human melanoma cells in dense microenvi-

ronments migrate via bleb-driven degradation of extracellular matrix components and does not follow the conventional proteolytic degradation[56]. It will be interesting to further explore this tentative amoeboid-like migration phase for high confinement and high cell motility in more detail with high-resolution microscopy and carefully tuned GelMA concentrations just below and above 30 mg/mL.

Our data are suggestive that TGF-β stimulation may drive spheroid unjamming by upregulating the expression level of MMP1. However, we acknowledge that the TGF-β pathway has pleiotropic effects and controls many other cellular characteristics [57]. For instance, TGF-β has been reported to affect cell-matrix adhesions by downregulating integrins [58] and to induce cellular traction forces during cell invasion [59, 60]. Confocal reflection microscopy images of MV3 spheroids in collagen (2.4 mg/mL) at the endpoint of invasion experiments (t = 24 hrs) indeed indicated that TGF-β treatment not only enhanced matrix degradation, but also activated cellular traction forces as evidenced by densified and aligned collagen fibers (Fig. 4.27). We note that the collagen images also revealed that the MV3 spheroids exerted larger traction forces on the matrix than A549 spheroids, as indicated by radially oriented collagen fibers around the MV3 spheroids as opposed to more uniform collagen networks around A549 spheroids [61]. These differences in the mechanical cell-matrix interplay could also have impacted the invasion, as tensile forces on collagen are known to influence the onset of invasion [62]. To our surprise, MMP inhibition in the epithelial-like A549 cells resulted in reduced E-cadherin levels compared to control conditions. Because E-cadherin levels can also be affected by compressive forces in 2D [63], we validated that the effects of the TGF-β and Batimastat treatments on E-cadherin levels were similar in the 3D spheroid invasion assays by analysing E-cadherin levels of 3D spheroid invasion assays with Western Blot (Fig. 4.29). As the E-cadherin levels have similar trends in 2D and 3D in response to the treatments, we show that these effects were not determined by compressive forces and/or cell-matrix interactions, but are the effects of the treatments. MMPs, including MMP1 and MMP2, have been shown to induce EMT by regulating E-cadherin levels [64–66]. Several MMPs are associated with E-cadherin cleavage and the soluble E-cadherin extracellular domain that results from cleavage was found to promote cancer invasion by in turn increasing MMP production [65, 67]. MMP-mediated E-cadherin cleavage is also found downstream of TGF-β activation, providing a pathway for reduced E-cadherin levels in TGF-β-treated A549. However, the downregulation of E-cadherin levels in response to MMP inhibition was unexpected, and to the best of our knowledge an effect that has not previously been reported. We propose this effect could be an interesting direction for future research to further elucidate the mechanisms behind MMP inhibitors, which so far failed in the clinic for cancer treatments [65].

In this work, we did not distinguish between invasion by cell migration versus cell proliferation. Proliferation could play a role in setting the onset time for invasion, as proliferation can increase spheroid packing densities and increase the active forces of cells that regulate solid-to-liquid transitions [68]. Furthermore, the initiation of invasion has been linked to solid tumor growth [69]. Tumor proliferation and invasion are interconnected processes and changes in proliferation could have impacted the normalized spheroid radius over time [70]. To improve our understanding of the contribution of proliferation in invasion, follow-up studies could measure proliferation rates or prolifer-

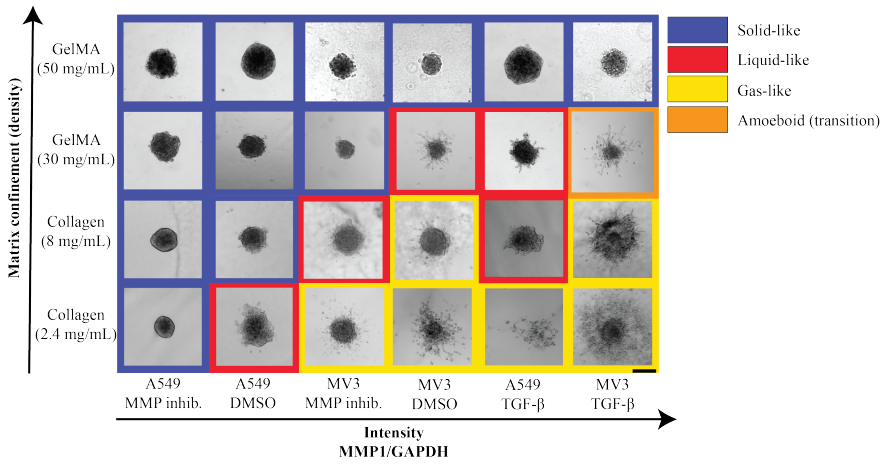

Figure 4.7: **Phase diagram describing (un)jamming transitions of MV3 and A549 cell spheroids in terms of the degree of matrix confinement (which depends on matrix type and concentration) and MMP1 expression level (which depends on cell type and treatment condition).** Images were ranked along the x-axis by the MMP1 expression level as quantified by Western blot analysis. Spheroids were classified as gas-like (yellow squares) when more than 10 cells dissociated from the spheroid during the experimental time window, liquid-like (red squares) when the spheroids developed protrusions longer than 25 µm, and solid-like (blue squares) otherwise. Amoeboid behavior (transitional phase) is shown in orange square for MV3 spheroids in GelMA (30 mg/mL). Images are bright-field images taken at t=24 hrs (MV3) and t=72 hrs (A549). Scale: 200 µm

ation could be blocked by adding chemical agents or cell synchronization [71], although these agents might cause undesired effects on the cells, e.g. by causing replication stress or increased cell death [72].

While jamming-unjamming transitions have become a well-established framework to explain cancer invasion, the underlying biological mechanisms are poorly understood. Recent studies have revealed possible mechanisms that impact plasticity pathways such as the ERK1/2 pathway, which triggers cell motility and results in collective invasive strands [16], and a mechanosensitive pathway, in which cellular confinement directly causes deformations of the cell nuclei accompanied by chromatin remodelling [73]. Here we showed evidence that EMT is also a mechanism involved in 3D unjamming transitions by regulating cell-matrix interplay. This is in line with earlier findings that reported EMT-independent unjamming transitions in 2D monolayers [53]. Our findings demonstrate that the vimentin expression level impacts the onset time of spheroid unjamming, while the MMP1 expression level impacts the subsequent spheroid expansion rate and associated unjamming transitions. Understanding the biological mechanisms

behind unjamming transitions is beneficial for cancer patients, as unjamming is considered a predictor for distant metastasis [74].

4.4. METHODS

4.4.1. CELL CULTURE

MV3 human melanoma cells that were three times xenografted in nude mice and selected for highly-metastatic behaviour (a kind gift from Peter Friedl), were cultured in DMEM-F12 (Dulbecco's Modified Eagle Medium, Thermo Scientific) supplemented with 10% Fetal Bovine Serum (FBS, Thermo Fisher) and 1% penicillin/streptomycin (Thermo Fisher). A549 human lung adenocarcinoma cells (CCL_185, ATCC) were cultured in DMEM (Gibco, #41965039), and supplemented with 10% FBS (Gibco) and 1% Antibiotic-Antimycotic solution (Gibco). All cells were incubated at 37°C and 5% CO_2, passaged at 80-90% confluency, and sub-cultured 2-3 times per week.

4.4.2. SPHEROID FORMATION

Spheroids were grown in a commercially available Corning^{TM} Elplasia^{TM} 96-well plate for high-throughput spheroid production. These well plates are round-bottom with an Ultra-Low Attachment (ULA) surface that prevents cell-surface attachment and promotes cell-cell adhesion. We used an initial seeding density of 40 x 10^3 cells (500 cells per microwell) for each well to produce 79 spheroids. Spheroids were ready to use after 4 days of culture in the wells and had an average diameter of approximately 200 ±30 µm for both cell lines (Fig. 4.28). We restricted the spheroid diameter to less than 250 µm to avoid a necrotic core.

4.4.3. HYDROGEL PREPARATION

Bovine hide collagen type I (purity ≥ 99.9%, Advanced Biomatrix) stock solutions (3 mg/ml and 10 mg/ml) were used to prepare 2.4 mg/ml and 8 mg/ml collagen gels, respectively. The collagen was made isotonic by adding 12.5 v/v% of 10x Phosphate Buffered Saline (PBS, Thermo Fisher) to collagen. In addition, 0.1 M sodium hydroxide was added to bring the pH to 7.4. All solutions were kept on ice. Pre-cooled Milli-Q (MQ) was added to bring the final collagen concentration to either 2.4 or 8 mg/mL. Final collagen dilutions were vortexed for 30 seconds and polymerized at 37°C in an µ-slide 8-well (Ibidi) for at least 45 minutes. Gelatin methacryloyl (GelMA) was purchased from Sigma Aldrich (300g bloom, 60% degree substitution). GelMA retains the thermo-reversibility of gelatin [75], but the methacrylic anhydride groups can undergo covalent cross-linking under UV light (365 nm) in the presence of a photoinitiator. We used 3 and 5wt% GelMA was used in experiments, with a 1:16 mass ratio of photoiniator (Lithium phenyl-2,4,6- trimethylbenzoylphosphinate, LAP; Sigma Aldrich). LAP and GelMA were dissolved together in Dulbecco's Phosphate Buffered Saline (DPBS; Gibco) at 37°C in a water bath for about 2 hours. The hydrogel was crosslinked using a UV-lamp (Spectroline, Serial no. 1832066) at a wavelength of 365 nm for 45 seconds.

4.4.4. 3D INVASION ASSAYS

Spheroids were embedded in collagen gels by a sandwich protocol, adapted from [76]. First, collagen gel layers of 80 µL were polymerized in µ-Slide 8 well chambers (ibidi) for 45 minutes at 37°C. Next, spheroids were transferred from the culture plate onto the collagen layers by carefully pipetting them in culture medium. Spheroids were incubated on the collagen gel for 30 minutes to ensure attachment. Next, culture medium was pipetted out of the chambers and collagen layers of 100 µL were added on top of the spheroids and polymerized for 45 minutes at 3°C. After polymerization, 200 µL of cell culture medium was added to the spheroid-collagen gels, which were then incubated at 37°C and 5% CO_2. For spheroids embedded in GelMA, we pipetted 125 µL of GelMA/spheroid suspension in a well of the µ-Slide 8-well chambers (ibidi). We then exposed the µ-Slide to 45 seconds of UV-light (365 nm) using a lamp, followed by addition of 200 µL culture medium.
Recombinant TGF-β was obtained from the lab of Peter ten Dijke, LUMC (stock concentration 5 µg/mL) and was diluted in culture medium to a final concentration of 10 ng/mL [77, 78]. Batimastat (BB-94) broad spectrum MMP-inhibitor (stock concentration 1 mM) was purchased from Abcam that was diluted to 30 µM in culture medium [79]. The supplemented media were added to the respective ibidi wells with spheroids embedded in hydrogels before incubation and imaging. Any cancer spheroids that made contact with the glass substrate or the side walls of the µ-Slide (ibidi) were excluded from analysis. Spheroid invasion was monitored using a Colibri Axio Observer 7 inverted microscope under bright-field settings with a 5x/NA 0.16 air objective for time-lapse imaging (multiple positions) at a time interval of 1 hr. MV3 spheroid invasion imaging was restricted to 24 hrs, while A549 spheroid invasion was imaged until 72 hrs. All experiments were conducted at 37°C, 90% humidity and 5% CO_2 using a stage top incubator (ibidi).

4.4.5. RHEOLOGY

Shear rheology of hydrogels was performed on a Kinexus pro+ rheometer (Malvern, UK), using a 20 mm stainless steel parallel plate and 0.5 mm gap. The collagen samples were pipetted on the bottom plate, which was held at 4°C using a Peltier system, the top plate was immediately lowered, and the temperature was set at 37°C to induce collagen polymerization. The GelMA samples were pipetted on the bottom plate at 37°C and were crosslinked using a UV lamp (Spectroline, Serial no. 1832066) for 45 seconds at 365 nm wavelength at a fixed distance of 2 cm from the sample. Immediately after crosslinking, the top plate was lowered. Mineral oil was added around the sample edge to prevent solvent evaporation. During and after polymerization, small amplitude oscillatory shear was applied to the hydrogels with a constant strain amplitude (0.5%) and frequency (1Hz) to measure the storage modulus (G') and loss modulus (G'').

4.4.6. IMAGE AND DATA ANALYSIS FOR 3D INVASION ASSAYS

We developed a custom-made MATLAB script to detect the spheroid boundary and disseminated single cells in bright-field time-lapse image series of invading spheroids. We first adjusted the image brightness and contrast using the MATLAB command 'imsharpen'. We then created a binary gradient mask by adjusting the image segmentation threshold to detect discontinuities in brightness using the derivative of a Gaussian filter. This

threshold value was optimized for each set of bright-field images. The binary gradient mask outlined the identified object, which was then post-processed to smoothen and dilate using the MATLAB command 'imdilate'. This dilated gradient mask finally underwent the 'fill hole' process using the MATLAB command 'imfill'. The spheroid boundary (outlined in red in Fig. 4.16) was detected by MATLAB command 'bwboundaries' that identifies exterior boundaries. From the boundary, we calculated the spheroid area and effective circular radius. To account for variations in initial spheroid size, we normalized the effective circular radius by its initial value at t=0. Single dissociated cells were identified with the same threshold parameters (highlighted in green in Fig. 4.16). In case individual cells were already present at t=0 (see Fig.4.16A), we subtracted these from the cell count at the end of the assay (24 hrs for MV3, 72 hrs for A549). Note that the cell counts likely underestimate the actual cell number since the limited contrast of the images made it difficult to distinguish whether cells close to the spheroid boundary had dissociated.

To identify multicellular protrusions of MV3 and A549 spheroids and determine their lengths, we developed another MATLAB script. First we converted 2D bright-field images from the Cartesian coordinate system (x,y) to a polar coordinate system (θ, r). Next we detect protrusions as peaks relative to the average spheroid radius(highlighted in cyan, see Fig. 4.23C, D). The protrusion length analysis was performed on images obtained at the end time point of each experiment (t=24 hrs for MV3, t=72 hrs for A549). The average protrusion length was used as a criterion to distinguish between a solid-like phase (length below 25 µm) versus a liquid-like state (length above 25 µm).

4.4.7. WESTERN BLOT ANALYSIS

For 2D Western Blot, bovine type I collagen (Procol, Advanced Biomatrix, 3 mg/ml) was diluted 1:100 with MilliQ water and pipetted into six-well plates (Thermo Fisher) to cover the surface and left to incubate for 2 hours at room temperature. The collagen coatings were washed twice with PBS. Next, MV3 cells (300,000/well) and A549 cells (400,000/well) were seeded in the coated plates and in uncoated plates in culture medium under control conditions (2 µL/mL DMSO) or with recombinant TGF-β (10 ng/µL) or Batimastat (30 µM, BB-94/Abcam). After 48 hrs, cells were washed with PBS, lysed with cold radioimmunoprecipitation buffer (RIPA, 100 µL/well, Thermo Fisher) and transferred to Eppendorf tubes. Lysed samples were agitated at 4°C for 30 minutes and stored at -20°C. For 3D spheroid invasion Western Blot, 3D invasion assays were made as described above with n=4 and incubated for 72 hrs at 37°C and 5% CO_2. After 72 hrs, collagen gels were removed from the wells with a spatula and collected in pairs in 15 mL tubes with 450 µL of PBS. For each tube, 150 µL of 80 mg/mL collagenase (C0130, Sigma Aldrich) was added and the tubes were incubated and agitated at 37°C for 3 minutes to degrade the collagen. Next, each tube was filled with 8400 µL of PBS and centrifuged for 5 minutes at 250 rcf at 4°C. Next, supernatant was removed and cell pellets were lysed in 100 µL RIPA buffer.

Laemmli buffer (2x, Bio-rad) and 4% β-mercaptoethanol (company) were added to the lysed samples, which were incubated at 95°C for 5 minutes. Sodium dodecyl sulfate-polyacrylamide gel electrophoresis (SDS-PAGE) was performed with Mini-PROTEAN TGX

gels (Bio-rad) using 100V for 1.5 hours. Western Blotting was executed with a Trans-Blot Turbo Transfer System (Bio-rad) and Trans-Blot Turbo Mini 0.2 µm PVDF Transfer Packs (Bio-rad). The membranes were blocked in 5% Bovine Serum Albumin (BSA, Thermo Fisher) in phosphate buffered saline (PBS, company) overnight. Membranes were stained with primary antibodies: rabbit anti-MMP1 (#54376, Bioke), mouse anti-MMP2 (#436000, Thermo Fisher), rabbit anti-MMP3 (#ab5915, Abcam), rabbit anti-MMP9 (#ab283575, Abcam), rabbit anti-E-cadherin (#ab40772, Abcam), mouse anti-vimentin (#ab8978, Abcam) and rabbit anti-GAPDH (#CST2118S, Bioke) in 5% BSA overnight on a shaker at 4°C. Membranes were washed thrice with 0.1% Tween (Sigma Aldrich) in PSB (PSB-T) on a shaker, and incubated for 3-5 hours with secondary antibodies: rabbit anti-mouse HRP (#ab97051, Abcam) and goat anti-rabbit HRP (#ab6728, Abcam) in PBS-T. Afterwards, membranes were washed thrice with PBS-T and imaged with an enhanced luminol-based chemiluminescent substrate kit (Thermo Fisher) on a gel imager (Bio-rad).

4.4.8. PORE SIZE AND VOID FRACTION ANALYSIS OF HYDROGELS

Collagen and GelMA hydrogels were prepared in µ-Slide 8 well chambers and were imaged by confocal reflectance on a Stellaris 8 confocal microscope (Leica), equipped with a white light laser and a hybrid detector (HyDS), using a 488 nm laser line and a 63x magnification objective (1.3 NA, glycerol immersion) at RT. We recorded Z-stacks over a total depth of 30 µm with a 2 µm step size. For the collagen networks, we used a custom-made python script [80], which implements the bubble method to measure the sizes of the pores in between collagen fibers (see Fig. 4.9). Confocal images were denoised using the total variation minimization method [81] on a slice-by-slice basis. A local threshold was then applied to obtain a binary confocal stack. The Euclidean distance map was determined, and a Gaussian filter was applied. Finally, the local maxima of the Euclidean distance map were determined, which represent the furthest distance from a fiber in the image. We selected these distances as half of the pore size. The GelMA hydrogels with their nanometric pores were too dense to be able to directly measure the pore size distribution. Instead, we performed a void fraction analysis on maximum intensity projections of confocal reflectance microscopy Z-stacks of GelMa and collagen hydrogels made in Fiji [82]. The images were adjusted for brightness and contrast by maximum intensity projection. The adjusted images were then converted to a binary image using the 'Make Binary' function in Fiji with white (1) pixels corresponding to hydrogel fibers and black (0) pixels corresponding to the voids. We determined the void fraction as the ratio of black pixels over the sum of black and white pixels.

4.4.9. GELMA HYDROGEL PERMEABILITY ANALYSIS

Permeability analysis was performed on GelMA hydrogels (30 and 50 mg/mL) to estimate their pore size. The permeability, K of a hydrogel can be obtained from Darcy's Law by estimating the flow velocity of tracer particles through the material. To do this, we used a microfluidic platform equipped with three channels, where the middle channel was filled with GelMA hydrogel and crosslinked by a UV-light source (365 nm) [78]. The top and bottom channels were operated using a pressure pump device to create a pressure gradient that drives the flow through the hydrogel channel at RT. The mi-

crofluidic chip was mounted on Zeiss Axio Observer 7 equipped with an ORCA Flash 4.0 V2 (Hamamatsu) digital camera with a resolution of 2048 × 2048 pixels. We used Rhodamine B dye (Merck Sigma) (1% v/v solution in 1X Dulbecco's Phoshate Buffer Solution from Sigma Aldrich) as a tracer particle. After applying a pressure gradient ΔP = 20 mbar, the displacement of the dye front was tracked by time-lapse imaging with a time interval of 30 seconds. Imaging was performed using 543 nm LED laser (excitation/emission: 543 nm/568nm) at 30% intensity and 1.58 seconds exposure time, and a 5x (NA 0.16/Air) objective. The images were then and converted into 8-bit color images using ImageJ [82]. A line was drawn in the direction of the flow to obtain a histogram of the fluorescence intensity as a function of distance. The fluorescence intensity is tracked by identifying the distance (pixel value × pixel length (0.62 μm) value at which the mean intensity of fluorescence is zero. This position was recorded for the next 10 consecutive images at 30 second interval. The difference between two consecutive images is divided by the time interval between images to obtain flow velocity. Averaging for each consecutive images thus gives the average flow velocity. From the measured velocity, we computed the hydraulic permeability of the GelMA hydrogels using the Darcy equation:

$$v = (\Delta P \times K)/(L \times \mu), \tag{4.1}$$

where μis the fluid velocity across the hydrogel (m/s), ΔP is the pressure gradient across the hydrogel (Pa), L is the length of the hydrogel channel in the direction of the flow (m), K is the hydraulic permeability (m^2), and μis the fluid dynamic viscosity (10^{-3} Pa.s). We recovered an average permeability of 2.36×10^{-16} m^2 for 30 mg/mL GelMA and 1.29×10^{-16} m^2 for 50 mg/mL GelMA. The corresponding pore sizes, calculated as the square root of the permeability, were 1.54 nm for 30 mg/mL GelMA and 1.14 nm for 50 mg/mL GelMA (for a detailed summary see Table 4.2).

4.5. SUPPLEMENTARY INFORMATION

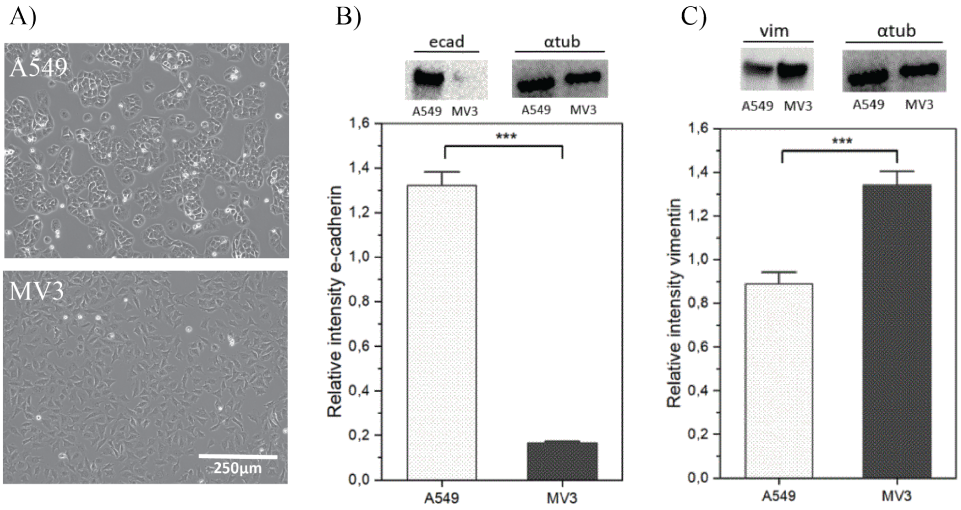

Figure 4.8: **Cell morphology and Western Blot analysis for A549 and MV3 cancer cells.** A) Bright-field images of the cells cultured in 2D. A549 cells (top panel) show clustering, which is a characteristic of cells expressing high levels of E-cadherin (epithelial marker). MV3 cells (bottom panel) show individual spindle-like cells with mesenchymal-like features. Scale bar: 250 µm. B) Western Blot analysis of A549 and MV3 cells for E-cadherin expression levels, showing that A549 cells are more epithelial-like than MV3 cells. (C) Corresponding Western Blot analysis for vimentin expression levels, showing that MV3 cells express significantly more vimentin than A549 cells.

Repeat	Average velocity	Hydraulic permeability (K, m^2)	Estimated pore size (nm)
GelMA (30 mg/mL)			
1.	0.54	2.43×10^{-16}	15.58
2.	0.51	2.29×10^{-16}	15.13
3.	0.53	2.38×10^{-16}	15.42
GelMA (50 mg/mL)			
1.	0.28	1.26×10^{-16}	11.22
2.	0.32	1.44×10^{-16}	12.00
3.	0.26	1.17×10^{-16}	10.81

Table 4.2: **Average pore size estimated from hydraulic permeability measurements for GelMA hydrogels with concentrations of 30 mg/mL (15.3 ± 0.18 nm) and 50 mg/mL (11.3 ± 0.5 nm).** The permeability was determined from the average flow velocity of Rhodamine B dye measured in permeation experiments performed in a microfluidic chip at a pressure gradient of 20 mbar.

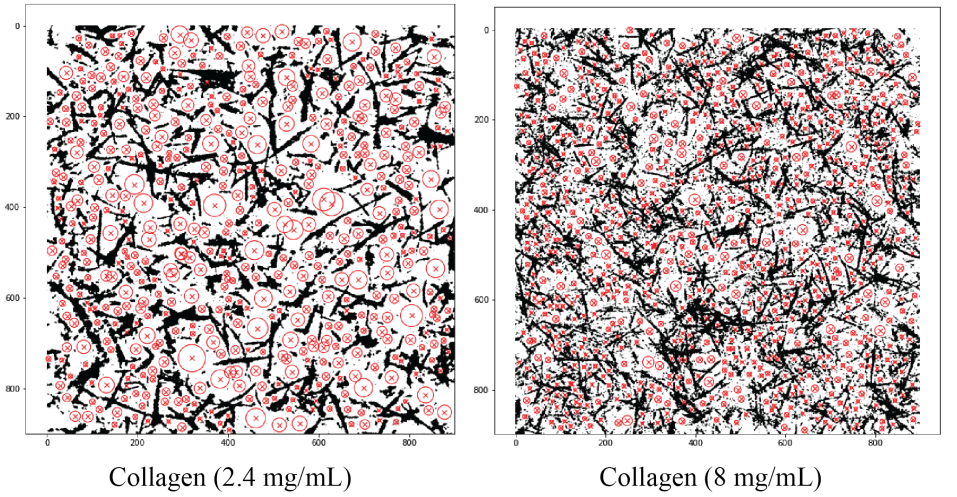

Figure 4.9: Binarized confocal microscopy reflection images of collagen networks with concentrations of 2.4 mg/mL (left) and 8 mg/mL (right) with fitted bubbles (red circles), to determine the pore size distribution. The x- and y-axes indicate the length scale in pixels.

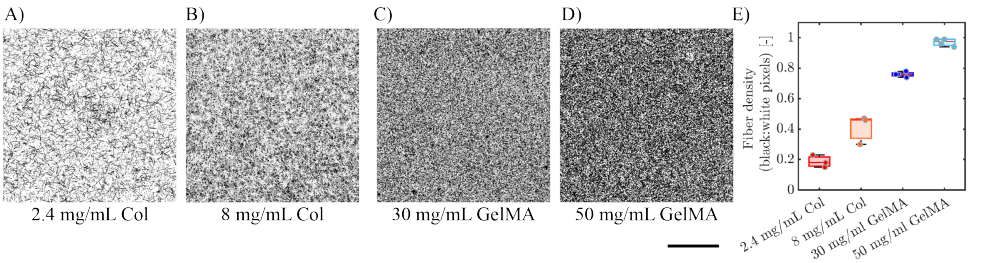

Figure 4.10: **Hydrogel fiber density measurements based on confocal reflectance images.** Binarized maximum intensity projections of confocal Z-stacks composed of 11 slices at 2 µm intervals for hydrogels of A) collagen (2.4 mg/mL), B) collagen (8.0 mg/mL), C) GelMA (30 mg/mL)< and D) GelMA (70 mg/mL). E) Fiber density (black to white pixel ratio) measurements for hydrogels. Data are averages with standard deviations for 3 repeats. Scale bar: 25 µm.

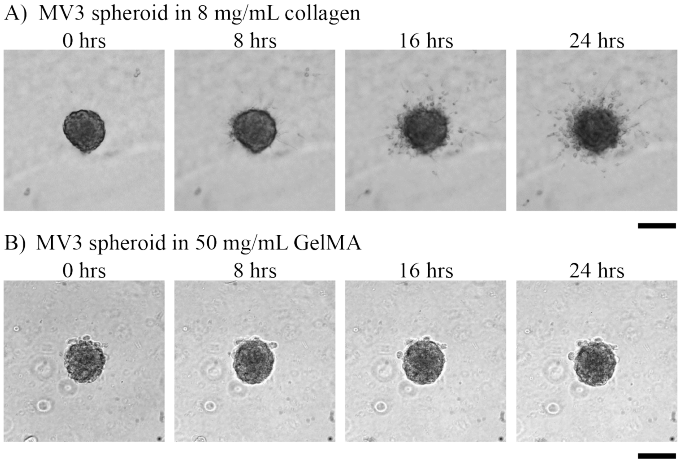

Figure 4.11: **MV3 spheroid invasion in collagen and GelMA matrices.** Bright-field images of MV3 spheroids at 8 hr time intervals in A) 8 mg/mL collagen and (B) 50 mg/mL GelMA at t=0, 8, 16 and 24 hrs. Scale bars: 200 µm. MV3 spheroids invaded into the collagen network, as seen from the spheroid protrusions and presence of disseminated single cells, but did not invade in GelMA hydrogel.

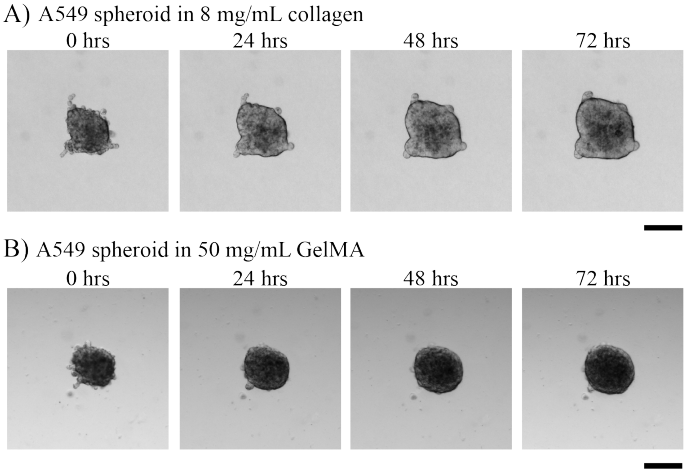

Figure 4.12: **A549 spheroid invasion in collagen and GelMA matrices.** Bright-field images of A549 spheroids at 24 hr time intervals in A) 8 mg/mL collagen and (B) 50 mg/mL GelMA. Scale bars: 200 µm. The A549 spheroids had an irregular shape with occasional protrusions. Over time, the spheroid boundary remained rather smooth and the spheroids uniformly expanded in size without the formation of protrusions or dissociation of single cells.

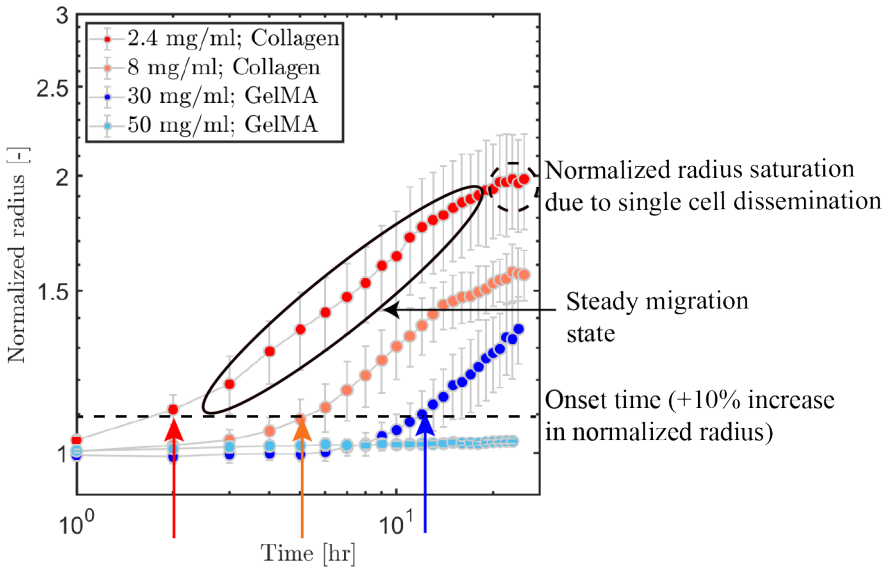

Figure 4.13: **Definition of invasion onset time and spheroid expansion, illustrated for MV3 spheroids.** The effective circular radius of MV3 spheroids normalized by its initial value is tracked as a function of time for spheroids in collagen and GelMA hydrogels (see legend). The invasion onset time is defined as the time point where the normalized radius reaches a value of 1.1 (indicated by the arrows and the horizontal dashed line). The expansion rate was defined as the power-law slope of the spheroid growth curves after the onset of invasion. Since the growth curves plateaued at long time due to the dissociation of cells from the spheroid (dashed circle), the curves were fitted within the time range enclosed within the solid ellipse. The maximum time for the fit range was taken as the time point where the difference in normalized spheroid radius became less than 0.01 between two successive time points.

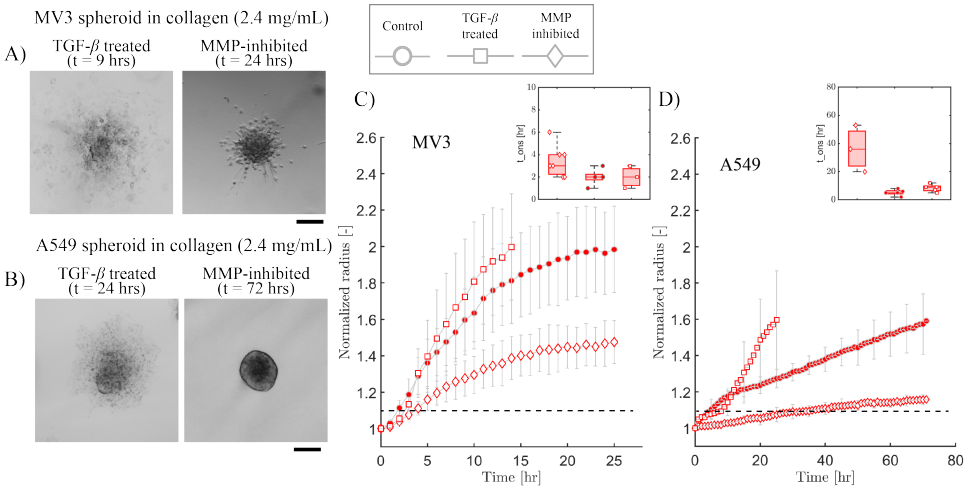

Figure 4.14: **Effect of TGF-β and MMP-inhibitor treatments on spheroid invasion in collagen (2.4 mg/mL).** A) Bright field images of MV3 spheroids treated with TGF-β (left, t=9 hrs) and with MMP-inhibitor (right, t=24 hrs). B) Bright field images of A549 spheroids treated with TGF-β (left, t=24 hrs) and MMP-inhibitor (right, t=72 hrs). Scale bars in A,B: 200 µm. C) Increase in spheroid radius with time for MV3 spheroids under control, TGF-β, and MMP inhibition conditions (see legend). D) Corresponding data for A549 spheroids. Horizontal dashed lines in C,D denote the threshold value for the normalized radius of 1.1 defined as the onset of invasion. Insets show the invasion onset times in control and treated conditions. Neither treatment affected the onset time of invasion much, except for MMP-inhibited A549 spheroids, where invasion was drastically delayed. Note that upon TGF-β treatment, the spheroid cores eventually disintegrated and sedimented to the bottom glass surface. In this condition we therefore only tracked invasion up to t=14 hrs for MV3 spheroids and up to t=24 hrs for A549 spheroids.

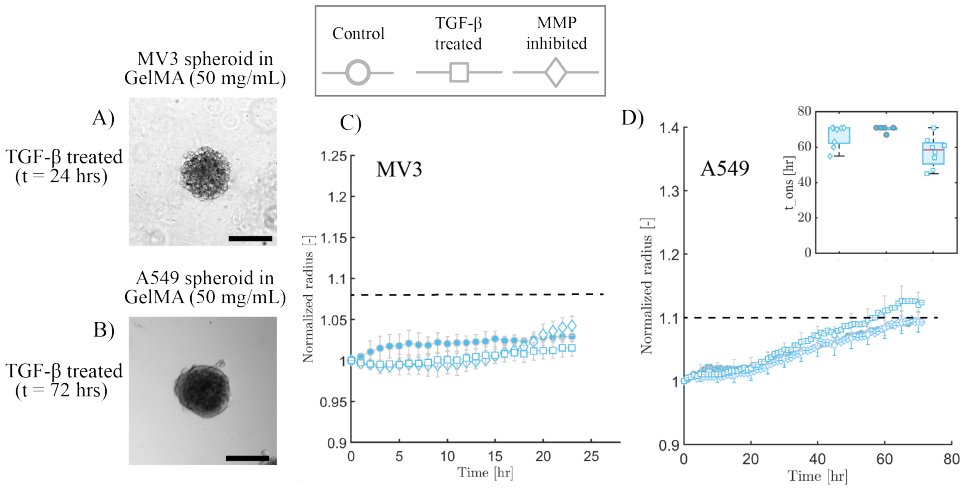

Figure 4.15: **Effect of TGF-β and MMP-inhibitor treatments on spheroid invasion in GelMA (50 mg/mL).** A) Bright field image of a MV3 spheroid treated with TGF-β at t=24 hrs. B) Bright field image of an A549 spheroid treated with TGF-β at t=72 hrs. Neither the MV3 nor the A549 spheroids showed protrusions or single cell dissemination, despite the TGF-β treatment. Scale bars in A, B: 200 µm. (C) Increase in spheroid radius with time in control, TGF-β treated and MMP-inhibited conditions (see legend on top) for C) MV3 spheroids and D) A549 spheroids. Horizontal dashed lines in C,D denote the threshold value for the normalized radius of 1.1 defined as the onset of invasion. Inset in D: onset time of invasion for A549 spheroids. TGF-β treated A549 spheroids had a slightly lower onset time (at t=57 hrs) compared to control and MMP-inhibited conditions (at t=68 hrs). Note that we could not determine the onset of invasion for the MV3 spheroids over the 24 hrs experimental time frame.

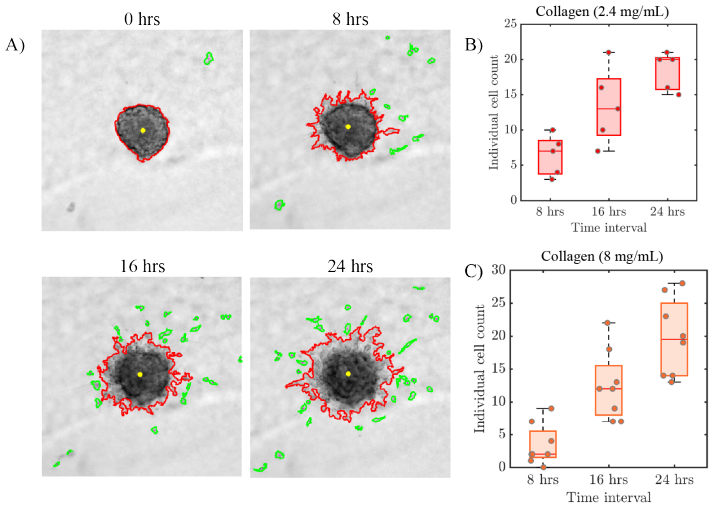

Figure 4.16: **Quantification of cell dissociation from MV3 spheroids in collagen matrices.** A) Bright-field images of MV3 spheroids in collagen (8 mg/mL) at 8 hr time intervals. The spheroid border is outlined in red while dissociated cells are outlined in green. B) Number of individual cells disseminated in 2.4 mg/mL collagen at time intervals of t=8, 16 and 24 hrs. C) Corresponding data for MV3 spheroids in 8 mg/mL collagen.

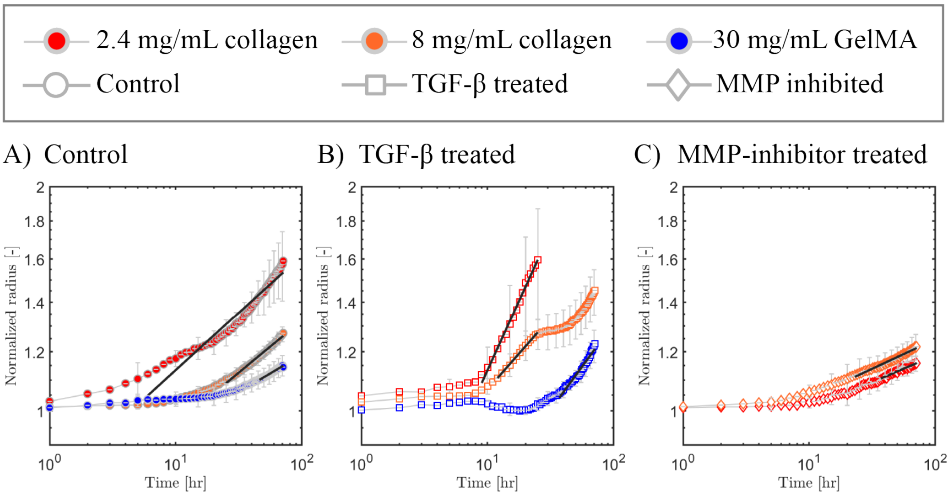

Figure 4.17: **Effect of TGF-β and MMP-inhibitor treatments on expansion rates of A549 spheroids.** Quantification of the increase in spheroid radius with time for A549 spheroids in collagen (2.4 mg/mL and 8 mg/mL) and GelMA (30 mg/mL) under A) control conditions, B) with TGF-β treatment, and (C) with MMP-inhibitor treatment. The expansion rates were determined as the power law slope of the curves after the onset of invasion. The solid black lines indicate the fits together with the temporal range.

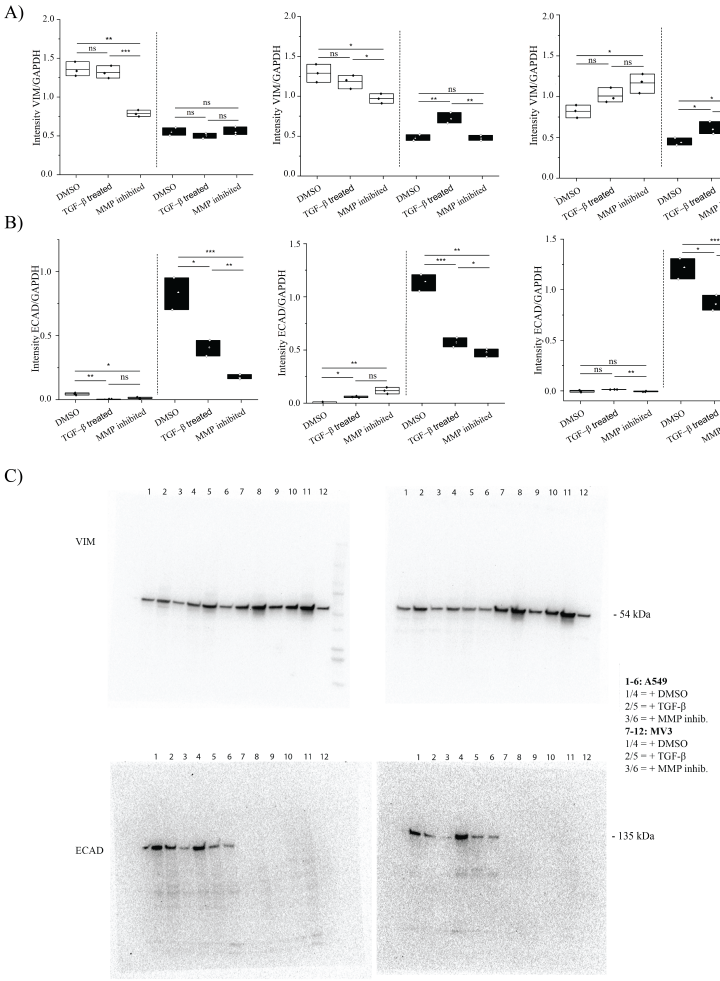

Figure 4.18: **Western Blot analysis for vimentin and E-cadherin protein expression levels in A549 and MV3 cells cultured in 2D.** We performed a total of n = 4 biological replicates for each condition (DMSO (control), TGF-β, and MMP-inhibitor treatments). One replicate of each is shown in the main text. Additional replicates are shown here. A) Three replicates showing vimentin expression levels normalized by GAPDH. B) Three replicates showing E-cadherin expression levels normalized by GAPDH. Two examples of Western Blot images are shown for C) E-cadherin and D) vimentin. The legend on the right shows the content of each lane (indicated by numbers above the gels).

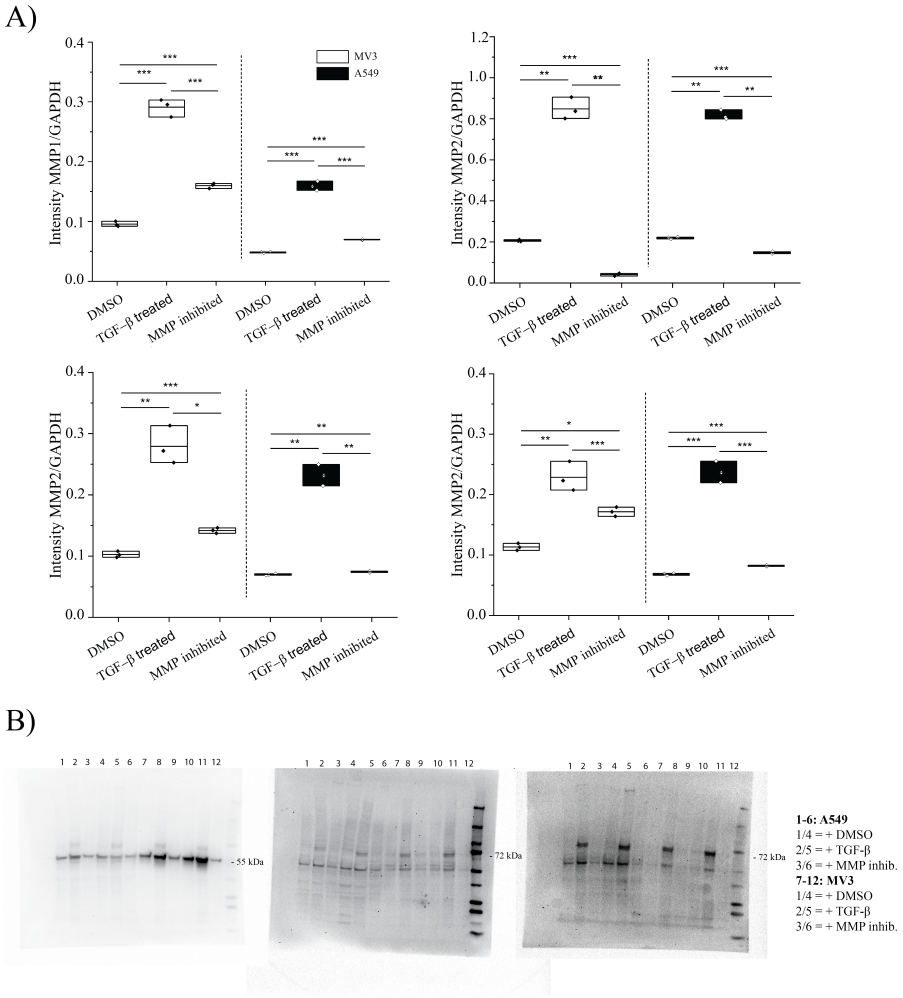

Figure 4.19: **Western Blot analysis for MMP1 and MMP2 protein expression levels in A549 and MV3 cells cultured in 2D.** We performed a total of n = 2 biological replicates for the MMP1 quantification and n = 4 for the MMP2 quantification, for different conditions: DMSO (control), TGF-β, and MMP-inhibitor treatments. One replicate of each is shown in the main text. Additional replicates are shown here. A) One replicate showing MMP1 expression levels normalized by GAPDH. B) Three replicates showing MMP2 expression levels normalized by GAPDH. C) Three examples of Western Blot images are shown for MMP1 (left) and MMP2 (middle and right). The legend on the right shows the content of each lane (indicated by numbers above the gels).

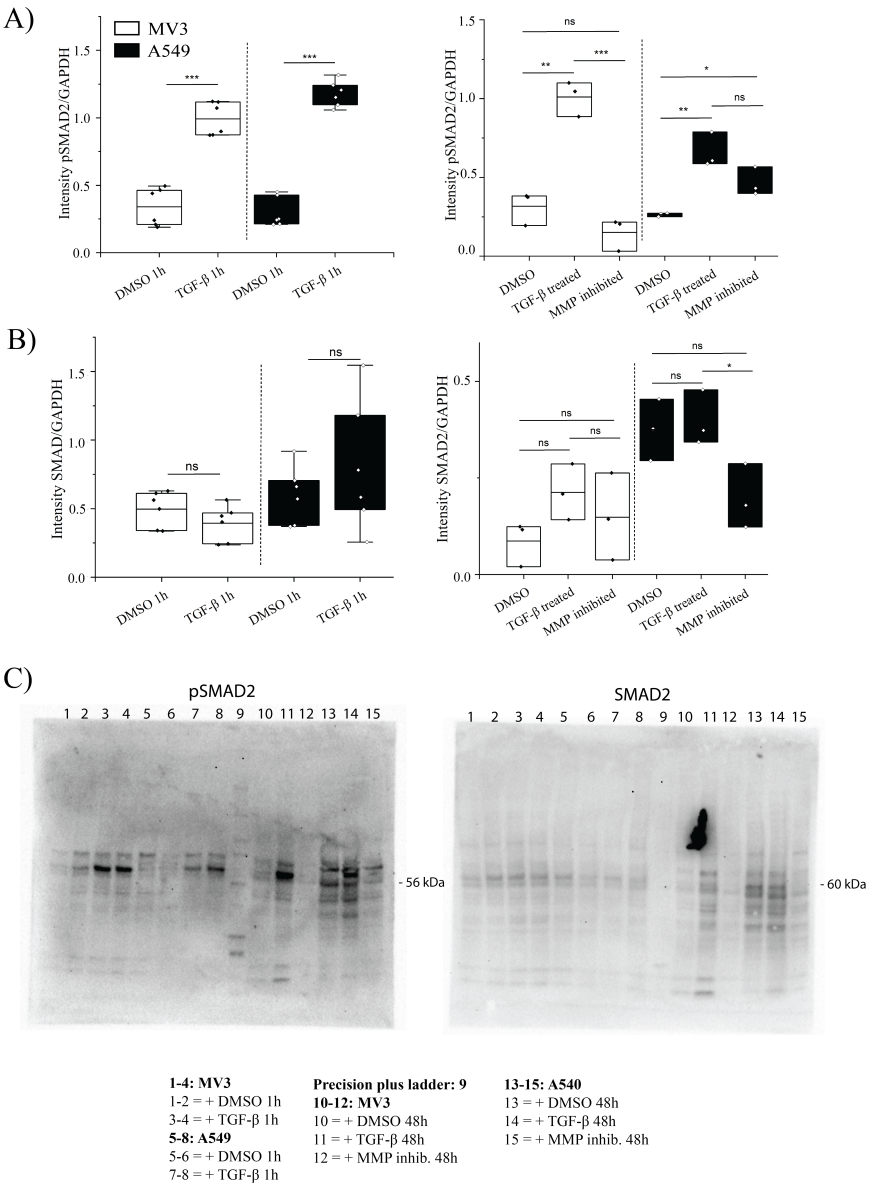

Figure 4.20: **Western Blot analysis for SMAD2 and pSMAD2 expression of MV3 and A549 cells cultured in 2D.** Left: Western Blot images for pSMAD2 (top) and SMAD2 (bottom). The legend on top shows the content of each lane (numbered on top of the gels). Protein expression levels of pSMAD2 (top) and SMAD2 (bottom) after 1 hr (middle) and 48 hrs (right)of DMSO (control, n = 2), TGF-β (n=2) of TGF-β and MMP inhibitor treatments (n=1).

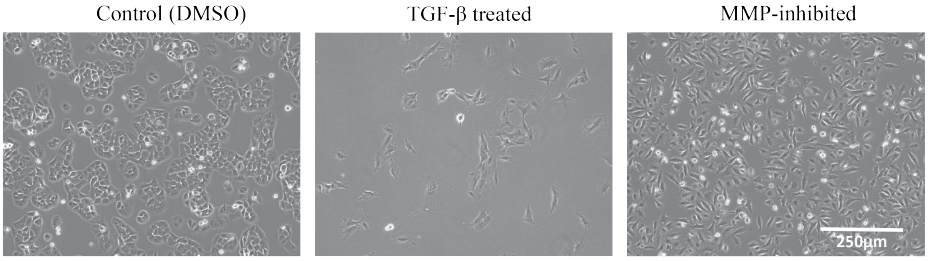

Figure 4.21: **A549 cell morphology in 2D cell culture under control (DMSO), TGF-β treated and MMP-inhibited conditions.** Bright field images were taken 2 days after seeding. Scale bar: 250 μm.

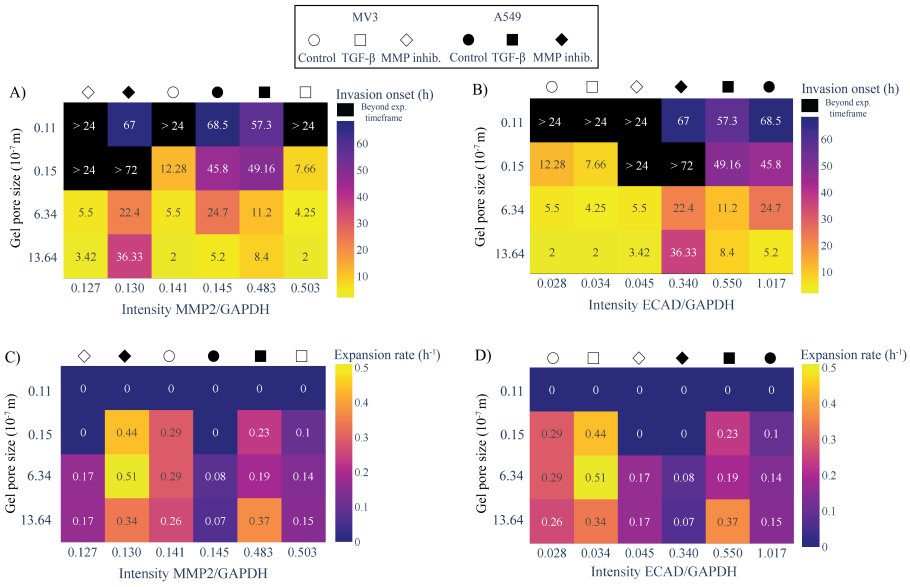

Figure 4.22: **Correlation of the invasion onset times and spheroid expansion rates with MMP2 and E-cadherin protein expression levels for MV3 and A549 spheroids.** A) Heat map showing the dependence of the invasion onset time (indicated by the number (in units of hrs) in each square and the color code, see color bar on the right) on hydrogel pore size (y-axis) and expression level of MMP2 (x-axis). B) Corresponding heat map showing the dependence of the invasion onset time on hydrogel pore size (y-axis) and expression level of E-cadherin (x-axis). Note that spheroids that did not invade during the time frame of the assay are shown in black. C) Heat map showing the dependence of the spheroid expansion rate (number (in units of hr^{-1}) in each square and color code, see color bar on the right) on hydrogel pore size (y-axis) and expression level of MMP2 (x-axis). D) Corresponding heat map showing the dependence of the spheroid expansion rate on hydrogel pore size (y-axis) and expression level of E-cadherin (x-axis). In all cases, data for MV3 and A549 spheroids were pooled and protein expression levels were normalized by GAPDH.

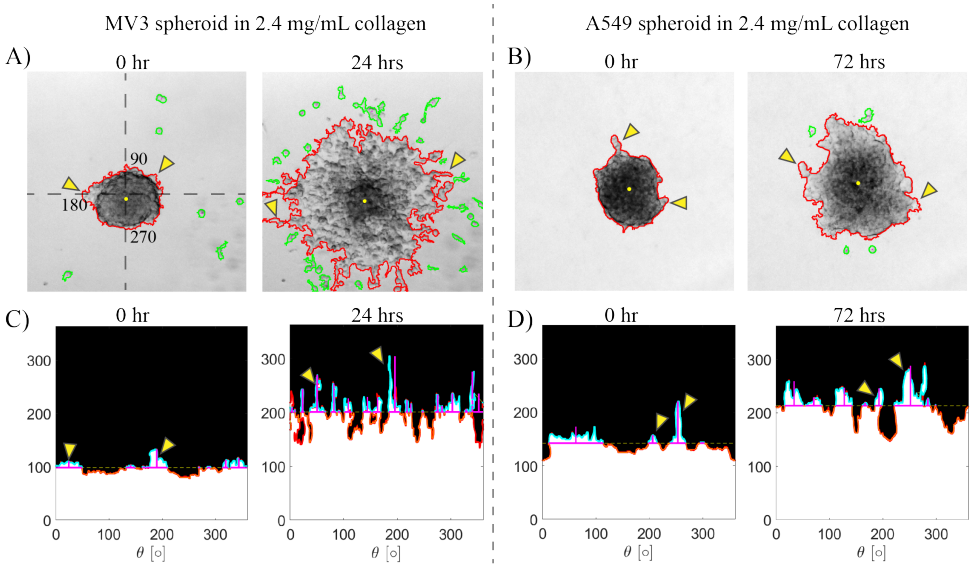

Figure 4.23: **Analysis of spheroid protrusions and single cell dissemination aimed at classifying the state (gas, fluid, liquid) of spheroids under different conditions.** A) Bright field images of a MV3 spheroid in 2.4 mg/mL collagen at t=0 (initial state) and t=24 hrs (final state). B) Bright field images of an A549 spheroids in 2.4 mg/mL collagen at t=0 hr (initial state) and t=72 hrs (final state). Spheroid boundaries are outlined in red while disseminated cells are outlined in green. The yellow arrowheads highlight examples of multicellular protrusions that grow over time. Note that both MV3 and A549 cells already showed some protrusions at t=0 hr. Additionally, the images often revealed some disseminated cells at t=0 hr. Therefore, in all cell count quantification, we subtracted the cells present at t=0 hr. C) Polar plots determined from the MV3 spheroid images in A, based on the assumption of radial symmetry. D) Corresponding polar plots for the A549 spheroid images in B. In both cases, multicellular protrusions are seen as peaks (yellow arrowheads highlight examples). The polar plots were used as a basis to detect each peak (i.e., multicellular protrusion) and quantify its maximum height relative to the average spheroid radius (horizontal red lines). Spheroids with average protrusion lengths greater than 25 μm were considered to be in a liquid-like (unjammed) state.

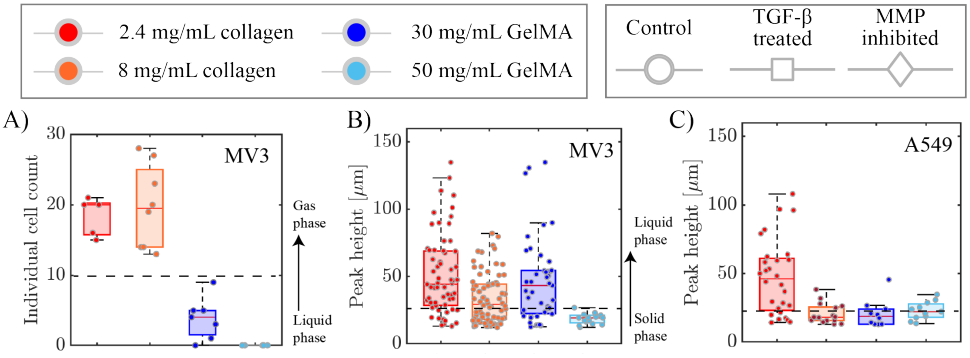

Figure 4.24: **Analysis of spheroid protrusions and single cell dissemination aimed at classifying the state (gas, fluid, liquid) of MV3 and A549 spheroids in control conditions.** A) Individual cell count analysis of MV3 spheroids in collagen (2.4 and 8 mg/mL) and in GelMA (30 and 50 mg/mL) matrices. Spheroids are considered to be in a gas-like state when the cell count is above 10 (above the horizontal dashed line) and solid-like or liquid-like when the cell count is below 10. MV3 spheroids were gas-like in collagen (2.4 and 8 mg/mL) and solid-like in GelMA (30 and 50 mg/mL GelMA). B) Protrusion lengths for MV3 spheroids. C) Protrusion lengths for A549 spheroids. Spheroids are considered liquid-like when the protrusion lengths are above 25 μm (above the dashed lines) and solid-like when the protrusion lengths are below 25 μm. MV3 spheroids were liquid-like in collagen (2.4 and 8 mg/mL) and 30 mg/mL GelMA hydrogels and solid-like in 50 mg/mL GelMA. A549 spheroids were liquid-like only in 2.4 mg/mL collagen and solid-like otherwise.

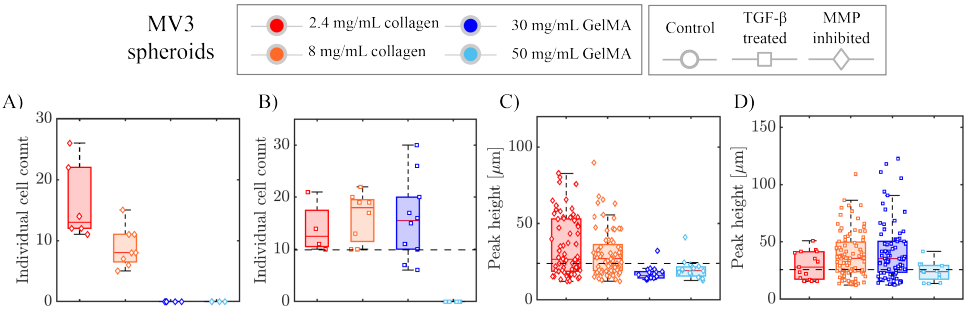

Figure 4.25: **Quantification of disseminated cells and protrusion lengths for MV3 spheroids in order to classify the state (gas, fluid, solid) of the spheroid.** A) Individual cell count analysis for MV3 spheroids treated with MMP-inhibitor in different collagen and GelMA gels (see legend on top). MMP-inhibitor treatment caused a strong (40-50%) drop in the cell count in collagen (2.4 mg/mL and 8 mg/mL) gels and blocked cell dissociation in 30 GelMA hydrogels. B) Corresponding data for MV3 cells treated with TGF-β. The dashed lines indicate the transition between a liquid/solid state (cell count below 10) and a gas state (cell count above 10). TGF-β treatment caused a large (73%) increase in cell count in 30 mg/mL GelMA compared to control conditions but did not result in any individual cell dissemination in 50 mg/mL GelMA. C) Protrusion lengths for MV3 spheroids treated with MMP-inhibitor in different collagen and GelMA gels. D) Corresponding data for MV3 spheroids treated with TGF-β. The dashed lines indicate the transition between a solid state (maximum protrusion length below 25 μm) and a liquid state (average protrusion length above 25 μm). Box plots show N = 5-10 spheroids per condition.

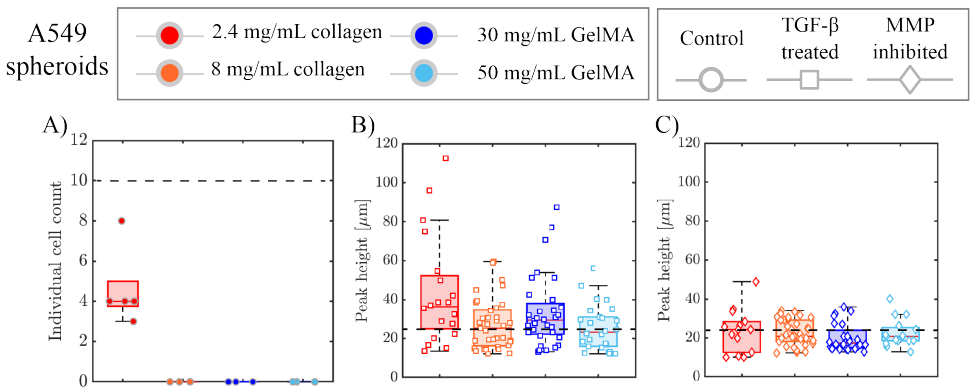

Figure 4.26: **Quantification of disseminated cells and protrusion lengths for A549 spheroids in order to classify the state (gas, fluid, solid) of the spheroid.** A) Individual cell count analysis for A549 spheroids embedded in collagen and GelMA matrices (see legend on top) in control conditions. The dashed line indicate the transition between a liquid/solid state (cell count below 10) and a gas state (cell count above 10). Under control conditions, the A549 spheroids only disseminated individual cells in 2.4 mg/mL collagen. Note that A549 spheroids embedded in 2.4 mg/mL collagen treated with TGF-β disintegrated and sedimented to the bottom, so we were unable to count the disseminated cells. At early times, however, we could observe cell dissociation, so we classify this condition as a gas-like phase. B) Protrusion lengths of A549 spheroids treated with TGF-β. A549 spheroids formed protrusions characteristic of a liquid-like state in 8 mg/mL collagen and in 30 mg/mL GelMA upon TGF-β treatment, whereas they were solid-like in control conditions. In 8 mg/mL collagen, the TGF-β-treated spheroids made shorter protrusions with an average length of 26 µm. No protrusions were observed for spheroids embedded in 50 mg/mL GelMA. C) Protrusion lengths of A549 spheroids treated with MMP-inhibitor. Upon MMP inhibition, A549 spheroids were liquid-like only in 2.4 mg/mL collagen. The dashed lines in B and C indicate the transition between a solid state (average protrusion length below 25 µm) and a liquid state (average protrusion length above 25 µm). Box plots show N = 5-10 spheroids per condition.

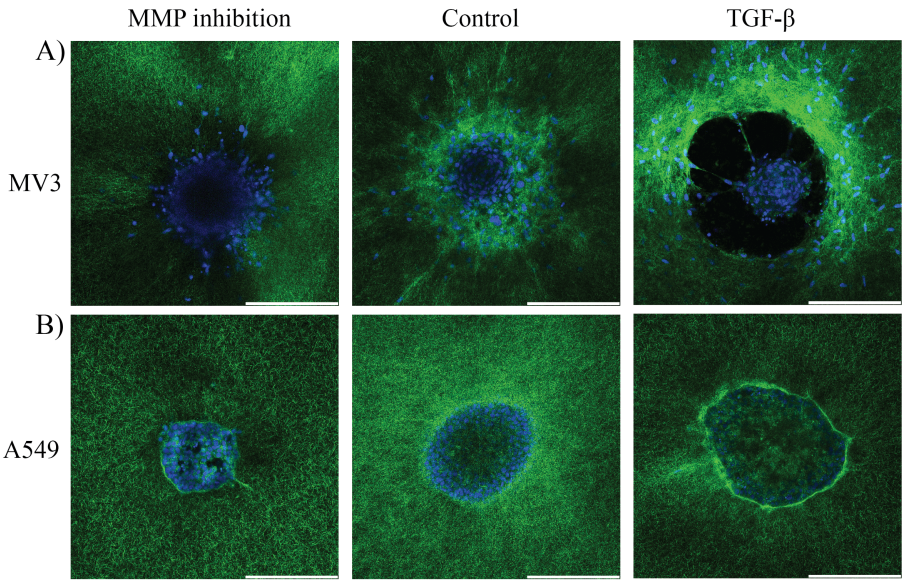

Figure 4.27: **Visualization of cell-mediated extracellular matrix remodelling for spheroids embedded in collagen (2.4 mg/mL).** Confocal images of A) MV3 and B) A549 spheroids in control conditions (middle) and with MMP-inhibition (left) or TGF-β treatment (right). Collagen fibers were imaged by reflection and are shown in green. Nuclei stained with Hoechst were imaged by fluorescence and are shown in blue. Scale bars are 250 µm. Compared to control conditions, TGF-β stimulation causes more matrix remodeling whereas MMP inhibition diminishes matrix remodeling. MV3 spheroids appear to exert higher traction forces on the collagen than A549 spheroids, as shown by radially oriented fibers around the spheroid under MMP inhibition and control conditions and extensive collagen accumulation upon TGF-β stimulation. Furthermore, the black void around the MV3 spheroid upon TGF-β stimulation is indicative of MMP-mediated matrix degradation.

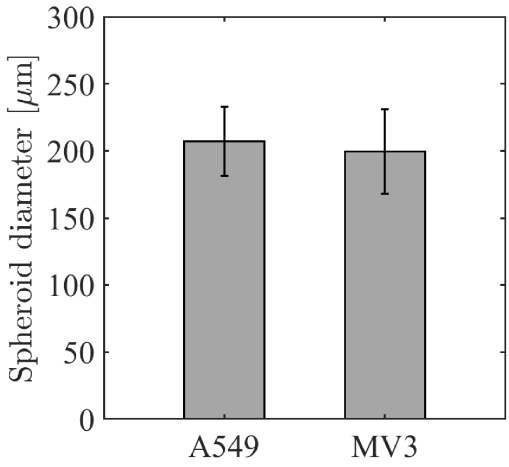

Figure 4.28: **Average diameter of MV3 (N = 80) and A549 (N = 85) spheroids at t=0 hr determined from bright field images.** The spheroids had comparable average diameters of 200±30 µm (MV3) and 207±26 µm (A549).

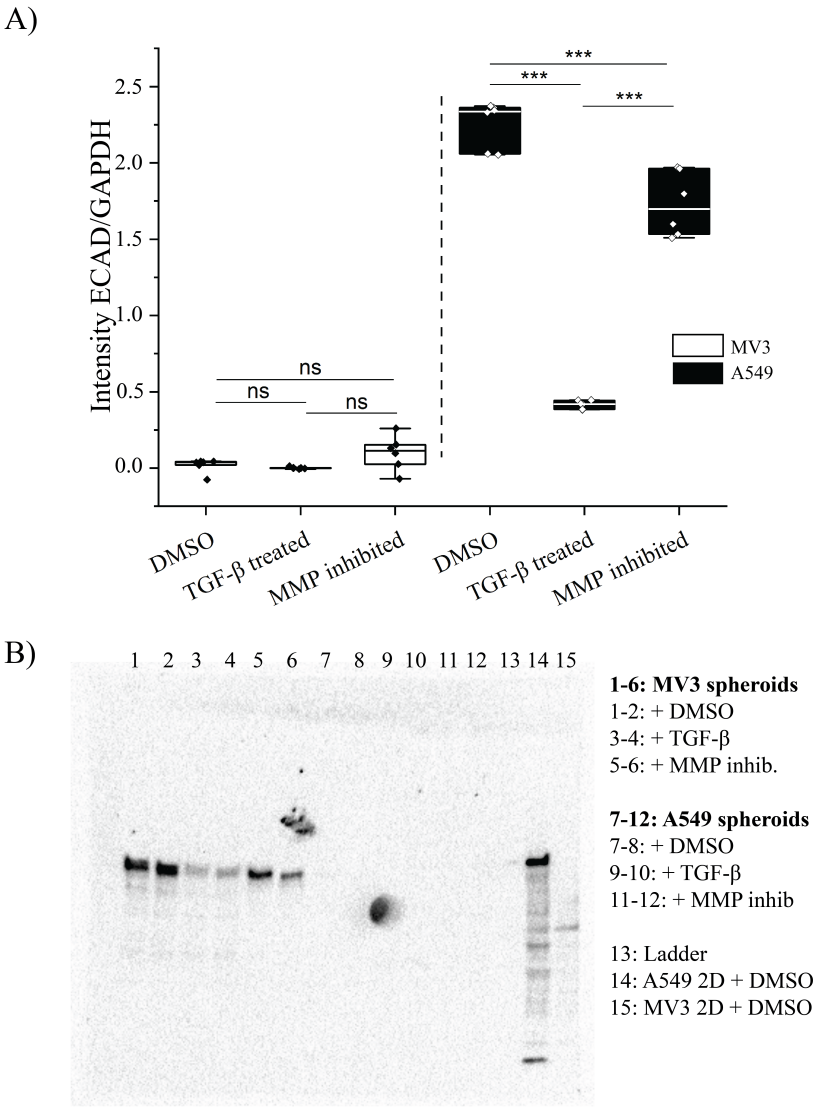

Figure 4.29: **Western Blot analysis for E-cadherin expression of 3D spheroid invasion assays in 2.4 mg/mL collagen.** A) Protein expression of E-cadherin after 72h of invasion with DMSO, TGF-β and Batimastat treatments in A549 and MV3 spheroids. B) Western blot images of E-cadherin. The legend shows the content of each lane (numbered on top of the blot).

REFERENCES

[1] G. W. Pearson, *Control of invasion by epithelial-to-mesenchymal transition programs during metastasis,* Journal of Clinical Medicine **8** (2019), 10.3390/jcm8050646.

[2] T. R. Cox, *The matrix in cancer,* Nature Reviews Cancer **21**, 217 (2021).

[3] E. Henke, R. Nandigama, and S. Ergün, *Extracellular matrix in the tumor microenvironment and its impact on cancer therapy,* Frontiers in Molecular Biosciences **6** (2020), 10.3389/fmolb.2019.00160.

[4] A. L. McGregor, C. R. Hsia, and J. Lammerding, *Squish and squeeze - the nucleus as a physical barrier during migration in confined environments,* Current Opinion in Cell Biology **40**, 32 (2016).

[5] K. M. Yamada and M. Sixt, *Mechanisms of 3D cell migration,* Nature Reviews Molecular Cell Biology **20**, 738 (2019).

[6] M. C. Whittle and S. R. Hingorani, *Disconnect between emt and metastasis in pancreas cancer,* Oncotarget **6**, 30445 (2015).

[7] A. Haeger, M. Krause, K. Wolf, and P. Friedl, *Cell jamming: Collective invasion of mesenchymal tumor cells imposed by tissue confinement,* Biochimica et Biophysica Acta - General Subjects **1840**, 2386 (2014).

[8] A. C. Canver, O. Ngo, R. L. Urbano, and A. M. Clyne, *Endothelial directed collective migration depends on substrate stiffness via localized myosin contractility and cell-matrix interactions,* Journal of Biomechanics **49**, 1369 (2016).

[9] M. Parlani, C. Jorgez, and P. Friedl, *Plasticity of cancer invasion and energy metabolism,* Trends in Cell Biology **33**, 388 (2023).

[10] J. Odenthal, R. Takes, and P. Friedl, *Plasticity of tumor cell invasion: governance by growth factors and cytokines,* Carcinogenesis **37**, 1117 (2016), https://academic.oup.com/carcin/article-pdf/37/12/1117/8233812/bgw098.pdf .

[11] S. Hao, L. Ha, G. Cheng, Y. Wan, Y. Xia, D. M. Sosnoski, A. M. Mastro, and S. Y. Zheng, *A Spontaneous 3D Bone-On-a-Chip for Bone Metastasis Study of Breast Cancer Cells,* Small **14**, 1 (2018).

[12] J. Huang, L. Zhang, D. Wan, L. Zhou, S. Zheng, S. Lin, and Y. Qiao, *Extracellular matrix and its therapeutic potential for cancer treatment,* Signal Transduction and Targeted Therapy **6** (2021), 10.1038/s41392-021-00544-0.

[13] J. shun Wu, J. Jiang, B. jun Chen, K. Wang, Y. ling Tang, and X. hua Liang, *Plasticity of cancer cell invasion: Patterns and mechanisms,* Translational Oncology **14**, 100899 (2021).

[14] Y. J. Liu, M. L. Berre, F. Lautenschlaeger, P. Maiuri, A. Callan-Jones, M. Heuzé, T. Takaki, R. Voituriez, and M. Piel, *Confinement and low adhesion induce fast amoeboid migration of slow mesenchymal cells,* Cell **160**, 659 (2015).

[15] M. Wang, B. Cheng, Y. Yang, H. Liu, G. Huang, L. Han, F. Li, and F. Xu, *Microchannel stiffness and confinement jointly induce the mesenchymal-amoeboid transition of cancer cell migration,* Nano Letters **19**, 5949 (2019).

[16] A. Palamidessi, C. Malinverno, E. Frittoli, S. Corallino, E. Barbieri, S. Sigismund, G. V. Beznoussenko, E. Martini, M. Garre, I. Ferrara, C. Tripodo, F. Ascione, E. A. Cavalcanti-Adam, Q. Li, P. P. Di Fiore, D. Parazzoli, F. Giavazzi, R. Cerbino, and G. Scita, *Unjamming overcomes kinetic and proliferation arrest in terminally differentiated cells and promotes collective motility of carcinoma,* Nature Materials **18**, 1252 (2019).

[17] O. Ilina, P. G. Gritsenko, S. Syga, J. Lippoldt, C. A. La Porta, O. Chepizhko, S. Grosser, M. Vullings, G. J. Bakker, J. Starruß, P. Bult, S. Zapperi, J. A. Käs, A. Deutsch, and P. Friedl, *Cell–cell adhesion and 3D matrix confinement determine jamming transitions in breast cancer invasion,* Nature Cell Biology **22**, 1103 (2020).

[18] W. Kang, J. Ferruzzi, C. P. Spatarelu, Y. L. Han, Y. Sharma, S. A. Koehler, J. A. Mitchel, A. Khan, J. P. Butler, D. Roblyer, M. H. Zaman, J. A. Park, M. Guo, Z. Chen, A. F. Pegoraro, and J. J. Fredberg, *A novel jamming phase diagram links tumor invasion to non-equilibrium phase separation,* iScience **24** (2021), 10.1016/j.isci.2021.103252.

[19] K. M. Yamada, A. D. Doyle, and J. Lu, *Cell–3D matrix interactions: recent advances and opportunities,* Trends in Cell Biology **32**, 883 (2022).

[20] A. Saraswathibhatla, D. Indana, and O. Chaudhuri, *Cell–extracellular matrix mechanotransduction in 3D,* Nature Reviews Molecular Cell Biology **24**, 495 (2023).

[21] J. Winkler, A. Abisoye-Ogunniyan, K. J. Metcalf, and Z. Werb, *Concepts of extracellular matrix remodelling in tumour progression and metastasis,* Nature Communications **11**, 1 (2020).

[22] W. Han, S. Chen, W. Yuan, Q. Fan, J. Tian, X. Wang, L. Chen, X. Zhang, W. Wei, R. Liu, J. Qu, Y. Jiao, R. H. Austin, and L. Liu, *Oriented collagen fibers direct tumor cell intravasation,* Proceedings of the National Academy of Sciences of the United States of America **113**, 11208 (2016).

[23] C. Gaggioli, S. Hooper, C. Hidalgo-Carcedo, R. Grosse, J. F. Marshall, K. Harrington, and E. Sahai, *Fibroblast-led collective invasion of carcinoma cells with differing roles for RhoGTPases in leading and following cells,* Nature Cell Biology **9**, 1392 (2007).

[24] L. Hui and Y. Chen, *Tumor microenvironment: Sanctuary of the devil,* Cancer Letters **368**, 7 (2015).

[25] L. Fattet, H. Y. Jung, M. W. Matsumoto, B. E. Aubol, A. Kumar, J. A. Adams, A. C. Chen, R. L. Sah, A. J. Engler, E. B. Pasquale, and J. Yang, *Matrix Rigidity Controls*

Epithelial-Mesenchymal Plasticity and Tumor Metastasis via a Mechanoresponsive EPHA2/LYN Complex, Developmental Cell **54**, 302 (2020).

[26] S. Ishihara and H. Haga, *Matrix Stiffness Contributes to Cancer Progression by Regulating Transcription Factors,* Cancers **14** (2022), 10.3390/cancers14041049.

[27] K. M. Wisdom, K. Adebowale, J. Chang, J. Y. Lee, S. Nam, R. Desai, N. S. Rossen, M. Rafat, R. B. West, L. Hodgson, and O. Chaudhuri, *Matrix mechanical plasticity regulates cancer cell migration through confining microenvironments,* Nature Communications **9** (2018), 10.1038/s41467-018-06641-z.

[28] M. H. Zaman, L. M. Trapani, A. Siemeski, D. MacKellar, H. Gong, R. D. Kamm, A. Wells, D. A. Lauffenburger, and P. Matsudaira, *Migration of tumor cells in 3D matrices is governed by matrix stiffness along with cell-matrix adhesion and proteolysis,* Proceedings of the National Academy of Sciences of the United States of America **103**, 10889 (2006).

[29] K. Wolf, M. te Lindert, M. Krause, S. Alexander, J. te Riet, A. L. Willis, R. M. Hoffman, C. G. Figdor, S. J. Weiss, and P. Friedl, *Physical limits of cell migration: Control by ECM space and nuclear deformation and tuning by proteolysis and traction force,* Journal of Cell Biology **201**, 1069 (2013).

[30] S. P. Carey, A. Rahman, C. M. Kraning-Rush, B. Romero, S. Somasegar, O. M. Torre, R. M. Williams, and C. A. Reinhart-King, *Comparative mechanisms of cancer cell migration through 3D matrix and physiological microtracks,* American Journal of Physiology - Cell Physiology **308**, C436 (2015).

[31] H. E. Balcioglu, L. Balasubramaniam, T. V. Stirbat, B. L. Doss, M. A. Fardin, R. M. Mège, and B. Ladoux, *A subtle relationship between substrate stiffness and collective migration of cell clusters,* Soft Matter **16**, 1825 (2020).

[32] S. Van Helvert, C. Storm, and P. Friedl, *Mechanoreciprocity in cell migration,* Nature Cell Biology **20**, 8 (2018).

[33] R. Reuten, S. Zendehroud, M. Nicolau, L. Fleischhauer, A. Laitala, S. Kiderlen, D. Nikodemus, L. Wullkopf, S. R. Nielsen, S. McNeilly, C. Prein, M. Rafaeva, E. M. Schoof, B. Furtwängler, B. T. Porse, H. Kim, K. J. Won, S. Sudhop, K. W. Zornhagen, F. Suhr, E. Maniati, O. M. Pearce, M. Koch, L. B. Oddershede, T. Van Agtmael, C. D. Madsen, A. E. Mayorca-Guiliani, W. Bloch, R. R. Netz, H. Clausen-Schaumann, and J. T. Erler, *Basement membrane stiffness determines metastases formation,* Nature Materials **20**, 892 (2021).

[34] S. M. Pupa, S. Ménard, S. Forti, and E. Tagliabue, *New insights into the role of extracellular matrix during tumor onset and progression,* Journal of Cellular Physiology **192**, 259 (2002).

[35] C. Melzer, R. Hass, J. von der Ohe, H. Lehnert, and H. Ungefroren, *The role of TGF-β and its crosstalk with RAC1/RAC1b signaling in breast and pancreas carcinoma,* Cell communication and signaling : CCS **15**, 19 (2017).

[36] B. N. Kim, D. H. Ahn, N. Kang, C. D. Yeo, Y. K. Kim, K. Y. Lee, T. J. Kim, S. H. Lee, M. S. Park, H. W. Yim, J. Y. Park, C. K. Park, and S. J. Kim, *TGF-β induced EMT and stemness characteristics are associated with epigenetic regulation in lung cancer,* Scientific Reports **10**, 1 (2020).

[37] S. Colak and P. ten Dijke, *Targeting TGF-β Signaling in Cancer,* Trends in Cancer **3**, 56 (2017).

[38] C. H. Heldin, K. Miyazono, and P. Ten Dijke, *TGF-β signalling from cell membrane to nucleus through SMAD proteins,* Nature **390**, 465 (1997).

[39] Y. Hao, D. Baker, and P. T. Dijke, *TGF-β-mediated epithelial-mesenchymal transition and cancer metastasis,* International Journal of Molecular Sciences **20** (2019), 10.3390/ijms20112767.

[40] A. Micalet, E. Moeendarbary, and U. Cheema, *3d in vitro models for investigating the role of stiffness in cancer invasion,* ACS Biomaterials Science and Engineering **9**, 3729 (2023).

[41] D. Pally and A. Naba, *Extracellular matrix dynamics: A key regulator of cell migration across length-scales and systems,* Current Opinion in Cell Biology **86**, 102309 (2024).

[42] E. Wiercinska, H. P. Naber, E. Pardali, G. Van Der Pluijm, H. Van Dam, and P. Ten Dijke, *The TGF-β/Smad pathway induces breast cancer cell invasion through the up-regulation of matrix metalloproteinase 2 and 9 in a spheroid invasion model system,* Breast Cancer Research and Treatment **128**, 657 (2011).

[43] L. R. Gomes, L. F. Terra, R. A. Wailemann, L. Labriola, and M. C. Sogayar, *Abstract 5266: TGF-β1 modulates the homeostasis between MMPs and MMPs inhibitors through p38 MAPK and ERK½ in highly invasive human breast cancer cells,* Cancer Research **71**, 5266 (2011).

[44] W. T. Purcell, M. A. Rudek, and M. Hidalgo, *Development of matrix metalloproteinase inhibitors in cancer therapy,* Hematology/Oncology Clinics of North America **16**, 1189 (2002).

[45] B. X. J. Tune, M. S. Sim, C. L. Poh, R. M. Guad, C. K. Woon, I. Hazarika, A. Das, S. C. Gopinath, M. Rajan, M. Sekar, V. Subramaniyan, N. K. Fuloria, S. Fuloria, K. Batumalaie, and Y. S. Wu, *Matrix Metalloproteinases in Chemoresistance: Regulatory Roles, Molecular Interactions, and Potential Inhibitors,* Journal of Oncology **2022** (2022), 10.1155/2022/3249766.

[46] F. R. Boroojeni, S. Naeimipour, P. Lifwergren, A. Abrahamsson, C. Dabrosin, R. Selegård, and D. Aili, *Proteolytic remodeling of 3d bioprinted tumor microenvironments,* Biofabrication **16**, 025002 (2024).

[47] Z. Liao, J. J. H. Lim, J. X. T. Lee, D. Chua, M. I. G. Vos, Y. S. Yip, C. B. Too, H. Cao, J. K. Wang, Y. Shou, A. Tay, K. Lehti, H. S. Cheng,

C. Y. Tay, and N. S. Tan, *Attenuating epithelial-to-mesenchymal transition in cancer through angiopoietin-like 4 inhibition in a 3d tumor microenvironment model,* Advanced Healthcare Materials **13**, 2303481 (2024), https://onlinelibrary.wiley.com/doi/pdf/10.1002/adhm.202303481 .

[48] H. Castro-Abril, J. Heras, J. del Barrio, L. Paz, C. Alcaine, M. P. Aliácar, D. Garzón-Alvarado, M. Doblaré, and I. Ochoa, *The role of mechanical properties and structure of type i collagen hydrogels on colorectal cancer cell migration,* Macromolecular Bioscience **23** (2023), 10.1002/mabi.202300108.

[49] A. Naylor, Y. Zheng, Y. Jiao, and B. Sun, *Micromechanical remodeling of the extracellular matrix by invading tumors: anisotropy and heterogeneity,* Soft Matter **19**, 9 (2022).

[50] A. Elosegui-Artola, A. Gupta, A. J. Najibi, B. R. Seo, R. Garry, M. Darnell, W. Gu, Q. Zhou, D. A. Weitz, L. Mahadevan, and D. J. Mooney, *Matrix viscoelasticity controls spatio-temporal tissue organization,* bioRxiv **22**, 2022.01.19.476771 (2022).

[51] O. Ilina and P. Friedl, *Mechanisms of collective cell migration at a glance,* Journal of Cell Science **122**, 3203 (2009).

[52] J.-A. Park, L. Atia, J. A. Mitchel, J. J. Fredberg, and J. P. Butler, *Collective migration and cell jamming in asthma, cancer and development,* Journal of Cell Science **129**, 3375 (2016).

[53] J. A. Mitchel, A. Das, M. J. O'Sullivan, I. T. Stancil, S. J. DeCamp, S. Koehler, O. H. Ocaña, J. P. Butler, J. J. Fredberg, M. A. Nieto, D. Bi, and J. A. Park, *In primary airway epithelial cells, the unjamming transition is distinct from the epithelial-to-mesenchymal transition,* Nature Communications **11**, 1 (2020).

[54] A. W. Holle, N. Govindan Kutty Devi, K. Clar, A. Fan, T. Saif, R. Kemkemer, and J. P. Spatz, *Cancer cells invade confined microchannels via a self-directed mesenchymal-to-amoeboid transition,* Nano Letters **19**, 2280 (2019).

[55] D. L. Pagès, E. Dornier, J. de Seze, E. Gontran, A. Maitra, A. Maciejewski, L. Wang, R. Luan, J. Cartry, C. J. Charlotte, J. Raingeaud, G. Lemahieu, M. Lebel, M. Ducreux, M. Gelli, J. Y. Scoazec, M. Coppey, R. Voituriez, M. Piel, and F. Jaulin, *Cell clusters adopt a collective amoeboid mode of migration in confined nonadhesive environments,* Science Advances **8**, 8416 (2022).

[56] M. K. Driscoll, E. S. Welf, A. Weems, E. Sapoznik, F. Zhou, V. S. Murali, J. M. García-Arcos, M. Roh-Johnson, M. Piel, K. M. Dean, R. Fiolka, and G. Danuser, *Proteolysis-free amoeboid migration of melanoma cells through crowded environments via bleb-driven worrying,* Developmental Cell (2024), https://doi.org/10.1016/j.devcel.2024.05.024.

[57] H. Zhao, J. Wei, and J. Sun, *Roles of tgf-β signaling pathway in tumor microenvirionment and cancer therapy,* International Immunopharmacology **89**, 107101 (2020).

[58] C. Dessapt, M. O. Baradez, A. Hayward, A. D. Cas, S. M. Thomas, G. Viberti, and L. Gnudi, *Mechanical forces and tgfβ1 reduce podocyte adhesion through α3β1 integrin downregulation,* Nephrology Dialysis Transplantation **24**, 2645 (2009).

[59] F. Lin, H. Zhang, J. Huang, and C. Xiong, *Substrate stiffness coupling tgf-β1 modulates migration and traction force of mda-mb-231 human breast cancer cells in vitro,* ACS Biomaterials Science & Engineering **4**, 1337 (2018).

[60] G. Cantelli, J. L. Orgaz, I. Rodriguez-Hernandez, P. Karagiannis, O. Maiques, X. Matias-Guiu, F. O. Nestle, R. M. Marti, S. N. Karagiannis, and V. Sanz-Moreno, *Tgf-β-induced transcription sustains amoeboid melanoma migration and dissemination,* Current Biology **25**, 2899 (2015).

[61] D. Böhringer, A. Bauer, I. Moravec, L. Bischof, D. Kah, C. Mark, T. J. Grundy, E. Görlach, G. M. O'Neill, S. Budday, P. L. Strissel, R. Strick, A. Malandrino, R. Gerum, M. Mak, M. Rausch, and B. Fabry, *Fiber alignment in 3d collagen networks as a biophysical marker for cell contractility,* Matrix Biology **124**, 39 (2023).

[62] K. S. Kopanska, Y. Alcheikh, R. Staneva, D. Vignjevic, and T. Betz, *Tensile forces originating from cancer spheroids facilitate tumor invasion,* PLoS ONE **11** (2016), 10.1371/journal.pone.0156442.

[63] G. Cai, A. Nguyen, Y. Bashirzadeh, S. S. Lin, D. Bi, and A. P. Liu, *Compressive stress drives adhesion-dependent unjamming transitions in breast cancer cell migration,* Frontiers in Cell and Developmental Biology **10**, 1 (2022).

[64] K. Wang, J. Zheng, J. Yu, Y. Wu, J. Guo, Z. Xu, and X. Sun, *Knockdown of mmp-1 inhibits the progression of colorectal cancer by suppressing the pi3k/akt/c-myc signaling pathway and emt,* Oncology Reports **43**, 1103 (2020).

[65] S. Niland, A. X. Riscanevo, and J. A. Eble, *Matrix metalloproteinases shape the tumor microenvironment in cancer progression,* International Journal of Molecular Sciences **23** (2022), 10.3390/ijms23010146.

[66] C. Scheau, I. A. Badarau, R. Costache, C. Caruntu, G. L. Mihai, A. C. Didilescu, C. Constantin, and M. Neagu, *The role of matrix metalloproteinases in the epithelial-mesenchymal transition of hepatocellular carcinoma,* Analytical Cellular Pathology **2019** (2019), 10.1155/2019/9423907.

[67] B. Nawrocki-Raby, C. Gilles, M. Polette, E. Bruyneel, J. Y. Laronze, N. Bonnet, J. M. Foidart, M. Mareel, and P. Birembaut, *Upregulation of mmps by soluble e-cadherin in human lung tumor cells,* International Journal of Cancer **105**, 790 (2003).

[68] D. Pinheiro and J. Mitchel, *Pulling the strings on solid-to-liquid phase transitions in cell collectives,* Current Opinion in Cell Biology **86**, 102310 (2024).

[69] T. S. Deisboeck, Y. Mansury, C. Guiot, P. G. Degiorgis, and P. P. Delsanto, *Insights from a novel tumor model: Indications for a quantitative link between tumor growth and invasion,* Medical Hypotheses **65**, 785 (2005).

[70] A. J. Crawford, C. Gomez-Cruz, G. C. Russo, W. Huang, I. Bhorkar, T. Roy, A. Muñoz-Barrutia, D. Wirtz, and D. Garcia-Gonzalez, *Tumor proliferation and invasion are intrinsically coupled and unraveled through tunable spheroid and physics-based models,* Acta Biomaterialia **175**, 170 (2024).

[71] G. Banfalvi, *Overview of cell synchronization,* in *Cell Cycle Synchronization: Methods and Protocols*, edited by G. Banfalvi (Humana Press, Totowa, NJ, 2011) pp. 1–23.

[72] A. Ligasová and K. Koberna, *Strengths and weaknesses of cell synchronization protocols based on inhibition of dna synthesis,* International Journal of Molecular Sciences **22** (2021), 10.3390/ijms221910759.

[73] M. V. Hunter, E. Montal, Y. Ma, R. Moncada, I. Yanai, R. P. Koche, and R. M. White, *Mechanical confinement governs phenotypic plasticity in melanoma,* bioRxiv (2024), 10.1101/2024.01.30.577120.

[74] P. Gottheil, J. Lippoldt, S. Grosser, F. Renner, M. Saibah, D. Tschodu, A. K. Poßögel, A. S. Wegscheider, B. Ulm, K. Friedrichs, C. Lindner, C. Engel, M. Löffler, B. Wolf, M. Höckel, B. Aktas, H. Kubitschke, A. Niendorf, and J. A. Käs, *State of cell unjamming correlates with distant metastasis in cancer patients,* Physical Review X **13** (2023), 10.1103/PhysRevX.13.031003.

[75] M. Nguyen, A. De Ninno, A. Mencattini, F. Mermet-Meillon, G. Fornabaio, S. S. Evans, M. Cossutta, Y. Khira, W. Han, P. Sirven, F. Pelon, D. Di Giuseppe, F. R. Bertani, A. Gerardino, A. Yamada, S. Descroix, V. Soumelis, F. Mechta-Grigoriou, G. Zalcman, J. Camonis, E. Martinelli, L. Businaro, and M. C. Parrini, *Dissecting Effects of Anticancer Drugs and Cancer-Associated Fibroblasts by On-Chip Reconstitution of Immunocompetent Tumor Microenvironments,* Cell Reports **25**, 3884 (2018).

[76] V. V. Artym and K. Matsumoto, *Imaging cells in three-dimensional collagen matrix,* Current Protocols in Cell Biology **48**, 10.18.1 (2010).

[77] A. Sinha, P. Mehta, C. Fan, J. Zhang, D. L. Marvin, M. van Dinther, L. Ritsma, P. E. Boukany, and P. ten Dijke, *Visualizing dynamic changes during tgf-β-induced epithelial to mesenchymal transition,* in *TGF-Beta Signaling: Methods and Protocols*, edited by Z. Zi and X. Liu (Springer US, New York, NY, 2022) pp. 47–65.

[78] Z. Rahman, A. Deep Bordoloi, H. Rouhana, M. Tavasso, G. van der Zon, V. Garbin, P. Ten Dijke, and P. E. Boukany, *Interstitial flow potentiates TGF-β/Smad-signaling activity in lung cancer spheroids in a 3D-microfluidic chip,* Lab on a Chip , 1037 (2023).

[79] K. M. Lugo-Cintrón, M. M. Gong, J. M. Ayuso, L. A. Tomko, D. J. Beebe, M. Virumbrales-Muñoz, and S. M. Ponik, *Breast Fibroblasts and ECM Components Modulate Breast Cancer Cell Migration through the Secretion of MMPs in a 3D Microfluidic Co-Culture Model,* Cancers **12**, 1173 (2020).

[80] E. G. Driever, I. Muntz, V. Patel, J. Adelmeijer, W. Bernal, G. H. Koenderink, and T. Lisman, *Fibrin clots from patients with acute-on-chronic liver failure are weaker*

than those from healthy individuals and patients with sepsis without underlying liver disease, Journal of Thrombosis and Haemostasis **21**, 2747 (2023).

[81] A. Kokaram, *Practical, Unified, Motion and Missing Data Treatment in Degraded Video,* Journal of Mathematical Imaging and Vision **20**, 163 (2004).

[82] J. Schindelin, I. Arganda-Carreras, E. Frise, V. Kaynig, M. Longair, T. Pietzsch, S. Preibisch, C. Rueden, S. Saalfeld, B. Schmid, J. Y. Tinevez, D. J. White, V. Hartenstein, K. Eliceiri, P. Tomancak, and A. Cardona, *Fiji: An open-source platform for biological-image analysis,* Nature Methods **9**, 676 (2012).

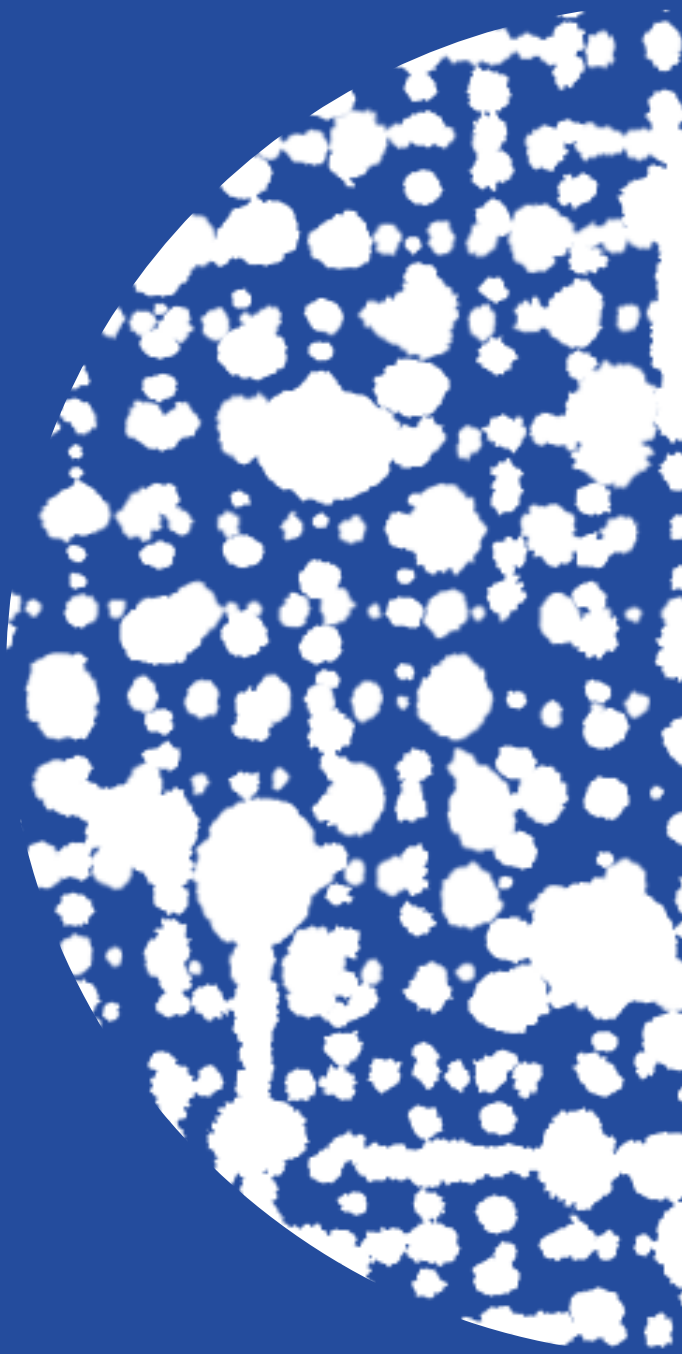

5

Conclusion and Outlook

This chapter highlights the key findings from the work described in previous chapters that focused on the influence of extra-cellular matrix (ECM), interstitial flow (IF) and cytokines to investigate cancer cell invasion. We developed physiologically relevant 3-D in vitro platforms (especially microfluidics) that enabled real-time evaluation of cancer cells interacting with their surrounding tumor micro-environment (TME). This approach led to a quantitative assessment of important parameters such as varying degrees of ECM confinement, interstitial flow rates and varying TGF-β concentration that were found to modulate cancer cell invasion behavior. Additionally, we used genetically modified cells with dual fluorescent reporters that enabled quantification of cell-signaling activity and epithelial to mesenchymal transition (EMT) protein expression [1, 2] especially when exposed to varying IF rates and exogenous TGF-β concentrations [3]. This thesis combines multiple research facets such as the use of 3-D in vitro (microfluidic) platform, spheroid models of epithelial and mesenchymal-like cancer cells, hydrogels with controlled compositions to mimic diverse tumor tissue architecture, biochemicals (cancer-related cytokines such as TGF-β) and small-molecule inhibitors (broad-spectrum MMP inhibitors, TGF-β receptor kinase inhibitor) that are commonly used as anti-cancer drugs [4–6]. With this multi-disciplinary project, we answered the research questions formulated in Chapter 1 that are briefly discussed in the next sections along with a perspective on future research direction.

5.1. 3-D MICROFLUIDIC APPROACHES TOWARDS CANCER MIGRATION STUDIES

In Chapter 2, we critically examined the most relevant and recent developments in 3-D cancer invasion studies to identify research gaps and shortcomings of the work performed in the past decade. Previous studies performed to mimic various TME components to investigate different stages of cancer progression, were mostly restricted to classical experimental techniques such as Boyden chambers, transwell membrane assays and use of animal and xenograft models [7]. These models lacked the ability to combine biophysical forces (such as IF) and biochemicals (cytokines) to investigate a synergistic role in cancer invasion behavior. Therefore, we highlighted the importance of microfluidic models that allow decoupling of multiple TME components to target specific biophysical or biochemical factors compared to animal and xenograft models. Research studies performed in 3-D microfluidic platforms allow direct visualization and quantification of cell migration parameters (speed, distance and morphology). It also enables to differentiate between different cell migration modes, such as individual or collective migration type, that is often linked to metastatic potential and cancer cell survival of certain tumor types [8]. Additionally, microfluidic models nowadays are often developed for drug screening and anti-cancer therapeutics and are widely accepted due to their promising potential to reduce dependency on animal models [5]. Future research work in microfluidics to study cancer disease progression requires:

1. Essential design upgrades that allow access to cancer spheroids and/or cells post-experiment to conduct additional genetic and protein expression analyses.

2. Research on alternative material to fabricate microfluidic devices as PDMS is hy-

drophobic and is prone to adsorbing anti-cancer drug molecules limiting drug-efficacy assessment especially in long-term studies.

This will require additional work to improve microfluidic platforms to replace animal models to a large extent in the near future and help close the gap between fundamental and pre-clinical research settings.

5.2. SYNERGISTIC RELATIONSHIP BETWEEN BIOPHYSICAL AND BIOCHEMICAL FACTORS

In Chapter 3, we investigated the effect of interstitial flow, an important biophysical force relevant in TME. We used genetically modified dual-reporter fluorescent labelled epithelial (less invasive) A549 lung adenocarcinoma cells [9], from which we formed 3-D spheroids and embedded them in GelMA hydrogel mimicking the lung tumor tissue stiffness (storage modulus, G' ≈ 200 Pa). This 3-D microfluidic model allowed a dynamic range of IF velocity (at 0.2 and 0.45 μm/s) generated by pressure gradient (at ΔP = 20 and 30 mbar). It has been hypothesized that IF upregulates endogenous TGF-β activity that in turn activates the Smad-signaling pathway [10]. The activation of Smad-signaling pathway essentially leads to the upregulation of metastatic transcription factors (such as SNAI1, ZEB1/2, TWIST) and ultimately increase in EMT protein (vimentin, N-cadherin) expression [2, 11]. In our study, we exposed A549 tumor spheroids to varying IF and exogenous TGF-β (0.1 - 10 ng/mL concentration) to investigate the potentiating effect of IF on Smad-signaling activity. The Smad-activity was measured via upregulation in CAGA-12-GFP fluorescence reporter transcriptional activity. This exogenous TGF-β and IF induced Smad-activity further led to an increase in vimentin protein abundance measured by VIM-RFP reporter fluorescence. Furthermore, the potentiating effect of IF in the presence of exogenous TGF-β led to an increased cellular motion activity observed at the spheroid periphery that can be linked to early dissemination and cell invasion activity.

We report that IF has two prominent effects, i.e. 1) shear (or compressive stress) on the spheroids activating additional mechanotransduction pathways and 2) enhanced mass-transport of TGF-β molecules to undergo active binding with TGF-β cell-surface receptors. These proposed mechanisms were validated with results obtained from two important experimental conditions; i.e. high IF/low TGF-β concentration (u_m = 0.45 μm/s/ C_0 = 1 ng/mL) that led to higher CAGA-12-GFP activity compared to low IF/high TGF-β concentration (u_m = 0.2 μm/s/ C_0 = 10 ng/mL) (see Fig.3.2.C). We hypothesized that a higher IF velcocity enhances exogenous TGF-β molecule penetration through the spheroid. This hypothesis was confirmed by the penetration of a proxy fluorescent reporter (Dextran-FITC, 20kDa) similar to TGF-β molecule (25 kDa) at similar IF flow rates (see Fig. 3.17). In addition, a higher IF (higher shear/compressive stress) may activate cell-surface mechanosensors [12, 13]. Many studies have reported the activation of integrins and focal adhesion kinase (FAK) receptors are involved in further downstream activation of intra-cellular signaling pathway [14, 15]. It is possible that IF induced signaling pathway may feed into the TGF-β induced Smad-pathway that produces an enhanced transcriptional CAGA-12-GFP response. Future work proposed to explore this hypothesis requires:

1. Specific genetic and pharmacological manipulation on signaling pathways (for eg. YAP/TAZ) will enable us to evaluate the activation of mechanosensors and mechanotransduction pathways.

2. Genetically engineered cells to express fluorescence upon activation of specific mechanosensors or mechanotransduction pathways at play.

3. Investigate the role of fluid-induced shear stress and compressive stress separately to identify their roles in cancer invasion.

5.3. ROLE OF CELL-ECM INTERPLAY IN 3D SPHEROID INVASION

In Chapter 4, we assessed the role of varying extra-cellular matrix (mechanical determinants) and the modulation of EMT protein (vimentin) and MMP protein levels (cell-intrinsic determinants) on spheroid phase-transitions derived from their invasion modes. We employed two different cell lines; epithelial (A549) lung cancer cells and mesenchymal-like (MV3) melanoma cancer embedded in natural (collagen) and semi-synthetic (GelMA) ECM matrices. These spheroids invade into their microenvironment via different invasion modes, broadly classified as disseminating many individual cells (gas-like), forming multicellular extensions or protrusions into the matrix (liquid-like) or with no characteristic change in spheroid shape corresponding to no-invasion (solid-like) [**?**]. Therefore, the ability of a spheroid to undergo from a solid to liquid/gas-like phase transition is referred to as unjamming effect. We observed that the ability of a spheroid to undergo unjamming is dominated by the matrix confinement (pore-size) parameter. As the matrix confinement increased, spheroids were restricted to their solid-like phase displaying no invasion (see Fig. 4.7. Furthermore, Fig.4.7 shows that the increase in MMP1 protein secretion (from TGF-β treatment) led to unjamming effect especially when A549 spheroids were embedded in collagen (8 mg/mL; TGF-β) and GelMA (30 mg/mL; TGF-β) due to the formation of cellular protrusions (liquid-like). Similarly, decrease in MMP1 protein intensity (from MMP-inhibitor treatment) limited spheroids to liquid or solid-like phase due to a significant reduction in single cell dissemination observed in MV3 spheroids embedded in collagen (8 mg/mL; MMP-inhibited) or GelMA (30 mg/mL; MMP-inhibited). Therefore, with this study we highlighted the importance of cell-ECM interplay on spheroid invasion that directly impact unjamming transitions.

In addition, we quantified the spheroid invasion capacity of MV3 and A549 spheroids via bright-field time series imaging that revealed the influence of matrices on the invasion onset time and the rate of invasion. We observed that onset of invasion and invasion rate together contribute to determine the spheroid invasion capacity. Matrix confinement (pore-size) has a strong influence on initiation of invasion (onset time), where smaller pore-size leads to a more delayed onset or even complete invasion inhibition (mostly observed in GelMA; 50 mg/mL). Moreover, from protein level analysis, we identified that vimentin protein level intensity has a strong correlation with invasion onset time (see Fig. 4.6B). Therefore, cells with a higher vimentin protein abundance (MV3) show immediate EMT and initiate invasion at $t_{ons} < 5$ hrs compared to A549 cells

($t_{ons} < 5$ hrs) with a lower vimentin protein abundance. On the other hand, we identified that matrix confinement parameters showed minimal influence on invasion rate of spheroids and were dominated by TGF-β or MMP-inhibitor treatment (see Fig.4.4). Moreover, Fig.4.6C revealed that invasion rates were strongly associated with MMP1 protein intensity. The increase in MMP1 protein secretion (from TGF-β treatment) increased the invasion rate in both A549 and MV3 spheroids. Hence, the influence of matrix confinement on invasion onset and TGF-β/MMP-inhibitor treatment together dictate the invasion capacity of a spheroid. Therefore, these findings further highlight the role of cell-matrix interactions essential in 3D-cancer invasion studies. Future work proposed to provide deeper insights in the modification of inherent matrix architecture and invasion modes requires:

1. Dynamic or real-time measurement of matrix mechanical parameters (stiffness, pore-size) before and after matrix remodelling and modification from cell secreted proteins.

2. High-resolution imaging to investigate different cell morphologies (mesenchymal or amoeboid) during invasion in highly confined tumor microenvironment important in cancer metastasis.

3. Inhibition or blocking of specific cell-surface and matrix receptors to elucidate biological mechanisms involved in jamming/unjamming transitions.

In this thesis, we achieved significant milestones that highlights our contribution to investigate cancer initiation and progression using novel bio-engineered solutions (especially microfluidics). These 3D in vitro platforms will significantly impact the future research output in various aspects of cancer biology ranging from disease modelling to drug screening. Creating a physiological relevant tumor microenvironment including tumor tissue architecture and essential cellular components still remains a big challenge and requires immediate attention. Collaboration of cancer biologists and engineers specializing in material science and fluid mechanics will ultimately benefit to design and develop novel strategies with biological relevance to address fundamental research gaps in cancer metastasis.

REFERENCES

[1] W. Wang, D. Douglas, J. Zhang, S. Kumari, M. S. Enuameh, Y. Dai, C. T. Wallace, S. C. Watkins, W. Shu, and J. Xing, *Live-cell imaging and analysis reveal cell phenotypic transition dynamics inherently missing in snapshot data,* Science Advances **6** (2020), 10.1126/sciadv.aba9319.

[2] Y. Hao, D. Baker, and P. T. Dijke, *TGF-β-mediated epithelial-mesenchymal transition and cancer metastasis,* International Journal of Molecular Sciences **20** (2019), 10.3390/ijms20112767.

[3] Z. Rahman, A. D. Bordoloi, H. Rouhana, M. Tavasso, G. van der Zon, V. Garbin, P. ten Dijke, and P. E. Boukany, *Interstitial flow potentiates TGF-β/Smad-signaling activity in lung cancer spheroids in a 3D-microfluidic chip,* Lab on a Chip **24**, 422 (2024).

[4] J. Mitchel, A. Das, M. O'Sullivan, I. Stancil, S. DeCamp, S. Koehler, J. Butler, J. Fredberg, M. A. Nieto, D. Bi, and J.-A. Park, *The unjamming transition is distinct from the epithelial-to-mesenchymal transition,* bioRxiv , 665018 (2019).

[5] K. P. Valente, S. Khetani, A. R. Kolahchi, A. Sanati-Nezhad, A. Suleman, and M. Akbari, *Microfluidic technologies for anticancer drug studies,* Drug Discovery Today **22**, 1654 (2017).

[6] M. Villalba, S. R. Evans, F. Vidal-Vanaclocha, and A. Calvo, *Role of TGF-β in metastatic colon cancer: it is finally time for targeted therapy,* Cell and Tissue Research **370**, 29 (2017).

[7] P. Mehta, Z. Rahman, P. ten Dijke, and P. E. Boukany, *Microfluidics meets 3D cancer cell migration,* Trends in Cancer **8**, 683 (2022).

[8] S. Van Helvert, C. Storm, and P. Friedl, *Mechanoreciprocity in cell migration,* Nature Cell Biology **20**, 8 (2018).

[9] D. L. Marvin, L. You, L. Bornes, M. van Dinther, N. Peters, H. Dang, S. K. Hakuno, M. Hornsveld, O. Kranenburg, J. van Rheenen, J. H. Rohling, M. P. Chien, P. Ten Dijke, and L. Ritsma, *Dynamic Visualization of TGF-β/SMAD3 Transcriptional Responses in Single Living Cells,* Cancers **14**, 1 (2022).

[10] M. A. Swartz and A. W. Lund, *Lymphatic and interstitial flow in the tumour microenvironment: Linking mechanobiology with immunity,* Nature Reviews Cancer **12**, 210 (2012).

[11] S. Colak and P. ten Dijke, *Targeting TGF-β Signaling in Cancer,* Trends in Cancer **3**, 56 (2017).

[12] F. Zanconato, M. Cordenonsi, and S. Piccolo, *YAP/TAZ at the Roots of Cancer,* Cancer Cell **29**, 783 (2016).

[13] H. J. Lee, M. F. Diaz, K. M. Price, J. A. Ozuna, S. Zhang, E. M. Sevick-Muraca, J. P. Hagan, and P. L. Wenzel, *Fluid shear stress activates YAP1 to promote cancer cell motility,* Nature Communications **8** (2017), 10.1038/ncomms14122.

[14] I. Jang and K. A. Beningo, *Integrins, CAFs and mechanical forces in the progression of cancer,* Cancers **11** (2019), 10.3390/cancers11050721.

[15] W. J. Polacheck, A. E. German, A. Mammoto, D. E. Ingber, and R. D. Kamm, *Mechanotransduction of fluid stresses governs 3D cell migration,* Proceedings of the National Academy of Sciences of the United States of America **111**, 2447 (2014).

PROPOSITIONS

1. Magnitude of biophysical force (interstitial flow) has a stronger influence compared to biochemical (TGF-β) concentration to produce an enhanced Smad signaling activity in lung cancer cells.
   This proposition pertains to chapter 3 of this thesis.

2. Interstitial flow plays a dual role in tumor progression; improved mass transport of cytokines and activation of cell surface receptors on tumor cells due to fluid-induced shear and compressive stress.
   This proposition pertains to chapter 3 of this thesis.

3. Use of semi-synthetic (GelMA) hydrogel alongside natural collagen reveal dominance of ECM pore-size and density compared to ECM stiffness on cancer invasion modulation.
   This proposition pertains to chapter 4 of this thesis.

4. Unjamming transition in spheroid invasion is associated with ECM degradation ability and MMP enzyme expression level from cancer cells.
   This proposition pertains to chapter 4 of this thesis.

5. 3-D microfluidic platforms enable an integrated assessment of tumor microenvironment components making it a popular choice to replace animal models.

6. Cancer pathogenesis and therapeutic research will benefit when the biological relevance of engineering approaches are duly acknowledged in clinical and preclinical sciences.

7. Accepting the intrinsic limitations at the cellular and molecular level to model inter-patient and intra-tumoral heterogeneity is necessary to advance preclinical studies.
   Golebiewska et al., BMC Cancer, 2023

8. Quality and delivery of collaborative projects can be influenced by the type of relationship with colleague(s) existing outside the project.

9. The probability/likelihood of obtaining an interview for your dream job without networking efforts is close to zero.

10. Elon Musk, Sam Altman and cryptocurrency will determine the next technological and financial revolution.

These propositions are regarded as opposable and defendable, and have been approved by the promotors dr. Pouyan E. Boukany and prof. dr. Valeria Garbin

ACKNOWLEDGEMENTS

A 4-year PhD trajectory is not just limited to an academic achievement but is a timeline that transcends your character, resilience and personality. These past years have taught me self-reflection, handle criticism and experience situations (personal and professional) that I would never be challenged if not for a PhD. For this, I give major credit to my supervisor and promotor, **Dr. Pouyan E. Boukany** who gave me the opportunity to pursue and thrive in a challenging PhD project. I am grateful for your attention, support and availability whenever I needed your guidance and opinion. I admire your network in the scientific community through which I could establish meaningful collaborations that led to several successful publications and projects. To my copromotor, **Prof. dr. Valeria Garbin**, I am inspired by your criticality, your attention to detail and suggestions to improve our work in the finest of details. I would like to thank you both for making my PhD a memorable experience.

Entering my third year of PhD (2022), I was introduced to **prof. dr. Peter ten Dijke** at LUMC, Netherlands on my first collaborative project. Since then, we organized monthly update meetings till the very last month of my PhD, ending with multiple collaborations and publications. Your passion for science and research is unmatched and has inspired me at the highest level to pursue a scientific career. Peter, I cannot thank you enough as I know that this PhD thesis would be incomplete without your supervision and guidance. In the last year of my PhD, I was fortunate to establish a collaborative project with **prof. dr. Gijsje H. Koenderink**, Bionanoscience, TU Delft. With only three update meetings organized in a full year, we completed a major project with maximum efficiency, quality and research output. **Gijsje**, your scientific supervision and attention to detail has given me a whole new perception to approach research questions, from planning, execution and writing a good publication.

Following up with collaborations and projects, my journey would be incomplete without **Anouk van der Net**. I am so glad that we met near the piano for the first time on the first floor of our building to casually present some interesting results that we had been working on individually. Since then, that piano area became our go-to place for all successive meetings and concluded with a shared first author publication. I have great respect and admiration for your scientific aptitude combined with time management, planning and execution skills. You kept me on my toes during our project and as I finished my PhD contract, I thank you for bringing our project to the finish line. One of my first collaborations, a bittersweet memory with one of my closest colleague (now a close friend hehe), **Pranav Mehta** deserves a special mention. We had our differences but in the end we have come even closer to establish a deep connection in and outside of work. **Pranav**, I appreciate that you always go out of your way to help me, to invite me at your place and feed me with the most delicious food. I look forward to your super interesting work getting published and wish you the best to finish your PhD. I also would like to thank **Shuang Zhang** from Erasmus MC where we collaborated on the fabrication of the microfluidic chip. Thank you for including me in your project and I was happy to be a co-author on your publication. Working with **Dr. Yusi Liu** was one of the smoothest collaborations. I am glad to be a part of your PhD and hope that our expertise benefited

you. Lastly, I would like to thank **Dr. Mahdiyeh Nouri Ghoushki** for a super promising collaboration with her 3D bioprinting expertise and cancer cells. Although we ran out of time to finish this project into a collaboration, I am happy that we initiated and took efforts to make it a coherent story. All the best for your next job and future endeavours.

I can write a separate acknowledgement chapter for the contribution that **Dr. Ankur Deep Bordoloi** has made in my PhD thesis. You arrived in Pouyan's group as I entered my final year and without wasting time I bombarded you with a ton of image and data analysis. You put me at ease during the final and the toughest year of my PhD by constantly reminding me of the quality of our work and praising me on little achievements. Your passion and willingness to help young researchers to achieve their goals is inspirational and admirable. I wish you success for your next endeavour and I hope you get your dream academic position. In the first few months, **Dr. Qian Liu** joined as a postdoc in our group. I hooked on to her and started mimicking her hydrogel techniques for my own project. Thank you Qian for teaching me endless laboratory and mammalian cell culture techniques. I give you the entire credit for introducing GelMA in our lab as I ended up using this hydrogel in all of my projects.

During these past years, I have had the opportunity to supervise many bachelor and master students: starting with **Sue van Deursen** then **Haifa Rouhana**, **Meryl Copray** and lastly **Ankit Sinha**. **Sue**, you were the first student I supervised on a remote project during the first-wave of Covid. One of the most difficult times for everyone, you delivered your best and made my supervision experience a memorable one. **Haifa**, you have played a vital role in helping me setting up the key aspect of the microfluidic system. You showed utmost resilience and delivered an extremely well written and documented report that I used as an example for every student I had later on. After a few years of supervision experience, I got the chance to work with **Meryl**. You had a bumpy start but quickly caught up and delivered straight A's. I was inspired by your time planning, your work ethics and your jovial and energetic personality at work. I would never forget that we would end up wearing the same outfit numerous times at work. I was honored to speak at your graduation ceremony about your accomplishments that has forever etched in my memory. **Ankit**, you have been a very independent and hardworking student. Especially during my last months of PhD, you gained my trust that you can handle things and finish your master project without my help. I look forward to your defence and wish you all the best for your future endeavours.

I am grateful to have been a part of the Product and Process Engineering group in the Chemical Engineering department, led by **prof.dr. Ruud van Ommen**. Thank you for leading a group with such diverse expertise that created a unique experience, especially during group presentations and journal club. I sincerely thank **Dr. Gabrie Meesters** for always sharing his experiences and most importantly helping me with CV and cover letter as I prepared myself to enter the job market. Your tips and tricks have been very useful in all the interviews I appeared for in the past months. For two consecutive years, I was responsible for LO1 course led by **Dr. Volkert van Steijn**. Thank you for providing me the opportunity to organize and teach this course as it gave me a platform to improve my teaching and soft skills. I would also like to thank all PPE PI's **Dr. Alina Rwei**, **prof. dr. Tony Kiss**, **Dr. Artur M. Schweidtmann** and **Dr. Ana Somoza Tornos** for their unique perception and ideas during journal clubs and meetings. PPE is incomplete without its

technicians, and **Kristen David** deserves a special mention. **Kristen**, your contribution in setting up the Boukany lab is colossal. Your organization skills and insistence for a safe and clean workspace from every lab user to ensure a smooth operation is worth complimenting. I also want to thank you especially for training my students on key laboratory techniques and developing them into responsible lab users. Lastly, I want to thank the PPE secretary **Leslie van Leeuwen** who organized amazing group activities and Christmas dinners during these past years and made it a memorable experience.

I feel at ease for knowing and being close to some truly compassionate individuals who have had great influence on my personal and professional growth. **Dr. Georg Pesch**, an inspiring and strong personality introduced in the formative years of my PhD. I felt a unique connection and was amazed by your outspoken and no BS attitude. My PhD journey felt complete when I met you in Boston in December 2024, exactly 4 years later our Rotterdam adventure. I always have had a little regret of not taking the initiative to interact with **Dr. Saeed Saedy** from the very first day. I eventually developed a deep respect and admiration for you as we had more conversations. Especially the rock solid advises from your experiences whenever I had doubts about my PhD. I am happy to know that I have formed a special bond with you where I can always text you to ask about any little thing that comes my way.

Dr. Aswin Muralidharan's wit and wisdom is unparalleled which is why I always turned to you bro whenever I needed some advice. Knowing that somehow you will know what is right was a blind trust and faith I put in you from my early days in Delft. On a lighter note, I have enjoyed several conversations with you and shared special memories cooking and playing numerous board games. Which brings me to **Isabel Bagemihl** and **Lukas Bagemihl** who literally gave us a second home when everything had shut down. Being there every weekend to cook, play games and spend entire evenings until early mornings is what kept my sanity in those difficult months. It is such a wholesome feeling to see you both progress in life, from getting married to your first born and now back in Hamburg to start a new life. I wish you both all the best and little Cleo a bright and healthy future. And the final member of our Covid gang, **Dr. Dominik Benz** who deserves a special mention for his improvement in spice tolerance as I challenged him every weekend for a whole year with some Indian cuisine. Thank you bro for accepting and tolerating my culinary adventure.

Apart from all the scientific and professional experience, I am grateful to have shared this journey with my office mates who have now earned special status in my life. **Ruben Boot**, who joined 2 weeks after my starting date turned out to be that special guy who brings out the best and worst in me. As soon as I found out that you like Justin Bieber, I was sold. Then Ryan Gosling, Dave Chappelle and many famous celebrities who we mimicked and admired was our little bonding moments. Our golden opportunity to visit Boston and experience the "Bitches be in Boston" moment was truly special and unforgettable. I look forward to more silly moments in the future and wish you success in your journey as a science communicator. You will always remain my "bubble boy". **Margherita Tavasso** is a legit female version of myself. From going to the gym to going shopping or eating like monsters, I am glad I found a partner in crime. There was an instant connection and we only grew closer and inseparable. I always look forward to us meeting and talking for hours as we can never run out of topics. I had an unforgettable

experience when I visited your family in Naples. I wish someday I could return you the favor when you visit India. I developed a special bond with **Rens Kamphorst** when we sat next to the big canal in Delft till 4 in the morning talking about our lives and getting to know each other from deep within. We then connected on music and started hosting our listening sessions to critique newly released albums and artists. Thank you for expanding my music knowledge and taking the initiative to attend concerts from Kendrick Lamar and JPEGMAFIA, an experience that I will never forget. One of the sweetest guy I have ever met is **Albert Santoso**. You were the only one who always complimented me on my outfits. You have been so kind to have invited me over multiple times to your place for such delicious food and special evenings. In the final months, entered this extremely energetic and awkwardly funny girl named **Lena Fasching** who sat right in front of me. I could not help but imitate and poke fun at your Austrian accent. Thank you Lena for being such a good sport when I was so mean to you. I tested you with my jokes and you reciprocated the same foolishness. It is so much fun when you are around as we are getting a lot more drunk than we usually did.

I have also had the privilege to share the office with some young blood who joined in my last year of PhD. Starting off with **Riccardo Dal Mas**, whose ability to connect words in conversation with puns and all kinds of random references is sheer talent in my opinion. I am super impressed by your discipline of going to the gym before work and still making it to the office before everyone else. Then came **Qing Li** who always had nice entertaining stories. It was so much joy to just watch and listen to you everyday naive struggles. Very quickly our office filled up with **Simone**, **Sophie**, **Gurhan**, **Marc** and **Ignasi**. Thank you guys from bringing new energy and fun to the last months of my PhD. I wish all of you the best of luck to finish your PhDs in the near future. In the other PPE office, I especially want to thank **Christian** for being a part of the organization committee of all the PPE group activities and christmas dinners. These days were extremely special and memorable and all credits goes to you and **Leslie** for making it such a beautiful experience. To the AI team, **Lukas**, **Gao**, **Giacomo** and **Max**, I wish you guys all the best for your PhD and for your future endeavours. And special thanks to **Gao** and **Lukas** for hosting for a real Chinese hotpot dinner experience. **Ming** all the best for your PhD and looking forward to attending your defence soon.

There are a few people that I have known from the very first days of my time in Netherlands back in Twente that have earned family-like status. **Parth**, **Husain**, **Vishwajit aka VVK**, **Ashwini** and **Akash** thank you so much guys for making my time in NL home-like. **Husain** and **VVK**, I give you special credit for invoking the passion of cooking in me as I only started to cook proper food when we lived together. **Parth**, if you hadn't been there, I would not be into fitness. I consider you my personal trainer from fitness to fashion. We have connected on a different level where we have texted the same thing at the same time multiple times that it is not a coincident anymore. **Ashwini**, you are a true comedic and I have so much joy doing silly jokes with you. **Akash**, bro from the time we shared a room during your internship and till today, it has been a long journey and I am happy that we are still together and there for each other. My time in Twente is incomplete without **Fernanda Akegawa Monteiro**. Our occasional phone calls would be a constant reminder of the comfort I have with you. I am so happy to call you my best friend as I can share with you anything without having a second thought. Thanks for

being there always by my side.

Every year I try to visit New Delhi, India, my hometown and catch up with all my friends in a very short period of time. These friends make my visit absolutely worth and memorable every time giving me the full experience and joy. My school friends **Udit**, **Divit**, **Akshat**, **Brijinder**, **Shivalik** and **Himanshu**, meeting you guys is an instant nostalgic feeling of my time in New Delhi. Then a special gang called P14 with its truest members; **Mohit**, **Aabhaas aka Abazz Deepu**, **Divyam**, **Sahil**, **Yash**, and **Mickey bhaiya** are real friends making my visit always a special and memorable one.

I also would like to thank my relatives (**Khala, Jami Uncle, Bade Chacha, Sahla Chachi** and cousins **(Sidrah, Daraab, Osaid, Owais, Yasser bhai, Nayab bhai and Maria apa)** who have supported me in this journey and always checked up on me whenever we met during my visit in India. Here in the Netherlands, **Karel** and **Margreet Bezstarosti** have given me a very warm welcome into their family and I always look forward to visiting them on weekends for a gezellig time.

My grandmother **(Mrs. Ayesha Rehman)** and I shared a very strong and deep connection. Her constant prayers and wishes are the reason behind my success. In 2021, she drew her last breath and this was the first big loss in my adulthood where I felt my entire childhood was over in a blink of an eye. Nani, I thank you for the faith and trust you put in me, and for all the prayers and good wishes you have showered upon me. To my brother, **Mr. Osama Rahman**, thank you for taking care of mummy and papa when I am gone. Your presence at home gives me comfort to stay abroad. I wish you all the best for your new journey making Kaamkhor a success and all of your future endeavours. To my father, **Mr. Matiur Rahman**, I have always looked up to you as an example of hard work, dedication and commitment. I have acquired so many qualities from your personality and as I turn into my 30s, I have even started to resemble you. I know you miss my presence more than mom and yet never mention it to me or ask me to come back only because you want the best for me. To my mom, **Mrs. Sabiha Rahman**, our weekly phone calls for hours to catch up on every single detail of our lives and to share both happy and sad moments is something I look forward till this day. Your blind faith and trust in me is deeply appreciated and gives me support and strength for every decision I make in my life. You have made the biggest sacrifice of letting your son go and live abroad only for me to have a successful future. And finally, **Dr. Suzanne Bezstarosti**, you have been the best thing that happened to me in the Netherlands. You are extremely caring, understanding and supportive which makes you the best companion I can wish for. I look forward to spending the rest of my life with you.

ABOUT THE AUTHOR

Zaid Rahman was born on the 19^{th} of May 1994 in New Delhi, India. Zaid began his academic journey with a deep interest and passion for technology and pursued his first professional degree in Bachelors in Nanotechnology from Amity University, Noida, India. From 2012-16, he was trained in subjects of modern physics especially quantum physics, thermodynamics and fluid mechanics. He performed a 6-month bachelor thesis research project at Bharat Petroleum Corporate Research and Development Centre, Greater Noida, India. There, he synthesized a nano-catalyst aimed to improve the hydrodesulfurization reaction efficiency of a commercial disease feed. Zaid graduated his B.Tech program with a first division with distinction and began his professional career as a Business Analyst in the medical device start-up company, Wrig Nanosystems Pvt. Ltd., based in New Delhi, India.

In August 2017, Zaid moved to the Netherlands and pursued a Master of Science (MSc.) in Nanotechnology at University of Twente, Enschede. He was awarded a 2-year University of Twente Scholarship (UTS) for his academic excellence. Educated and trained at state of the art of MESA+ Nanolab, he mastered several sophisticated microfabrication techniques and performed his thesis project in Mesoscale Chemical Systems led by prof. dr. J.G.E (Hans) Gardeniers. There, he designed and fabricated a microfluidic device using photo-lithography technique for droplet formation with precise control over droplet production speed and size. He also visited the Lung Bioengineering and Regeneration Centre at Lund University, Sweden to incorporate patient-derived tissue material and cells in the microfluidic chip for tissue regeneration application. Zaid successfully defended his thesis in August 2019 and graduated first division with distinction.

Motivated and inspired by the academic research environment in leading Dutch universities, Zaid began his PhD in October 2019 under the supervision of Dr. Pouyan E. Boukany in the Department of Chemical Engineering at Delft University of Technology, The Netherlands. In his PhD, he focused on developing 3D in vitro (microfluidic) platforms to mimic a physiologically relevant tumor microenvironment to investigate cancer cell signaling and invasion activity. Zaid has contributed to and successfully led multidisciplinary collaborations with biologists at Leiden and Erasmus Medical Centers. Following up with this expertise and delving into further complexity of 3D cancer models and tumor microenvironments, he is now employed as a post-doctoral researcher at the Department of Medical Oncology in Laboratory of Tumor Immunology led by prof. dr. J.E.M.A (Reno) Debets at Erasmus MC, Rotterdam. Here, he will investigate the patient specific metastasis drivers, immune subsets and associated phenotypes in patient-derived organoid models co-cultured with immune cells.

List of Publications

Journal publications related to this dissertation:

3. A. van der Net*, **Z. Rahman***, A. D. Bordoloi, I. Muntz, P. T. Dijke, G. H. Koenderink, P. E. Boukany “Interplay between matrix mechanical properties and cancer cell invasion." *under revision, * equal author contribution)*

2. **Z. Rahman**, A. D. Bordoloi, H. Rouhana, M. Tavasso, G. V. D. Zon, V. Garbin, P. T. Dijke, P. E. Boukany “Interstitial flow potentiates TGF-β/Smad-signaling activity in lung cancer spheroids in a 3D-microfluidic chip." *Lab on a Chip*, 2024.

1. P. Mehta* , **Z. Rahman*** , P. T. Dijke, P. E. Boukany, "Microfluidic meets 3D cancer cell migration.", *Trends in Cancer*, 2022, *(* equal author contribution).*

Other journal publications:

1. S. Zhang, T. Bastiaan, J. van de Peppel, G.J. Kremers, M. Koedam, G. R Pesch, **Z. Rahman**, R. M Hoogenboezem, E. MJ Bindels, J. W. van Neck, P. E Boukany, J. PTM van Leeuwen, B. CJ van der Eerden, "Microfluidics-based evidence that mesenchymal stromal cells-derived biochemical factors and biomechanical signal synergize to control endothelial cell function.", *Acta Biomaterialia*, 2022.

Conference proceedings/presentations:

6. **Z. Rahman**, A. D. Bordoloi, H. Rouhana, M. Tavasso, G. V. D. Zon, V. Garbin, P. T. Dijke, P. E. Boukany, American Society of Cell Biology, Boston, USA, *Poster Presentation*, December 2023.

5. **Z. Rahman**, A. D. Bordoloi, H. Rouhana, M. Tavasso, G. V. D. Zon, V. Garbin, P. T. Dijke, P. E. Boukany, Dutch Biophysics, Veldhoven, the Netherlands, *Oral Presentation*, October 2023.

4. **Z. Rahman**, A. van der Net, A. D. Bordoloi, G. H. Koenderink, P. E. Boukany, & Physics @ Veldhoven, Veldhoven, the Netherlands, *Oral Presentation*, April 2023.

3. **Z. Rahman**, H. Rouhana, M. Tavasso, V. Garbin, P. T. Dijke, P. E. Boukany, hDMT Annual Consortium meeting, Amersfoort, the Netherlands, *Oral Presentation*, November 2022.

2. **Z. Rahman**, H. Rouhana, M. Tavasso, V. Garbin, P. T. Dijke, P. E. Boukany, EMBL Defining and Defeating Metastasis Symposium, Heidelberg, the Netherlands, *Poster Presentation*, June 2022.

1. **Z.Rahman**, V. Garbin, P. E. Boukany, Physics @ Veldhoven, Veldhoven, the Netherlands, *Online Poster Presentation*, January 2021.